acta physica slovaca vol. 58 No. 1, 1 – 154 February 2008

NEW ISOTOPE TECHNOLOGIES IN ENVIRONMENTAL PHYSICS

P.P. Povinec^{a,1}, M. Betti^{b}, A.J.T. Jull^{c}, P. Vojtyla^{d}
^{a} *Faculty of Mathematics, Physics and Informatics, Comenius University*
Mlynská dolina F-1, SK-84248 Bratislava, Slovakia
^{b} *European Commission, Joint Research Centre, Institute for Transuranium Elements*
P.O. Box 2340, 76137 Karlsruhe, Germany
^{c} *NSF Arizona AMS Laboratory and Departments of Physics and Geosciences*
University of Arizona, Tucson, AZ 85721-0081, USA
^{d} *European Organization for Nuclear Research (CERN), Geneva, Switzerland*

Received 17 April 2008, accepted 24 April 2008

As the levels of radionuclides observed at present in the environment are very low, high sensitive analytical systems are required for carrying out environmental investigations. We review recent progress which has been done in low-level counting techniques in both radiometrics and mass spectrometry sectors, with emphasis on underground laboratories, Monte Carlo (GEANT) simulation of background of HPGe detectors operating in various configurations, secondary ionisation mass spectrometry, and accelerator mass spectrometry. Applications of radiometrics and mass spectrometry techniques in radioecology and climate change studies are presented and discussed as well. The review should help readers in better orientation on recent developments in the field of low-level counting and spectrometry, and to advice on construction principles of underground laboratories, as well as on criteria how to choose low or high energy mass spectrometers for environmental investigations.

PACS: 07.85.Nc, 24.10.Lx, 29.20Ba, 29.30.Ep, 29.40Mc, 29.40.Wk, 82.80.Ms, 92.60.Ry, 98.70.Sa

KEYWORDS: Radionuclides; Depleted uranium; HPGe detectors; Liquid scintillation spectrometry; Low-level counting; Underground laboratory; Monte Carlo simulation; GEANT; In situ underwater gamma-spectrometry; Mass spectrometry; Secondary ionisation mass spectrometry; Inductively coupled plasma mass spectrometry; Thermal ionisation mass spectrometry; Resonance ionisation mass spectrometry; Accelerator mass spectrometry; Radioecology; Climate change

---

[1] E-mail address: povinec@fmph.uniba.sk; formerly at the International Atomic Energy Agency, Monaco.

Contents

Introduction

Investigations with environmental radionuclide tracers began about 60 years ago with applications of cosmogenic (^{14}C and ^{3}H) and natural (^{210}Pb, ^{226}Ra) radionuclides. This has been a rapidly developing field, which has included studies on behaviour of radionuclides in the environment, use of natural and anthropogenic radionuclides as tracers of environmental processes, marine radioactivity studies, radiation protection, radioecology, etc., to mention at least a few of them. These studies have always been limited by the techniques available for sampling and analysis of radionuclides in the environment. As the levels of radionuclides observed at present in the environment are very low, high sensitive analytical systems are required for carrying out environmental investigations. Sampling techniques have developed from simple devices into the present robotic systems based on ROVs (Remotely Operating Vehicles) and other sophisticated sampling technologies, which use satellite views of areas for the optimisation of sampling. For example in the marine environment, where the research work has been heavily depending on the new technologies, we have seen a replacement of time consuming and expensive large volume water sampling (500 L) from several km water depths by Rosette multisampling systems (operating with 12-24 bottles of $\sim$10 L volume) enabling high resolution water sampling of the water column within one or two casts only (Povinec, 2004).

State of the art of analytical technologies have always been a limiting factor for environmental radioactivity studies, either because of the fact that the available sensitivity was not high enough to get meaningful results, or the required sample size was too big to carry out such investigations, very often with limiting financial resources. In the field of radioanalytical technologies we have moved from simple radiochemical methods and gas counters to efficient robotic radiochemical techniques and sophisticated detectors working on line with powerful computers, often situated underground or having anticosmic and/or anti-Compton shielding to protect them against the cosmic radiation, and thus considerably decreasing their background and increasing their sensitivity for analysis of radionuclides in the environment at very low-levels.

Further, the philosophy of sampling and laboratory measurements has changed, where appropriate, to in situ analysis of radionuclides in the air, on land, in water and in the sediment, thus enabling development of isoline maps of radionuclide distributions in the investigated environments. There has also been an important break-through in the philosophy of radionuclide analysis in the laboratory from the concept of counting of radioactive decays (and thus waiting for them) to the direct counting of atoms (as they would be stable isotopes) using high sensitive mass spectrometers working either with low energy ions (e.g. Thermal Ionisation Mass Spectrometry – TIMS, Inductively Coupled Plasma Mass Spectrometry – ICPMS, Resonance Ionisation Mass Spectrometry – RIMS, Secondary Ionisation Mass spectrometry - SIMS), or with accelerated ions to levels of tens or hundreds of MeV in Accelerator Mass Spectrometry (AMS) systems.

All these developments have enabled to carry out research which has not been possible before either because of lack of sensitivity or required sample size. Simultaneously, it has also been possible to proceed from analyses of bulk samples to compound specific analyses, e.g. by a combination of gas chromatographs (a selection of specific compounds) and mass spectrometers (isotope analysis). This move from simple analytical techniques to the present sophisticated state of the art technologies has been accompanied by a considerable change in the philosophy of environmental studies as well, from institutional investigations from the fifties to the seventies, to global international investigations carried out in recent years, e.g. WOCE (World Ocean

Circulation Experiment), CLIVAR (Climate Variability and Predictability), PAGES (Past Global Changes), to mention at least a few of them.

As the topic is very wide, it has not been possible to cover all aspects of sampling and radionuclide analyses in detail; the emphasis has been on recent developments in the field. Similarly, the list of references, although very comprehensive, could not cover all the work done, but again it is mostly listing only the recent publications. Several conferences on low-level counting and spectrometry have been organised in the past, where more detailed information can be found (e.g. Povinec and Usačev, 1977; Povinec 1982a; Povinec 1986; Povinec 1987; Garcia-Leon and Madurga, 1991; Povinec, 1991a; Povinec, 1992; Garcia-Leon and Garcia-Tenorio, 1994; Holm *et al.*, 1996; Cook *et al.*, 1996; Povinec, 1999; Kutschera *et al.*, 2000; Schwaiger *et al.*, 2004; Povinec and Sanchez-Cabeza, 2006). A few monographs have been published as well, where readers can find more specific information (Theodorson, 1996; Debertin and Helmer, 1998; Tuniz *et al.*, 1998; Povinec, 2008). For example sampling techniques (Scott and Dixon, 2008; Macášek, 2008; Povinec, 2004), radiochemical separation methods (Aoyama and Hirose, 2008; Povinec, 2004), statistical data evaluation (Currie, 2008), applications of the neutron activation analysis for determination of long-lived radionuclides (Hou, 2008), and *in situ* techniques using mobile gamma-ray spectrometers, helicopters and airplanes (Tyler, 2008), have recently been covered in specific reviews. New trends in mass spectrometry techniques for analysis of long-lived radionuclides including ICPMS (Roos, 2008) and RIMS (Erdmann *et al.*, 2008) have recently been reviewed as well.

In the present review we discuss in detail some recent developments in measuring techniques using radiometrics and mass spectrometry methods. We focus here on the main breakthrough which in the radiometrics sector has been development of underground laboratories for low-level counting. Monte Carlo simulations of detector background characteristics have been important pre-requisite when designing low-level counting systems, also important when working in laboratories situated hundreds of meters underground, where radioactive purity of construction materials and radon concentration in the air become dominant factors controlling the detector background. These techniques are described in detail with the aim to help and encourage readers with interests in low level counting to build underground laboratories. *In situ* underwater techniques represent a new approach in analysis of environmental radionuclides that have been recently applied for radionuclide mapping of seabed sediments and/or stationary monitoring of radionuclides in the aquatic environment. A transfer from bulk sample analysis to particle analysis has been another example of breakthrough in mass spectrometry, which is described in detail using SIMS. AMS is covered as well, as it has been the most important, really a revolutionary break-through in analytical methodologies for long-lived environmental radionuclides. Recent progress in environmental studies is illustrated by several examples in environmental radioactivity studies, as well as in climate change studies.

We hope by publishing this review to offer readers an overview of recent developments in isotope technologies, encourage and advice them how to build the state of the art analytical laboratories for environmental research.

Acknowledgements

The authors thank Prof. V. Bužek, the Chief Editor of *Acta Physica Slovaca*, for his invitation to write this review. PPP would like to thanks his colleagues from the International Atomic Energy Agency's Marine Environment Laboratories (IAEA-MEL) in Monaco, as well as from the Comenius University of Bratislava (UNIBA) for fruitful collaboration. MB thanks her colleagues at the Institute of Transuranium Elements for assistance, and AJTJ is grateful for the technical support of the staff of the NSF Arizona AMS Laboratory and for support from NSF grant EAR0448461 and 0622235.

Fruitful collaboration and discussions with numerous colleagues from Australia (K. Fifield of the Australian National University of Canberra; M. Hotchkis of the Australian National Science and Technology Organisation of Sydney), Brazil (J. de Oliveira, Instituto de Pesquisas Energéticas e Nucleares, Sao Paulo), Canada (L. Keiser of the University of Toronto), France (P. Bailly de Bois, Institut de Radioprotection et de Sureté Nucléaire, Octeville; C. Musa, Commisariat l'Energy Atomique, Paris), Georgia (S.V. Pagava of the University of Tbilisi), Germany (H. Nies, Bundesamt fuer Seeschiffahrt und Hydrographie, Hamburg), India (B.L.K. Somayajulu of the Physical Research Laboratory of Ahmedabad), Ireland (T.P. Ryan, Radiation Protection Institute of Ireland, Dublin), Italy (M. Laubenstein, Instituto Nazionale Fisica Nucleare, Gran Sasso), Japan (M. Aoyama and K. Hirose of the Meteorological Research Institute, Tsukuba; O. Togawa of the Japan Atomic Energy Research Institute of Tokai; K. Komura of the University of Kanazawa), Korea (G.H. Hong of the Korea Ocean Research and Development Institute of Seoul), UK (P.J. Kershaw and D. Woodhead of the Centre for the Environment, Fisheries and Aquaculture of Lowestoft), USA (W.C. Burnett of the State University of Florida; Z. Top of the University of Miami), as well as from international organizations, namely P. Aggarwal, K. Froehlich and M. Groening (IAEA, Vienna), M. Hult (EC Institute for Reference Materials and Measurements, Geel) has been appreciated. This work has been partially supported by IAEA (project No. 14301/R0) and VEGA (project No. 1/0108/08).

1 Underground Low-Level Counting and Spectrometry

Underground installations for low-level counting and spectrometry represent the most significant break-through in radiometrics technologies for non-accelerator nuclear and particle physics, cosmic ray physics and environmental physics. An increasing number of experiments have been devoted to the detection of very rare events, e.g. experiments on solar neutrinos, double beta-decay, searches for dark matter and experiments in environmental physics have gained a continuously growing interest in modern physics. Their common feature is a utilization of high sensitive low-level counting spectrometers, operating very often underground (e.g. Heusser 1995; Povinec, 2004, 1994).

Already early experiments on solar neutrinos (Davis *et al.*, 1966) showed that an underground environment is a necessary prerequisite for rare nuclear and particle investigations. However, it has been stress only recently that even for conventional low-level counting experiments the underground environment is a must, if high sensitivity is required (Loosli *et al.*, 1986; Heusser, 1994). In contradiction to large scale experiments, such as solar neutrino experiments or double beta decay experiments, environmental experiments do not require deep underground installations of the order of 1000 m w.e. (the unit “water equivalent” is used to normalize for different shield environments, e.g. rock, lead, iron, etc.). A considerable improvement of counting parameters can be reached even at depth of the order of tens of meters of w.e. The nucleonic component of cosmic rays is significantly reduced even in such low depths, what has considerable effect on the detector background.

Very important recent development in the radiometrics sector of analysis of radionuclides in the environment has also been the availability of large volume HPGe detectors (about 200% relative efficiency compared to a 76 mm in diameter and 76 mm long NaI(Tl) detector). However, because of the large volume and mass of an HPGe detector, interactions between cosmic rays and the detector affect considerably its background characteristics. An anticosmic shielding and/or underground operation of detectors has become therefore important for their optimum utilization for analysis of environmental radionuclides (Heusser, 1994; Povinec, 1994; Heusser, 1995; Reyss *et al.*, 1995; Niese *et al.*, 1998; Neder *et al.*, 2000; Neumaier *et al.*, 2000; Vojtyla and Povinec, 2000; 2006; Semkow *et al.*, 2002; Povinec, 2004; Povinec *et al.*, 2004; Schroettner *et al.*, 2004).

1.1 Detector Background

The main sources of background in a low-level counting system are:

(i) cosmic rays

(ii) radionuclides in the detector environment

(iii) radon

For better understanding of cosmic ray induced background and its effect on counting sensitivity of the detection system we need to review sources of the detector background in detail.

1.1.1 Cosmic Rays on the Earth Surface and Underground

Composition and Fluxes of Cosmic Rays. Primary cosmic rays (CR) are high energy particles consisting mainly of protons, alpha particles ($\sim$ 13 %) and heavier nuclei ($\sim$ 1 %). They

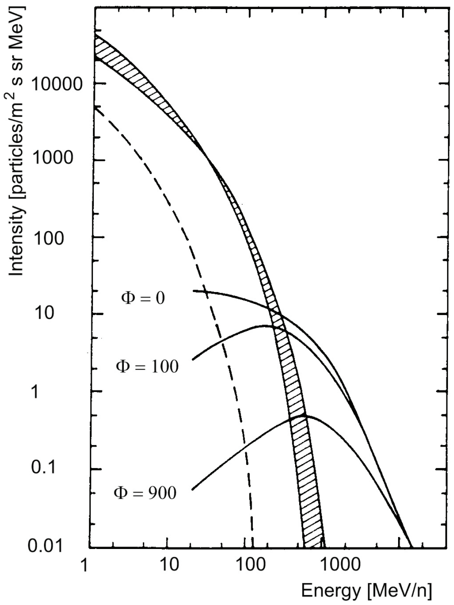

Fig. 1.1. Time averaged galactic (modulated) cosmic ray spectra for different modulation parameter Φ, solar protons with characteristic rigidity $R_0 = 100\text{-}150$ MV (dashed area), and of solar alpha-particles (broken line) (modified from Castagnoli and Lal, 1980).

originate either outside of the solar system (galactic cosmic rays), or they are emitted by major flares on the Sun (solar cosmic rays). The galactic cosmic rays (GCR) have higher energies (mostly in the energy interval from 0.1 to 100 GeV), but lower mean fluxes (about 3 particles $\mathrm{cm}^{-2}\mathrm{s}^{-1}$), whereas the solar cosmic rays (SCR) have lower energies (from 5 to 100 MeV), but higher fluxes (about 100 particles $\mathrm{cm}^{-2}\mathrm{s}^{-1}$). A comparison of cosmic ray fluxes at various energies is presented in Figure 1.1 (Castagnoli and Lal, 1980).

The primary cosmic rays interact with atmospheric nuclei and produce various secondary CR particles, like nucleons, hyperons, mesons, light nuclei, etc. These secondary particles have high energies enough to undergo nuclear collisions and to produce next generations of particles. Some of the particles are unstable, and produce new particles in decay processes (muons, electrons, positrons, neutrinos, photons, etc.). Especially GCR particles produce in the Earth's atmosphere a large number of secondary particles – neutrons, protons and pions, which have enough energy to interact again and to develop hadronic and electromagnetic cascades. The hadronic cascade contains strong interacting particles, like protons, neutrons and pions. The energy spectrum of neutrons can be expressed as

$$p_n(E)dE = Ee^{-E/E_0}dE, \tag{1.1}$$

where the temperature of the excited nucleus E_0 is around 1 MeV. Because of the fact that neutrons do not loose energy by ionisation, their pass length in the atmosphere is longer and their flux is higher than that of protons.

The electromagnetic cascade contains electromagnetic and weak interactions particles, like electrons, positrons and photons. These particles do not contribute to nuclear reactions in the atmosphere. Finally, at sea level we have a huge number of secondary CR particles distributed over $\sim$ 1 km^2 that originated from one high energy galactic proton. The relative intensities of charged particles at sea level are as follows: 1 for muons, 0.34 for neutrons, 0.24 for electrons, 0.009 for protons and 0.0007 for pions. The muon flux at sea level is about 1.9 muons cm^{-2}s^{-1} (Gaisser, 1990).

Some of the particles finally end in nuclear reactions with atmospheric nuclei (O, N, Ar, Ne, Kr, Xe) and produce cosmogenic nuclides (e.g. ^{3}H, ^{7}Be, ^{10}Be, ^{14}C, ^{37}Ar, ^{39}Ar, ^{81}Kr, etc.). For example ^{14}C is produced in the reaction ^{14}N(n,p)^{14}C.

The secondary cosmic ray particles observed at the sea level can be therefore grouped into three main components:

(i) a hard component, consisting mainly of muons;

(ii) a nucleonic component, consisting of neutrons (97 %) and protons;

(iii) a soft component, consisting of electrons, positrons and photons.

The flux of soft component particles can be considerably decreased due to electromagnetic showers in materials with high atomic number, like lead, iron, mercury, etc. The layer of 20 cm of lead is enough to leave behind a neglecting number of soft radiation particles. This is the reason why conventional passive shields of low-level detectors contain 10-20 cm of lead (or 20-40 cm of iron).

On the other hand, the flux of hard component particles cannot be decreased by the reasonable thickness of shielding material. This can be only done by installation of detectors deep underground. However, a partial elimination of the hard component in the detection system is possible using an anticoincidence shielding.

A composition and fluxes of primary and secondary CR particles are given in Table 1.1. The total flux of CR is 300 particles m^{-2}s^{-1}, the hard component is 190 particles m^{-2}s^{-1}, the soft component is 50 particles m^{-2}s^{-1}and the nucleonic component is around 60 particles m^{-2}s^{-1}. About 75% of all particles at sea level are penetrating particles, mostly muons. The sea level vertical flux ratio for protons to muons is about 3 % at 1 GeV/c (0.5 % at 10 GeV/c).

Variations of cosmic rays. Primary cosmic rays undergo several types of variations which considerably change their energy spectra and fluxes. Figure 1.1 shows typical spectra and fluxes of galactic and solar cosmic rays. The modulation effect of the 11 year solar cycle (the most prominent variation in the GCR intensity) on the galactic component of CR can be seen as well. Due to this effect the flux of GCR particles with the energy above 0.1 GeV vary by a factor of 3 (at the energy 0.1 GeV this may be as high as 6 times). At energies above 10 GeV this effect is negligible.

The differential spectra of primary galactic particles can be described by the formula

$$I(E,\Phi) = C\frac{E(E+2mc^2)(E+m+\Phi)^{-2.65}}{(E+\Phi)(E+2mc^2+\Phi)} \tag{1.2}$$

with

$$m = 780e^{-2.5\times10^{-4}E} \tag{1.3}$$

where E is the particle kinetic energy, Φ is a modulation parameter, m is the mass of the proton, c is the velocity of light, and $C = 1.244 \times 10^6$cm^{-2}s^{-1} MeV^{-1} is a normalization factor. The modulation parameter Φ takes into account the influence of the solar modulation ($\Phi = 100$ MeV for the interstellar unmodulated spectrum, and $\Phi = 900$ MeV for the solar activity maximum) (Castagnoli and Lal, 1980). During a period of high solar activity (the sunspot maximum) the solar wind modulation effect is maximal, what causes a minimal galactic flux, and vice versa.

The time averaged solar flare CR spectra are well represented over a wide range of energies by a single exponential rigidity spectrum

$$dN/dR = k\, e^{-R/R_0}, \tag{1.4}$$

where R_o is the characteristic rigidity (Figure 1.1). Solar flare particles predominantly occur just before or after the maximum of the 11 year solar cycle.

Both cosmic ray variations can cause significant changes in background of low-level system if a proper shielding is not applied, especially, if a long counting is required. There can be sudden changes in the galactic flux also due to Forbush decreases, associated with changes in the Earth's magnetosphere during periods of high solar activity. The fluxes of cosmic ray particles also depend on the geomagnetic latitude, being higher at polar regions.

Tab. 1.1. Composition and fluxes of primary and secondary (at sea level, outside of laboratory) cosmic-ray particles (UNSCEAR, 1993).

Cosmic rays	**Composition**	**Energy**	**Flux** [m^{-2} s^{-1}]	**Relative flux** %
Primary				
	Protons			86
	Alpha-particles			12.7
	Heavier nuclei			1.3
Galactic		0.1 - 1000 GeV	~ 30 000	
Solar		5 - 100 MeV	~ 1 000 000	
Secondary (at sea level)				
Hard component	Muons	0.1 - 1000 GeV	190	
Nucleonic component	Neutrons		64	
	Protons		1.4	
	Pions		0.13	
Soft component	Electrons Positrons		46	

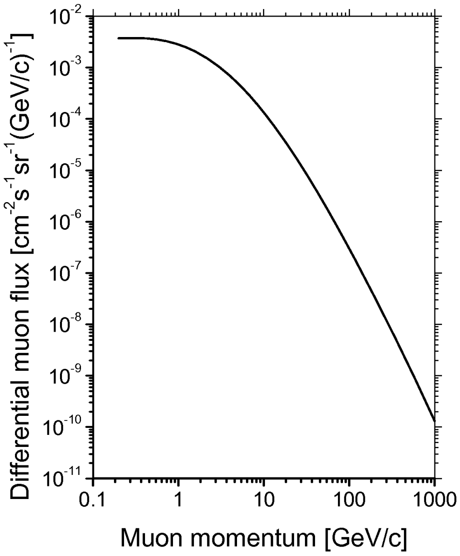

Fig. 1.2. Differential muon spectrum at sea level (modified from Allkofer and Grieder, 1984).

The third most important source of cosmic ray variations that can significantly influence low background installations is associated with changes of the muon flux in the atmosphere, so called barometric effect. Muons originate in the upper layers of the Earth's atmosphere. The layer of their origin is fluctuating according to the barometric pressure. If the barometric pressure is high, then the place of their origin is shifted to upper layers because of the shift of critical atmospheric masses. On the other hand, if the barometric pressure is low, then the critical layer is shifted to lower heights. Muons (negative or positive) are unstable particles with the mean life time of 2 μs. Therefore, if their place of origin is in upper atmospheric layers, they should overcome a longer distance to reach the Earth's surface, and part of them with lower energies (velocities) will decay on the way. The muon flux at the Earth's surface will be therefore higher at a lower barometric pressure. The fluctuating muon flux can significantly change the detector's background, if a proper shielding is not applied. The counting system should be calibrated against changes in the barometric pressure by measuring background at different barometric pressures, and by applying suitable correction factors. However, this approach is correct only in the case of slow changes of the barometric pressure. Sudden changes of barometric pressure which can occur several times during long-term measurements, and subsequent changes in the muon flux may cause false results, if corrections are not properly applied.

Penetration of muons through shielding. We have already seen that the soft component of secondary CR may be easily eliminated by 20 cm of lead. On the other hand, the penetration power of the hard component (muons) is much stronger. The differential muon flux depends strongly on the muon momentum. Allkofer and Grieder (1984) compiled available data and constructed the muon spectrum presented in Fig. 1.2 which has been used in our simulations. We

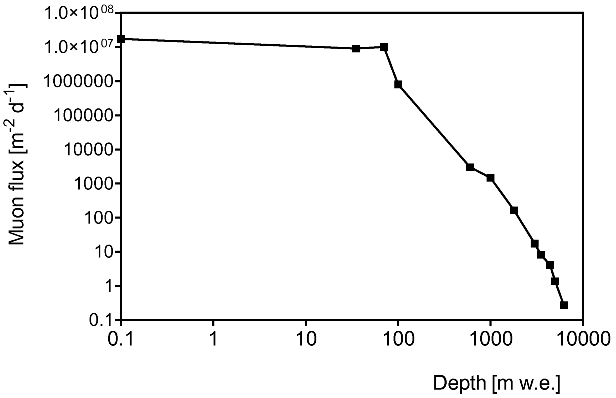

Fig. 1.3. Measured muon fluxes in underground laboratories (data compilation from literature).

see that the prevailing part of muons have momenta between 0.5-10 GeV/c, and the differential flux decreases rapidly with higher momenta. The muon flux at sea level has a mean energy of about 2 GeV and a differential spectrum falling as E^{-2}. The angular distribution can be expressed by the simplified formula

$$j = j(0)\cos^2\vartheta, \tag{1.5}$$

where $j(0)$ is the vertical flux and ϑ is the zenith angle.

This behaviour of muons makes real difficulties for a design of an optimum shield for low-level counting. In a surface laboratory the lead should not be too thick to increase the contribution of neutrons produced by muons to the total background. To decrease this neutron component a layer of anti-neutron shield, based on light, low Z materials, like polyethylene, paraffin, etc., for neutron slowing down and a subsequent capture, preferably in (n, α) reactions on Li or B, should be added to the lead shield. However, these reactions are accompanied by emissions of soft gamma-rays, which may subsequently increase a photon background in the shield.

The best way how to solve this complicated problem is therefore to install the detection system underground, deep enough, where the muon component is relatively low. Various underground physics experiments require different reductions of the muon intensity. Large scale experiments (e.g. solar neutrino experiments, double beta-decay experiments) require overburden of shielding at least around 1 km w.e. For conventional low-level counting installations such depths are not necessary. Such underground laboratories are not usually available at the place, their dedicated construction is very expensive and their operation is usually complicated and expensive. However, as we shall see later, a shielding of a few 10 m w.e. has great influence on the background reduction. For a comparison, Figure 1.3 shows a decrease of the muon flux with the rock overburden measured in underground laboratories

Muons therefore make the most important contribution to the detector's background, although their contribution to nuclear reactions in the atmosphere and lithosphere is much lower in comparison to nucleons. However, nuclear reactions of muons can be of importance when heavy shields are used. A partial elimination of their contribution to the detector's background is possible by utilization of an anticoicidence system. Although a reduction in the background over a factor 100 can be obtained in gas proportional counters (Povinec, 1978), the best solution is to install the low-background system deep underground, where the flux of muons is several orders of magnitude lower than in a surface laboratory.

Protons from the nucleonic component of cosmic radiation have low intensity compared to neutrons and, moreover, they are converted to neutrons in nuclear reactions with shielding materials of the building and a metallic shield. Therefore only muons and neutrons (the hard component of cosmic rays) are important for background induction, as especially in the case of muons they can easily penetrate the shielding materials surrounding the detector.

The nucleonic component of secondary CR (mostly neutrons) is dramatically changing with depth, and a shielding of about 10 m w.e. may decrease the flux by 4 orders of magnitude. Shielding against soft component particles (electrons, positrons, photons) can be easily done by 15-20 cm of pure lead with minimum radioactive contamination, or with some other heavy material like iron or copper. As we have already mentioned, primary and subsequently also secondary CR undergo strong intensity variations that heavily influence counting parameters of low background detection systems. To decrease their negative influence, especially during long counting times, the best solution is to install the counting systems underground.

Buildings and other shielding structures absorb secondary neutrons (200 g cm^{-2}) better than muons (2000 g cm^{-2} at sea level). Therefore, the relative composition of hard cosmic radiation varies according to the distance below the surface. At low depths ($\sim$ 10 m w.e.) muons are by far the prevailing component of cosmic radiation. The muon energy spectrum is shifting to higher energies with increasing depth as the softer spectrum is gradually filtered out.

Secondary neutrons (actually we should call them tertiary, to distinguish them from the neutrons produced in the upper atmosphere) are produced in the shielding (building materials, metallic shielding) by muon capture and fast muon nuclear interactions. At moderate depths ($\sim$ 30 m w.e.), the negative muon capture prevails as the muon energy spectrum is rich in low energy muons that are likely to be stopped. On the other hand, fast muon nuclear interactions dominate deep underground ($>$ 100 m w.e.).

However, not only particle flux magnitudes, but also mechanisms and efficiencies of background induction processes are important. Muons deposit tens of MeV energy in an HPGe detector by direct ionisation. This is outside of interest for most of low-level counting applications. The main processes by which cosmic muons induce detector background are electromagnetic processes which are taking place in the metallic shield. Muons generate delta electrons that radiate bremsstrahlung initiating electromagnetic particle showers. Photons from showers are then forming a background radiation as they can penetrate through thicker layers of material. For muons of higher energies there is also a contribution from direct electron-positron pair formation and muon bremsstrahlung. For muons of lowest energies, muon decay positrons and electrons with energies up to 52 MeV, and negative muon nuclear capture, contribute as well.

Processes including a production of nuclei are even more complicated to study. During muon capture, the atomic number Z of a nucleus decreases by one, and the nucleus radiates gamma-rays and fast neutrons when re-arranging its structure. These processes lead to activation of shielding and detector materials. Heusser (1995) estimated the flux of neutrons produced by muon capture to be 1.1×10^{-4} cm^{-2}s^{-1} for the muon flux of 8×10^{-3} cm^{-2} s^{-1}. A part of high energy muons ($>$ 100 Ge) also interacts with nuclei via virtual photons, causing their spallation accompanied by emission of numerous hadrons. These reactions are another source of tertiary neutrons which are important in deep underground laboratories.

A muon-induced background gamma-spectrum of a Ge detector is characterised by a dominant 511 keV annihilation peak and a continuum peaking at about 200 keV. The integral background count rates are within 0.6-1.6 s^{-1} at sea level, depending on the size of the detector, the detector and shield materials and the shield lining. Annihilation peak count rates are usually ~ 0.01 s^{-1}. The comparison of background spectra measured with various shielding material shows that the continuum decreases with the increase in the atomic number Z of the shielding material and its maximum shifts to higher energies. The reason is in a stronger self-absorption of induced radiation in higher Z materials. Thin layers (mm) of lining have a significant influence on the shape and background counting rate (Vojtyla and Povinec, 2006).

An efficient way to eliminate the muon induced background is the use of anticosmic (guard) detectors surrounding the main analysing detector (Heusser, 1994, 1995; Vojtyla *et al.*, 1994; Semkow *et al.*, 2002; Povinec *et al.*, 2004; Schroettner *et al.*, 2004). These detectors register cosmic muons before they generate secondary particles in the shield, and anti-coincidence electronics rejects such background counts. Gas proportional chambers placed inside the shield have a small efficiency for gamma-rays, and they can introduce additional radioactive contamination into the shield (Heusser, 1994, 1995; Vojtyla *et al.*, 1994). NaI(Tl) detectors used as anticosmic shielding have much better efficiency for gamma-rays, however, due to contamination of crystals and glass of photomultipliers by ^{40}K, it is not advisable to use them inside a shield, unless they are part of an anti-Compton spectrometer (Povinec, 1982; Povinec *et al.*, 2004). At present mostly plastic scintillators or large proportional chambers placed outside of the shield are used. The advantage of proportional chambers is their small count rate (~ 200 s^{-1}), and hence negligible corrections for dead time. Plastic scintillation detectors, although having higher counting rates, they have advantage that can detect neutrons as well.

The basic mechanisms of background induction by neutrons in Ge detectors are their capture and nuclear excitation by inelasting scattering. A neutron induced gamma-ray spectrum of a Ge detector contains a number of lines that can be attributed to nuclei in a detector working medium (Ge isotopes), and to nuclei of materials in the vicinity of the detector. Their intensities depend on the size of the detector, the cryostat and shielding materials, and most importantly on the shielding depth below the surface. Heusser (1993) compiled a large number of gamma-lines observed so far in background gamma-ray spectra. A characteristic feature of neutron induced background spectra are saw-tooth shaped peaks with energies of 595.8 keV and 691.0 keV corresponding to inelasting scattering of fast neutrons on ^{74}Ge and ^{72}Ge. The Ge nuclei de-excite almost immediately compared to the time of charge collection and the de-excitation energy is summed with the continuously distributed recoil energy of the nucleus. Therefore, these peaks have sharp edges from a lower energy side and tails towards higher energies. The summation does not take place during de-excitation of long-lived isomer states of Ge isotopes that de-excite after collection of the charge from the primary process. The most intensive lines of this kind are those of ^{75m}Ge and ^{71m}Ge ($T_{1/2} = 47.7$ s and 21.9 ms, respectively) with energies of 139.7 keV and 198.3 keV and count rates of up to 2×10^{-3} s^{-1}. Further, lines coming from the shielding materials can be identified in neutron induced background spectra, e.g. ^{206}Pb, ^{207}Pb, ^{63}Cu and ^{65}Cu (Heusser, 1993; Vojtyla *et al.*, 1994).

Neutrons also induce a background continuum and the annihilation peak, probably via hard gamma-rays emitted from highly excited nuclei. Hard gamma-rays loose their energy by Compton scattering, and initiate electromagnetic showers during their passage through shield materials. The shaped of the continuum is ruled by Z of the material and lining used, similarly as in the case of muon induced background. The neutron induced background can be minimised with antineutron shields consisting of layers made of low Z materials for their slowing down (e.g. polyethylene, paraffin) with admixture of boron or lithium for their capturing. However, their usefulness depends on shielding layers situated above the laboratory. If neutrons are mostly tertiary, i.e. produced in the shield, the neutron absorbing layer should be the innermost layer. This leads, however, to large shield dimensions and hence higher shield costs, as the neutron absorbing layer should be tens of cm thick to be efficient enough. For shields situated deeper underground (> 10 m w.e.) where tertiary neutrons produced by cosmic muons prevail, a better solution would be to use an anticosmic shielding place outside of the shield.

Although the anticosmic shielding is very effective way to decrease the detector background, it cannot be 100 % effective in eliminating the effects of cosmic rays. However, a substantial overburden by placing the detection system deep underground can have profound effects on the background reduction. Down to a few tens of m w.e. cosmic rays still prevails, and an anticosmic shielding would be still useful. In the transition region to a few hundreds of m w.e., cosmic rays are still of importance, however, radioactivity free materials for the construction of detectors and shields become more and more important. Below about a thousand m w.e. the cosmic ray background is already negligible. The hadronic component of cosmic rays is efficiently removed by the first 10 m w.e. (Heusser, 1995), and comic muon induced particle fluxes (tertiary neutrons, photons) are ruled by the penetrating muon component.

There are two other background components that were not covered earlier as they are negligible for surface laboratories, but important for specific applications carried out deep underground: neutrons can also be created in uranium fission and (α, n) reactions in surrounding materials. The estimated flux of about 4.5×10^{-5} cm^{-2} s^{-1} corresponding to the average U and Th concentrations in the earth crust (Heusser, 1992) is negligible compared to that generated by cosmic rays in shallow depths, but it is important in experiments carried deep underground. These neutrons can also penetrate thick shields and induce background either directly or via a long-term activation of the construction material. The simplest way of eliminating this background source is to shield the U and Th containing walls with a neutron shielding material of sufficient thickness (at least 20 cm).

The secondary cosmic ray particles can induce background not only in one event by interactions in the detector and surrounding materials that are shorter in time than the resolution time of electronics, but also by production of radioactive nuclei in materials intended to be used underground but processed and stored at sites with higher cosmic ray fluxes. The cosmic activation component is caused by short-lived radionuclides (e.g. $^{56-58}$Co, ^{60}Co) produced primarily in other target elements such as copper or iron. The activated contamination can be sometimes more important than the residual primordial contamination. The most important mechanisms of the activation are secondary neutrons (at shallow depths or higher altitudes), and by negative muon capture and fast muon interactions (at underground laboratories). Many short-lived radionuclides can be produced during the time of an intercontinental aeroplane flight due to high fluxes of secondary cosmic ray particles (mostly neutrons) at altitudes of about 10 km. At shallow and deep shielding depths, after filtering out secondary neutrons, fast muon interactions and negative muon capture activate materials either directly by disintegration and changing nuclei, or through tertiary neutrons. Compared to the direct background induction, the fast muon interactions at shallow shielding depths are more important than the muon capture.

^{65}Zn, ^{57}Co, ^{58}Co and ^{54}Mn are produced at saturated production rates of tens to hundreds of

μBq kg^{-1} by the activation of germanium at sea level. ^{54}Mn is also produced at a high saturated production rate of 4.5 mBq kg^{-1} in iron used for the construction of shieldings (Brodzinski *et al.*, 1990). The magnitude of background due to cosmic ray activation is, e.g. in the case of saturated ^{65}Zn activity of 0.44 mBq kg^{-1} in germanium at sea level in a 1 kg Ge detector, which gives an integral background rate above 50 keV of only 11 counts per day (Brodzinski *et al.*, 1990).

1.1.2 Radionuclides in the Detector Environment

Detector. The most sophisticated techniques for reducing the background will be unsuccessful if the detector is made of contaminated materials. Selecting radio-pure materials for the detector is important as these materials are close to the detector sensitive volume and radiation from them is detected with high efficiency. Most materials are contaminated with the primordial radionuclides, ^{40}K, ^{238}U and ^{232}Th (Table 1.2).

Complex production processes and contacts with various reagents increase the probability of contamination with primordial radionuclides. Usually, each production step must be checked to be sure that the produced material will be free of contaminants to the desired level. Physical and chemical procedures to which to processed material is subjected, result in isolated impurities (e.g. ^{210}Pb, ^{226}Ra, ^{228}Tl) as elements of the decay series have different properties and the chain breaks down.

In fabricating metals, the redox potential is generally an important factor influencing the degree of radio-purity that can be achieved. That is probably the reason that copper can be produced very cleanly and is widely used in low-level counting applications. Its redox potential of 0.337 V is high compared to those of K, U and Th and their progenies. Cooper is routinely purified after melting by electrolytic dissolution and subsequent redeposition in solution even in large scale production.

The contribution of radioactivity of detector materials to the background depends significantly on the detector type. It is usually lowest for semiconductor detectors as in this case a detection medium has to be very pure merely to enable the proper function of a semiconductor

Tab. 1.2. Radionuclide contamination of materials used for construction of detectors and shields.

Material	^{40}**K** [Bq kg^{-1}]	^{228}**Tl** [Bq kg^{-1}]	^{226}**Ra** [Bq kg^{-1}]
Quartz	< 1	0.1-1	0.1-10
Aluminized mylar	< 30	1-5	1-5
Berylium	< 20	0.1-3	1-10
Epoxy	10-1000	5-100	1-1000
Molecular sieve	~ 100	~ 50	~ 100
Electrolytic copper	0.001-5	0.001-5	0.001-5
Aluminum	0.5-15	0.1-50	0.1-50
Stainless steel	0.1-20	1-20	1-30
Lead	0.001-10	0.01-10	0.01-100

diode (a charge collection). The material is cleaned from primordial radionuclides and also from ^{137}Cs as a by-product through zone refining and crystal pulling. The background originates in parts placed around the crystal, and closer a part is the cleaner it should be. Materials used for crystal holders, end-caps and signal pins have to be selected most carefully.

To obtain the best results the crystal holders should be made of electrolytic copper (~ 0.1mBq $\times$kg^{-1} of ^{238}U, ^{232}Th and ^{40}K), but this can reduce the transparency for low-energy gamma-rays. Low-Z aluminium is widely used, but it is usually contaminated with U and Th. However, aluminium devoid of these radionuclides to the 100 ppt level is available and is now used in low-level versions of detectors. Insulating materials (Teflon, PTFE. etc.) are usually radio-pure (< 1 ppm K). All materials used must be cleaned of surface contamination using acid, or be electropolished.

The care in selecting materials for detector encapsulation may be unnecessary if two other sources of background, molecular sieve and electronic circuits, are not removed. A molecular sieve is used to maintain the vacuum in the cryostat and can contain up to 100 Bq kg^{-1} of ^{238}U, ^{232}Th and ^{40}K. Specially prepared activated charcoal with massic activities below 1 Bq kg^{-1} of ^{226}Ra and 20 Bq/kg is an alternative. Vacuum maintaining substances should be placed far from the crystal and behind the shield. If the cooled FET assembly is close to the crystal, the loss in energy resolution is negligible.

For HPGe detectors, the background from contamination can be as low as a few counts per day in peaks of radionuclides in question, and therefore negligible compared to other components in systems operating in moderate shielding depths.

Shielding Materials. A detector should be placed in a massive shield, best made of high Z material, to minimise the environmental background. An anticoincidence detector with high efficiency for gamma-radiation (e.g. NaI(Tl), BGO – bismuth germanate) can be used to further decrease the detector background, and usually also scattered photons, when working as an anti-Compton gamma-ray spectrometer (Debertin and Helmer, 1998). A comparison of background gamma-ray spectra with and without massive shield can be found e.g. in Sýkora *et al.* (1992). A background spectrum is usually dominated by ^{40}K (1461 keV), ^{214}Bi (609.3 keV and 1120.3 keV) and ^{208}Tl (583.1 keV and 2614.7 keV). The integral background of an unshielded Ge gamma detector of usual size is ~ 100 s^{-1}. In the energy region above 200 keV and under the Compton edge of the ^{208}Tl peak, the background is reduced by two orders of magnitude by placing the detector inside the shield. Except for the 511 keV annihilation peak, attenuation factors for lines of the radionuclides in question are in agreement with the assumed absorption properties of the shielding layers for gamma-radiation of corresponding energy. On the other hand, the continuum in the spectrum is attenuated almost independently of the energy (Vojtyla, 1996). It could be expected that the photons of lower energies would be absorbed more efficiently than those with higher energies. The reason that this does not occur is that the lower energy photons are continuously replenished by Compton-scattered photons of higher energies when passing through the thick layer of material. In this way, the continuous spectrum reaches an equilibrium shape with a general attenuation coefficient. Smith and Lewin (1990) using Monte Carlo simulation, found a mass attenuation coefficient of 0.045-0.050 cm^2 g^{-1} for both high-Z and low-Z shielding materials.

It is not worth increasing the thickness of the shielding over about 150 g cm^{-2} because other background components begin to dominate the total background. Muon-induced background together with a usually smaller neutron component rule the background beyond this thickness. Moreover, increasing the thickness of a high-Z material like lead enhances the production of tertiary neutrons by negative muon capture (mostly at low altitudes below sea level) and fast muon interactions (deeper underground). Paradoxically, the background increases slightly due to interactions of tertiary neutrons when increasing the shield thickness over 150 g cm^{-2}.

Lead has proven to be the best material for bulk shields as it is cheap, has good mechanical properties, a high atomic number, low neutron capture cross-section, small neutron gamma yields and a low interaction probability for cosmic rays including the forming of radionuclides by activation. However, its intrinsic radioactivity can often be disturbing. Many authors investigated the origin of lead contamination in the past (Kolb, 1988); Heusser, 1993). When using gamma spectrometry to check lead contamination, ^{210}Pb and its progenies ^{210}Bi and ^{210}Po are hidden contaminants as they cannot be clearly identified by gamma lines. Due to the long half-life of ^{210}Pb (22 years), the abundance of these radionuclides in lead can be much higher than expected from secular equilibrium. ^{210}Pb itself does not contribute to the background of Ge gamma-spectrometers as its very soft beta (E$_{max}$ of 16.5 keV and 63 keV) and gamma (46.5 keV) radiations cannot escape self-absorption. The background is induced by the progeny ^{210}Bi emitting hard beta radiation with end-point energy of 1161 keV. Beta-radiation generates bremsstrahlung in the high-Z material, and also lead X-rays with energies of 72.8 keV, 75.0 keV, 84.9 keV and 87.4 keV. The continuum peaks at around 170 keV. As the end-point energy of ^{210}Bi is not sufficient for efficient pair production, the annihilation peak cannot be observed in the spectrum.

Concentrations of ^{210}Pb reported in the literature range from 0.001 to 2.5 kBq kg^{-1} (Povinec *et al.*, 2004). Ordinary contemporary lead has a ^{210}Pb massic activity of $\sim$ 100 Bq kg^{-1}. Lead with ^{210}Pb massic activity of about 1 Bq kg^{-1} is commercially available, lead with a lower activity is very expensive. Once ^{210}Pb is present in lead it cannot be removed by any chemical procedure and the only way to eliminate it is to wait several half-lives for its decay. Old lead is an alternative to modern radioactive pure lead, however, its supply from water pipes, sunken shiploads or the ballast of sailing ships are limited. Moreover, old lead may not always be radioactive pure. If uranium was not removed, ^{210}Pb will have been supplied from the uranium decay series from the beginning of lead production.

Another possibility is to use old iron plates or rods for the detector shielding. A recent iron may be dangerous because of ^{137}Cs contamination from Chernobyl fallout, or due to a contamination during its production (usually by ^{60}Co). Therefore iron should be always tested before purchasing. Electrolytic copper is a better material, however, it is much more expensive than iron or ordinary lead. Also *in situ* production of cosmogenic radionuclides in copper may be disadvantageous when operating at shallow depths.

Radionuclides Outside of the Detector. The sources of background radiation are decay product of nuclei in U and Th decay series and ^{40}K. Generated gamma-radiation is critical and therefore a massive metallic shielding is required to protect detectors. A typical sea level gamma-ray flux above 50 keV at 1 m above ground is 10 photons cm^{-2} s^{-1}, representing the most intensive photons flux to which an unshielded detector is exposed. The cosmic photon flux is less than 1 % of the environmental flux. A contribution from all other primordial radionuclides to the detector background is negligible.

The average concentrations of primordial radionuclides in the continental upper crust are 850 Bq kg^{-1} of ^{40}K, 100 Bq kg^{-1} of ^{87}Rb, 44 Bq kg^{-1} of ^{232}Th and 36 Bq kg^{-1} of ^{238}U (Table 1.3). Except for ^{232}Th, the concentrations are about twice as small in soils, but large variations can occur. The highest concentrations are found in granites and pegmatites. Secular equilibrium in decay series is rarely achieved in surface and near surface geological environments because the radionuclides in the chain migrate and take part in various chemical and physical processes. A special case is radon which breaks each series and can, due to its inert nature, migrate far from the rock or soil surface. Therefore radon will be treated separately in this chapter later.

The impact of cosmogenic radionuclides produced in the atmosphere on the background of Ge detectors is usually negligible. Large amounts of radionuclides were released to the environment during the Chernobyl accident. Relatively long-lived ^{137}Cs is still present as a surface contamination of construction materials, therefore it should be checked and removed if present, especially in materials used for the detector construction.

1.1.3 Radon

Background induced by radon is part of the environmental radioactivity background, but because of its specific nature it will be covered separately. Two radon isotopes – ^{222}Rn and ^{220}Rn found in the detector environment belong to the ^{238}U and ^{232}Th series, respectively. We already discussed that these primordial radioelements are present in all construction materials. As radon is an inert gas, it diffuses after its formation from the walls to the vicinity of the detector. The radon concentration can vary between 0.1-100 Bq m^{-3} in living and working areas (Beláň *et al.*, 1992).

From the point of view of gamma background, the ^{222}Rn ($T_{1/2}$= 3.82 day) progenies - ^{214}Pb (242.0 keV, 295.2 keV and 351.9 keV) and ^{214}Bi (609.3 keV and 1120.3 keV) are more important than the ^{220}Rn ($T_{1/2} = 55.6$ s) progenies – ^{212}Pb (238.6 keV) and ^{208}Tl (583.1 keV and 2614.7 keV), as the ^{220}Rn half-life is much shorter.

The easiest method of eliminating the radon background is to flush the cavity around a detector with nitrogen evaporating from the Dewar (Brodzinski, 1991; Sýkora *et al.*, 1992). A flow rate of about 2 L per minute is sufficient. A small overpressure that builds up expels radon from the detector cavity. More sophisticated systems use shield cavities that can be evacuated and filled with radon-free gas, e.g. nitrogen or old air (Heusser, 1991). Plastic materials should not

Tab. 1.3. Radionuclides in natural rocks.

Rock	^{40}**K** [Bq kg^{-1}]	^{232}**Th** [Bq kg^{-1}]	^{238}**U** [Bq kg^{-1}]
Granite	1000-3000	70-200	30-300
Basalt	200-1000	10-50	6-30
Sandstone	300-15000	8-40	6-30
Limestone	50-400	1-10	3-40
Salt	< 10	0.02	0.04

be placed inside the shield as their surface draws radon progenies by electrostatic attraction. If these measures are not taken, the radon contribution to the detector background can be several counts per hour, even in well ventilated laboratories.

A comparison of ranges of various background components in a typical well-designed 1 kg low-level HPGe detector inside a lead shield with good ventilation is presented in Table 1.4.

1.2 Underground Installations

The background of a low-level counting system is a limiting factor in many new applications. A detailed analysis of background (Heusser, 1994; Povinec, 1994) has shown that many counting systems have not been optimised in relation to background interferences. Even with sophisticated anti-Compton or anticosmic spectrometers placed in surface laboratories, the background is still too high to substantially decrease the size of samples, to be comparable to the size of samples used for mass spectrometry. The reason is that in a well designed passive shield, a cosmic ray-produced background plays a dominant role. We already discussed that while the nucleonic component (mainly neutrons) is attenuated at 10 m w.e. by about 4 orders of magnitude, the muonic component remains at this shielding layer without notable reduction (by a factor of 2 only). To decrease the muonic component by a factor of 10, shielding of over 50 m w.e. is needed. At 1000 hg/cm^2 depth, the reduction in muon flux can be as high as 10^6 (Povinec, 1994).

The behaviour of muons makes the design of an optimum shield for low-level counting very difficult. In a surface laboratory, if the lead shield is too thick muons will produce neutrons and thus increase the quantity of neutrons in the total background. The best solution to this complex problem is to install the detection system underground at sufficient depth, where the muon flux is relatively low. Limestone or sandstone are preferable to granite because of radionuclide contamination (^{40}K, Th, U series) and will have a lower (by a factor of 10) neutron production due to (α, n) reactions.

There has been several underground low-level counting systems build at depths between 15 m w.e. to 6000 m w.e. We shall discuss separately shallow and deep laboratories, concen-

Tab. 1.4. Detector background components for a low-level HPGe detector of 1 kg mass located in a lead shield of 10 cm thick.

Background component	**Integral counting rate** [s^{-1}]
Environmental radionuclides	30 - 300
Muons	0.3 - 2
Cosmic neutrons	0.03 – 0.2
Radionuclides in the shield	0.01 – 0.2
Radon and its daughters	0.01 – 0.1
Radionuclides in the detector	0.003 – 0.03
Detector activation by cosmic rays	0.0004 – 0.002

trating only on gamma-spectrometers with HPGe detectors. Discussions on gas counters can be found e.g. in Povinec (1994. The effective cross section of a Ge detector is usually much smaller than that for a gas detector, however, because of its higher detector density, a Ge-detector is more sensitive to cosmic-ray induced background. Therefore, there have been more laboratories operating Ge-detectors underground than gas detectors. The underground Ge-spectrometry started with Fiorini's pioneering work on double beta-decay search of ^{76}Ge in the Mont Blanc tunnel laboratory, when Ge detector was used both as a source and a detector (Alessandrello *et al.*, 1986).

1.2.1 Shallow Underground Laboratories

MPI Heidelberg laboratory (15 m w.e.). The underground laboratory of the Max Planck Institut für Kernphysik in Heidelberg was probably the first laboratory that has been using an underground environment for everyday low-level gamma-spectrometry work, originally with NaI(Tl) detectors, and later with Ge detectors (Heusser *et al.*, 1982). As the laboratory is located at the depth of 15 m w.e. only, an anticosmic shielding against cosmic muons made of proportional chambers surrounding the passive shield (15 cm of lead plus 5 cm of iron) has been installed. Thanks to the anticosmic shielding and the use of radionuclide free construction materials a factor of 20 background reduction in the low energy part of the gamma-ray spectrum has been reached. The air surrounding the Ge detector has been removed by radon free nitrogen which decreased the gamma-peaks of ^{214}Bi by a factor of 12. The laboratory has been mostly used for testing of low background Ge and gas detectors, and construction materials used in Gran Sasso solar neutrino (Heusser, 1995) and double beta-decay experiments (Klapdor-Kleingrothaus *et al.*, 2004). A comparison of background spectra of a recently built specially designed HPGe detector system tested in MPI Heidelberg and operating at Gran Sasso (3800 m w.e.) has shown that a reduction of about 2 orders of magnitude has been obtained (Heusser *et al.*, 2006).

TU Garching laboratory (20 m w.e.). A special room was build with concrete walls and a 5 m thick layer of soil was brought on it. In this lab besides other installations a germanium spectrometer was installed in a lead shield, together with an anticoincidence shielding consisting of plastic scintillators (Niese, 2008).

University of Arizona at Tucson laboratory (25 m w.e.). A dating laboratory was constructed under the building at 10 m depth, where liquid scintillation spectrometers "Quantulus" made by Wallac have been installed. Their background for ^{14}C measurements is reduced by a factor of 2 (Kalin and Long 1989).

IAEA-MEL Monaco laboratory (35 m w.e.). The International Atomic Energy Agency's Marine Environmental Laboratories (IAEA-MEL) underground facility in Monaco has been constructed under an underground parking at a depth of 12 m. The laboratory has been using four HPGe detectors located in a common lead shield surrounded by anticosmic veto-shielding made of plastic scintillation detectors (Povinec *et al.*, 2004, 2006a). The laboratory is equipped with ventilation and an air conditioning system maintains overpressure in the laboratory, stable humidity and temperature. The laboratory also contains an anti-Compton gamma-ray spectrometer

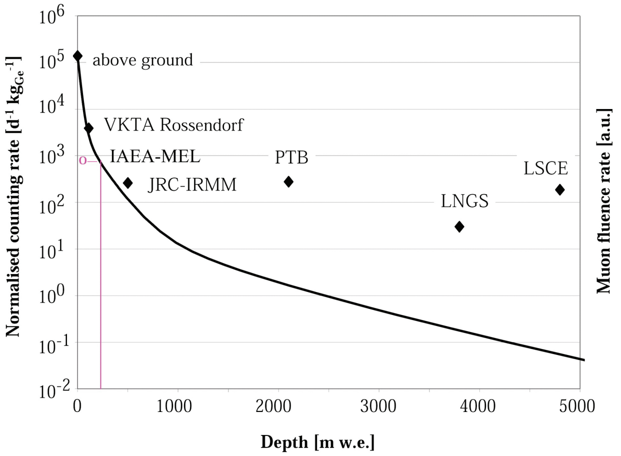

Fig. 1.4. Normalised integral background counting rates (40-2700 keV) of HPGe detectors operating by CELLAR laboratories at various depths. The solid line represents the muon flux in arbitrary units normalized to the background counting rate above ground. Abbreviations of underground laboratories: at 110 m w.e. – Verein für Kernverfahrenstechnik und Analytik (VKTA at Rossendorf), at 500 m w.e. - Joint Research Centre-Institute of Reference Materials and Measurements (JER-IRMM at Geel), at 2100 m w.e. – Physikalisch-Technische Bundesanstalt (PTB at Braunschweig), at 3800 m w.e. - Laboratori Nationali del Gran Sasso (LNGS, at Assergi), at 4800 m w.e. – Laboratoire des Sciences du Climat et de l'Environnement (LSCE, at Modane), and at 35 m w.e. – IAEA-MEL at Monaco, the only laboratory in this figure with anti-cosmic veto (modified after Laubenstein *et al.*, 2004).

with NaI(Tl) anticoincidence shielding, that may also operate as a concidence gamma-gamma spectrometer. A low-background liquid scintillation spectrometer Quantulus have also been installed in this underground laboratory. The laboratory has mostly been used for analysis of gamma-emitters in marine samples, as well as for development of reference materials. Using the HPGe spectrometers with anticosmic shielding it has been possible to analyze ^{137}Cs in seawater samples of 10 L only. This reduction of sample volume by a factor of 10 has considerably decreased not only a sampling time, but enabled to do research which was not possible before. The reduction in sample size also allows the same sample to be used for gamma-ray spectrometry as well as for mass spectrometry measurements (e. g. ICPMS, TIMS or AMS analyses of water samples for uranium and plutonium isotopes). Although the Monaco laboratory is operating at 35 m w.e. only, thanks to the anticosmic veto-shielding its background is comparable with laboratories operating at depths of around 250 m w.e., as it is documented in Figure 1.4, where integral backgrounds of HPGe detectors operated by CELLAR (Collaboration of European Low-level Underground Laboratories) groups are presented.

NASA-JSC laboratory (50 m w.e.). The Radiation Counting laboratory was build 20 m underground for the measurement of extraterrestrial samples at the NASA Johnson Space Center (JSC), Houston, Texas (Lindstrom *et al.* 1990). The laboratory has been mostly used for analysis of cosmogenic radionuclides in lunar samples and meteorites.

Holborn laboratory (60 m w.e.). The laboratory is located in an underground tunnel of the London subway, and operated by the Birkbeck College (Barton, 1991). The laboratory has been used for testing HPGe and scintillation detectors for dark matter searches.

University of Bern laboratory (70 m w.e.). The laboratory has been installed at 25 m depth in a cellar under the Physical Institute of the Bern University (Loosli *et al.*, 1986). Low radioactive concrete (40 cm thick) made of serpentinite and Danish cement was used for internal coating of walls. The laboratory is housing proportional counters (for analysis of ^{14}C, ^{37}Ar, ^{39}Ar), liquid scintillation spectrometers and HPGe detectors.

1.2.2 Medium-Depth Underground Laboratories

VKTA Dresden laboratory (125 m w.e.). The VKTA (Verein für Kernverfahrenstechnik und Analytik at Rossendorf) laboratory is installed at a depth of 47 m in a cave formerly housing an old brewery. The shielding consists from outside to inside of 10 mm of a new steel, 270 mm of granulate hard steel, 36 mm of an old steel, 30 mm of lead and 12 mm of an old steel. The total surface thickness is 210 g cm^{-2}. For a thermal isolation a 10 m thick layer of polystyrene fume (styropore) is used. The detectors itself are shielded separately with 10 to 17 cm of lead (Niese, 1998; 2008). The activity of ^{222}Rn in the cave is high, up to 200 Bq/m^3. Therefore heated fresh air is introduced from outside into the laboratory. The evaporated nitrogen from the cryostat is used to replace the radon containing air within the shielding of the detector. The laboratory is housing several HPGe detectors.

Tbilisi University Laboratory (180 m w.e.). The University of Tbilisi is operating an underground laboratory in a tunnel (shielded by sand rock by about 80 m thick) connecting the Botanical garden with the center of the town (Pagava *et al.*, 1992). The laboratory occupies a part of a hall (200 m^2) used for investigations of fluxes of cosmic muons and neutrons. Ge detectors and liquid scintillation spectrometers housed in the laboratory has been used for environmental studies including radiocarbon dating.

Grand Coulee Dam laboratory (260 m w.e.). The Batelle Memorial Institute at Richland has installed counting devices in a gallery of the Grand Coulee Dam, 110 m under the top of the dam. The solid concrete provides 78 m of horizontal shielding downstream and 13 m upstream. The laboratory has been used for the investigation of the sources of background in NaI(Tl) and HPGe spectrometers (Kaye *et al.*, 1972).

Ogoya laboratory (270 m w.e.). The laboratory was constructed by the Low-Level Radioactivity Laboratory of the Kanazawa University, Japan, in a tunnel of a former copper mine with an overburden of 135 m of rock (Komura and Hamajima, 2004). More than 10 HPGe detectors installed in the laboratory have been used for atmospheric and marine radioactivity studies.

JER-IRRM Geel laboratory (500 m w.e.). The JER-IRRM (Joint Research Centre-Institute for Reference Materials and Measurements at Geel) laboratory was constructed in a special mine designed for investigations of the behaviour of nuclear wastes in clay. A place at 225 m depth was reserved for the low-level counting laboratory. The laboratory is equipped with various HPGe detectors and doing research in nuclear physics and metrology (Hult *et al.*, 2000; 2006).

Oroville Dam Laboratory (600 m w.e.). The laboratory is situated in the powerhouse of the dam in the foothills of the Sierra Mountains of California, and operated by the University of California for investigations of double beta decays (Caldwell, 1991).

1.2.3 Deep Underground Laboratories

Baksan Neutrino laboratory (660 and 4400 m w.e.). The low-level counting laboratory is situated at 660 m w.e. in one of the horizontal caves in the Baksan valley (North Caucasus) and operated by the Institute of Nuclear Studies of Russian Academy of Sciences in Moscow. For reducing the detector background from the environmental shale rock, a two-layer wall has been installed. The outer one consists of concrete from low-activity dunite and the inner one is made of dunite without cement (Pomansky, 1986; Klimenko *et al.* 1986). Later a new laboratory was installed in a cave in a depth of 4400 m w.e. where rare decay experiments have been carried out.

INR Solotvina laboratory (1000 m w.e.). The laboratory is situated in a former salt mine (430 m rock overburden) in Solotvina, west of Ukraine, and operated by the Institute for Nuclear Research of the Ukrainian National Academy of Sciences in Kiev. Due to a low-radioactive contamination of salt, the natural background is about two orders of magnitude lower than in other underground laboratories. The radon concentration in the air is below 33 Bq m^{-3}. The Laboratory has been used for the investigation of rare nuclear processes (e.g. double beta-decay; Zdesenko, 1991).

The Soudan laboratory (1800 m w.e.). The laboratory is located in an iron mine in Minnesota and operated by the School of Physics and Astronomy of the University of Minnesota for neutrino physics experiments. At a depth of 1800 m w.e. the number of cosmic ray particles is reduced by five orders of magnitude (Litchfield *et al.*, 1991).

PTB Braunschweig laboratory (2100 m w.e.). The Physikalisch-Technische Bundesanstalt (PTB) underground laboratory for dosimetry and spectrometry is located in the Asse salt mine, near Braunschweig. At the laboratory depth of 925 m the cosmic muon flux is reduced by 5 orders of magnitude. There is also an advantage of a low activity of the surrounding rock salt and low concentration of radon in the air. The laboratory is housing several HPGe detectors and doing research in environmental radioactivity and metrology (Neumaier *et al.*, 2000).

Canfranc laboratory (2450 m w.e). The laboratory is constructed in a tunnel at Canfranc in the Spanish Pyrenees. Zaragoza University, in collaboration with many foreign institutes, has been carried out in the Canfranc laboratory experiments on rare nuclear decays (Morales, 1991).

Gotthard laboratory (3000 m w.e.). The laboratory is situated in the Gotthard tunnel with about 1000 m of rock overburden. The laboratory has been operated by the University of Neuchatel, and used for double beta-decay and dark matter searches (Treichel *et al.*, 1991).

LNGS laboratory (3500 m w.e.). The LNGS (Laboratori Nationali del Gran Sasso at Assergi) is the largest underground laboratory in the world, located about 120 km from Rome in a tunnel under the Gran Sasso Mountain. The laboratory consists of three large experimental halls and several small rooms. The 1400 m rock cover gives a reduction factor of the cosmic ray flux of about one million; moreover, the neutron flux is thousand times less than on the surface, thanks to the low uranium and thorium content of the dolomite rocks of the mountain. The laboratory has been used for experiments in nuclear physics (double beta-decay), particle physics (neutrino oscillations with a beam from CERN accelerator) and nuclear astrophysics (solar and supernova neutrinos, dark matter searches), as well as for HPGe detectors (Heusser, *et al.*, 2006), and liquid scintillation spectrometers (Plastino and Kaihola, 2006) background investigations. The laboratory is operated by the Italian Instituto Nazionale Fisica Nucleare in collaboration with many institutes from Italy and abroad.

Homestake gold mine laboratory (4400 m w.e.). This has been the oldest underground laboratory established by late Raymond Davis of Brookhaven National Laboratory in 1965 for investigations of solar neutrino reactions (Davis *et al.*, 1966). The laboratory has also been used for other purposes, e.g. for background suppression studies of Ge-detectors using selected non-radioactive materials and pulse shape discrimination for obtaining very low background (Brodzinski, 2005).

LSCE Modane underground laboratory (4800 m w.e.). The LSCE (Laboratoire des Sciences du Climat et de l'Environnement) laboratory is placed in the middle of the Fréjus tunnel which links Modane to Bardonecchia through the France-Italy border. The rock overburden is 1780 m. The laboratory is using several halls, the largest are hosting NEMO (Arnold *et al.*, 2005) and EDELWEISS (Martineau *et al.*, 2004) experiments. HPGe detectors and liquid scintillation spectrometers used for environmental research are located in small rooms.

Sudbury Neutrino Observatory (6200 m w.e.). The laboratory is located in the Creighton mine where 1000 ton D_2O Čerenkov detector was installed to look for cosmic neutrinos. The laboratory has been operated by the Queens University Kingston, Ontario, Canada (SNO, 2005).

Further developments. It has been clear that a considerable reduction in the detector background can be obtained only in laboratories operating deep underground. The muon flux with the rock overburden measured in underground laboratories presented in Figure 1.3 shows that at the depth below 3000 m w.e. only negligible fluxes, below 10 muons per m^2 per day have been measured.

However, it looks like that for the present state of the art of HPGe low background detectors the optimum depth would be around 1000 m w.e. Although in deeper laboratories the cosmic-ray muon flux is much weaker, in present installations it does not improve anymore background characteristics of HPGe detectors, as documented in Figures 1.4 and 1.5.

Therefore, a further reduction in the detector background would be possible only with a new generation of HPGe detectors, specially designed and produced for deep underground operations. Special requirements must also be applied for construction of detectors bodies and their shieldings where only high purity materials with minimum radionuclide contamination should

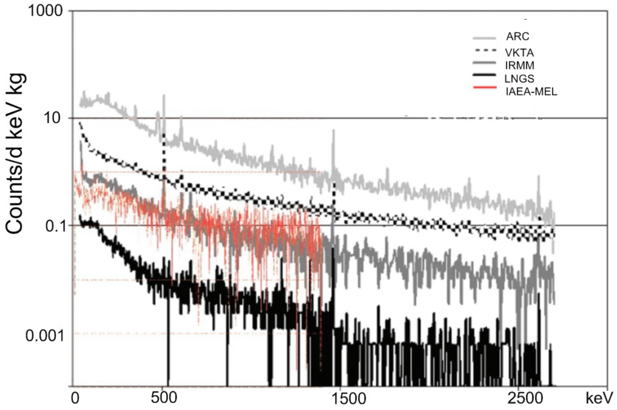

Fig. 1.5. Background spectra of HPGe detectors of the CELLAR laboratories operating at various depths. Abbreviations: at the surface with anticosmic veto (Austrian Research Centre, ARC). Other laboratory abbreviations as in Fig. 1.4 (modified after Laubenstein et al 2004).

be used. Similarly, a radon free environment surrounding the detector will be a must, especially for long-term measurements. Installations with HPGe crystals directly immersed in a liquid nitrogen bath could be a solution, e.g. in experiments searching for neutrinoless double beta-decay (Heusser *et al.*, 2006). The highly radio-pure cryogenic liquid serves there simultaneously as a shielding against external radiation and as a coolant.

2 Monte Carlo Simulation of the Detector Background

The development of a simulation code for background induction by cosmic rays is useful for optimisation of a counting system in respect to its background characteristics. The prediction of detector background characteristics can be made before the system is built, that can optimise the system characteristics, and it can also save money during the construction. Systematic investigations of the influence of various parameters on the detector background can be carried out as well. Monte Carlo simulations of background have been facilitated by the development of physics software and availability of powerful computers. As the processes leading to background induction are very weak processes that occur with low efficiencies, large numbers of events have to be processed to obtain results with acceptable statistical uncertainties.

We noticed that background components of a typical low-level HPGe detector, not situated deep underground, are cosmic radiation (cosmic muons, neutrons and activation products of construction materials), radionuclides present in construction material (including the detector itself), radon and its progenies. For a present-day, carefully designed low-level HPGe spectrometer, the dominating background component is cosmic radiation, mainly cosmic muons (Heusser, 1995; Theodorson, 1996; Vojtyla and Povinec, 2000; Laubenstein *et al.*, 2004; Povinec, 2004). High energy cosmic particles are initiating a large number of complicated physical processes leading to background induction. In order to quantify the background, it is necessary to deal with rather complicated detector-shield assembles and physics. Obviously analytical solutions are not possible and the only way to solve this problem is Monte Carlo simulation of interaction processes.

Although the most effective way of increasing the factor of merit of a counting system is to increase counting efficiency and the amount of sample in a detection system, usually the only possible way is to decrease the detector background. Therefore investigations of detector background were the most frequent studies in low-level counting and spectrometry (Heusser, 1994, 1995; Povinec, 1994, 2004; Zvara *et al.*, 1994).

In a single Ge gamma-ray spectrometer there is no protection against cosmic muons, therefore a spectrometer with anticosmic shielding will greatly reduce background levels. The anticosmic shield can be made of gas or plastic scintillation detectors, which surround the lead shield housing the HPGe detector (Heusser, 1994; Vojtyla *et al.*, 1994; Heusser, 1995; Semkow *et al.*, 2002; Povinec *et al.*, 2004; Schroettner *et al.*, 2004).

Another possibility is to use an anti-Compton spectrometer, which is a powerful tool for reducing the detector's background as it combines both anticosmic and anti-Compton background suppression (Debertin and Helmer, 1998; Povinec *et al.*, 2004). The most sophisticated spectrometric system is, however, the multidimensional coincidence/anti-Compton gamma-ray spectrometer (Cooper and Perkins 1971; Povinec, 1982) in which signals from the analysing detectors (nowadays HPGe) create three-dimensional spectra (volumetric peaks) which can contain both coincidence and anticoincidence events.

We shall simulate background characteristics of HPGe detectors operating in surface and underground laboratories under various arrangements. Monte Carlo code based on the CERN's GEANT code (CERN, 1990; 1993) will be used in these calculations.

2.1 Physical Basis of the Simulation

2.1.1 Source Term - Cosmic Muons

If a detector itself and the shield have been constructed from selected radioactivity free materials, then the dominating background component for a shallow installation is the flux of cosmic muons. Usually the detection systems are placed deep enough, where a contribution to the background from secondary neutrons is negligible. Therefore, cosmic muons and their interactions with the counting system are the most important for the background induction.

The first thing for assembling a code for simulation of background by cosmic muons we need to know their actual fluxes on the Earth. As cosmic muons are the most intensive and most penetrating particles at the sea level (we do not consider neutrinos), there are many experimental data available (Allkofer and Grieder, 1984). An ideal solution how to represent a muon flux would be to derive a function that would take into account all the parameters on which the muon flux depends. However, this would be too complicated approach as the flux depends on too many parameters, which change with time. The task is therefore to derive a simple standard description of the muon flux used as input to background simulation codes while being aware of magnitude and sense of possible deviations for a simulated system. We shall present only the basic parameters on which the cosmic muon flux depends, and the experimental basis for developing the code.

The muon flux depends strongly on the altitude, therefore we need to consider the real arrangements. We shall consider in our case that the detection system is placed almost at the sea level, representing differences in air mass overburden of less than 40 g cm^{-2} which can be neglected. The muon flux is higher at higher latitudes and lower near to the equator, as the Earth's magnetic field deflects primary cosmic rays at equatorial latitudes more intensively due to the stronger magnetic field. A comparison of integral muon fluxes measured in various latitudes at sea level shows that within the latitude range 40° - 60° (most of the industrially developed world), the muon flux varies by about 6 % (Allkofer & Grieder, 1984) - therefore we can neglect these differences. The differential muon spectrum compiled by Allkofer and Grieder (1984) (Figure 1.2) has been used in our simulations.

As cosmic muons are produced mostly by primary protons which prevail in cosmic radiation, positive muons will also prevail in the muon flux. This positive charge surplus depends on the multiplicity of particles produced during spallation reactions in the upper atmosphere, with a weak dependence of the muon charge ratio μ^+/μ^- on the muon momentum. Figure 2.1 shows the data on the muon charge ratio μ^+/μ^- for muons in vertical direction compiled from Allkofer (1975). The higher is the energy transferred during spallation of a nucleus, the higher is the particle multiplicity and lower is the μ^+/μ^- ratio. The ratio should decrease with increasing muon momentum, however, muons created in spallation with a low energy have low energy as well, and they have a little chance to reach the Earth's surface. Low energy muons found at sea level were created in reactions of secondary nucleons consisting from the same number of protons and neutrons so that the μ^+/μ^- ratio approaches 1 for decreasing momenta. This results in a maximum of muon charge ratio of about 1.3 at approximately 5 GeV/c. For very high muon momenta, the μ^+/μ^- ratio starts to increase because muons are produced not only in pion decays, but also in kaons decays in this region. However, the variation of the muon charge ratio is not so dramatic. The differences in behaviour of positive and negative muons in respect to

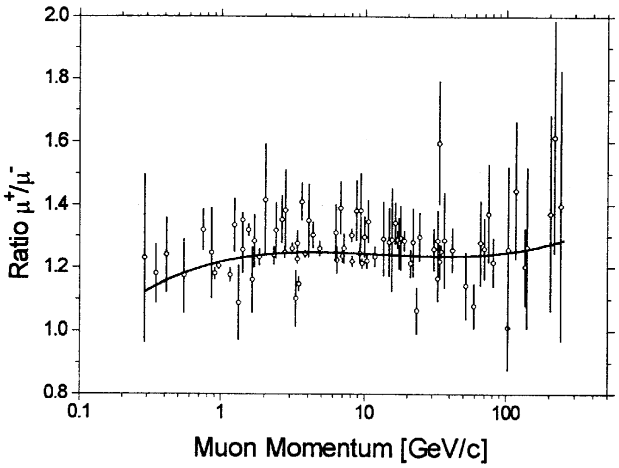

Fig. 2.1. Muon charge ratio in dependence on the muon momentum (compiled from Allkofer, 1975).

background induction are important only for muon decay and muon capture, which are minor contributors to the total background. Therefore a momentum independent muon charge ratio $\mu^+/\mu^- = 1.28$ can be accepted to simplify the model (Allkofer, 1975).

The differential cosmic muon flux also depends on the polar angles, ϑ (the zenith angle) and ϕ (the azimuth angle). The major dependence is on the zenith angle. The muon flux in slanted directions is influenced by atmospheric absorption, muon decay and Earth's magnetic field. Muons, which are produced mostly in higher altitudes, must travel a longer distance to the Earth's surface if they come from slanted direction, so that some of them, depending on their energy, lose all energy by ionisation or decay. In general, the larger is the zenith angle ϑ, the smaller is the muon flux, and the spectrum is relatively depleted in lower energies. The Earth's magnetic field bends muon trajectories depending on the muon charge sign. The trajectories of positive muons are different from those of negative muons when observed in the East-West plane. Different trajectory lengths cause different surviving probabilities, so that the differential muon flux depends also on the azimuth angle ϕ. This dependence is stronger for muons of lower momenta (below 5 GeV/c). In the eastern direction, a trajectory of a negative muon is shorter than that of a positive one produced at the same altitude, therefore the spectrum is relatively enriched in negative muons. In the western direction, it is contrary. There is a deviation from the general behaviour for directions close to the horizontal for muons of the highest energies (above about 500 GeV/c) when the differential flux increases with the zenith angle ϑ (Allkofer and Grieder, 1984). This is explained by the following: there are two possible fates for pions produced in the upper atmosphere. Either they decay to muons or they initiate a nuclear reaction. A pion moving in almost horizontal direction spends most of its time in thin air column so the chance for decay is higher compared to the concurring nuclear reaction. However, we do not need to include this effect to the model as it applies only to muons with the highest energies that have negligible fluxes (see Figure 1.2).

Three parameters are required to describe the differential muon flux at a fixed point: the

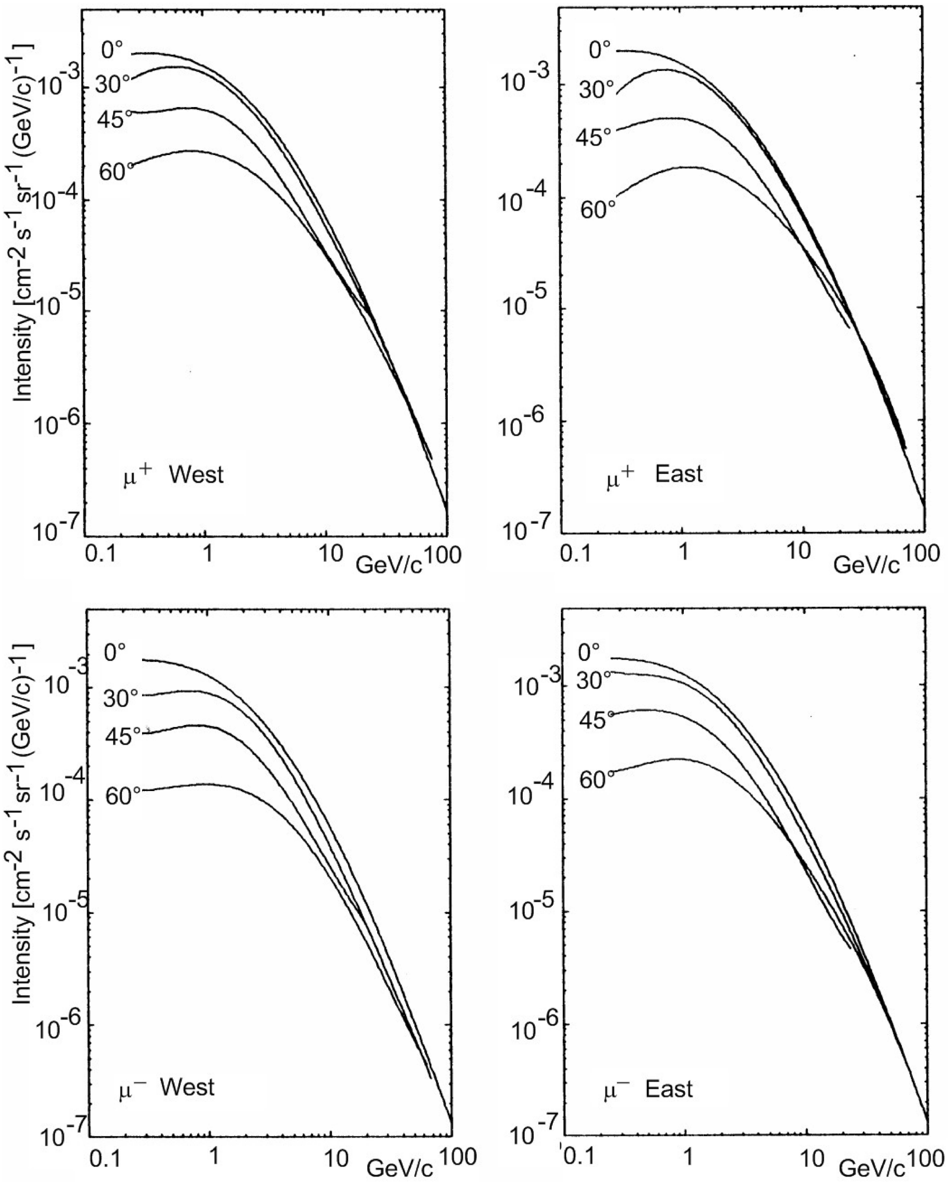

Fig. 2.2. Spectra of positive and negative muons measured in various directions (compiled from Allkofer and Grieder, 1984; Allkofer *et al.*, 1971; Moroney and Parry, 1954).

muon momentum p, the zenith angle ϑ and the azimuth angle ϕ. In principle, a fit over these three parameters could be done provided a sufficiently consistent and broad data would be available. A compilation of the best data set from Allkofer and Grieder (1984) is presented in Figure 2.2, for

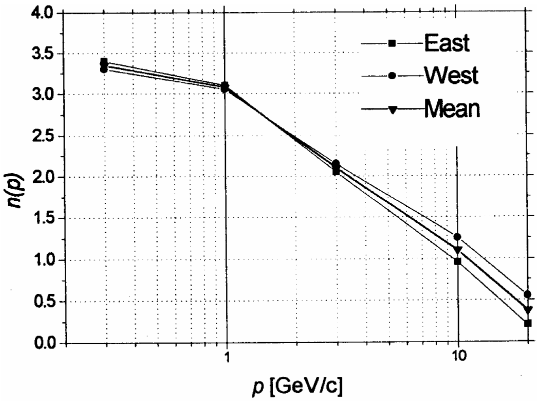

Fig. 2.3. Dependence of the exponent $n(p)$ in the expression of the differential muon flux on the muon momentum (modified from Moroney and Parry, 1954).

the differential muon momentum spectra in zenith angles $\vartheta = 0°$, 30°, 45° and 60° separately for positive and negative muons, and eastern and western directions. The data for $\vartheta = 0°$ were calculated using the muon charge ratio fit from Figure 2.1, and the vertical muon fluxes given by Allkofer *et al.* (1971). The data for $\vartheta = 30°$ and 60° were compiled from Allkofer and Grieder (1984), and Allkofer *et al.* (1971). The data for $\vartheta = 45°$ were taken from Allkofer (1975). The dependence of the differential muon flux $j(\vartheta, p)$ on the zenith angle ϑ can be expressed generally as

$$j(\vartheta, p) = j(0, p) \cos^{n(p)} \vartheta, \tag{2.1}$$

where the exponent $n(p)$ depends on the muon momentum p, differently for the eastern and western directions. Figure 2.3 shows $n(p)$ data compiled from Allkofer and Grieder (1984). The exponent $n(p)$ decreases from $p \approx 3.3$ with increasing muon momentum, and reaches zero for $p > 30$ GeV/c, when the muon flux is considered to be isotropic. In the case when a simulated detection system has axial symmetry around the vertical axis, the variations in azimuth angle ϕ are averaged out and ϕ-independent values of $n(p)$ can be used. When assessing the overall accuracy of any cosmic muon background simulation, we have to take into account that the muon flux varies also with time. Long-term variations are attributed to the eleven year solar cycle, diurnal and 27 day cyclic variations have also been observed. The solar wind, which is intensive during periods of high solar activity, declines the primary cosmic rays from their way to the Earth. The effect is most pronounced for secondary neutrons, but can also cause muon flux variations, which are usually within 5 %. Short-term variations (from 2 hour to 2 days) due to magnetic storms (Forbush decreases) can occur as well.

There are also seasonal variations of cosmic muon flux which can be observed in middle latitudes. They are caused by variations of the tropopause height which rises from about 9 km in winter to about 15 km in summer. Therefore the height in which muons are mostly produced varies with the tropopause height. In summer, when muons are produced higher, most of them do not survive their longer way to the sea level and they decay. Therefore the cosmic muon flux is less intensive in summer (by about 7 % from the average) than in winter, when it is by about

6 % greater than the average flux. Short-term variations known as barometric effect originate in variations of the atmospheric air pressure. At low pressure, the atmospheric depth through which muons have to penetrate is thinner, and more muons succeed to reach the Earth surface. Deviations by more than a few % occur due to this effect, therefore background of a detection system situated above the surface without a proper anticosmic shielding should be corrected for the barometric effect.

We are dealing with too many parameters which affect the actual muon flux, and it is therefore difficult to include all of them into the simulation. As these variations are usually smaller than 10 %, we can neglect them in calculations. Such accuracy is acceptable as the background enters the factor of merit in the square root ($F = \varepsilon/\sqrt{B}$, where ε is the efficiency of the detector and B is its background).

2.1.2 Interaction Processes

Muons. Processes with muons that might be important for background induction will be discussed as the first. The details of the methods used in GEANT are given in the CERN (1990; 1993) reports. Muons do not interact in strong interactions, and therefore they loose and deposit energy in matter mostly due to electromagnetic interactions. Because cosmic muons have high energies, the ionisation process which is most important for massive charged particles, has some peculiarities, the most important of which is the production of energetic **delta electrons**. In collisions with atomic electrons, which are mediated by Coulomb interactions, atoms may be excited or electrons can get enough energy to leave atoms. The energy spectrum of liberated electrons is very wide, from almost zero energy up to the maximum energy ($T_{\max}$) that can be transferred to an (almost) unbound electron given by the kinematics law

$$T_{\max} = \frac{2mc^2\left(\gamma^2 - 1\right)}{1 + 2\gamma\frac{m}{M} + \left(\frac{m}{M}\right)^2}, \tag{2.2}$$

where m is the electron mass, M is the muon mass, γ and c have their usual meaning. For a muon with the momentum of 10 GeV/c, the maximum kinetic energy transferable to an electron is as much as 4.8 GeV. Clearly, electrons with such high energies can generate other particles mostly due to bremsstrahlung. The standard Bethe-Bloch formula for ionisation losses of non-relativistic massive charged particles cannot be applied for ultra-relativistic cosmic muons. The presence of high energy delta electrons has two main consequences: (i) the energy lost by a particle in a thin layer of material has larger statistical fluctuations than expected from a simple Gaussian distribution; (ii) there can be a difference between the energy lost and the energy deposited in thin material layer.

A more realistic GEANT option is the explicit generation of delta rays with the calculation of quasi-continuous energy loss using the restricted Bethe-Bloch formula. The definition of delta electrons is quite vague and depends on the regions of energies of interest. If the electron kinetic energy cut, T_{cut},is introduced, below which the electron is considered to deposit all its energy in one point, and not to transport it in any form to other points in the set-up, the restricted Bethe-Bloch formula for $T_{\max} > T_{\text{cut}}$ has the form (CERN, 1992)

$$\frac{1}{\rho}\left(\frac{dE}{dx}\right) = D\frac{z^2 Z}{A\beta^2}\left[\ln\frac{\sqrt{T_{\max}T_{\text{cut}}}}{1} - \frac{\beta^2}{2}\left(1 + \frac{T_{\text{cut}}}{T_{\max}}\right) - \frac{\delta}{2} - \frac{C}{Z}\right], \tag{2.3}$$

where $D = 4\pi N_a r_e^2 mc^2 = 0.307$ MeV cm^{2}g^{-1}. A, Z and ρ are the mass number, atomic number and density of the material, respectively; z is the particle charge, and $I = 16Z^{0.9}$ eV is the effective ionisation potential. The factor δ is a correction for the density effect, and C is the shell correction term. For $T_{\max} < T_{\mathrm{cut}}$ the formula has a different form (CERN, 1992).

Most of the muon induced background in Ge gamma-spectrometers is caused by bremsstrahlung radiation of delta electrons. As the energy region of interest is above a few tens of keV, the electron kinetic energy cut above which delta electrons should be explicitly generated should also be a few tens of keV, at least in the inner layers of the shield and in the detector itself. Therefore $T_{\max}$ will always be greater than T_{cut} for cosmic muons.

The differential cross-section of delta electron production in interactions of muons (spin $1/2$) can be written as (CERN, 1992)

$$\frac{d\sigma}{dT} = 2\pi r_e^2 m \frac{1}{\beta}\frac{1}{T^2}\left[1 - \beta^2 \frac{T}{T_{\max}} + \frac{T^2}{2E^2}\right], \tag{2.4}$$

where T is the electron kinetic energy, E is the muon energy, and the other symbols have the usual meaning. Far below the kinematic limit, $T_{\max}$, the delta electron spectrum is inversely proportional to the square of its kinetic energy, and the number of electrons produced above a given threshold is inversely proportional to the threshold energy. There are well established facts on delta electron production. The lower the delta electron cut, T_{cut}, the more realistic the simulation of the ionisation process is achieved. However, the process requires more computing time as more particles have to be processed.

A muon of energy E moving in the field of a nucleus of charge Z can create an **electron-positron pair** through a 4th order QED process with a differential cross-section (CERN, 1985)

$$\frac{\partial^2\sigma}{\partial v \partial \rho} = \alpha^4 \frac{2}{3\pi}\left(Z\lambdabar^2\right)\frac{1-v}{v}\left[\phi_e + \left(\frac{m}{M}\right)^2 \phi_\mu\right], \tag{2.5}$$

where

$$v = \frac{E^+ + E^-}{E} \tag{2.6}$$

and

$$\rho = \frac{E^+ - E^-}{E}. \tag{2.7}$$

Here, α is the fine structure constant, $\lambdabar$ is the Compton wavelength, E^+ and E^- are the total energies of the positron and the electron, respectively; the terms ϕ_e and ϕ_μ can be found in the CERN (1985) report. There are kinematic ranges for the fraction of muon energy transferred to pair ν

$$\frac{4m}{E} = v_{\min} \le v \le v_{\max} = 1 - \frac{3}{4}\sqrt{e}\frac{M}{E}Z^{\frac{1}{3}} \tag{2.8}$$

and

$$0 = \rho_{\min} \le |\rho(v)| \le \rho_{\max}(v) = \left[1 - \frac{6m}{E^2(v-1)}\right]\sqrt{1 - \frac{4m}{vE}}. \tag{2.9}$$

There is an energy threshold of 2.04 MeV ($4mc^2$) for this process. The dominant contribution comes from the low ν region. In GEANT, this process is simulated for the muon energy range 1-10^4 GeV using parametrised expressions for cross sections with an inaccuracy of no more than 10 % (CERN, 1990). It is possible to set an energy cut for the resulting pair higher than the kinematic limit. In this case, the energy expended by the muon for the production of a pair is treated as a quasi-continuous loss, and the muon is absorbed at the interaction point. There is no reason to use higher cuts in simulations of background induction as the direct pair production is an important process, and an acceleration of computation is not significant.

As muons are massive particles, **muon bremsstrahlung** takes a place in the Coulomb field of the nucleus. We shall not present here any formulae for calculating a differential cross-section of this process as they are too complicated (CERN, 1985). Muon bremsstrahlung events are quite rare but very powerful so that a muon can lose a large fraction of its energy in one interaction. Therefore, it contributes significantly to mean energy losses of high energy muons (about 3 MeV/(g cm^{-2})) for 1000 GeV muons in iron (CERN, 1985). The hard photon produced generates an electromagnetic shower in the material. Due to its high energy, a shower can contain up to 10^5 particles with energies above 50 keV. GEANT simulates this process in the muon energy range 1-10^4 GeV with accuracy of parametrised cross-sections not worse than 12 % (CERN, 1990). As for the direct pair production, it is possible to set an energy cut below which the muon bremsstrahlung is treated as a quasi-continuous energy loss. However, this process is rare and the computation acceleration is negligible.

The **multiple scattering of muons** on atoms in the material should be covered as well to complete the list of electromagnetic processes with muons. This process is characterised by numerous elastic collisions with the Coulomb field of nuclei, and to a lesser degree with the electron field, which leads to a statistical declination of a muon from its original direction. It is important only for muons below about 1 GeV/c, and it gains importance as the muon approaches zero kinetic energy. However, the expressions are too complex to be presented in this review.

Another process that should be taken into account is the **muon decay**, a well-known weak process that occurs mostly when a muon has been stopped within the detector installation. The cause is a relatively long mean life-time of 2.197 μs, which is prolonged due to the relativistic time dilatation for energetic cosmic muons. A positive (negative) muon decays to a positron (electron) and neutrinos escaping from the set-up according to the decay schemes

$$\mu^+ \rightarrow \mathrm{e}^+ + \nu_e + \overline{\nu}_\mu \tag{2.10}$$

and

$$\mu^- \rightarrow \mathrm{e}^- + \overline{\nu_e} + \nu_\mu, \tag{2.11}$$

respectively. A decay accompanied by a photon emission occurs in 1.4 ± 0.4 % cases. There is a kinematic limit for the positron (electron) momentum in the muon rest system given as

$$p_0 = \frac{1}{2} Mc \left(1 - \frac{m^2}{M^2} \right) = 52.8\ \mathrm{MeV}/c \tag{2.12}$$

if we consider mass-less neutrinos. The standard V-A weak interaction model gives for the positron (electron) momentum, p_e, spectrum, neglecting terms of m/E (Morita, 1973)

$$p\left(x\right) = \frac{M^5 g_\mu^2 c^4}{16\pi^3 \hbar^7} \left[\left(1 - x\right) + \rho \frac{2}{9} \left(4x - 3\right) \right] x^2 \tag{2.13}$$

with

$$x = \frac{2p_e}{Mc}, \tag{2.14}$$

which is in good agreement with experiment for $\rho = {}^3\!/_3$. Most of the positrons (electrons) have high energies and are likely to generate electromagnetic showers if a muon decays in a high-Z material like lead. GEANT treats decay of particles in a general way so that the four-momenta of the decay products are generated with isotropic angular distribution in the centre-of-mass system, and then transformed into the laboratory system. The consequence of such a general approach is the simplification of the momentum spectra of the decay products. The decay accompanied by gamma-ray emission is not simulated. However, it was found in a detailed simulation that the muon decay is only a minor process in background induction by cosmic muons.

Negative muon capture is a concurrent process to negative muon decay in a material. A negative muon is attracted by the nucleus, and if it does not succeed in decaying, it finally falls to the 1s level of a muonic atom. Due to its 207 times bigger mass compared to electron, a large part of the muon probability distribution function in the 1s state rests within the nucleus, especially in heavy nuclei. The relatively long life-time of muons allows the basic weak process

$$\mu^- + p \to n + \nu_\mu \tag{2.15}$$

to take place. Simple kinematic calculations show that a free neutron could gain only 537 MeV of kinetic energy while the rest escapes with the muon neutrino. However, in a nucleus, a higher energy is transferred to the nucleus (typically 10-20 MeV) because of the non-zero proton momentum and nuclear effects. The binding energy of negative muons in heavy nuclei can be quite high, e.g. 10.66 MeV in lead. On the bases of experimental data (Suzuki *et al.*, 1987) it can be calculated that muon capture without muon decay occurs in natural Pb, Cd, Cu, Fe and Al in 97 %, 96 %, 93 %, 90 % and 61 %, respectively. As more than 99 % of muons in a counting system equipped with a lead shield stop in lead due to its high mass fraction in the whole system (calculated in a simulation), practically all the stopped negative muons are captured without electron emission. The muon capture is therefore the most intensive source of tertiary neutrons in laboratories placed in moderate shielding depths. After the negative muon capture the excited nucleus de-excites by the emission of several neutrons. Emission of charged particles in heavy elements is suppressed due to the Coulomb barrier at these energies. In lead, 1.64 ± 0.16 neutrons are emitted in average (Morita, 1973). The probabilities of multiplicities of the emitted neutrons are 0.6 % for no neutron, 59.1 % for one neutron, 23.6 % for two, 5.1 % for three and 12.4 % for four neutrons. The neutron energy spectrum for lead was measured by Schröder *et al.* (1974). It contains an evaporation part expressed as

$$\frac{dN(E)}{dE} \propto E^{5/11} e^{-E/\theta} \tag{2.16}$$

in the energy region of 1 to 4 MeV. The effective nuclear temperature θ is 1.22 MeV. The part of the neutron spectrum above 4.5 MeV decreases exponentially

$$dN/dE \propto e^{-E/E_d} \tag{2.17}$$

and is attributed to direct pre-compound emission. The decrement energy E_d is 8 ± 1 MeV, and the fraction of the high-energy distribution integrated from 4.5 to 20 MeV accounts for 9.7-1.0 % of the total spectrum. Later Kozlowski *et al.* (1985) extended the measurements of the neutron spectrum up to 50 MeV and found a decrement energy E_d in the energy region 10-50 MeV of 8.6 ± 0.5 MeV, which is in accordance with that measured by Schröder *et al.* (1974).

The de-excitation of a nucleus may be completed by emission of several gamma-rays, however, there are no reliable data on gamma-ray energies and intensities for the materials in question. Also X-rays with correspondingly higher energies can be emitted from muon-atomic levels during the descent of the muon to the 1s level. Although such X-rays are used for material analysis, they have not been identified in background spectra, and their contribution is considered to be negligible.

At high muon energies **photonuclear muon interactions** occur, which can be mediated via a virtual photon, interacting with nucleons. The total cross-section per nucleon can be expressed for muons above 30 GeV as (CERN, 1990)

$$\sigma = 0.3\,(E/30)^{0.25} \tag{2.18}$$

It is considered to be constant (0.3 μb/nucleon) for muons below 60 GeV. The macroscopic cross-section for muons below 30 GeV in lead is only $2.0 \cdot 10^{-6}$ cm^{-1} and increases only slowly for higher muon energies. As in muon bremsstrahlung, the fast muon interaction is characterised by rare but very hard events. Therefore, despite its small cross-section, it contributes to mean energy losses of high-energy muons. However, the contribution is still only about 5 % (< 0.5 MeV g^{-1} cm^{2}) of the total energy losses of high energy muons in iron, and even less for heavier materials (RPP, 1994). GEANT treats fast muon nuclear interactions in the same way as the hadronic shower simulation code GEISHA (Fesefeldt, 1985). The energy and angle of a final state muon is generated according to the free quark parton model. The hadrons are generated in an approximate way. The virtual photon replaced by the real pion of random charge with the same kinetic energy and inelastic scattering of the pion on the nucleus is simulated. While the final state generated in this way gives a good approximation for calorimetric purposes, the kinematics of the final state may be a rather poor approximation (CERN, 1990).

Electrons, Positrons and Photons. The muon interactions in a shield result in production of energetic electrons, positrons and photons. Therefore, processes with these particles will also be discussed as they mediate the interaction of a muon with a detector medium.

Ionisation and delta electron production is the first process we need to deal with. There are some important differences between interactions of electrons and positrons due to the quantum effect of the impossibility of distinguishing between two electrons. The first manifestation is ionisation and delta electron production by electrons and positrons. The maximum energy transferable to a free atomic electron by a positron is as much as the initial positron kinetic energy, while for the electron, only half of the initial electron kinetic energy can be transferred. This leads to different formulae for continuous energy losses by ionisation (Berger-Seltzer formulae; Sternheimer, 1971), as well as different formulae for delta electron production by electrons (e^-e^- Möller scattering) and by positrons (e^+e^- Bhabha scattering; (CERN, 1992). GEANT uses explicit theoretical formulae for sampling these processes.

Due to a continuous photon spectrum, a **bremsstrahlung of electrons** is of interest in the detector background. It was theoretically investigated by Seltzer and Berger (1985) who calculated photon spectra for elements with Z = 6, 13, 29, 47, 74 and 92 in the electron kinetic energy range 1 keV – 10 GeV, and they reported reasonable (within a few %) agreement with experiments. The parametrisation introduces errors of bremsstrahlung cross-sections of less than 15 % for electron kinetic energies below 1 MeV, and less than 6 % for electron kinetic energies from 1 MeV to 10 TeV. The errors of photon spectrum parametrisation are smaller than 12 %, typically a few % (CERN, 1990). Energy losses due to soft bremsstrahlung (a photon energy below an energy cut than can be set by the user) are added to the quasi-continuous energy losses, and no photons are explicitly generated.

There are important differences between bremsstrahlung of positrons and electrons at low energies. They can be taken into account using a correction factor which is a function of T/Z^2 (Kim *et al.*, 1986). For example, the total electron bremsstrahlung cross-section for production of photons above 10 keV in lead is greater by almost 50 % than for positrons, if the electron and positron kinetic energies are 1 MeV (CERN, 1990). This correction is included in GEANT.

Another process of interest is the **positron annihilation** that can take place with a free or loosely bound atomic electron, during which two photons are emitted, or with a strongly bound electron (mostly in the K-shell), during which only one photon is emitted, as the excessive momentum is taken up by the atom. The cross-sections of the two-photon and one-photon annihilations are given by the Heitler formulae and sampled in GEANT. One-photon annihilation, with electrons only in the K-shell is considered. More complicated annihilation schemes are not simulated as their contribution is negligible. The contribution of the one-photon annihilation is largest for heavy materials, as much as 20 % for ≈ 400 keV positrons in lead, and it decreases for lower and higher positron energies.

The **photoelectric effect** cross-sections, as well as the K, L_I and L_{II} shell energies are directly parametrised in the GEANT. The relative errors of the cross-sections are less than 25 % near the shell-energy edges, and less than 10 % elsewhere. X-ray and Auger electron emissions are also simulated.

The **Compton-scattering** total cross-sections are parametrised in the GEANT with relative uncertainties not exceeding 6 % in the photon energy region from 20 keV up to 100 GeV. The Klein-Nishina formula is used for the differential cross-sections, i.e. the Compton-scattering is treated as taking place on free electrons. Neglecting the binding energies and momenta of atomic electrons has crucial influence on the resulting electron energy spectrum near the Compton-edge. The Compton-edge is blurred in reality and not so sharp as calculated using the Klein-Nishina formula. Therefore a response function of a Ge detector can never be computed with sufficient accuracy around the Compton-edge using the present versions of GEANT.

The **electron-positron pair production** cross-sections are parametrised in the GEANT with relative uncertainties less than 5 %. Relative errors of the parametrisation of the cross-sections for the Rayleigh scattering (coherent scattering on atoms without changing the photon energy, but changing the photon direction) are less than 10 % for photon energies below 1 MeV.

Hadrons. GEANT for simulation of hadron transport, hadron interactions and hadron showers utilises translations of hadron transport codes GEISHA (Fesefeldt, 1985) and FLUKA (Aarnio *et al.*, 1990). These codes are mostly intended for interactions of hadrons at high energies, and therefore they do not simulate processes important for the background induction properly. Fortunately, except for the negative muon capture, processes with muons which leads to hadronic showers (fast muon nuclear interactions, nuclear photoeffect with high energy photons, and photo-fission) are rare and unimportant for the total resulting background. In particular, neutrons are tracked down to 10 keV, and then simply absorbed without generation of particles emitted during the de-excitation of a compound nucleus. Therefore, even if an additional routine would be written for the negative muon capture in lead including neutron and photon emissions, the resulting neutrons could not be transported correctly with the plain GEANT. Other neutron transport codes, better suited for these processes must be employed. One of such codes is MCNP (LANL, 1986), frequently used for calculation of production rates of radionuclides, however, simulations of the background induced by neutrons would need some improvements.

2.2 Simulation Codes

2.2.1 Simulations for Surface Laboratories

As the code is too complicated to be described in detail in this chapter, the reader should see the GEANT documents for more information on the code system and its environment (CERN, 1990; CERN, 1993). However, we present the code description in such detail that readers can build a similar application not only for simulation of detector characteristics, but also its possible applications in radioecology, radiation biophysics and space sciences.

We shall describe first a simulation of background of HPGe detectors placed in a lead shield at the sea level. Later we shall go underground, and we shall also include an anti-Compton shielding. The GEANT code has already been validated and results compared for HPGe spectrometers operated in surface laboratories (Povinec *et al.*, 2006a).

The GEANT code (CERN, 1993) is written in FORTRAN and the simplified flow chart used in simulations is given in Table 2.1. Not all the modules listed in the flow chart must be contained in the code source (Vojtyla, 1995). Most of them are linked to the executive file from the library during linking. The modules that must be provided by the users are typed in bold. We shall describe step by step the code source for simulation of background characteristics of a coaxial HPGe detector of 200 % relative efficiency located at sea level in a lead shield with 15 cm thick walls.

The module reserves an array for *ZEBRA* dynamic memory manager, calls initialization module (*UGINIT*), starts event processing (*GRUN*) and terminates the run (*UGLAST*). After declaration of *COMMON* blocks the standard GEANT initialization is performed and the file *spec.dat*, which contains steering variables is opened. Then the routine *SPCLEAR* is called to clear the simulated background spectra. Next, kinematics cuts are defined to the default value of 50 keV, the energy threshold, below which particles are considered to be absorbed, and therefore they are not further tracked. The cut *PPCUTM* set to 2.14 MeV refers to the pair production by muons, which has a kinematic limit. Variables, which are not standard in GEANT, but which are to be read by the routine *GFFGO* from *spec.dat* (unit logical number 5), must be defined prior running *GFFGO*. This is done in calls to the routine *FFKEY* (*CERNLIB* routine). The parameters of *FFKEY* describe amnemonic code – a 4-character string, a FORTRAN name of the variable, a dimension in the case of an array, and a FORTRAN type (integer, real, etc.). A subroutine *ISEE* contains starting seed of the random number generator *RNDM* (*CERNLIB* routine). *ISSHP* defines a shield shape and *DETPOS* defines the position of the detector in the shield. Depending on the shape of the shield, a muon generator for a cylindrical shield or for a rectangular shield is initialized calling routines *HISRINIT* or *HISRINIB*. The detector parameters are given in a separate subroutine *DETEC*.

Separate subroutines simulates ionisation loses of particles (*LOSS*). Delta electrons above the cut are produced explicitly, and quasicontinuous energy loss is calculated according to the restricted Bethe-Bloch formula. The coherent Rayleigh scattering of photons is covered in *RAYL*.

The *DETEC* also defines the geometry of the set-up. The geometry of the set-up is reduced to boxes and tubes filled with materials and tracking media. The large mother volume contains

Tab. 2.1. Simplified flow chart used in simulations.

Routine name	**Description**
GZEBRA	Init. of ZEBRA system management
UGINIT	User routine to initiate the run
GINIT	Initialisation of GEANT variables
GFFGO	Interpretation of steering data cards
GZINIT	Init. of ZEBRA core div. And link areas
GPART	Creation of particle data structure
GMATE	Creation of material data structure
User code	Description of geometrical set-up
GPHYSI	Preparation of cross-section and energy loss
	Tables for materials in use
GRUN	Loop over events
GTRIGI	Initialisation of event processing
GTRIG	Event processing
GUKINE	Generation of event initial kinematics
GUTREV	User defined start of tracking
GTREVE	Loop over all tracks in the event
GUTRAK	Tracking control by user
GTRACK	Tracking of current track
GFINDS	Find current volume in the set-up
GUSTEP	Recording of space points
GUPARA	Called if particle falls below threshold
GTGAMA	Tracking of the particle according to type
GFSTAT	Fill banks for volume statistics
GSTRAC	Store info. about current track segment
GTMEDI	Finds in which medium current point is
GUDIGI	Computation of digitisation
GUOUT	Output of the current event
GITRIGC	Clearing of memory for the next event
UGLAST	User termination routine
GLAST	Standard GEANT termination

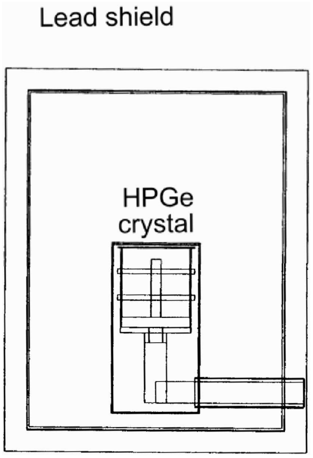

Fig. 2.4. A set-up of a coaxial HPGe detector of p-type in a lead shield used in simulations.

all daughter volumes inserted inside this volume which defines the master reference coordinate systems. At the beginning of the routine, geometrical parameters of used volumes are calculated according to dimensions of the shield, and stored in arrays for later use. Similarly, materials, including atomic and mass numbers, density, radiation length, etc., are described in the GEANT subroutine *GSMATE* or *GSMIXT* for mixtures. Next, the tracking media parameters are calculated for given materials by calls to the *GSTMED*.

The volumes used in the set-up are defined in the GEANT routine *GSVOLU*, including the geometrical set-up. Their positions are given in the GEANT routine *GSPOS*. The rotation matrix for rotation of horizontal part of the detector cryostat is calculated calling the GEANT routine *GSROTM*. The HPGe detector configuration, based on a dead layer and the active layer is included there as well. An example of a coaxial p-type HPGe detector configuration in a lead shield used in simulations is presented in Figure 2.4.

The concept of lead with higher cuts was used to speed up the computations, as it is not necessary to produce low energy delta electrons in the outer shells of the shield, which can have only negligible influence on the detector background. The acceptable thickness of the inner lead shell with lower cuts (2.5 cm) was tuned in test simulations, which shortened the computation time by about a factor of 4.

The next routine provided by the user is the routine *GUKINE* that generates kinematics for the particle(s), starting every event. The purpose is to push coordinates of the incident muon (vertex) and coordinates of its momentum vector into stacks containing kinematics of particles to be tracked. This is done by calling the GEANT routine *GSVERT* through the 3-element array *VERTEX*. The coordinates of the momentum vector are stored by calling the GEANT routine *GSKINE* through the 3-element array *PLAB*. The type of particle is communicated through the input parameter *IKINE*. The communication between the routines goes via the *COMMON* variables *IKINE* and *PKINE*. This routine also contains a variable *ENERGY* which defines the energy deposited in the sensitive volume of the HPGe detector. This is the output that we are interested in.

For a simulation of irradiation of a shield with detector in free space (undisturbed by overburden materials), we can consider the muon flux to be homogeneous, though not isotropic. This means that the function describing the differential muon flux $j(p, \vartheta, \phi)$ is constant in every point of space. The volume of a shield is convex in most cases, therefore every muon, which hits the shield, enters its volume only once. We neglect improbable events when muons are scattered back to the shield, for example from the floor. The time T corresponding to the number of N simulated events is calculated using a simple scaling equation

$$T = \frac{N}{dN/dt}, \tag{2.19}$$

where dN/dt is the number of muons that hit the shield in a time t. The number of muons passing through a unit area during a unit time, and their angle and momentum distributions depend on whether the area is horizontal or vertical. In general, the number of muons that hit a unit area with a normal vector $\vec{\sigma}$ in unit time is given as

$$\frac{dN}{dSdt} = \int dp \int\limits_{\Omega} j\left(p, \vartheta, \varphi\right) \vec{\sigma}\vec{\omega} d\Omega, \tag{2.20}$$

where $\vec{\omega} = (\cos\varphi \sin\vartheta, \sin\varphi \sin\sigma, \cos\sigma)$ is a unit vector in the direction of the space angle $d\Omega$. It should be integrated throughout all space from which muons hit the area from outside. For horizontal areas we have

$$\left(\frac{dN}{dSdt}\right)_h = \int dp \int\limits_0^{2\pi} d\varphi \int\limits_0^{\pi/2} d\vartheta j\left(p, \vartheta, \varphi\right) \sin\vartheta \cos\vartheta \tag{2.21}$$

Because $\vec{\sigma} = (0, 0, 1)$ (sinϑ stems from dΩ). For vertical areas

$$\left(\frac{dN}{dSdt}\right)_v = \int dp \int\limits_{\Phi-\pi/2}^{\Phi+\pi/2} d\varphi \int\limits_0^{\pi/2} d\vartheta j\left(p, \vartheta, \varphi\right) \sin^2\vartheta \cos\left(\Phi - \varphi\right) \tag{2.22}$$

as $\vec{\sigma} = (\cos\Phi, \sin\Phi, 0)$, where Φ is the azimuth angle of the vector normal to the area dS. The muon impact rate can be calculated integrating Eqs. (2.21) and (2.22) over the whole shield surface except the basis (there is no muon flux from the bottom). The definition of angles and vectors is illustrated in Figure 2.5. For a simple model of the muon flux, not depending on the azimuth angle φ, the integrals in Eqs. (2.21) and (2.22) equal to

$$\left(\frac{dN}{dSdt}\right)_h = \int \frac{2\pi}{n(p) + 2} j\left(0, p\right) dp, \tag{2.23}$$

$$\left(\frac{dN}{dSdt}\right)_v = \int 2I(n) j(0, p) dp, \tag{2.24}$$

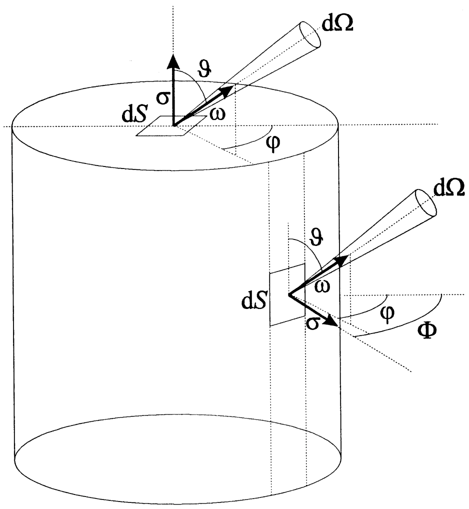

Fig. 2.5. Geometry for calculation of muon interactions with HPGe detectors using the GEANT code.

where $I(n)$ is an integral of the type

$$I(n) = \int_{0}^{1} x^n \sqrt{1 - x^2} dx. \tag{2.25}$$

The total impact rate of muons falling from the top on a rectangular shield with a height H and a basis $A \times B$ is given as

$$\frac{dN}{dt} = \int \pi r^2 \frac{2\pi}{n+2} j(0,p) dp + \int 4\pi H R I(n) j(0,p) dp. \tag{2.26}$$

The total impact rate of muons hitting from sides a rectangular shield with a height H and a basis $A \times B$ is given as

$$\frac{dN}{dt} = \int AB \frac{2\pi}{n+2} j(0,p) + \int 4H(A+) I(n) j(0,p) dp. \tag{2.27}$$

The first integral represents muons falling on the horizontal area from the top, while the second one corresponds to muons hitting the shield from sides. As we already noticed the factor $n(p)$ depends on the muon momentum p.

As the angular and momentum distributions are different for vertical and horizontal areas, each case is treated separately. The probability that a muon hits a horizontal or a vertical area is proportional to the first and the second integral in Eq. (2.26) or (2.27), respectively. The probability that the absolute value of the muon momentum will be p is proportional to the function standing in the respective integral in Eq. (2.26) or (2.27).

The probabilities of hitting horizontal and vertical areas, as well as probabilities of all considered muon momentum absolute values are calculated during the initialisation phase of the simulation code in the user routines *HISRINIT* or *HISRINIB*.

The range of muon momenta 0.2-100 GeV/c was found to be sufficient for background simulations. The muon impact rates both from the top (*TOPM*) and from the sides (*SIDEM*), and their branching ratios were calculated as well. For generating absolute value of muon momentum a CERNLIB routine *HISRAN* was used. This routine generates random numbers according to histogram values. The whole muon momentum range was divided into 999 bins with 0.1 GeV/c. The respective values in histogram bins (arrays *YTOPM, YSIDEM*) are calculated in *HISRINIT*, resp. *HISRINIB* according to Eq. (2.26) and (2.27) as well.

The muon momentum and geometry of the interaction is covered in the routine *MUGENT* which works as follow:

i) The case of hitting the shield on a horizontal or on a vertical area is sampled with probabilities proportional to *BRANCH*;

ii) An impact point on the top horizontal area or on side vertical areas is selected with a uniform distribution (a constant integral flux);

iii) The absolute value of the muon momentum is selected according to the respective distribution (which has been pre-computed), and the factor n corresponding to the given muon momentum is then calculated;

iv) In the case of a horizontal area, the azimuth angle ϕ is sampled from the interval (0, 2π) with the uniform distribution. The zenith angle ϑ is sampled from the interval (0, $\pi/2$) with the distribution proportional to $\cos^{n+1}\vartheta\sin\vartheta$. In the case of a vertical area, the azimuth angle ϕ is sampled from the interval ($\Phi-\pi/2$, $\Phi+\pi/2$) with the distribution proportional to $\cos(\phi-\Phi)$, and the zenith angle ϑ is sampled from the interval $(0, 2\pi)$ with the distribution proportional to $\cos^n\vartheta\sin^2\vartheta$. The distributions take into account possible impact angles, definition of the differential muon flux per unit space angle, as well as the scalar product of the unit vector in the muon momentum direction and normal vector of the surface area.

v) Finally, the Cartesian coordinates of the muon momentum vector are calculated as

$$\vec{p} = (-p\cos\varphi\sin\vartheta, -p\sin\varphi\sin\vartheta, -p\cos\vartheta). \tag{2.28}$$

The East-West effect has not been taken into account as it is important only for muons with momenta below about 0.5 GeV/c, which do not contribute significantly to the background, and a system set-up is often cylindrically symmetric. The weak dependence of the muon charge on the muon momentum was neglected as well, and for all muons the mean value of 1.28 was used. The muon charge was sampled with the probability of 0.561 for positive muons, and 0.439 for negative ones.

The defined differential muon flux was tested by comparing the commonly accepted value of the integral muon flux ($p >$ 0.35 GeV/c) through a horizontal area unit (Allkofer and Grieder, 1984)

$$J_h = \int dp \int j(p,\vartheta,\varphi)\cos\vartheta d\Omega \quad = \quad 144 \quad \pm \quad 9\ \mathrm{muons/m}^2 s, \tag{2.29}$$

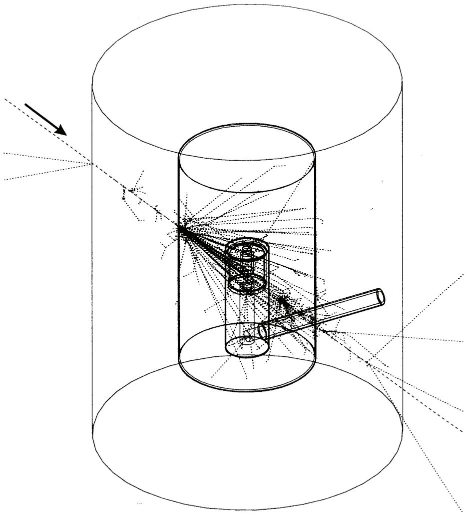

Fig. 2.6. Simulation of muon pass through a HPGe detector using a GEANT code (muon momentum 50 GeV/c; energy deposited in the crystal was 1717 keV).

and of the omnidirectional muon flux

$$J_0 = \int dp \int j(p, \vartheta, \varphi) d\Omega \quad = \quad 190 \quad \pm \quad 12\,\mathrm{muons/m}^2 s \tag{2.30}$$

with calculated fluxes, which were in the first case 147 muons/m^{2}s, and 202 muons/m^{2}s in the second case. Thus a reasonable agreement has been obtained with experimental results of Allkofer and Grieder (1984), as both values are within quoted uncertainties. Figure 2.6 shows a typical picture of a muon passing and interacting with the shield and the Ge detector.

The next necessary routine provided by the user is *GUSTEP* which is called at the end of each tracking step. This routine enables to accumulate energy depositions in single tracking steps through the GEANT variable *DESTEP* which contains the amount of energy deposited in the current medium in the current step. The number of medium is tested, and if it is equal to the number of sensitive Ge crystal , *ENERGY* is incremented by *DESTEP*. The test of *DESTEP* on zero prevents multiple incrementation by floating point zero.

The next important procedure performed within *GUSTEP* is pushing the kinematics of particles generated during the current step from a temporary structure *GCKING* into the stack of particles to be tracked. This is done by calling the GEANT routine *GSKING* for all particles except neutrinos in a loop.

After the event has been completed, the user routine *GUOUT* is called to store the information gained during the event tracking. The total energy deposited in the sensitive volume of Ge detector is stored in the variable *ENERGY*, and used to increment background spectra. Two spectra are formed, the first one in the energy region 0-1500 keV in 4096 channels, and the second one comprises the energy range 1.5 – 100 MeV, also presented in 4096 channels. After the last event has been processed the termination routine *UGLAST* is called. The routine updates previously computed background spectra and prepares the steering file for the next run.

The GEANT routine *GRNDMO* and the CERNLIB routine *RDMOUT* retrieve the random number seeds enabling to continue random number sequences in the next run correctly. The seeds must not be random, otherwise the generators would give unpredictable results. The generator *RNDM* starts with the seed 12345 and the first sequence of the generator *GRNDMO* starts with the pair of seeds 9876 and 54321. The $i^{\rm th}$ (one of 215) sequences of *GRNDMO* can be started with seeds of 1 and 0. The last routine called from *UGLAST* is the GEANT routine *GLAST* which performs the standard GEANT termination with the statistical output.

2.2.2 Simulations for Underground Laboratories

Description of the transport of cosmic muons underground depends on the considered depth. In shallow depths of a few tens of m w.e., only muons with energies below a few GeV are filtered out, and the observed spectrum is fed by muons which have had originally bigger energies. The energy losses of muons below about 500 GeV are mostly due to quasi-ionisation. For muons of higher energies, discrete processes (bremsstrahlung, fast muon nuclear interactions) start to dominate. The transport of muons in the lower energy range is simpler as the muons change their energy almost continuously, and they do not change their directions significantly. In the higher energy range, significant fluctuations of both energy and direction can occur. If the prevailing part of the muon spectrum observed underground stems mostly from muons with original energies below a few hundreds of GeV, the attenuation of the muon flux can be taken into account simply by accounting for mean ranges and integrated energy losses of muons.

We shall focus in this paper on shallow depth underground laboratories, where several approximations have to be taken into account:

i) we expect that the overburden rock has the same composition with depth and there are no fluctuations in muon ranges and energy losses in the rock;

ii) there is no deviation from the original muon direction due to multiple scattering to small angles.

Although the both effects take place, they are usually ignored in coarse calculations of the muon transport underground as they are partly smoothed-out due to continuous energy and angle spectra of cosmic muons (Gaisser, 1990). The simulation of the muon–induced background under the overburden is similar to that at sea-level, however, the muon rejection and the momentum reduction algorithms should be applied. After calculating the kinematics of the muon, the range of the muon in rock is calculated and compared to the slanted depth of the counting system $X = D/\cos\vartheta$, where D is the vertical depth and ϑ is the muon zenith angle. If the range is shorter than the slanted depth, the event is rejected. Otherwise, the original muon momentum p_0 is reduced according to the formula

$$p_{red} = p_0 - r^{-1}(x), \tag{2.31}$$

where $r^{-1}(x)$ is the inverse function of a function describing the range of muons in dependence on the muon momentum $r(p)$. It is assumed that the rock has a standard rock composition with a density of 2.65 g cm^{-3}, the average mass number $A = 22$ and the average atomic number $Z = 11$ (Heusser, 1995). The transport of muons through the standard rock was simulated using

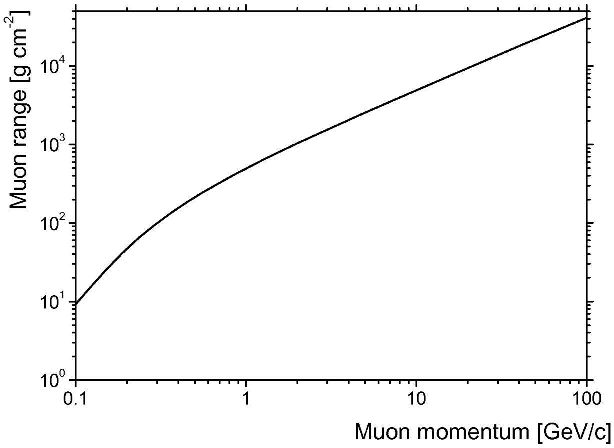

Fig. 2.7. Mean range of muons in standard rock (density 2.65 g cm^{-3}, average mass number $A = 22$ and average atomic number $Z = 11$) calculated using the GEANT code.

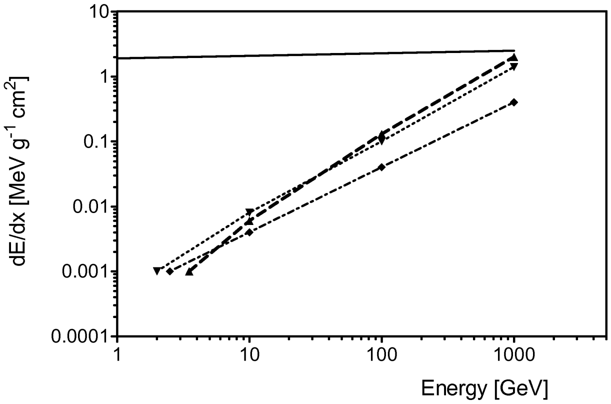

Fig. 2.8. Calculated muon energy loss in standard rock from ionisation, bremsstrahlung, pair production and nuclear reactions.

GEANT and data on mean ranges for various muon momenta are presented in Figure 2.7. The uncertainty of the muon range distribution in the investigated muon momentum range is below 10 %.

As muons interact with matter by electromagnetic and weak interactions only, their energy losses are predominantly due to ionisation. This can be noticed from Figure 2.8, where a simulated contribution of ionisation, bremsstrahlung, pair production and nuclear reactions as a function of muon energy is shown. It can be also seen that at higher energies muons can produce a significant neutron flux. At depths below 10 m w.e. this contribution is higher than from the nucleonic component of cosmic rays.

A comparison of simulated fluxes of secondary cosmic ray particles under different shielding

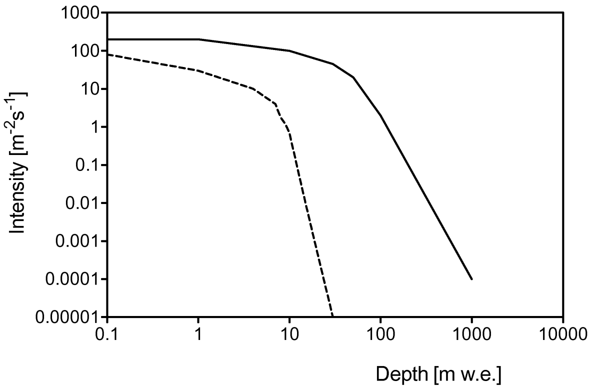

Fig. 2.9. Calculated fluxes of secondary cosmic rays in standard rock at various depths: muons (solid line); neutrons (broken line).

layers is presented in Figure 2.9. While the nucleonic component (mostly neutrons) is attenuated at 20 m w.e. by 3 orders of magnitude, the muonic component is reduced by 80 % only. To decrease the muonic component by a factor of 10 requires shielding below 50 m w.e. The simulated attenuation of the muon flux with the depth reasonably well follows the experimental curve obtained from underground laboratories (Figure 1.3).

Table 2.2 summarizes neutron fluxes from fission and (α,n) reactions for different rocks. As expected the production rates from granites dominate.

2.3 Simulation Results and Comparison with Experiments

2.3.1 Design of an Underground Laboratory - HPGe Detectors with Anticosmic Veto

Simulation Results for a Single HPGe Detector. The developed simulation code was tested for existing set-ups so the obtained results can be compared with measurements. The simulated background gamma-ray spectrum of a HPGe detector operating at the surface was in good agreement with measured background continua throughout all energies, except for energies below 100 keV, where the simulated counting rates were lower by about 10 %. The simulation also

Tab. 2.2. Calculated neutron fluxes from fission and (α,n) reactions in different rocks.

Rock type	**Neutron flux** [$\mathrm{kg}^{-1}\mathrm{d}^{-1}$]
Granite	60
Salt	20
Sandstone	5
Limestone	4

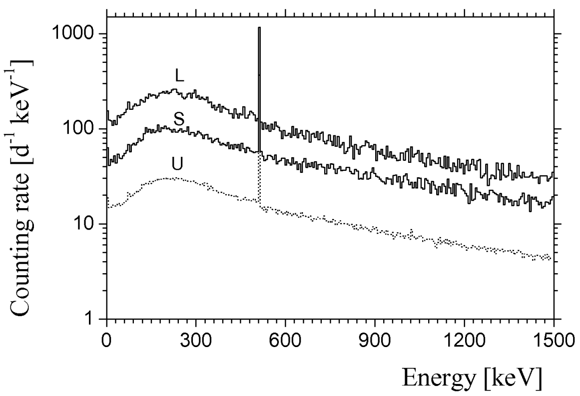

Fig. 2.10. Simulated background spectra for the HPGe coaxial detector of 200 % relative efficiency located in a surface laboratory in a large (L) and a small (S) lead shield without any lining. The underground spectrum (U) was simulated for the same detector in the S-shield located at 20 m w.e.

overestimates the count rate in the annihilation peak by about 40 %, which can be explained by assuming a complete charge collection in the HPGe detector in the simulation.

Shields of three sizes were used in simulations:

(i) small (S) shield is close to the detector and only a minimum of space is available inside (diameter of the well 42 cm, height 51 cm);

(ii) medium (M) size shield is intended for 1 liter samples (diameter 60 cm, height 70 cm);

(iii) large (L) shield can take even larger samples (diameter 100 cm, height 120 cm).

A thickness of 15 cm of lead has been found to be the optimum shielding thickness for large volume HPGe detectors situated at sea level or at shallow depths underground. If thicker shielding was used in simulations, the background was higher due to interactions of muons with the shield. The resulting background spectra of the coaxial p-type HPGe detector (relative efficiency 200 %) are shown in Figure 2.10 for the lead shield without any lining. The simulation clearly shows that the smallest background is obtained in the smallest shield.

This has been a surprising results as in previous low-level counting studies opposite recommendations could be found (e.g. Watt and Ramsden, 1964). An equilibration of radiation takes place for very large shields. If the detector dimensions are small compared to the inner dimensions of a shield, a larger inner surface area radiating secondary particles generated by cosmic-muons is compensated by a smaller place angle. The small background obtained for shields close to the detector (S-size) can be partly explained by a kind of self-anti-coincidence. The cosmic-muons inducing the highest probable background must pass through material layers close to the inner surface of the shield. If the shield is tight, these muons also pass close to the sensitive volume of the Ge crystal and therefore they are likely to hit it. However, if this happens, tens of MeV of energy is deposited in the sensitive volume, rejecting the given event from the lower-energy part of the background spectrum. The background spectra of small shields are

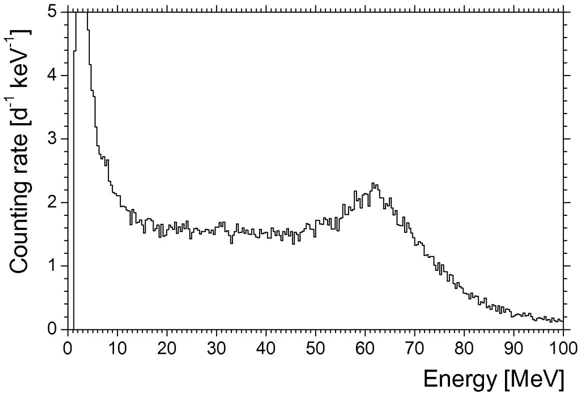

Fig. 2.11. Background gamma-ray spectrum at high energy region (HPGe coaxial detector of 200 % relative efficiency located in a surface laboratory).

relatively depleted in the region below 500 keV and the effect is more pronounced for the annihilation peak. This implies that this effect indeed takes place. However, the special simulation with direct deposition by muons in a Ge detector switched-off showed that it accounts for only about 30-40 % of the total effect. The rest is probably caused by a lesser amount of high-Z material radiating secondary particles in small shields. It is interesting that the background depends only slightly on the shape of the shield if the inner shield dimensions are preserved. Rectangular shields provide only a few percent greater backgrounds than cylindrical ones.

The background levels also strongly depend on the internal lining of the shield. As can be seen from Table 2.3 thick layers of low-Z lining increase the detector background. For example, the maximum in the continuum for the lead shield lined with 1.0 cm of Cu is over 2 times greater than that of the corresponding lead-only shield. This effect was also observed experimentally (Lindstrom *et al.*, 1990, Heusser, 1993) and explained as a consequence of smaller self-absorption coefficients for lower-Z materials. On the other hand, shields with lower-Z lining have smallest count rates in the annihilation peaks and above about 500 keV.

The shield dimensions should be kept as small as possible (depending on the largest sample size intended for analysis), as the smallest background is obtained in the smallest shield (without any lining, i.e. only with lead walls). For example, it is not worth leaving an extra space in the shield of the well-type detector if samples are only analysed inside the detector well. If the lead X-rays are disturbing, a thin descending Z lining is superior. It is advisable to design the shield so that the lining can be easily removed. Thick lower-Z linings should be completely avoided.

The effect of an underground installation on the HPGe detector background can also be seen in Figure 2.10 and Table 2.3. At the rock overburden of 20 m w.e. the background spectrum has been reduced by a factor of 3.

The spectra above about 20 MeV are almost identical independently of the shield because this is the region where direct ionisation by cosmic muons prevails. Figure 2.11 shows a dominant peak in the simulated spectrum at 61 MeV which corresponds to the track length of muon in the Ge crystal (the ionisation loses of muons in Ge are 7.3 MeV cm^{-1}).

Design of an Underground HPGe Spectrometer with Anticosmic Veto. When designing a new underground gamma-ray spectrometry laboratory we should notice that the most important recent breakthrough has been production and utilisation of large volume HPGe crystals with excellent energy resolution that permits the analyses of various radionuclides in composite samples, selectively and very often non-destructively (e.g. in sea sediments). Efficiencies of recently produced HPGe detectors reached 200 % (relative to 76 mm dia × 76 mm long NaI(Tl) crystal). For majority of environmental applications, a simple γ-ray spectrometer with an HPGe detector of about 100 % efficiency (especially if the sample size permits the use of a well detector) is the usual choice. In single HPGe spectrometers there is not any protection against cosmic ray muons, therefore a spectrometer with an anticosmic shielding will provide much better sensitivity.

Tab. 2.3. Simulated backgrounds of the 200 % relative efficiency HPGe detector in various shielding arrangements at the surface and 20 m w.e. (relative uncertainties are below 2 %).

Shielding	**Integral counting rate in 0-1.5 MeV interval [s^{-1}]**	**Counting rate under the 0.511 MeV peak [10^{-2} s^{-1}]**
150 mm Pb + 1 mm Cd + 2 mm Cu		
Cylindrical - small	0.88	2.2
- medium	1.50	5.2
- large	1.92	6.9
Rectangular - small	0.99	2.4
- medium	1.59	5.6
- large	1.95	7.8
Underground - rect. small	0.32	0.8
150 mm Pb		
Rectangular - small	0.91	2.7
- medium	1.40	5.7
- large	1.73	7.5
Underground - rect. small	0.29 (experimental value at 35 m w.e. is 0.24)	0.9
150 mm Pb + 5 mm Cu		
Rectangular - small	1.18	2.3
- medium	1.73	5.4
- large	2.08	7.7
Underground – rect. small	0.39	0.8

Fig. 2.12. A detail of a lead shield housing 4 HPGe detectors with anticosmic veto made of plastic scintillation detectors.

Fig. 2.13. A view of the IAEA-MEL's underground laboratory with lead shield housing 4 HPGe detectors (centre), an anti-Compton spectrometer (left) and a Quantulus liquid scintillation spectrometer (right).

We shall illustrate the applications of the Monte Carlo simulations in designing the underground CAVE (**C**ounting l**A**boratory for en**V**ironmental radionuclid**E**s) laboratory which has recently been constructed at the IAEA-MEL Monaco (Povinec *et al.*, 2004, 2005, 2006a) The CAVE laboratory is situated in an underground cellar in a car parking area at a depth of 35 m w.e. The laboratory is equipped with a common lead shield housing four large volume HPGe detectors (Figure 2.12). An anticosmic veto shielding was made of plastic scintillation detectors surrounding the lead shield which protect the HPGe detectors against cosmic radiation. Such a novel design, supported by Monte Carlo simulations, when several HPGe detectors are shielded against cosmic rays by a common guard detection system has been used for the first time in low-level gamma-ray spectrometry. The CAVE also houses (Figure 2.13) an anti-Compton gamma-ray spectrometer, comprising an n-type HPGe detector and NaI(Tl) anticoincidence shielding placed in a lead shield, and a liquid scintillation beta-spectrometer, which will be described later.

The lead shield housing 4 HPGe detectors is made of two layers. The outer layer is made of an ordinary lead 7.5 cm thick. The second, the internal layer which is 5 cm thick, is made of very low activity lead, which was specially ordered for the underground laboratory (^{210}Pb activity is below 0.1 Bq kg^{-1}). The lead shield is surrounded on all sides and from the top by plastic scintillation sheets 7 cm thick, which are viewed by 5 cm diameter photomultipliers. The plastic scintillation detectors are connected with HPGe detectors in anticoincidence, so they work as a guard for HPGe detectors, eliminating effects of nucleonic component on their background, and partially also the effects of the hard component of cosmic rays that is composed mainly of muons. HPGe detectors (coaxial p-type) were specifically designed for low-level gamma-ray spectrometry in an underground laboratory. They are of U-type with preamplifiers housed outside of the lead shield, however, the FET is mounted on a Cu plate connected to the cooling finger. Only materials with minimum radionuclide contamination were used for the detector construction. Four types of HPGe detectors are housed in the common lead shield surrounded by the anticosmic guard – (i) A 100 % relative efficiency coaxial detector (CANBERRA) with cryostat made of electrolytic copper with carbon window; (ii) A 150 % relative efficiency well type detector (CANBERRA) with cryostat made of electrolytic copper (well dimensions – 32.5 mm diameter, depth 73 mm), well walls made of thin copper; (iii) A 170 % relative efficiency coaxial detector (EURISYS) with cryostat and window made of pure aluminium. (iv) A 200 % relative efficiency well type detector (CANBERRA) with cryostat made of electrolytic copper (well dimensions – 25 mm diameter, depth 60 mm), well walls made of thin copper. ORTEC NIM modular electronics have been used for signal processing and data acquisition. During all measurements radon is expelled from the detector chambers by the evaporation of nitrogen from the detector's Dewar containers, thus keeping stable background during measurements (Sykora *et al.*, 1992). It should be stressed that this detection system is used only for analysis of low activity samples.

The measured background of HPGe detectors with anticosmic veto-shielding is compared in Table 2.4. As the volumes of the detectors differ significantly, it is necessary to compare their background characteristics per kg of Ge. It is interesting to notice that the total detector background per kg of Ge, in the energy window 40-2000 keV, is decreasing with increasing detector volume, i.e. from 290 h^{-1}kg^{-1} Ge for the 100 % efficiency detector, to 205 h^{-1}kg^{-1} Ge for the 200 % efficiency detector. However, the background with the anticosmic veto-shielding does not follow this rule, but clearly shows a larger contribution of radioactive contamination of the detector construction materials to its background. The lowest total background with the anticosmic veto-shielding was obtained for the 150 % efficiency detector (27 h^{-1}kg^{-1}Ge), the highest for the 170 % efficiency detector (59 h^{-1}kg^{-1} Ge). The 170 % efficiency detector have the cryostat made of "pure" aluminium, however, this has been clearly contaminated by U and Th (and their decay products), as well as by ^{40}K. Generally aluminium is from the point of view of radioactive contamination not suitable construction material. It is important therefore that construction materials are carefully tested by the manufacturing companies for the presence of radionuclides before the detector construction, especially for the detector's cryostat and its window. However, it has also been a surprise that three detectors with copper cryostats ordered as low background detectors for an underground laboratory from the same company (CANBERRA) had very different background characteristics. It looks like that the companies cannot guarantee similar detector background characteristics even when using similar construction materials.

The highest background reduction with the anticosmic veto-shielding (Table 2.4) was obtained for the 150 % efficiency detector (factor 9), and the lowest for the 170 % efficiency detector (factor 4). The 100 % and 200 % efficiency detectors have the reduction factors within these limits (factors 7 and 6, respectively). The obtained background reduction factors are considerably lower than we would expect from Monte Carlo simulations (see discussion for the anti-Compton spectrometer). We know from gas counting systems (Povinec, 1978) that an anticosmic veto-shielding may decrease the background of a proportional detector located in a surface laboratory even by a factor of 100. The lower background reduction factors obtained for HPGe detectors located in an underground laboratory may be due to several reasons:

(i) A partial reduction of the detector background due to the underground operation, as the muon flux at 35 m w.e. has decreased by a factor of 4;

(ii) HPGe detectors have a higher efficiency to scattered gamma-quanta which are both of cosmic ray origin and of radioactive contamination of detector construction materials;

(iii) Leakage of muons through the anticosmic shielding, either due to the shielding geometry or their energy off-set in the scintillation veto-detector;

(iv) Cosmic ray secondaries produced by muons passing the lead shield which were not discriminated by the anticoincidence circuit, as it activation time was too short (40 μs in our case) compared with the development time of a cosmic ray shower in the lead shield (200 μs). However, because of dead time problems of HPGe spectrometers with anticosmic shielding, it is usually difficult to increase the width of the gate signal in the anticoincidence circuit above 50 μs.

As hard cosmic ray particles will produce more secondaries in thick lead shield, the lead thickness should be optimised for a given depth below the earth surface (e.g. 150 mm for surface laboratories). Too thick lead shield may be therefore contra productive for obtaining good background characteristics. As for the operation of a semiconductor detector the diode material, in our case Ge, must be very clean to keep loses of charge collection on the detector electrodes as low as possible, the most probably the detector contamination is caused by a cryostat material, which is usually (and preferably) electrolytic copper.

The detector window may also be important, if a combination of copper, aluminium, beryllium or carbon materials are used. If the threshold energy need not be very low, it looks like that the best material is electrolytic copper. If a low energy window is required, a carbon fiber

Tab. 2.4. Characteristics of HPGe detectors in the IAEA-MEL's underground laboratory.

Detector characteristics	**100 %**	**150 %**	**170 %**	**200 %**
Type	Coaxial	Well	Coaxial	Well
Cryostat material	Cu	Cu	Al	Cu
End-cap material	C	Cu	Al	Cu
Ge mass [kg]	2.15	2.50	3.29	4.18
Background at 40-2000 keV [$h^{-1}kg^{-1}$]	290	239	230	205
Background at 40-2000 keV with anticosmic veto [$h^{-1}kg^{-1}$]	40±3	27±2	59±4	33±3
Reduction factor	7.2	8.9	3.9	6.2

window may be the best choice. There are other construction materials that could affect the detector background as well. Preamplifier is usually situated outside of the lead shield, however the FET transistor is connected directly with the diode, as well as a copper cooling finger. These parts, together with soldering contacts, may be therefore crucial for obtaining a low detector background.

The first important finding is that the annihilation peak at 511 keV is still dominant in all background spectra. This peak is produced by annihilation of electrons and positrons in the shield and in the detector, which are products of the interaction of secondary cosmic rays with materials surrounding the detector. The second important finding is a large background continuum, which has a maximum at around 200 keV. This background continuum is produced by the interactions of cosmic muons with the lead shield, as we already discussed.

From background spectra of HPGe detectors operating in various underground laboratories, normalized to the detector mass (Figure 1.5) we can see that the CAVE underground laboratory operating at 35 m w.e. with anticosmic veto-shielding has backgrounds comparable with underground laboratories operating with a passive shielding at 250 m w.e. depth (e.g. Pagava *et al.*, 1992; Niese *et al.*, 1998; Komura and Hamajima, 2004). This is even better seen in Figure 1.4 where integral backgrounds of HPGe detectors divided by the mass of the Ge crystal, operating in different underground laboratories are compared (Laubenstein *et al.*, 2004). Therefore, an anticosmic shielding in an underground laboratory operating at a shallow depth is extremely important for reducing the detector background, and should be widely used. This figure also shows that for the present state of the art of HPGe low background detectors the optimum depth would be around 1000 m w.e. Although in deeper laboratories the cosmic ray muon flux is much weaker, it does not improve anymore background characteristics of HPGe detectors. We believe that a further reduction in the detector background would be possible only with a new generation of HPGe detectors, specially designed (and produced!) for deep underground laboratories. Special arrangements must be also made how to decrease a radon contribution to the detector background, especially if frequent changes of samples in the detection system are required (Heusser *et al.*, 2006).

2.3.2 Design of an Underground Laboratory - Anti-Compton (Coincidence) Spectrometer

Simulation Results for an Anti-Compton Spectrometer. The anti-Compton spectrometer is a powerful technique for reducing the detector's background because it combines both the anticosmic and the anti-Compton suppression of background (Debertin and Helmer 1998). It rejects electronically principal detector pulses that coincide with signals originating in detectors surrounding the principal detector (the active shield). The coincident electronic signals from the active shield and the principal detector are generated by Compton scattered γ-rays from the detector, and by cosmic rays, which give rise to a continuous background spectrum and raise detection limits for the γ-rays with energies in this spectral region (e.g. in the case of analysis of ^{137}Cs in the presence of ^{40}K). The scattered photons escaping from the principal detector volume can be detected by a sufficiently large NaI(Tl) or BGO crystal surrounding the detector. The simplest anti-Compton spectrometer can be made using a Ge detector and an NaI(Tl) crystal with a well. Using a Ge detector in a large NaI(Tl) crystal (about 30 cm dia. × 30 cm long), the Compton suppression factor should reach values above 10 (for $E_\gamma \leq 1.5$ MeV) and thus decreasing detection limits more than three times (Zvara *et al.*, 1994).

Usually, a well designed anti-Compton spectrometer can be used simultaneously as a coincidence and anti-Compton spectrometer, and by adding a β-ray detector, as a triple coincidence spectrometer (e.g. for radionuclides emitting γ-rays in cascades (like ^{60}Co) or for positron emitters (like ^{22}Na, ^{26}Al). Although detection efficiency is reduced in coincidence spectrometers, a considerable decrease in background (by about two orders of magnitude) makes these spectrometers superior for very low-level gamma-ray spectrometry (Zvara *et al.*, 1994). The most sophisticated spectrometric system is the multi-dimensional γ-ray spectrometer (Cooper and Perkins, 1971; Povinec, 1982) in which signals from the analysing detectors form three-dimensional spectra (volumetric peaks) which can contain both coincidence and non-coincidence peaks. Analysing electronics, if two HPGe detectors are used, require 8000×8000 channels, which, with present state of the art computer electronics, is not difficult. The background can be reduced by about two orders of magnitude and three-dimensional spectra enable better identification of the peaks registered (Cooper and Perkins, 1971).

Several detection modes can be used when operating the coincidence-anticoincidence gamma-ray spectrometer:

(i) A single HPGe mode;

(ii) An anti-Compton mode;

(iii) A gamma-gamma coincidence mode (e.g. Staníček and Povinec, 1986; Povinec *et al.*, 2006);

(iv) A triple coincidence mode (e.g. Sýkora and Povinec, 1986);

(v) A summing coincidence mode (e.g. Sýkora and Povinec, 1986);

(vi) A beta-gamma coincidence mode (e.g. Zvara *et al.*, 1994);

(vii) A beta-gamma-gamma coincidence mode (e.g. Zvara *et al.*, 1994).

The simulations were done for an anti-Compton shielding made of NaI(Tl) annulus of 11 cm in the inner diameter, 30 cm of the outer diameter and the height of 40 cm (constructed at IAEA-MEL, Monaco). An NaI(Tl) stopcock of 7.6 cm in diameter and 7.6 cm long closed the annulus from one side. An n-type coaxial HPGe detector of 100 % relative efficiency was inserted inside the NaI(Tl) annulus. The whole detector set-up was placed inside a shield made of 10 cm thick lead, dimensions of 70 × 70 cm, and length of 90 cm. There are two possibilities how to position the detectors in the shield – horizontally or vertically. A draw of the horizontal installation used in the simulation is shown in Figure 2.14. Simulations were carried out separately for both installations.

The code for the horizontal installation has a more complicated muon generator than the standard codes described earlier. Because the basis of the box is not a square, bombardment of sides of different areas has to be correctly sampled so that impact rates are proportional to the respective areas. The anti-Compton shield reduces not only the Compton-continuum but also the cosmic-muon induced background. The reduction is very efficient due to the high detection efficiency of NaI(Tl) crystals for secondary cosmic-ray particles and gamma-rays.

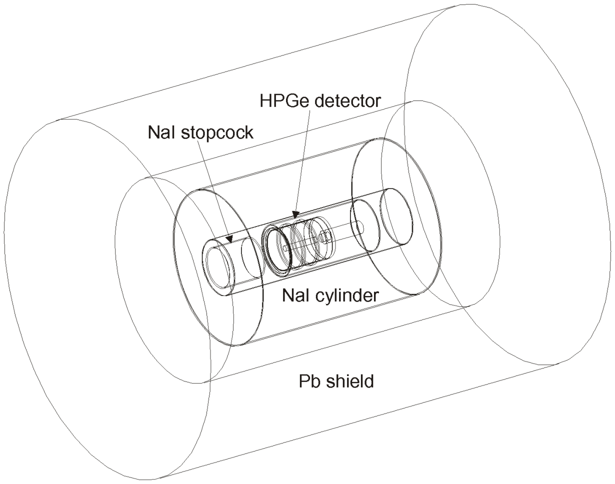

Fig. 2.14. Geometry of the HPGe-NaI(Tl) anti-Compton gamma-ray spectrometer.

Additional codes were used for simulations of the anti-Compton spectrometer in the vertical and horizontal set-up with fixed shield dimensions as described above. Three energy deposition variables *ENERG1, ENERG2* and *ENERG3* containing energy depositions in the HPGe detector, annular NaI(Tl) and the NaI(Tl) stopcock, respectively, were used. The simulated spectra were saved in six arrays: HPGe spectrum up to 3 MeV and 100 MeV with and without active Compton suppression, and spectra of the annulus and stopcock NaI(Tl) detectors up to 300 MeV. The anti-Compton shield has been regarded active if the energy deposited at least in one of the NaI(Tl) detectors had been above 50 keV.

The code for the horizontal set-up has a little more complicated muon generator than the codes described so far. A box is bombarded by cosmic muons instead of horizontally positioned cylinder allowing us to use the already written functions for kinematics distributions. As the basis of the box is not a square, bombardment of sides of different areas have to be correctly sampled so that the impact rates are proportional to the areas.

The obtained results for the vertical and horizontal anti-Compton shield arrangements at sea level and underground are summarized in Figure 2.15. The simulated background spectra at 20 m w.e. underground show the same features as those at sea level, but the background is reduced by a factor of ~ 3 that was observed also in the passive set-ups. A striking feature of the background spectra is that the difference between the horizontal and vertical arrangements is small in the lower energy region, however, it is visible. Therefore, below the energies of 1000 keV the vertical arrangement may be slightly better than the horizontal one. In the region above ~ 10 MeV the spectra differ significantly (Figure 2.16), as the contribution of the secondary processes in the shields is negligible, and the direct ionisation by muons prevails.

The energy deposition spectra in the annular and stopcock NaT(Tl) detectors placed at 20 m w.e. for the horizontal and vertical positions are shown in Figure 2.17. The spectra confirm high efficiency of the anticoincidence detectors. The peak observed in the spectrum represents the track length of muon in the NaI(Tl) crystal.

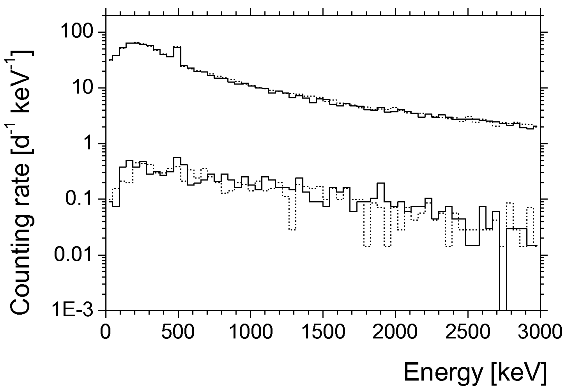

Fig. 2.15. Simulated background spectrum of the anti-Compton spectrometer with 100 % HPGe detector located in underground laboratory at 20 m w.e. (top – Compton suppression off; bottom – Compton suppression on; horizontal position – solid line; vertical position – dots).

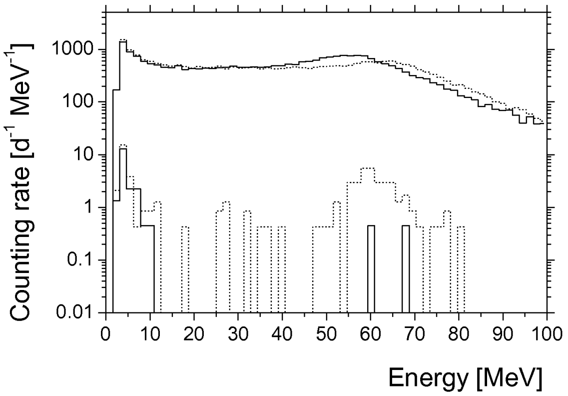

Fig. 2.16. Simulated high energy background spectrum of the anti-Compton spectrometer with 100 % HPGe detector located in underground laboratory at 20 m w.e. (top – Compton suppression off; bottom – Compton suppression on; full lines – a horizontal position; dots – a vertical position).

Background reduction factors obtained by the anti-Compton rejection calculated for the 100 % relative efficiency HPGe detector for energies up to 3000 keV are presented in Figure 2.18. They depend on the energy, reaching values of about 200 for the lowest energies (50-100 keV) and decreasing down to about 40 at 1500 keV. A cosmic-muon rejection factor of about 40 (at around 1 MeV) can be reached when the anti-Compton rejection is operational. However, such high cosmic-muon rejection factors can be reached only if construction materials with negligible radionuclide contamination have been used for the construction of the HPGe detector, its cryostat, NaI(Tl) detectors and the passive shielding.

In such situation, the cosmic-muon background is reduced to such a level that other background components prevail, like those from the residual contamination of the detectors and

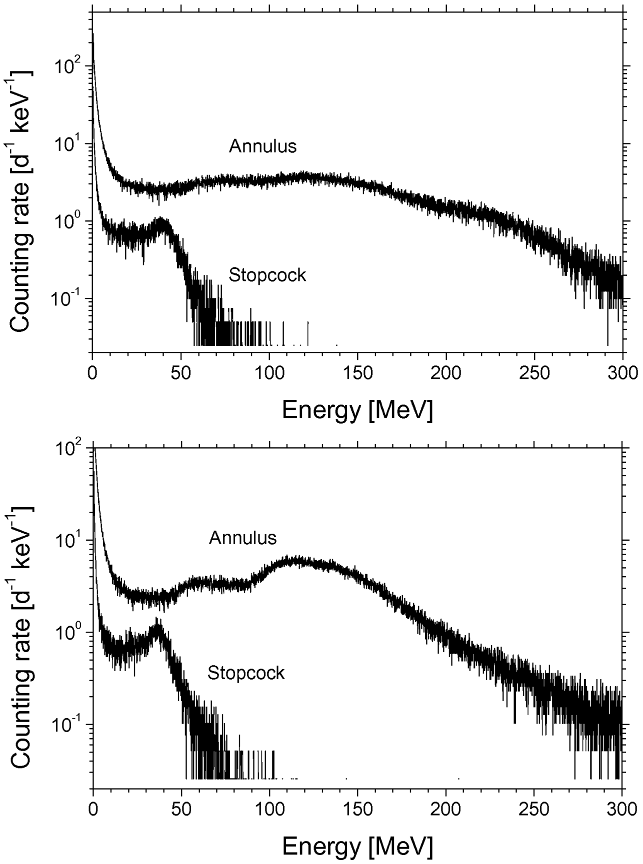

Fig. 2.17. Simulated high energy background spectra in the annular and stopcock NaI(Tl) detectors located in underground laboratory at 20 m w.e. in vertical (left figure) and horizontal positions (right figure).

shielding materials, or from radon, especially for the underground facilities.

Design of an Underground Anti-Compton Spectrometer. The tested concidence-anticoincidence (anti-Compton) gamma-ray spectrometer (Figure 2.19) has as the main gamma-ray detector an n-type HPGe detector (ORTEC) of 100 % relative efficiency (the resolution @ 1.33 MeV ^{60}C line is 2.35 keV, the peak/Compton ratio is 64). The detector arrangement is of a U-type with a preamplifier situated outside of the lead shield, however the FET is mounted on Cu plate connected with cooling finger. The detector cryostat is made of electrolytic copper, the window is made of high purity aluminium. The HPGe detector is surrounded by NaI(Tl) shielding (described above). A double side Si beta-ray detector (ORTEC), located between the HPGe detector and the top NaI(Tl) detector has been used in beta-gamma coincidence studies as well. All detectors are housed in a shield of 10 cm thick, made of ordinary lead previously used for shielding of gas proportional detectors. The background spectrum of this anti-Compton gamma-ray spec-

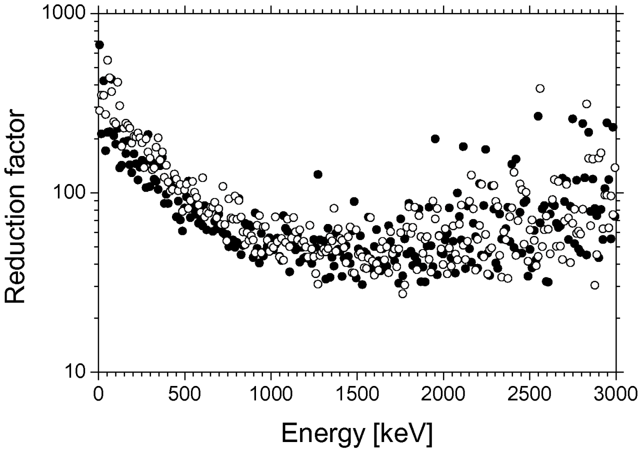

Fig. 2.18. Background reduction factors for the anti-Compton gamma-ray spectrometer at sea level (open circles – vertical position; dots – horizontal position).

trometer is shown in Figure 2.20. The backgroundwith anti-Compton shielding has decreased in the energy interval 30-2500 keV by a factor of 5. However, it can be noticed that the 100 % HPGe detector has in the background spectrum several gamma-lines from natural radionuclides, probably due to a contamination of the ordinary lead shield (an internal low activity lead shielding has not been installed yet).

A radioactive contamination of the construction material plays a crucial role in a low-level anti-Compton spectrometer, which is mainly responsible for its background characteristics, although the shielding geometry of the anti-Compton spectrometer is usually much better than that of a detector with anticosmic veto-shielding only. As HPGe detectors have similar background characteristics, the radioactive contamination may originate in the NaI(Tl) annulus and stopcock detectors, and in photomultipliers. The dominant contaminant in this case is ^{40}K, which is very difficult to remove from the NaI(Tl) detectors. Another possibility would be to use a BGO scintillation detector, which because of higher detection efficiency could have smaller dimensions. However, the radioactive contamination in this case is even worse due to presence of radioactive bismuth and lead in the material.

Because of contamination problems anti-Compton gamma-ray spectrometers will not reach a lowest possible background. They are, however, useful detection systems when a non-destructive analysis of samples containing a wide range of gamma-ray emitters should be carried out, e.g. analysis of low energy gamma-emitters in the presence of high energy ones (e.g. ^{137}Cs (662 keV) versus ^{40}K (1.46 MeV) in sediments.

Another example is advantageous use of gamma-gamma spectrometers when searching e.g. for gamma-emitters with cascade gamma-quanta (like ^{60}Co). Figure 2.21 presents gamma-gamma spectra as measured with a ^{60}Co source using the anti-Compton spectrometer in different modes. It can be seen that the highest selectivity for cascade gamma-quanta can be reached with coincidence mode. Such an arrangement can improve the spectrometer sensitivity by an order of magnitude.

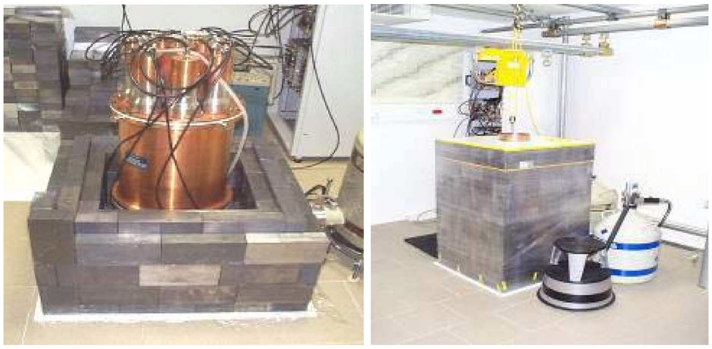

Fig. 2.19. Construction of the anti-Compton gamma-ray spectrometer in the IAEA-MEL's underground laboratory (100 % HPGe detector surrounded by NaI(Tl) detectors in a lead shield).

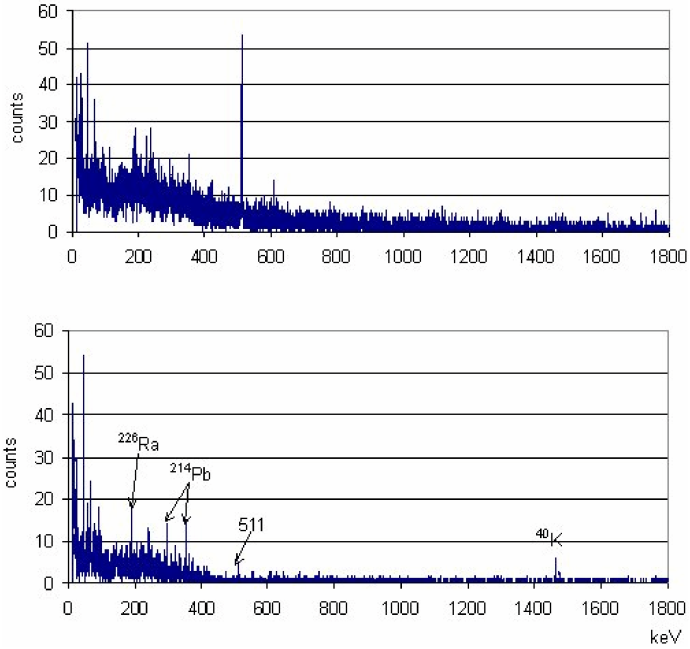

Fig. 2.20. Background spectrum of the anti-Compton spectrometer with 100 % HPGe detector measured for 60,000 s in the IAEA-MEL's underground laboratory at 35 m w.e.

Figure 2.22 compares gamma-ray spectra obtained by a single HPGe detector (70 % relative efficiency) with HPGe-NaI(Tl) (10 cm in diameter and 10 cm long NaI(Tl) crystal) coincidence spectrometer installed in the Comenius University of Bratislava laboratory. The sensitivity of the coincidence mode is clearly visible, as the background and the Compton continuum from ^{40}K has been decreased more than other of magnitude. The detection limit for ^{60}Co in the IAEA-414

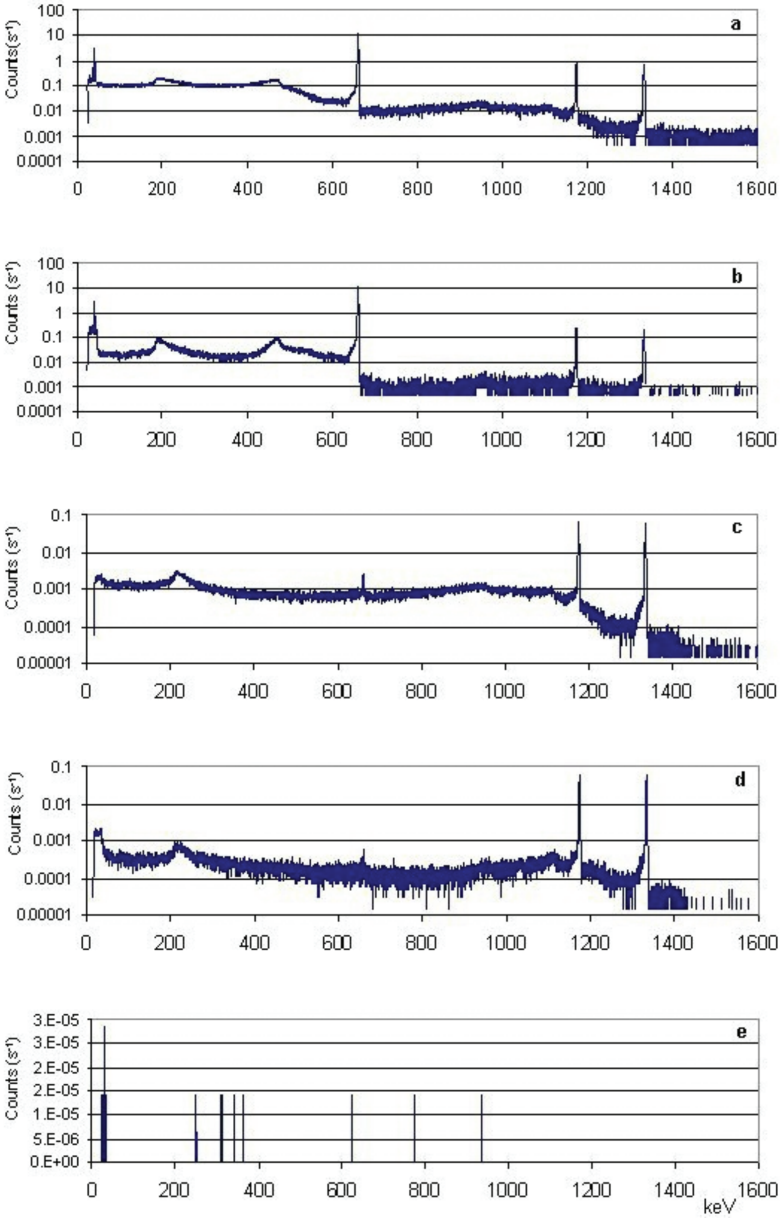

Fig. 2.21. Spectra of ^{60}Co and ^{137}Cs measured with anti-Compton spectrometer (a – single gamma-spectrometer; b – anti-Compton spectrometer; c – coincidence gamma-gamma spectrometer; d – coincidence gamma-gamma spectrometer with Compton suppression; e – background in the gamma-gamma coincidence mode.

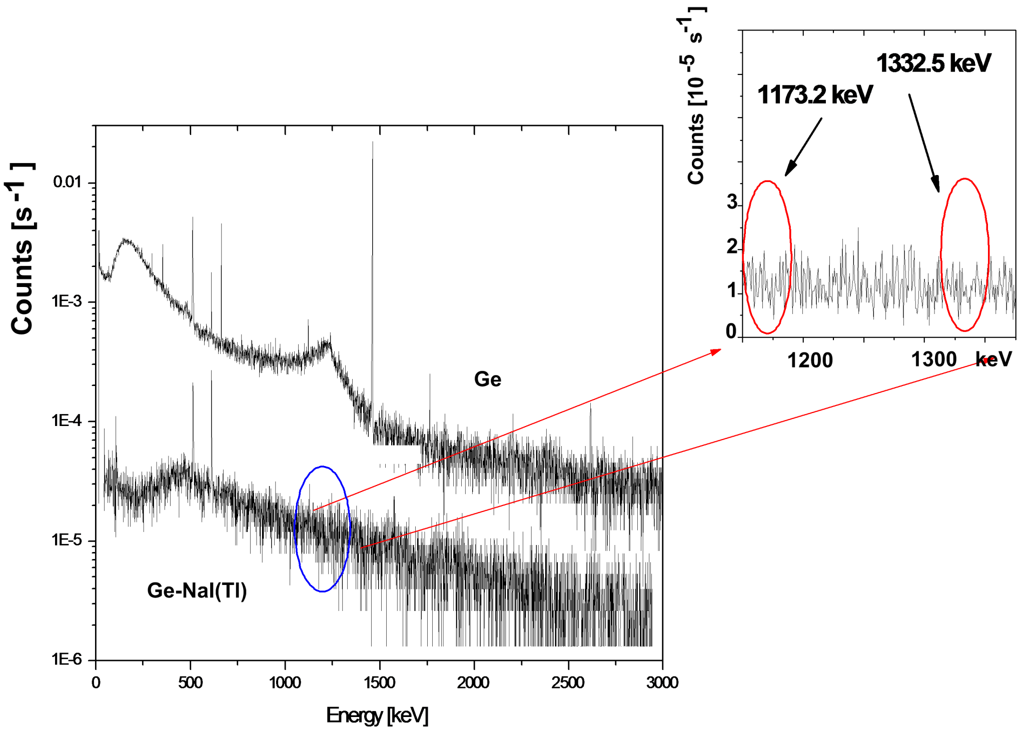

Fig. 2.22. A comparison of single and HPGe-NaI(Tl) coincidence spectra of IAEA-414 refererence material.

reference material (a mixture of Irish Sea and North Sea fish) has been given at 80 mBq kg^{-1} dry weight.

Remarks on Simulations and Laboratory Design. We have seen that the Monte Carlo simulation tools based on the GEANT proved to be capable to model background characteristics of HPGe detectors and thus to optimise the design of low-level gamma-ray spectrometric installations. A computing power is not anymore problem, as desk top computers of sufficient speed and power are available. Therefore the influence of various parameters on the detector background can be studied well in advance, and the cosmic-muon induced background can be estimated before a low-level detector system is constructed. Simulations of characteristics of HPGe detectors placed inside a lead shield without and with anti-Compton shield in surface or shallow underground laboratories revealed useful trends in design of such systems. Given the detector set-up, its background spectra induced by cosmic ray muons can be scaled down by a factor corresponding to the shielding depth. Generally, a radioactive contamination of construction parts of the shield and HPGe detectors itself is still dominating factor as the obtained background was always higher than predicted by Monte Carlo simulations. No important differences were observed when the anti-Compton system was positioned horizontally or vertically. An NaI(Tl) anti-Compton gamma-ray spectrometer inside a passive shield has a detrimental effect on the cosmic-muon induced background if the anti-Compton rejection is switched off because of a thick layer of a relatively low-Z material, compared with standard shielding materials like lead.

On the other hand, a cosmic-muon rejection factor of at least 40 (at around 1 MeV) is predicted when the anti-Compton rejection is operational. In such situation, the cosmic-muon background is reduced to such a level that other background components should prevail, like those from the residual contamination of the detector and anti-Compton shield materials, or from radon, especially in underground facilities. However, such high cosmic-muon rejection factors can be reached only if construction materials with negligible radionuclide contamination have been used for the construction of the HPGe detector, its cryostat, the surrounding NaI(Tl) detectors and the passive shield, and the detector operates in a place with low radon concentration.

The underground counting laboratory with anticosmic shielding of detectors has permitted to effectively decrease the background of large volume HPGe detectors, especially when operating in anticosmic, anti-Compton or coincidence modes. The anticosmic shielding has proved to be a valuable investment as the background of HPGe detectors operating at shallow depths is comparable with underground laboratories operating at moderate depths of about 250 m w.e. For example, in the case of analysis of ^{137}Cs in seawater samples it has been possible to decrease the sample volume by about a factor of 10, which greatly reduces sampling time, and the same seawater volumes could be used for gamma-ray spectrometry as well as for mass spectrometry measurements (Povinec, 2004).

3 Radiometrics Spectrometry and Applications in Environmental Studies

In this chapter we shall briefly discuss results on alpha and beta-ray spectrometry, and on *in situ* underwater gamma-ray spectrometry. We shall also discuss a few recent applications of radiometrics techniques in environmental research.

We have seen that muon-induced background becomes important for large volume HPGe detectors as the most prominent peaks observed (e.g. annihilation peak, neutron activation peaks) have been due to cosmic ray interactions. Alpha-ray spectrometry is free of cosmic ray interferences as the detector medium is very thin and light (silicon) and the registered energy is relatively high (typically between 3 and 6 MeV).

Beta-ray spectrometry is somewhere between - the detection medium (gas, liquid scintillator) is usually of low density, however, typical energies are below 1 MeV. Therefore cosmic ray background will be especially important for low energy beta-ray emitters (like ^{3}H and ^{14}C), therefore, tritium and radiocarbon detectors should also benefit from an underground operation.

3.1 Low-level Alpha-Ray Spectrometry

Semiconductor Alpha-ray Spectrometry (SAS) has become a well matured technique for the analysis of α-ray emitters (mainly actinides, but also ^{210}Po, ^{226}Ra and others) subsequent to the introduction of semiconductor silicon detectors. As the typical energy range of α-rays from investigated α-ray emitters is between 3 and 6 MeV, SAS has been widely used in environmental studies. Other techniques, like ionisation chambers and track detectors have not been so often used in the analysis of environmental samples, mainly because of poorer resolution.

Therefore, the most important developments in SAS have been in the radiochemistry sector, as previously discussed. However, one development we would like to mention here, as the major disadvantage of high resolution SAS compared to mass spectrometry techniques is the difficulty in resolving ^{239}Pu and ^{240}Pu peaks. Large surface (about 10 mm in diameter) silicon detectors frequently used in SAS cannot resolve this duplet. However, by using high resolution silicon detectors and special deconvolution software, this problem can be solved (Leon Vintro et al., 1996). The disadvantage here is that because of the smaller detector surface, sensitivity is lower and only samples with relatively higher concentrations of α-ray emitters can be analysed. This is one of the reasons why mass spectrometry techniques are more widely used for analysis of Pu isotopes in the environment.

3.2 Low-level Beta-Ray Spectrometry

There are several radionuclides (both natural (e.g. cosmogenic ^{32}P, ^{32}Si) as well as anthropogenic (e.g. ^{3}H, ^{85}Kr, ^{90}Sr,^{241}Pu)) found in the environment which are still analysed by beta-ray counting or beta-ray spectrometry, mainly because their half-lives are too short to be analysed e.g. by AMS. For some beta-ray emitters, like ^{14}C and ^{129}I, which were previously analysed by beta-ray spectrometry, AMS is at present the most widely used technique. Other radionuclides, like ^{99}Tc are still analysed by β-ray spectrometry, although ICPMS (and AMS) have been successfully applied as well, and in the future, mass spectrometry techniques will prevail for these radionuclides.

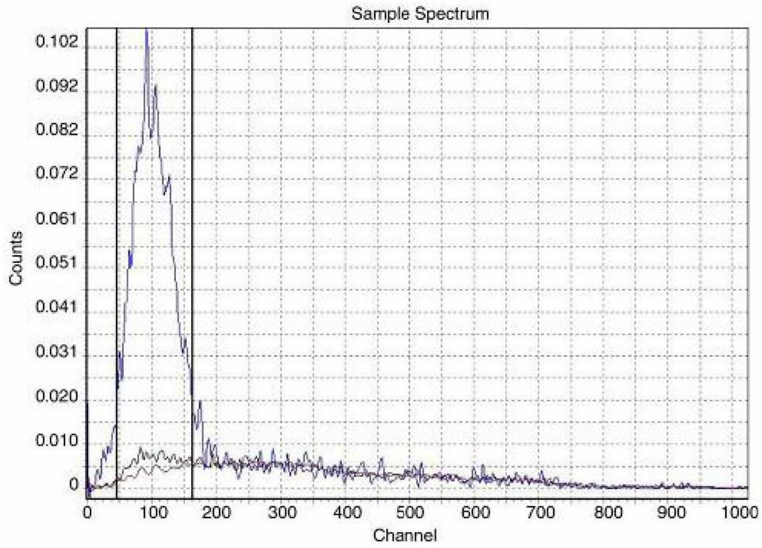

Fig. 3.1. ^{3}H spectra (top: standard; middle: a sample; bottom: background) measured by Quantulus LSS using Insta-Gel Plus cocktail (11 ml of water and 9 ml of Packard Insta-Gel scintillator).

The most important breakthrough in β-ray spectrometry was the introduction of low background Liquid Scintillation Spectrometers (LSS) (Theodorsson, 1996), which are now mainly used for the analysis of short-lived beta-ray emitters in the environment. The advantage over low-level gas counting (Povinec, 1991b) is their higher efficiency as well as that LSS can in fact operate as a beta-ray spectrometer, registering only those β-electrons with energies inside the beta-ray spectrum, and not all beta-electrons registered by e.g. Geiger-Müller counters. We shall illustrate the possibilities of LSS techniques using a few examples – ^{3}H (maximum energy of beta-electrons 18.6 keV; $T_{1/2} = 12.3$ y) and ^{241}Pu (maximum energy of beta-electrons 20.8 keV; $T_{1/2} = 14.4$ years). ^{3}H analysis by LSS without enrichment has a detection limit of about 2 TU (1 tritium unit (TU) is the ratio of 1 atom of ^{3}H/10^{18} atoms of ^{1}H). Operation of the LSS underground can improve the detection limit by about a factor of two. Electrolytic enrichment can further lower the detection limit to 0.01 TU, which is similar to the value obtained by ^{3}He ingrowth mass spectrometry.

For ^{3}H analysis of surface waters contaminated by discharges, simple LSS is the best solution. Figure 3.1 shows a typical ^{3}H spectrum of a water sample (4 TU), a background sample (0.4 min^{-1}) and a ^{3}H standard (about 20 % efficiency) as obtained by WALLAC's Quantulus spectrometer. The Quantulus spectrometer benefits from the low background resulting from the anticoincidence shielding of the counting vial. Similar counting parameters are obtained by the Packard LSS, which uses the pulse shape discrimination method for decreasing the spectrometer's background. Recently an electrolysis apparatus utilising Solid Polymer Electrolyte (SPE) has been developed (which greatly simplifies the enrichment procedure) and with LSS ^{3}H concentrations in water down to 0.01 TU can be measured (Saito *et al.*, 2000).

Another good example of the advantageous use of LSS is ^{241}Pu. As it is a pure β-ray emitter,

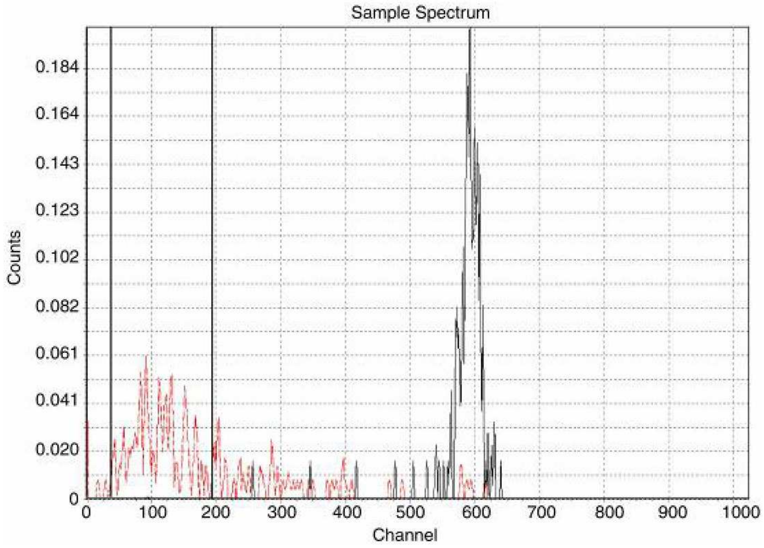

Fig. 3.2. ^{241}Pu beta-ray spectrum (left) and ^{238,239,240}Pu α-ray spectrum (right) measured by Quantulus LSS. Pu separated from Irish Sea sediment was electrodeposited on stainless steel disc and inserted into a Teflon vial with 5 mL Insta-Gel cocktail (Packard).

it cannot be analysed simultaneously with other plutonium isotopes using α-ray spectrometry. However, the disk with electrodeposited Pu after α-ray spectrometry measurement can be placed in a polyethylene vial containing a liquid scintillator (e.g. the Insta-Gel cocktail produced by Packard). Using Pulse Shape Analysis (PSA) method α-rays can be separated from β-rays registered by LSS (Figure 3.2). Typical counting parameters are: 5 ml of cocktail, 12 % efficiency, 0.3 min^{-1} background and detection limit 0.03 Bq (Liong Wee Kwong *et al.*, 2001).

^{241}Pu has highest activity concentrations in environmental samples compared to other Pu isotopes, however, a direct counting is not sufficiently sensitive for many applications. Therefore, the more preferable method is leaching plutonium from the stainless steel disk after α-ray spectrometry (or to separate a portion of Pu sample before its electrodeposition on the disk) and dissolving the sample in the counting vial, enabling 4π geometry measurements, thus increasing detection efficiency by a factor of two (Liong Wee Kwong *et al.*, 2001).

3.3 *In-Situ* Underwater Gamma-Ray Spectrometry

A complimentary detection method to a traditional sampling and laboratory analysis can be a direct, *in situ* analysis of radionuclides, e.g. in the air, in the soil, water or sediment. We shall focus in this paper only on underwater gamma-ray spectrometry and applications in the aquatic environments. Such a novel approach can have several advantages, e.g. complicated and laborious sampling, preconcentration and separation techniques and long-term measurements are not necessary; mapping of gamma-emitters in large surface areas is possible which would require long-term programmes (Jones, 2001; Osvath *et al.*, 1999a; Osvath and Povinec, 2001); screening of sunken or dumped radioactive object (Osvath *et al.*, 1999b); and continuous analysis of radionuclides in water replacing a sporadic short-term sampling and analysis, enabling a real time reporting of data; searching for temporal changes, and development of time series (Wedekind *et al.*, 2000; Povinec, 2004; van Put *et al.*, 2004; Osvath *et al.*, 2005; Povinec *et al.* 2006b).

The systems most commonly used for underwater gamma-ray spectrometry are based on NaI(Tl) (or BGO – bismuth germanate) detectors. The advantage of NaI(Tl)-based systems is firstly related to the high detection efficiency of NaI(Tl) crystals at much lower cost than equivalent Ge crystals. Moreover NaI(Tl)-based systems can be built sufficiently robust and are adequate for long-term underwater deployment. In addition polycristalline NaI(Tl) materials can be obtained with identical optical characteristics but far better thermal and mechanical strength than single crystals, thus further improving the shock resistance and thermal stability of the system. The drawbacks of NaI(Tl)-based systems are the high power consumption for the operation of the photomultiplier tube and a relatively poor energy resolution of the detector (with peaks tens of times wider than those in spectra recorded with Ge detectors).

HPGe-based systems on the other hand have the advantage of good energy resolution and hence excellent radionuclide identification capability (Povinec *et al.*, 1996). However, in terms of ruggedness, autonomy and power consumption, they are generally less performing than NaI(Tl)-based systems. Recently electrically-cooled HPGe γ-ray detectors using Stirling cycle refrigerators have been developed. The size of such a detector assembly including the crystal and the refrigerator is small and its power consumption can be only $\sim$1 W. A submersible electrically-cooled HPGe γ-ray detector system of this type, operational to 500 m depth, was successfully tested by Kobayashi *et al.* (1998).

Other available types of detectors, such as CsI crystals (pure or doped with Tl or Na), fluorides (e.g. CsF, BaF_2) or semiconductor detectors which do not require external cooling (e.g. CdTe, CdZnTe, HgI_2, GaAs), have in general not become competitive with NaI(Tl) and HPGe detectors mainly because of their lower efficiency for the detection of gamma-rays in the energy interval 30-3000 keV.

Higher energy beta-rays emitters, like ^{90}Sr, could be monitored in water either via Cherenkov radiation and/or bremsstrahlung. We shall describe in detail two detection systems developed in IAEA-MEL in Monaco used either for seabed gamma-mapping or for stationary monitoring of radionuclides in the aquatic environment.

3.3.1 Towed NaI(Tl) Detector Systems

Two towing detection systems were developed at IAEA-MEL Monaco. The larger one consisted of a HPGe detector (20 % relative efficiency) with propane cryogenic cooling, and a 100 mm in diameter and 150 mm long NaI(Tl) crystal (Povinec *et al.*, 1997). It was used for investigations of radioactive dumping sites and gamma-mapping of Novaya Zemlya bays (Osvath *et al.*, 1999b).

We shall describe here in detail the smaller system consisting of a NaI(Tl) probe, a shipboard computer and a DC power supply (Osvath & Povinec, 2001). The stainless steel tubular probe casing contains a 152×51 mm NaI(Tl) ruggedised crystal, a high gain photomultiplier tube, pressure, temperature and seabed roughness sensors and electronic circuit boards which provide power to the sensors and process the signals (Figure 3.3). Data are transferred from the probe to the logging computer every second and can be sequentially stored with this frequency or at other user-selected time intervals. A 300-channel spectrum is generated, covering the energy

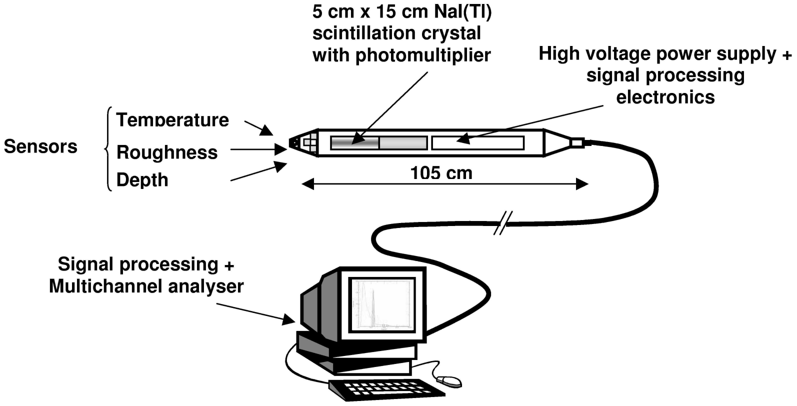

Fig. 3.3. Small underwater gamma-ray spectrometer with electronics.

range from 100 keV to 3000 keV. The logging programme on the PC allows the monitoring of the spectrum recording and of the total count rate, bottom ruggedness, pressure and temperature. The energy calibration of the gamma-ray spectrometer was carried out using ^{137}Cs and ^{60}Co radioactive sources. The energy resolution for 662 keV (^{137}Cs) gamma-rays was 6.5 %. The efficiency calibration was done using a ^{137}Cs source dispersed in a polyethylene tank 1 m in diameter and 1 m high, filled with fresh water. The tank was also filled with seawater with natural concentration of ^{40}K (1462 keV), ^{226}Ra, ^{222}Rn and its daughter products. Background measurements were carried out with the detector immersed in the tank filled with fresh water (Povinec *et al.*, 2006b).

The system was used in several field trips, e.g. for mapping of gamma-emitters in sediments in Mururoa and Fangataufa lagoons, in the coastal Irish Sea (Osvath *et al.*, 2005), and for in situ measurements of radon decay products in coastal Sicily (Povinec et al., 2006) and Brazil (Povinec *et al.*, 2008a).

3.3.2 Stationary NaI(Tl) Detector System

NEMO (Nautic Environment Marine Observatoire), a stationary underwater monitoring system, based on a NaI(Tl) detector was recently built in IAEA-MEL (Figure 3.4). It records gamma-ray spectra in water together with a suite of environmental parameters including seawater temperature, conductivity, current speed and direction (Osvath *et al.*, 2005). These data may be transmitted via a satellite link to a base station at the IAEA-MEL at Monaco. The monitor's capabilities can be further expanded by adding sensors for meteorological (wind speed and direction, air temperature and pressure) and oceanographic measurements (wave height, direction and period, water temperature and salinity profiles, light attenuation, Chlorophyll-A and hydrocarbons). Such a complex data set can be useful as input to transport models.

The NaI(Tl) detector (76 mm in diameter and 76 mm long), shown in Fig. 3.4 as RADAM (Radioactivity Detection and Measuring System), made of ruggedised crystal has 7 % resolution for 662 keV gamma-rays (^{137}Cs). The calibration of the NaI(Tl) detector was carried out in a tank filled with seawater spiked with ^{137}Cs. The efficiency was estimated as 2.1×10^{-4}s^{-1}/(Bq m^{-3})

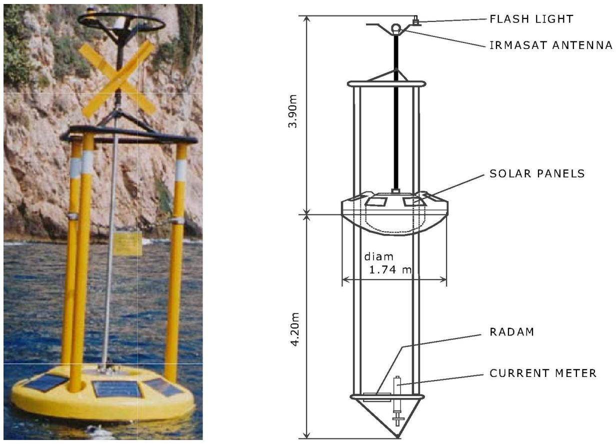

Fig. 3.4. NEMO (Nautic Environment Marine Observatoire) buoy in Monaco Bay, and construction details (RADAM is 5 cm in diameter and 15 cm long NaI(Tl) detector).

net count rate under the ^{137}Cs photopeak. The limit of detection for ^{137}Cs in water is 19 Bq m^{-3} for a 24 hour spectrum integration time or 4 Bq m^{-3} for 30 days integration time. The current speed and direction are measured with a 3-axis ultrasonic transducer, with ranges of 0 – 300 cm s^{-1} and 0-360° and uncertainties of 3 % and 2°, respectively. The temperature sensor has an operational range of -5°C to +45°C with an uncertainty of 0.1°C. Salinity is determined from conductivity measurements performed with an electrode-less induction type cell. The sensors are suspended 4 m underwater on a structure attached to a floating buoy (Figure 3.4). The buoy is equipped with signal processing electronics including a microcomputer and a marine transceiver, and with a set of lead-acid batteries. An integrated GPS receiver continuously records the buoy's position. These instruments and batteries are maintained in a nitrogen atmosphere in an air-tight/water-tight instrument container. The Observatory's autonomy is supported by a set of solar panels installed on the instrument container. The satellite antenna and visual signaling devices are mounted on the top deck, about 4 m above water level.

The NEMO observatory operated in the Monaco Bay, as well as in the northern Irish Sea searching for changes in the current system and monitoring ^{137}Cs releases from the Sellafield (UK) reprocessing facility (Osvath *et al.*, 2005).

3.4 Applications of Radiometrics Techniques in Environmental Studies

We shall present a few applications of radiometrics techniques in marine radioactivity studies where high sensitive methods are required to obtain meaningful results. The applications here have been limited by availability of suitable size of samples, sampling of which has been time consuming and very costly (e.g. when we consider that a water or sediment sample should be brought on the ship deck from depths of a few thousands meters. As the available space is limited, we present only a few typical examples where new techniques have been applied.

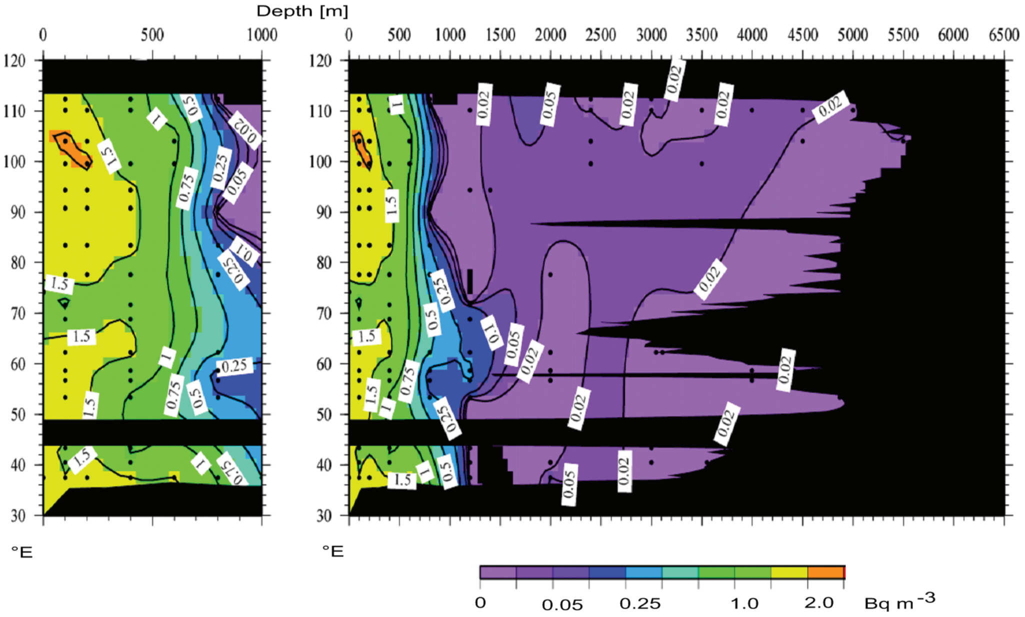

Fig. 3.5. ^{137}Cs transect along the 20°S latitude in the Indian Ocean. Clear subsurface ^{137}Cs maxima around 100 and 60°E can be seen. The observed maximum ^{137}Cs activity concentration (2.1 mBq/L) at 100°E is the highest one measured in the Indian Ocean, which is comparable with levels observed in the central north-west Pacific Ocean (Povinec *et al.*, 2008a).

3.4.1 Caesium-137 Profiles in Indian Ocean Waters

It has been recognised that global fallout ^{137}Cs is powerful tracer for studying exchange of seawater between the ocean basins because due to global fallout higher deposition regions are found in the western part of mid latitudes in the North Pacific. In the framework of the SHOTS (Southern Hemisphere Ocean Tracer Studies) project water profile samples were collected during the round the globe BEAGLE2003 (Blue Ocean Global Expedition) and analysed for ^{137}Cs content (Aoyama *et al.*, 2008).

The ^{137}Cs transect along the 20°S latitude in the Indian Ocean shown in Figure 3.5 represents the first high density sight of ^{137}Cs distribution in the South Indian Ocean (Povinec *et al.*, 2008a). This has been possible thanks to analysis of ^{137}Cs in underground laboratories, which enabled to obtain required sensitivity for 10 times smaller volumes of water samples. For sampling of small (10 L) water samples was thus possible to use Rosette systems, what was not possible before, as large volume samplers ($>$ 100 L), requiring long sampling times, had to be used.

Figure 3.5 clearly shows a presence of two cores of higher ^{137}Cs concentrations at 100°E and 60°E in the water column depth between 100 and 200 m. The subsurface maximum of ^{137}Cs concentration measured near 100°E (2.1 mBq/L) is the highest level observed in southern hemisphere seawater, which is of the same level as the maximum ^{137}Cs concentration observed in North Pacific surface water (Povinec *et al.*, 2003a).

It is impossible to construct the observed ^{137}Cs cores only from a direct input of global fallout ^{137}Cs onto the Indian Ocean. Therefore, the ^{137}Cs cores must be due to an input of the North Pacific ^{137}Cs throughout the Indonesian seas into the cyclonic eddy of the Indian Ocean subtropical gyre, which has also been supported by oceanographic measurements. By a factor of three higher ^{137}Cs inventories than would be expected from global fallout in the South Indian Ocean along the 20°S latitude (up to 1240 Bq/m^2), which are comparable with ^{137}Cs inventories in the north-western Pacific, confirm an input of the North Pacific ^{137}Cs into the South Indian Ocean subtropical gyre.

The estimated residence time of ^{137}Cs in surface waters of the subtropical Indian Ocean ($\sim$ 30 years) is by a factor of 2 higher than for the North Pacific, documenting an accumulation of caesium in the Indian Ocean subtropics. All these findings suggest that the South Indian Ocean subtropical gyre is significant reservoir of anthropogenic pollutants that have been transported from the North Pacific to the south on a time-scale of several decades, which has important implications for the protection of the marine environment.

A reasonably good agreement has been obtained between the WOCE tritium and SHOTS ^{137}Cs data for the southern Indian Ocean (Figure 3.6), indicating a similar distribution of both radionuclides in the South Indian Ocean between 1995 and 2004. The obtained ^{137}Cs data sets for Atlantic, Indian and Pacific Oceans showed a reasonable agreement with WOCE tritium data. However, an unexpected transport of ^{137}Cs has been found from the North Pacific to the South Pacific subtropical gyre, having important implications for circulation of water masses in the world ocean, with possible impact on climate change (Aoyama *et al.*, 2008).

3.4.2 Applications of *in situ* Underwater Gamma-ray Spectrometers

Mururoa and Fangataufa Lagoons. A survey of Mururoa and Fangataufa lagoons was carried out with the aim to assess their radioactive contamination (water, sediment and biota) after nuclear weapons testing (Povinec *et al.*, 1999). ^{60}Co and ^{137}Cs were the main gamma-ray emitters present in lagoon sediment. The in situ sediment measurements were used to guide the sediment sampling campaign in the most contaminated areas of the lagoons where surface tests of nuclear weapons had taken place. A distribution of ^{60}Co in the Fangataufa lagoon sediment showed activities up to 60 kBq m^{-2} (Figure 3.7). A good correlation ($R^2 = 0.8$) found between ^{60}Co and ^{239,240}Pu concentrations (^{239,240}Pu is the radionuclide of main interest in lagoon sediments) enabled the estimation of ^{239,240}Pu inventories on the basis of ^{60}Co mapping and analysis of ^{239,240}Pu in sediments (Osvath *et al.*, 1999a).

Novaya Zemlya bays. Novaya Zemlya bays in the Kara Sea were visited with the aim to assess radioactive contamination of water and sediment after dumping of radioactive wastes there (Povinec *et al.*, 1997). Figure 3.8 shows a HPGe spectrum recorded at one of the stations in Stepovoy Bay. The far superior resolution of the HPGe detector has enabled observation of a low ^{137}Cs concentration which was not visible in the NaI(Tl) spectrum. The spectra obtained with the HPGe detector represent the first set of high resolution seabed gamma-ray spectra ever recorded *in situ*. The ^{137}Cs sediment contamination close to dumped radioactive containers was up to 10 kBq kg^{-1} dry weight (Osvath *et al.*, 1999b).

Mapping of Coastal Sediments in the Irish Sea. Seabed gamma-mapping of radionuclides (mainly ^{137}Cs) was carried out in the Irish Sea close to the Sellafield reprocessing facility. Fig-

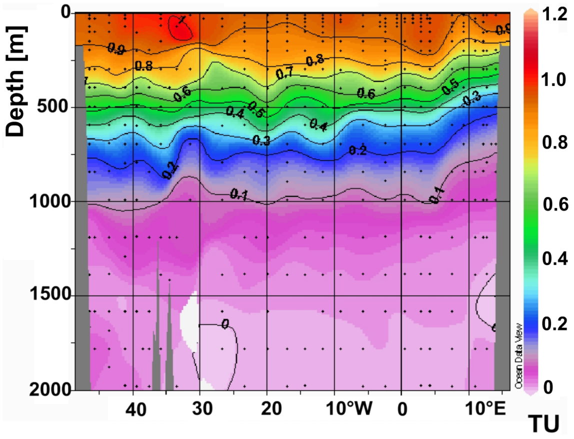

Atlantic (1993)

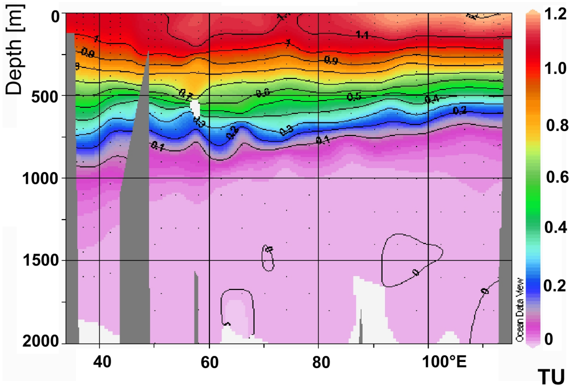

Indian (1995)

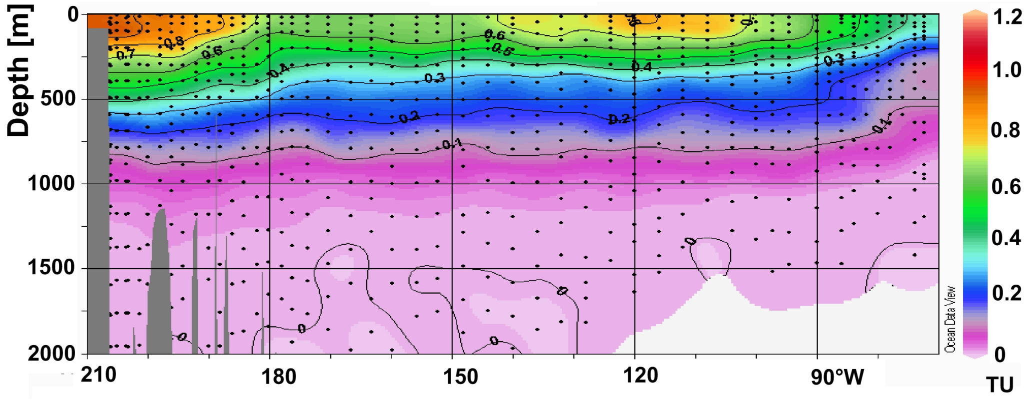

Pacific (1992)

Fig. 3.6. Tritium transects along the 20°S latitude in the Atlantic, Indian and Pacific Oceans as constructed from the WOCE database (`www.woce.edu`).

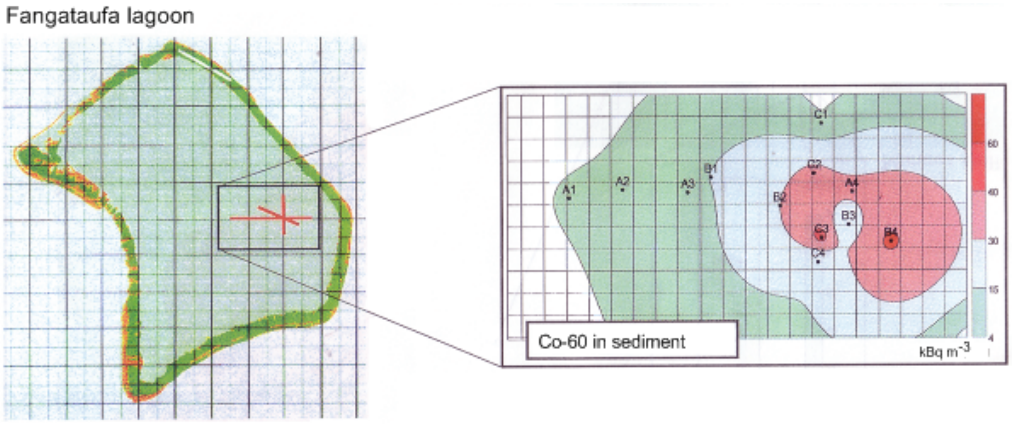

Fig. 3.7. Distribution of ^{60}Co in Fangataufa lagoon sediment.

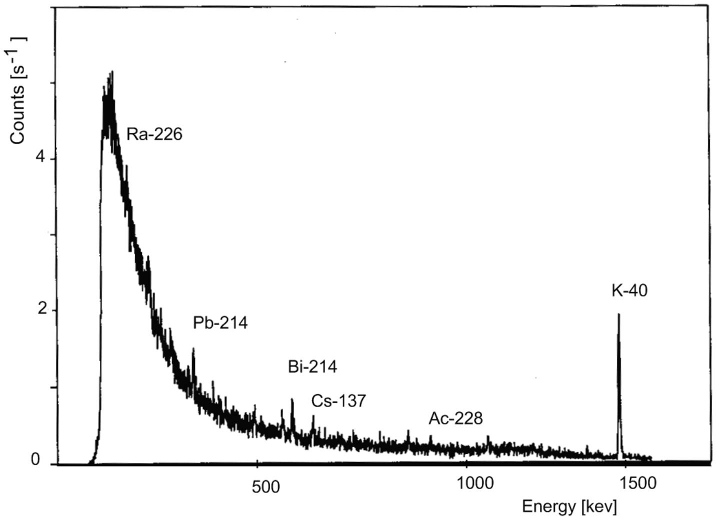

Fig. 3.8. Gamma-ray spectrum recorded by a HPGe detector with propane cooling in Stepovoy Bay, Novaya Zemlya.

ure 3.9 shows the distribution of ^{137}Cs in surface sediment close to the outlet of liquid discharges from the Sellafield reprocessing facility. The measured ^{137}Cs levels in the sediment were up to about 1 kBq kg^{-1} dry weigth. They were lower by 40-70 % than the results obtained 10 years ago, documenting that a remobilisation of ^{137}Cs in sediment of the Irish Sea has been effective (Osvath and Povinec 2001).

NEMO Observatory in the Irish Sea. In situ stationary monitoring of radionuclides in seawater in the NW Irish Sea with satellite data transmission to IAEA-MEL Monaco was carried out

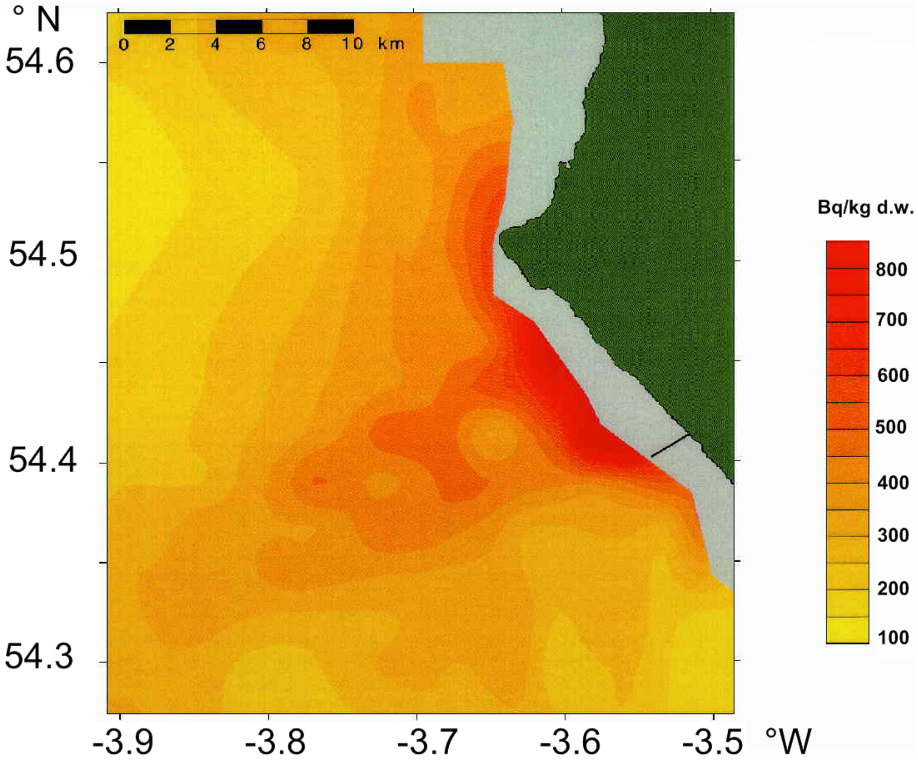

Fig. 3.9. ^{137}Cs massic activity of surface sediments (Bq kg^{-1} dry weiht) in the Irish Sea close to Sellafield (UK) reprocessing facility.

with the aim to search for resuspension of ^{137}Cs from sediment and to study possible changes in its concentration in surface water associated with releases from the Sellafield reprocessing facility, as well as with changes in circulation patterns of the western Irish Sea gyre during the summer months. The obtained results indicate that at the timescale of months no significant changes were detectable in ^{137}Cs concentration in seawater. Fluctuations of ^{137}Cs levels over shorter time-scales would have been within the range of uncertainty of the determinations (Osvath *et al.*, 2005). Figure 3.10 shows a gamma-ray spectrum of water (at 4 m depth) taken with the NEMO observatory in the Irish Sea during a heavy rain when the ^{137}Cs peak (662 keV) was completely masked by the ^{214}Bi peak (609 keV) as a result of wash out of radon decay products from the air. The dominant peak in the spectrum is due to ^{40}K.

Submarine groundwater discharge (SGD) studies offshore Sicily. The *in situ*, fully automatised gamma-ray spectrometers for continuous monitoring of radionuclides in the aquatic environment were also applied for monitoring of natural radionuclides such as ^{40}K, ^{228}Ra and radon decay products, which are commonly used as tracers for studying marine and coastal processes. One of the frequently studied coastal processes is SGD, because of its potential importance for

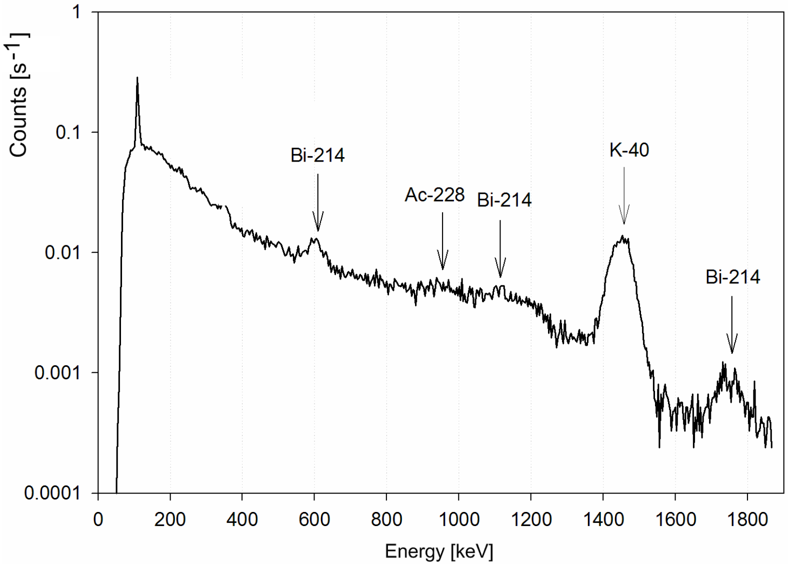

Fig. 3.10. Gamma-ray spectrum of water (at 4 m depth) taken with the NEMO observatory in the Irish Sea during a rain when the ^{137}Cs peak (662 keV) was masked by the ^{214}Bi peak (609 keV) as a result of wash out of radon decay products from the air.

management of fresh water resources in coastal areas. The new technologies developed in recent years have been used to carry out temporal and spatial monitoring of SGD via analysis of radon and its decay products emitting gamma-rays. Radon is a conservative tracer and because its concentration in groundwater is much higher than in seawater, it is an ideal tracer for studying groundwater-seawater interactions (Burnett et al, 2006).

^{222}Rn is a decay product of ^{226}Ra (half life 1600 y) in the ^{238}U natural decay chain, and thanks to its short half life (3.82 d) it is a suitable tracer for studying dynamic systems that are usually found in coastal regions. ^{222}Rn daughters are short lived radionuclides such as ^{214}Pb, ^{214}Bi, etc., which further decay by alpha and beta decays to medium lived ^{210}Pb (22.2 y) and ^{210}Po (138 d), and finally to the stable ^{206}Pb. In the ^{232}Th natural decay chain there is another radon isotope, ^{220}Rn (also called thoron), with a shorter half life (55.6 s). ^{220}Rn is a decay product of ^{224}Ra (half life 3.66 d) which further decays to several short lived daughter products including ^{208}Tl (half life 183 s), and finally to the stable ^{208}Pb.

As short lived daughter products of both radon isotopes, ^{222}Rn and ^{220}Rn, emit gamma-rays, *in situ* gamma-ray spectrometry would be a suitable non-destructive technique of their analysis in seawater, replacing time consuming analysis of ^{222}Rn in the marine environment. *In situ* gamma-ray spectrometry has the advantage that it can also simultaneously analyze other radionuclides, e.g. ^{40}K, ^{228}Ra (via its daughter ^{228}Ac), ^{234}Th-^{234}Pa and others. The best visible gamma-lines in the gamma-ray spectrum of seawater are due to ^{214}Bi (609, 1120 and 1765 keV) for ^{222}Rn daughters, and due to ^{212}Pb (239 keV) and ^{208}Tl (583 and 2615 keV) for ^{220}Rn decay products.

Time series of ^{222}Rn in seawater, salinity and tide were recorded with the small NaI(Tl)

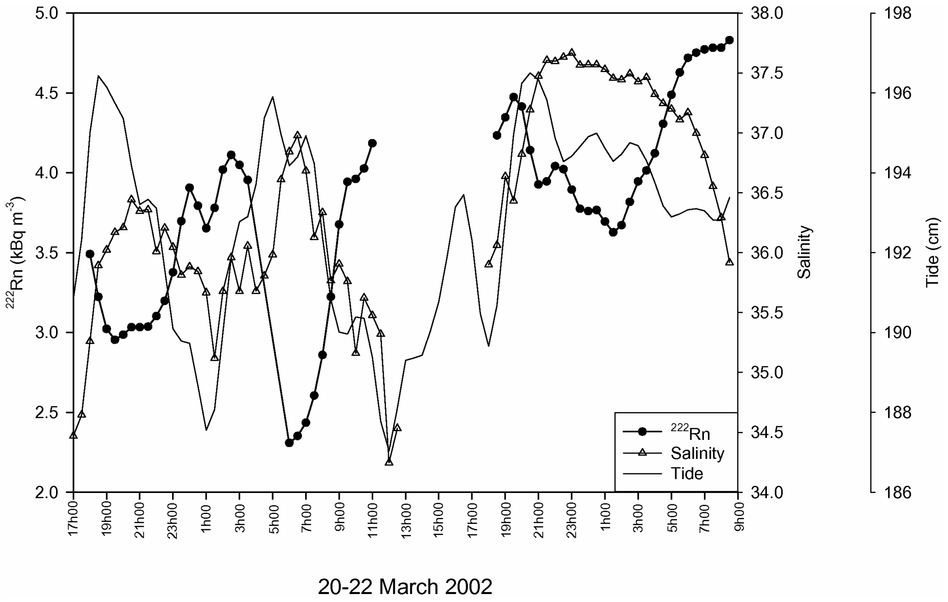

Fig. 3.11. Time series of radon concentration (kBq m^{-3}) in seawater offshore Donnalucata (Sicily) *vs.* salinity and tide.

submersible detector at a site close to the coast in the south-eastern Sicily (near Donnalucata town). Results presented in Figure 3.11 document that after the maximum tide the ^{222}Rn activity concentration of seawater was minimum (down to 2.3 kBq m^{-3}), and after the minimum tide the ^{222}Rn activity concentration was at maximum (up to 4.8 kBq m^{-3}) with a delay of about one hour. A shift of approximately two hours was observed between the maximum tide and the salinity maximum. It is interesting to see that even small changes in the water level, observed e.g. during March 21 and 22, made corresponding changes in ^{222}Rn activity concentrations (Povinec *et al.*, 2006b).

SGD Studies Offshore Ubatuba, Brazil. Continuous underwater gamma-ray spectrometry measurements were carried out in several bays along the Ubatuba coast, especially in Flamengo and Picinguaba Bays, where spatial mapping was carried out, and at the Oceanographic Base of the University of Sao Paolo, about 20 meters from the coast, where time series of radon daughters in seawater were investigated Povinec *et al.*, 2008b). The ^{222}Rn activity concentration in seawater during time series measurements varied between 1.0 and 5.2 kBq m^{-3}, while the tide varied between 4.4 and 5.6 meters. Generally, the salinity record follows the tide record, however, on November 26 a delay in the salinity record was observed. The usual inverse relationship between the ^{222}Rn activity concentration in seawater and tide/salinity was not observed during November 22, despite of large variations in water level. The observed changes in salinity during this time were, however, also smaller than during 25th and 26thNovember. The inverse relationship between the ^{222}Rn activity concentration in seawater and tide/salinity was, however, again estab-

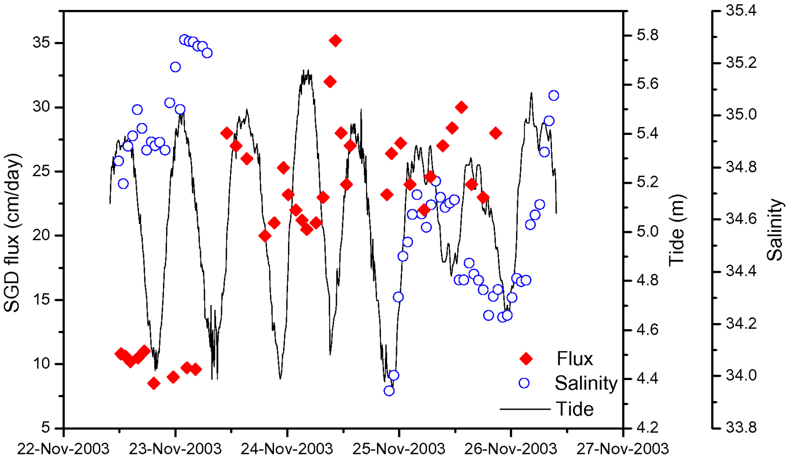

Fig. 3.12. Calculated SGD rates based on continuous gamma-spectrometry of ^{222}Rn decay products offshore Ubatuba (Brazil) vs. salinity and tide.

lished from 23$^{\rm rd}$ to 25$^{\rm th}$ November, when a few hours shift between the tide minimum/maximum and the ^{222}Rn maximum/minimum activity concentration was observed.

Concentration of ^{222}Rn in water can be then used for estimation of groundwater fluxes entering the sea together with radon from the sea-bottom. The radon flux F_{Rn} may be expressed as

$$F_{\rm Rn} = \frac{I_{\rm Rn}}{(1 - \frac{e^{-\lambda t}}{\lambda})}, \tag{3.1}$$

where $I_{\rm Rn}$ is the radon inventory of the water column and λ is the decay constant of ^{222}Rn. After several ^{222}Rn half-lives the SGD flux entering the sea can be expressed as

$$F_{\rm SGD} = \frac{\lambda I_{\rm Rn} - \lambda I_{\rm Ra} + E \pm M}{C_{\rm Rn}}, \tag{3.2}$$

where $\lambda_{\rm Ra}$ is the production rate of ^{222}Rn from ^{226}Ra, E is the atmospheric evasion of radon, M represents the horizontal mixing of radon, and C_{Rn} is the ^{222}Rn concentration in the pore water. The calculated SGD fluxes from radon measurements show similar patterns with time as the ^{222}Rn concentrations (Figure 3.12). The SGD fluxes varied between 8 and 35 cm d^{-1} (the unit is cm^3/cm^2 per day), with an average value of 21 ± 10 cm d^{-1}, and were in reasonable agreement with those obtained from seepage measurements. Generally, these results showed large temporal variations in SGD fluxes, as the spatial ^{222}Rn activity concentrations observed at 8 stations varied between 50 and 200 Bq m^{-3} (Povinec *et al.*, 2008b).

Thanks to elevated concentrations of ^{232}Th in the region it was possible to measure for the first time non-destructively ^{228}Ra in seawater (via its daughter gamma-ray emitter ^{228}Ac). ^{228}Ra activity concentrations measured in Flamengo and Picinguaba bays varied between 1.6 and 3.3 Bq m^{-3}. They were following the ^{222}Rn concentrations measured at the same stations.

4 Mass Spectrometry

Several mass spectrometric techniques have been successfully applied in the past for analysis of radionuclides in the environment. They have used traditional isotope mass spectrometers, like those used for the analysis of light isotopes such as ^{2}H, ^{3}He, ^{4}He, ^{13}C, ^{15}N, ^{18}O, etc. ^{3}He, which is a decay product of ^{3}H, has also been successfully analysed for determination of very low concentrations of tritium.

ICPMS and TIMS have been used for the analysis of several long-lived radionuclides, along with RIMS (Michel, 2001; Povinec, 2005; Roos, 2008; Erdmann *et al.*, 2008). Innovations in SIMS enabled to proceed from bulk sample analysis to analysis of single micro-particles (Betti *et al.*, 2008).

AMS has increased the number of radionuclides from ^{14}C to transuranics, and because the background of the system is significantly reduced by accelerating analysed ions to several tens or hundreds of MeV, and become the most sensitive technique at present for the analysis of long-lived radionuclides in the environment (Jull *et al.*, 2008; Fifield, 2008).

In the present paper we shall focus on detail description of SIMS and AMS techniques, and their applications in radioecology and climate change studies.

4.1 ^{3}H – ^{3}He Mass Spectrometry

Direct analysis of environmental ^{3}H levels by isotope mass spectrometry is not possible because of the high background and relatively short half-life of ^{3}H ($T_{1/2} = 12.3$ y). However, the ^{3}H decay product, ^{3}He is very rare, so its analysis is most suitable for measuring ^{3}H concentrations down to 0.01 TU. At present, this is the most sensitive method of isotopic analysis as isotopic ratios of ^{3}H/^{1}H can be measured down to 10^{-20}, what represents the lowest isotopic ratio analysed in the environment. The only disadvantage of the ^{3}He method is the long waiting period (about 6 months) for in-growth of ^{3}He in a water sample hermetically sealed in a glass flask. On the other hand, if appropriate sampling techniques and containers are used for water sampling, it is possible to analyse ^{3}He and ^{4}He gas in the water column simultaneously. The helium isotopes can give additional information on the water age (^{3}H – ^{3}He method) and on circulation of water masses in the ocean (^{4}He). If a given water parcel in the sea is not subject to mixing with water of different ages, the relation between its ^{3}He content becomes the time (age) elapsed since the last contact with the atmosphere (Schlosser *et al.*, 1999).

As an example, we present in Figure 3.6 the high density profile of ^{3}H in the water column of the south hemisphere ocean developed in the WOCE programme (`www.woce.edu`). WOCE has been the most comprehensive study done till now with radionuclides as oceanic tracers, in which the spatial resolution exceeded that achieved by GEOSECS programme from seventies by about a factor of ten. The WOCE ^{3}H sections provide valuable information on differences in spreading of water masses between the basins, and from the surface into the interior of the World Ocean on a time scale about 10 years.

4.2 Inductively Coupled Plasma Mass Spectrometry

ICPMS has developed into a powerful technique for the analysis of elements, stable and long-lived radioactive isotopes in the environment. With the introduction of the present state of the art high resolution ICPMS machines, this technique competes with TIMS in many respects. The principal advantages of ICPMS are its capability to determine long-lived radioisotopes of metallic elements down to fg levels, to analyse aqueous samples directly and rapidly (in a few minutes), the low cost per analysis and small sample size.

However, ICPMS is not free of matrix and isotopic effects, and the formation of chlorides and oxides requires extra careful purification procedures, e.g. extraction chromatography. A steady increase over the past decade in radioanalytical applications using ICMPS has resulted in a decrease in both the price of instruments and detection limits. New generation sector field instruments with double-focusing and even multi-collector systems have improved sensitivity (by about an order of magnitude) and precision over traditional quadrupole machines (Ross, 2008; Wyse *et al.*, 2001). ICPMS has been used in both higher-resolution and lower-resolution modes. The higher-resolution mode has the advantage of addressing polyatomic interferences, although it cannot solve all the problems with isobaric interferences, which may be caused by incomplete separation chemistry. On the other hand, maximum sensitivity can be reached in the lower-resolution mode. Thus a combination of the two modes appears to be the best compromise for reaching maximum sensitivity and controlling interferences. The higher count rates under lower-resolution mode give better analytical peaks with lower uncertainties and optimal data quality.

Analytes with a relatively strong probability of polyatomic interferences on the isotopes of interest (e.g. ^{238}U which produces a hydride peak that would interfere with ^{239}Pu) should always be scanned. Even so there are problems with the relatively poor abundance sensitivity of sector field ICPMS in the measurement of isotopes with one mass below an abundance peak (e.g. ^{237}Np in the presence of high ^{238}U), and two mass units below (e.g. ^{230}Th in the presence of ^{232}Th, or ^{236}U in the presence of high ^{238}U content). Even when sample matrices are reasonably clean and care has been taken to minimize oxides during tuning, measurements made near the detection limit are sensitive to overestimation due to polyatomic interferences. The use of chromatographic resins (Lee *et al.*, 2001) has been found to be a suitable technique for processing small volumes, removing possible interferences by additional cleaning, as well as for cleaning leached plutonium samples electrodeposited on stainless steel disks, previously analysed by SAS.

Production and certification of reference materials has also gained from the introduction of ICPMS , as this has been used as an effective method for the certification of concentrations of Th, U, Pu isotopes in various reference materials – seawater, sediment and biota (Lee *et al.* 2001; Inn *et al.* 2001; Lee *et al.*, 2008).

Although molecular, isobaric and isotopic interferences remain crucial for successful operation of ICPMS, this technique has a large potential for automation by direct coupling with new generation of chromatography instruments.

ICPMS has been widely applied e.g. on analysis of long-lived radioisotopes of actinides in seawater, sediment and biota, like Th, U, Np and Pu isotopes (e.g. Lee *et al.*, 2001; Roos, 2008). Long-lived fission radionuclides like ^{99}Tc and ^{129}I have been studied in seawater and seaweeds. Usually solution neutralisation has been applied for liquid samples with detection limits below pg. The ETV technique has also been used for determining U and Pu isotopes in seawater and ^{129}I in seaweeds.

Figur 4.1 shows typical example of ^{239}Pu and ^{240}Pu water profile activity concentrations (together with ^{240}Pu/^{239}Pu mass ratios) taken during the IAEA'97 NW Pacific Ocean cruise close to the Enewetak Atoll (Povinec *et al.*, 2003a). The medium depth peak, located at 500 m water

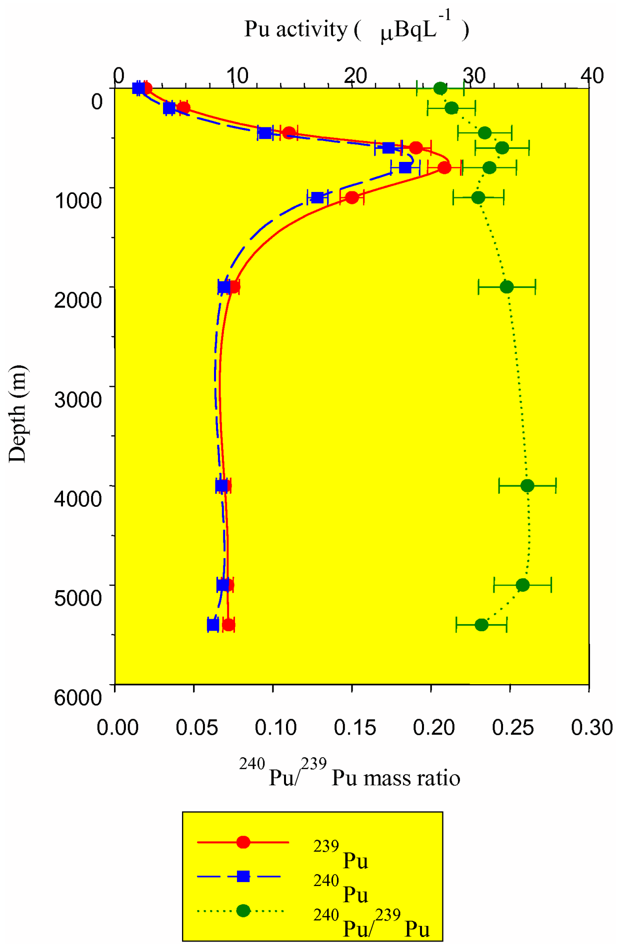

Fig. 4.1. Plutonium isotopes profile in the North-West Pacific Ocean measured by ICPMS.

depth, is clearly visible for both radionuclides, as well as the higher concentrations measured in the bottom sample. The ^{240}Pu/^{239}Pu ratio is higher than expected from global fallout (0.186), indicating the influence of close Bikini and Enewetak atolls affected by nuclear weapons tests on Pu concentrations in the water column of the Pacific Ocean (Povinec, 2004).

4.3 Secondary Ionisation Mass Spectrometry

Mass spectrometry techniques in general and specifically SIMS have found widespread applications in environmental studies due to their abilities to determine isotopic abundance for the characterization of radioactive particles both for nuclear safeguards of clandestine nuclear activities, as well as for monitoring of radioactivity in the environment during routine operations, as well as in case of radiological alarms (Becker, 2008; Betti, 2005; Betti *et al.* 2006).

Microparticles bearing radionuclides, such as uranium, plutonium, neptunium and americium, can enter into the environment and then into the human food chain via different processes. These can be related to the nuclear fuel cycle as well as to clandestine nuclear activities. Moreover, nuclear weapons tests and nuclear accidents have contributed in the past to the spread of radioactive particles in the environment. The necessity of reliable techniques for their characterization, for investigation of their chemical and isotopic compositions, as well as for studies of oxidation states of elements like uranium and plutonium in the environment, are urgent radiological issues (Jernström *et al.*, 2004; Eriksson *et al.*, 2005). Mass spectrometric techniques, can be exploited for revealing the isotopic composition of the transuranic elements present in the particles and in this way to wide information obtained from radiometric methods for better understanding sources and origin of the particles.

After the first Gulf War (1990-1991), the demand for the determination of trace elements and for the identification and characterization of microparticles to reveal the existence of unidentified bulk nuclear materials has increased considerably. Further important applications included the safeguard commitments to search for undeclared nuclear activities. Several nuclear institutes have been engaged in the identification of nuclear materials from unknown activities, having the facilities to handle and to analyze active and/or contaminated samples. Several years ago the capability of analytical chemistry to reveal ongoing undeclared nuclear activities by the analysis of environmental and swipe samples was demonstrated. In particular, the determination of the isotopic composition of single particles has been recognized to be of the utmost importance in environmental monitoring for nonproliferation in nuclear safeguards and forensic investigations.

The EC Institute for Transuranium Elements (ITU) in Karlsruhe has been actively involved in development of several physical analytical techniques. SIMS has been applied for the identification and the characterization of microparticles stemming from nuclear activities (Tamborini *et al.*, 1998; 2004). It has also been used in combination with electron probe microanalysis (EPMA) and glow discharge mass spectrometry (GDMS) for the characterization of environmental samples contaminated with traces of radioisotopes (Lefèvre *et al.*, 1996. Other authors have used SIMS for investigations of single particles of uranium and plutonium. In particular, the accuracy, and precision of SIMS has been studies for the isotopic determination of uranium and plutonium in glass microparticles (Simons, 1986) and in claymicrospheres (Stoffels *et al.*, 1994) have been demonstrated. Betti *et al.* (1999) described the application of SIMS in nuclear forensic investigations with the aim to characterize and identify the origin of plutonium in particles, as well as highly enriched uranium in environmental particles.

In this review we shortly summarise the principles of SIMS and the application of the technique in environmental studies are illustrated in a few examples. For a more detailed description of the technique the reader is can consult Benninghoven *et al.* (1987).

4.3.1 SIMS Principles

SIMS is based on the mass spectrometry of ionised particles that are emitted when a surface, usually a solid, is bombarded by energetic primary particles, which may be electrons, ions, neutrals or photons. The emitted or "secondary" particles will be electrons, neutral species, atoms or molecules, or atomic and cluster ions. The large majority of species emitted are neutral, but it is the secondary ions that are detected and analysed by the mass spectrometer. This is a process that provides a mass spectrum of a surface and enables a detailed chemical analysis of a surface or solid to be performed.

Today, SIMS has an acknowledged place among the major techniques of surface analysis and micro-structural characterisation of solids. Profiling or other applications of SIMS that are not static are referred to as dynamic. Dynamic SIMS has found extensive applications throughout the semiconductor industry where the technique had a unique capability to identify chemically the ultra-low levels of charge carriers in semiconductor materials and to characterise the layer structure of devices.

SIMS has been particularly noted for its outstanding sensitivity of chemical and isotopic detection. Quantitative or semi-quantitative analysis can be performed for small concentrations of most elements in the periodic table, including the lightest. However, the high versatility of SIMS is mainly due to the combination of high sensitivity with good topographic resolution, both in depth and (for imaging SIMS) laterally. Its generally superior trace element sensitivity, capability for spatial resolution in three dimensions and for isotope measurements, as well as potential for identification of chemical compounds in many cases, make SIMS one of the preferred methods for the solution of many analytical problems.

Deficiencies, however, still exist in the capability of SIMS for quantitative elemental analysis compared to other surface techniques (e.g. the Auger spectroscopy, X-ray photoelectron spectroscopy, electron microprobe techniques, etc.). These deficiencies can be traced to the extreme dependence of relative and absolute secondary ion yields on several parameters. Among these the following are the most important:

- matrix effects;
- surface coverage of reactive elements;
- angle of incidence of primary beam with respect to the sample surface;
- angle of emission of detected ions;
- mass-dependent transmission of the mass spectrometer;
- energy band-pass of the mass spectrometer;
- dependence of detector efficiency on element.

A quantitative elemental SIMS analysis poses a twofold problem. Firstly, spectral interpretation, namely, the extraction of total detected isotopic ion currents assignable to elemental and molecular ions from a complete SIMS spectrum of the sample; secondly, spectral quantification, namely the calculation of elemental concentration from total isotopic elemental (and molecular) ion currents. Difficulties in spectral interpretation are considerably reduced if high resolution mass analysers ($M/\Delta M > 3000$) are used for mass analysis of secondary ions because most of the commonly occurring isotopic and molecular interferences (e.g., hydrocarbons, oxides, hydrides) can be resolved.

A diagram of a SIMS instrument with double-focusing mass analyser is represented in Figure 4.2. The secondary ion mass spectrometry is based on:

- bombardment of the sample surface by focused primary ions, with sputtering of the outmost atomic layers;

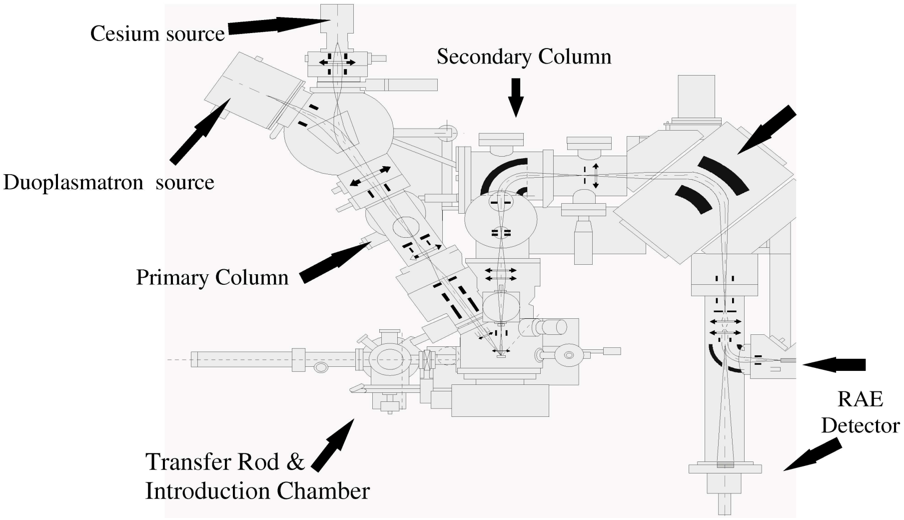

Fig. 4.2. Diagram of a double focusing SIMS (reproduced from Török *et al.* (2004) with permission of Elsevier).

- mass spectrometric separation of the ionised secondary species (sputtered atoms, molecules, clusters) according the their mass-to-charge ratios;
- collection of separated secondary ions as quantifiable mass spectra, as in-depth or along-surface profiles, or as distribution images of the sputtered surface.

The primary ions are normally produced by a duoplasmatron type of gas source such as O_2^+, O^-, N_2^+, Ar^+, by surface ionisation as for Cs^+ and Rb^+, or by liquid-metal field ion emission as Ga^+ and In^+. The most common primary ions used are the oxygen ions, Cs^+ and Ga^+ions. The ions are accelerated and focused to a selected impact area on the specimen. The collision cascade following the incidence of a primary ion results in the implantation of the primary particle, reshuffling of some 50-500 matrix atoms, and emission of secondary particles, neutral or ionised. Secondary ions from the specimen are extracted into the mass spectrometer, which can consist of electric (ESA)/magnetic deflection fields or be of the quadrupole or time-of-flight design. Secondary ions with a given mass-to-charge ratio and within a certain interval of kinetic energy are collected for pulse or current measurement, ion-optic imaging, and data processing.

The different ways of operating a SIMS instrument are presented in Figure 4.3. In the microscope mode, a defocused primary ion beam (5-300 μm) is used for investigating a large surface. In the microprobe mode, a focused primary ion beam ($< 10\mu$m) is used for investigating a very small portion of the surface and detecting inclusions in bulk material. The lateral resolution is defined by the primary ion beam size.

Sensitivity and Quantification. Figure 4.4 shows schematically the types of analytical information that can be obtained by SIMS analysis. A SIMS spectrum normally shows mass peaks that are characteristic of the sputtered solid but affected by experimental factors. For instance,

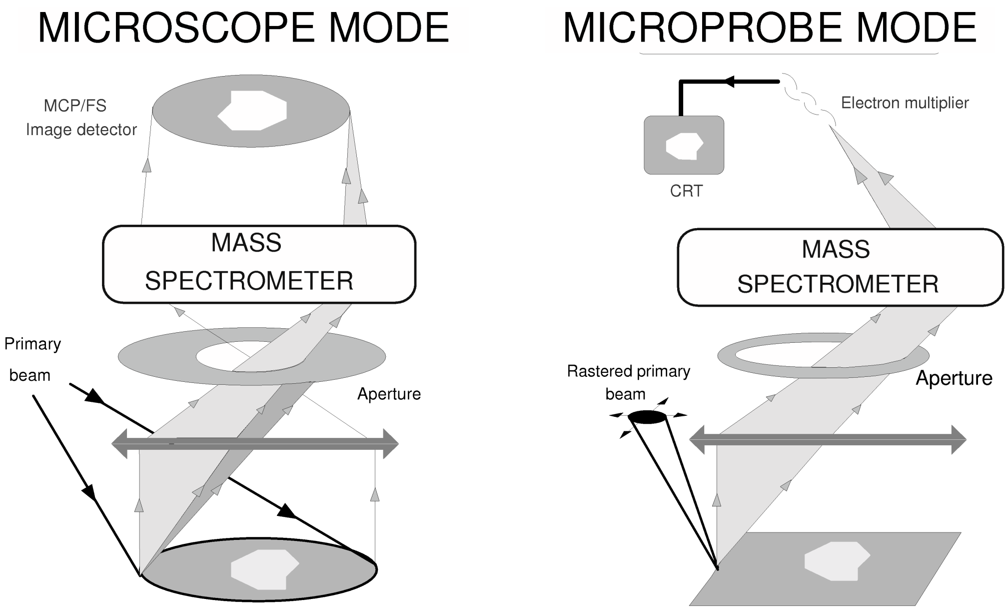

Fig. 4.3. Operating Modes of SIMS (reproduced from Török *et al.* (2004) with permission of Elsevier).

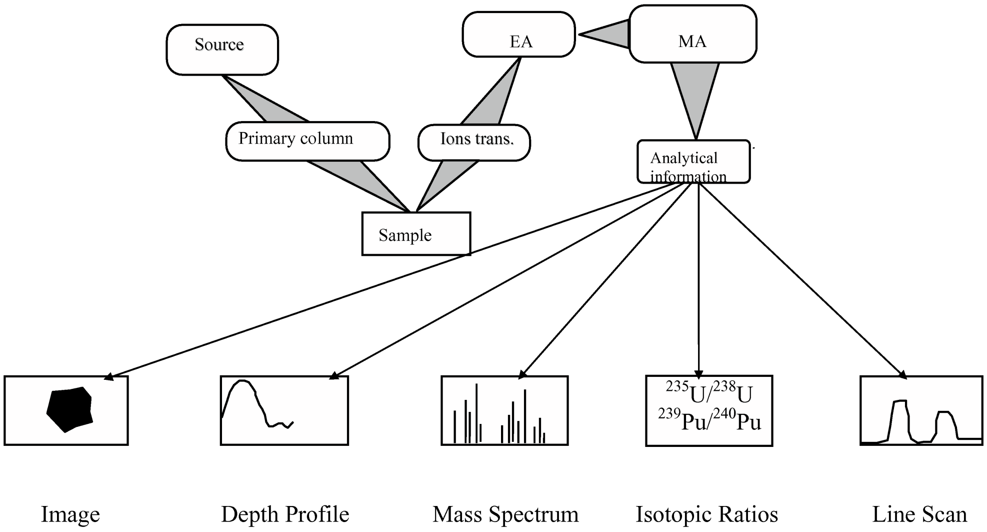

Fig. 4.4. Analytical information obtainable from SIMS analysis (reproduced from Török *et al.* (2004) with permission of Elsevier).

among these factors the following should be mentioned: type, intensity, energy and incidence angle of the primary ions; the transmission of the secondary ions and the selectivity for them in the mass analyser; the type of detector. There are, effectively, two spectra: that of the matrix and that of the impurities.

The task of analytical SIMS is to quantify the secondary ion currents, that is to convert the intensity of one or several peaks characteristic of an element to its corresponding concentration c_e. When a primary ion beam with a current density, i_p, strikes the sample, collision cascades are initiated, resulting in, among other things, the emission of secondary ions. These ions are partially detected with an instrument transmission, η, as a mass spectrum of ions from an analysed area, A. The detected positive or negative current of an ionic species M at the mass number M will be:

$$I_M = I_p S P_M \eta_M \gamma_M b_M c_e \tag{4.1}$$

where I_p is equal to $i_p A$ and P is the probability that the particle (atomic or molecular) will emerge as the last step of the sputtering and recombination cascade. S is the sputtering yield (secondary particles per primary ions), γ_M is the positive or negative ionisability of M (ions per atom or molecule), and b$_M$ is the isotopic abundance of M in the element.

Absolute Sensitivity. In a situation where the prime goal is to detect trace elements of as low a concentration as possible, without consideration of sample consumption and analytical volume (e.g., in bulk analysis), the suitable figure of merit is the detected secondary ion current of an element A per unit of atomic concentration $c(A)$, that is the absolute sensitivity $S_a(A)$:

$$S_a(A) = N^q(A)/c(A), \tag{4.2}$$

where N^q is the detected current (in counts per second) of element A in charge state q.

Practical Sensitivity. The practical sensitivity, $S_p(A)$, takes into account the fact that in different analytical situations different primary beam currents may be appropriate:

$$S_p(A) = N^q(A)/I_p c(A). \tag{4.3}$$

This definition of practical sensitivity does not provide a figure of merit independent of material consumption. The same value would be obtained on different samples for the element A if, at the same primary beam current, the secondary ion currents of element A are identical, even if X sputters much faster than Y.

Yields. If the amount of sample is limited or the sampling volume has to be small, the appropriate figure of merit is the useful yield, $\tau_a(A)$. It is defined as the number of detected secondary ions/s, $N^q(A)$, of element A per number, $n(A)$, of sputtered A (atoms/s) from the same sampling volume:

$$\tau_a(A) = N^q(A)/N(A) = S_p(A)/Y_{\text{tot}} \tag{4.4}$$

Using the previously introduced figures of merit, the fundamental SIMS formula can be alternatively written as:

$$\begin{aligned} N^q(A) &= S_a(A)c(A) \\ &= S_p(A)N_p c(A) \\ &= \tau_a(A)N_p Y_{\text{tot}} c(A) \end{aligned} \tag{4.5}$$

where S_a is measured in counts per second (cps) and dimensionless units have to be chosen for S_p and τ_a. When S_a, S_p or τ_a are known, Eq. (4.5) provides a simple means for calculation of elemental concentration, $c(A)$, from the measured secondary particle current, N^q.

Recently, the results of an inter-laboratory round robin exercise on the sensitivity of SIMS instruments have been published (Tamborini *et al.*, 2004). The exercise has been performed using metallic uranium and uranium oxide particles as test samples. The practical sensitivity and useful ion yield were measured as comparison parameters. The inter-laboratory standard deviation in the determination of the practical sensitivity was 37 % and that of useful ion yield 28 $\%$. Determination of practical sensitivity and useful ion yield using standard samples on a daily or weekly basis resulted in a good method for optimising the measurement system and establishing quality control of the SIMS measurements.

Sensitivity Factors. Quantitative results in SIMS can be achieved by external standards or by utilising the concept of sensitivity factors. Under scrupulously reproducible conditions of analysis, and using external standards with composition and microstructures not too different from the analysed samples, useful calibration factors may be obtained. However, long-term instabilities in analysis (instrumental drift, changes in primary beam conditions, vacuum effects, crystalline effects) make the use of absolute sensitivity factors hazardous. It is generally found to be both very feasible and more reliable to utilise the simultaneously measured ion current, i_r, of a matrix reference element, r.

It has been found that relative sensitivity factors (RSFs) remain practically constant within quite wide ranges of concentrations, that is, that the differences are only weakly dependent on concentration. Excellent results obtained using RSFs has been reported, for example, for steels, binary alloys, glasses and semiconductors. The dominant sources of variation and irreproducibility in absolute and relative sensitivity factors are connected with the ionisability of the elements.

4.3.2 Isotope Ratio Measurements by SIMS

Instrumental Parameters and Matrix Effects. SIMS provides the capability of resolving fine-scale (some μm) isotopic variations within single mineral grains and analysing fine-grained minerals without the need for physical separation. Instrumentation and technical advances have led to improvements in precision to the point where reproducibility is often better than 1‰ and within 1-5 times that of conventional analysis for H, C, S, B, and O isotopes. These precision levels allow the ion microprobe to be usefully applied to the study of a variety of geological processes, as well as opening new areas of research in cosmochemistry. In fact, during the last fifteen years SIMS has been increasingly used for the analysis of light stable isotope ratios in geological and cosmochemical studies (Riciputi *et al.*, 1996; Lyon *et al.*, 1995; Leshin *et al.*, 1997; Deloue *et al.*, 1991; Jones *et al.*, 2004; Ito *et al.*, 2004).

However, limitations still restrict the use of the ion microprobe in geological studies. Isotopic fractionation occurs at a variety of stages during SIMS analysis, including sputtering, ionisation, extraction, transmission of the secondary ions through the mass spectrometer, and secondary ion detection. More problematic is the “matrix effect”, wherein the chemical composition of the analyte affects measured isotope ratios. The combination of these effects, which almost always favour the light isotope and can result in fractionations of a few to 100’s of per mil from the “true” value, is termed the instrumental mass bias. To obtain accurate isotope ratio measurements the mass bias needs to be adequately quantified and controlled. The correction of mass bias is straightforward when matrix-matched standards are available. However, most matrices are complex, requiring either an extensive suite of standards (that can be time consuming, expensive, and difficult to develop) or predictive models that relate mass bias to sample composition.

Riciputi *et al.* (1998) reviewed the factors that influence instrumental mass bias during SIMS analysis of light stable isotope ratios in minerals focusing primarily on compositional matrix effects. Moreover, they have reviewed empirical models that relate mass bias to matrix composition. Fitzsimons *et al.* (2000) have reviewed the analytical precision in stable isotope measurements. Assuming that isotope ratios were taken in such a way as to avoid time-fluctuations, the precision was determined by the Poisson counting statistics and SIMS could compete with conventional bulk analysis if counting times of several hours were used. The gradual shift in mass fractionation with time could be corrected for by the analysis of reference materials. The final precision of a corrected isotope ratio largely depended on the scatter in the sample and the reference material.

The introduction of a multicollection system has been a significant breakthrough towards better measurement reproducibility (de Chambost *et al.*, 1997). However, there are still some limiting instrumental factors preventing one from reaching the desired precision of a few tenths $^0\!/_{00}$. These instrumental issues are the instrumental mass fractionation variability and the electron multiplier (EM) gain drift (as far as EM detectors are involved) (Slodzian *et al.*, 2001). Schumacher et al. (2004) have reported the results of experimental procedure improvements in order to control these two instrumental effects for different types of isotope ratios. They demonstrated that multicollection systems allow improvement of measurement reproducibility for isotope ratios on SIMS instruments provided that the other sources of measurement variability are well controlled. Results for both silicon and oxygen isotopes demonstrate that an experimental error as low 0.2 per mil is achievable whenever both were measured either with Faraday cup detectors or combining one Faraday cup and one electron multiplier (EM).

The introduction of an automatic control of the beam centering for controlling the mass fractionation has significantly improved the measurement reproducibility. For oxygen ^{16}O/^{18}O ratio, with a total integration time of 2 min per spot, a STDE (%) of 0.2 per mil has been demonstrated in zircon. A model has been developed to monitor and to apply a post correction for the EM drift. The pertinence of model has been presented. However, it was found that the EM yield stability is good enough for reaching an experimental precision in the range of 0.2 per mil without need for drift correction.

Single Micro-Particles. Single particles in the 1-10 μm range remains a challenging application of SIMS. Nittler and Alexander (2003) developed an analytical system for the fully automated determination of isotopic ratios in μm-sized particles on the basis of ion imaging and new algorithms to localize the particles. A 75×75 or 150×150 μm sample area were scanned with a Cs^+ or O^- primary ion beam, focused to a spot with diameter of 1 or 0.5 μm, respectively. Once localized, the particles of interest were then individually analysed with a focused ion beam scanned over an area of 3×3 μm. Use of optical encoders circumvented the poor reproducibility of the commercial sample stage and positioned the beam within 1 μm of a predefined point. The statistical error on ^{28}Si and ^{29}Si using the peak-jumping mode was 2.6 and 2.7, respectively, while the intrinsic uncertainty remained within 3. The accuracy of Al isotope determinations

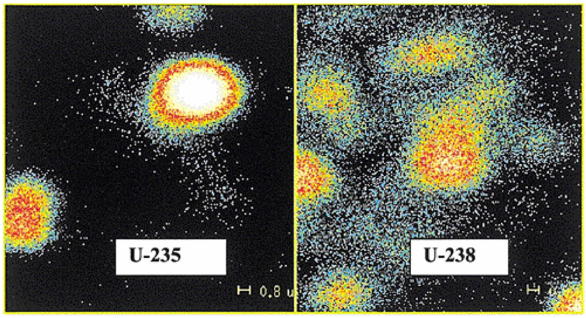

Fig. 4.5. Images acquired for the masses 235 and 238 of the uranium isotopes over a sample area of 250 × 250 μm. The colours are related to the intensity of the signal that increases from the blue through the red to white.

was within the counting error of 10-15. The automated analysis typically processed 300 particles per day, depending on the number of grains per area and their size.

Tamborini and Betti (2000) and Betti *et al.*, (1999) used SIMS for the characterisation of plutonium and highly enriched uranium in nuclear forensic analysis. They measured the uranium isotopic composition with a typical accuracy and precision of 0.5 %. As for Pu, the isotopic ratio 239/240 was determined and resulted in agreement with the results from thermal ionisation mass spectrometry. Figure 4.5 shows the images acquired for the masses 238 and 235 of the uranium isotopes over a sample area of 250 × 250 μm. Figure 4.6 shows the images acquired for the masses 239 and 240 of a plutonium particle. In Figure (a) and (b) a particle with a diameter of 3.5 μm and of 15 μm, respectively, are represented.

SIMS data has been used to complement that from TIMS and scanning electron microscopy (SEM). The isotopic ratios obtained by SIMS for the uranium and plutonium particles have been compared with those obtained by TIMS. As for the dimension and shape, the plutonium particles, from their SIMS image, were found to be consistent with those observed by SEM. Furthermore, SIMS has been used to obtain a complete spectrum of the trace elements contained in a microparticle. From the trace elements present and their concentration in microparticles of plutonium and uranium, the history of the sample can be revealed, namely the physical/chemical and/or industrial processes the sample has undergone.

The same authors have measured ^{18}O/^{16}O isotope ratio by SIMS in uranium oxide microparticles (Tamborini *et al.*, 2002) for nuclear forensic diagnostic. The same group (Török *et al.*, 2004) has exploited SIMS, in combination with other instrumental analytical techniques, for the characterisation of soil particles bearing depleted uranium (DU). The particles localised by the automated SEM with gun shot residue program were then analysed by SIMS for uranium isotopic ratios.

An interesting example to mention is discovery of enriched uranium in Mediterranean sediments. SIMS isotope analysis has confirmed the presence of enriched ^{235}U (from 1 to almost 70 %). Earlier film exposures of the sediment sample and its neutron irradiation in a reactor indicated a presence of hot particles. Figure 4.7 presents SIMS images of a particle extracted from the sediment containing highly enriched uranium. For these particles also the signal relevant to lead isotopes, which may interfere with uranium isotopes, was recorded. Actually, in the sam-

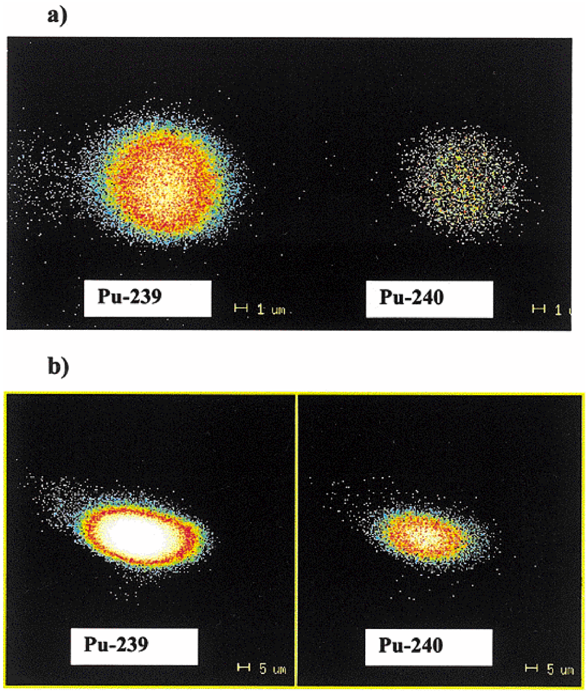

Fig. 4.6. Images acquired for the masses 239 and 240 on plutonium particles. (a) Particle with a diameter of 3.5 μm. (b) Particle with a diameter of 15 μm.

ples the lead is prevalent, but it was not found inside the particles containing the highly enriched uranium. The uranium mass 235 is well visible in the SIMS scan (Povinec *et al.*, 2008c).

More specific applications of SIMS for the characterisation of real samples are described in detail in coming sections.

4.3.3 Characterisation of Depleted Uranium Particles

Depleted uranium (DU) is the by-product in the production of enriched uranium for civil uses (nuclear fuels). If, as feed material for the enrichment reprocessed uranium is employed, DU can contain traces of minor actinides and fission products (Betti, 2003). Due to its physical properties (e.g. high density that is about twice that of lead) it finds applications for civil and military uses. For instance, it is employed in counterweights or ballast in aircraft; radiation shield in medical equipment; as containers for the transport of radioactive material and chemical catalyst (Betti, 2003). Depleted uranium ammunitions have been used during the Gulf war and the conflicts in Bosnia-Herzegovina as well as in Kosovo. Radiological assessments on the effects of dispersion of uranium into the environment as well as investigations of the chemical- and radio-toxicity of uranium have been carrying out (JERN, 2003).

Several authors characterized depleted uranium particles collected in soil samples in Kosovo and Kuwait using different instrumental analytical techniques (Danesi *et al.*, 2003; Török *et al.*,

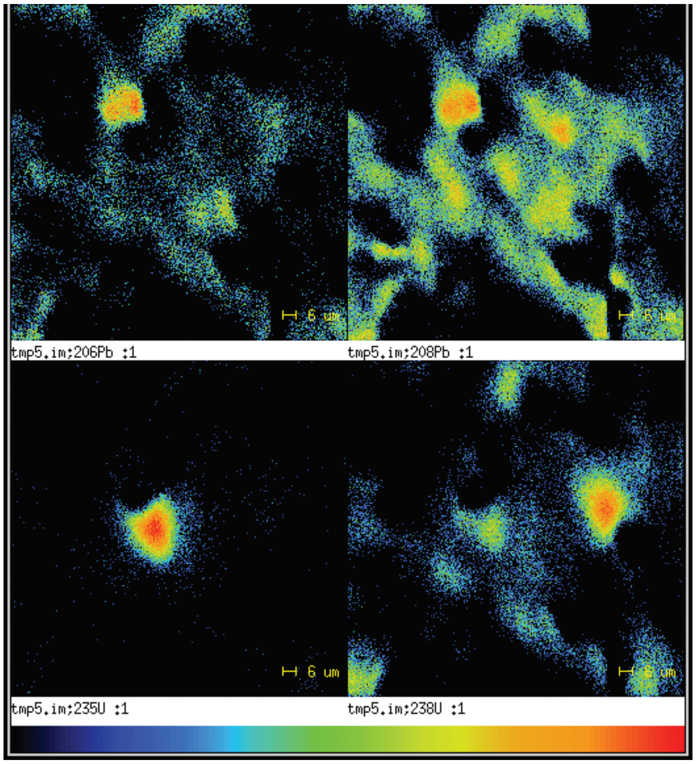

Fig. 4.7. SIMS images of a particle extracted from Mediterranean sediment containing highly enriched uranium. In the upper part the signal relevant to the 206 and 208 mass is shown, which is not present in uranium masses 235 and 238 shown at the bottom of the figure. The presence of lead in the hot particle is therefore ruled out. The colour scale indicates the intensity of the signal from black to read.

2004; Salbu *et al.*, 2005). The common strategy consisted in separating the particles from the soil samples and use X-ray for the determination of their chemical composition coupled, in some cases with scanning electron microscopy. μ-XRF as well as SEM-EDXRF can be employed to obtain information of the particle size distribution of the particles. Measurements performed independently by two different groups of investigation found that the most of the identified depleted uranium particles in the samples were in the range of some μm in diameter (less than 10 μm). Exceptional larger particles, up to 40 μm (Danesi *et al.* 2003) were also detected.

In order to detect the isotopic composition of the depleted uranium particles, SIMS has been the most appropriate technique as already extensively used for this scope for particles of different origin (Tamborini *et al.*1998, 2002; Tamborini and Betti 2000; Betti *et al.*, 1999; Erdmann *et al.*, 2000). Soil particle samples collected from Kosovo area a few years after the war showed the presence of fine particles with depleted uranium as major component which were easily identified by SIMS (Török *et al.*, 2004). The ultrafine uranium particles were often attached to larger soil particles and contained Ti and Al being typical components of the penetrator and its cladding. The particles localized by the automated SEM with gun shot residue program were then analyzed

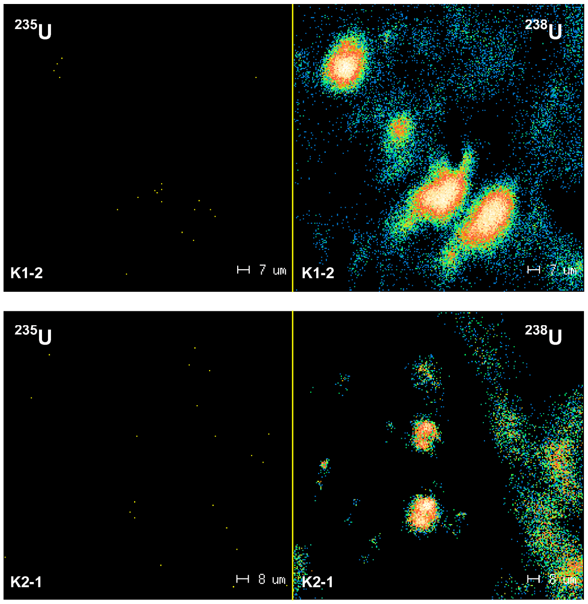

Fig. 4.8. Images of the 235 and 238 uranium isotopes in depleted uranium particles separated from soil samples stemming from Kosovo sites.

by SIMS as for uranium isotopic ratios. The results obtained clearly revealed the presence of DU and traces of ^{236}U were also detected. In Figure 4.8 the SIMS isotopic images for uranium isotopes ^{238}U and ^{235}U are reported. Clearly due to the depletion of uranium the mass 235 cannot be revealed. The results obtained from the measurements of the particles are reported in Table 4.1.

As for ^{234}U and ^{236}U, due to the low signal intensity the error is often larger. In general, the total uncertainty on the minor isotopes is decreasing (better counting statistics) when the enrichment increases. The uncertainty on the ^{236}U is significantly higher than that on the ^{234}U because the 236 intensity is obtained after correction for hydride contribution and the respective errors are propagated into the 236 uncertainty. With such a particle diameter ($\approx$ 1 μm), the precision that can be achieved is considered the detection limit of the method in these conditions. The signal on mass 239 (due only to the formation of ^{238}UH$^+$ molecules) is used to correct the signal on mass 236 for the contribution of ^{235}UH$^+$. As for ^{235}U in this case the uncertainty is not strongly depending from the intensity of the signal but from other parameters, e.g. the analysis time.

Török *et al.* (2004) investigated also the chemical composition of the DU particles by μ-XRF and EMPA as well as the uranium oxidation states by μ-XANES. The results showed that uranium is present in the particles mostly in the U(IV) form, the maximum ratio of U(VI) to the total U content was obtained as 24 % indicating that the particle contained mainly the less mobile form of U. Salbu *et al.* (2003) also analyzed DU particles from Kosovo using micro-XANES. Based on the results for 12 particles, the authors claimed that approximately 50 % of the DU particles were in the form of UO, while the remaining DU particles were U_3O_8, or a mixture of oxidized forms. Due to the fact that in both studies the number of particles analyzed was not statistically significant, we can conclude that the results are in agreement showing the potentiality of the technique in providing valuable information of the percentage of the presence of the element as distributed in different oxidation states.

Salbu *et al.* (2005) also studied the oxidation states of uranium in DU particles stemming from Kuwait. They found that, compared to well-defined standards, all investigated particles were oxidized. Furthermore, in this investigation, the authors demonstrated that the DU originated from reprocessed uranium. In fact, from the analysis of the particles by accelerator mass spectrometry, the presence of ^{236}U was revealed.

4.3.4 Uranium Particles from a Nuclear Reprocessing Plant

The British Nuclear Fuels plc (BNFL) establishment at Sellafield (UK) has been releasing authorized discharges of low level radioactive waste into the Irish Sea since 1952. The peak period for the releases occurred in the 1970s, since then the level of discharges has been reduced (Betti *et al.* 2004). The most important part of the discharged waste originates both from the cooling ponds in which the spent Magnox fuel elements are being stored prior to re-processing, and from the 'sea tanks' where low level liquid wastes are collected and neutralized before being discharged. Actinides, namely Np, Pu, Am and Cm detected in both cooling pond water and 'sea tank' water have been found to be mainly attached with particulate matter. Bulk profiles of a core sediment have been studied for Np, Pu, Am and major fission products (Perna *et al.*, 2005).

Tab. 4.1. Isotopic composition obtained by SIMS for particles of depleted uranium separated from a sample collected at 5-10 cm depth. (Reproduced with the permission of Elsevier from Török *et al.* 2004).

Particle	$^{234}U/^{238}U$		$^{235}U/^{238}U$		$^{236}U/^{238}U$		^{234}U		^{235}U		^{236}U		^{238}U	
N°	Ratio	1σ	Ratio	1σ	Ratio	1σ	wt %	1σ	wt %	1σ	wt %	1σ	wt %	1σ
1	**1.09E-05**	6.30E-06	**2.03E-03**	1.06E-04	**3.60E-05**	1.22E-05	**0.001**	0.001	**0.200**	0.010	**0.004**	0.001	**99.795**	0.011
2	**1.46E-05**	6.98E-06	**2.04E-03**	1.51E-04	**3.92E-05**	1.22E-05	**0.001**	0.001	**0.201**	0.015	**0.004**	0.001	**99.794**	0.015
3	**7.49E-06**	8.13E-06	**2.04E-03**	2.01E-04	**3.38E-05**	2.50E-05	**0.001**	0.001	**0.201**	0.020	**0.003**	0.002	**99.795**	0.020
4	**2.46E-05**	8.26E-06	**2.06E-03**	1.52E-04	**4.60E-05**	2.05E-05	**0.002**	0.001	**0.203**	0.015	**0.005**	0.002	**99.790**	0.015
5	**2.21E-05**	2.21E-05	**1.92E-03**	1.93E-04	**3.58E-05**	2.29E-05	**0.002**	0.002	**0.189**	0.019	**0.004**	0.002	**99.805**	0.019
6	**2.70E-05**	1.26E-05	**2.03E-03**	1.16E-04	**6.05E-05**	1.54E-05	**0.003**	0.001	**0.200**	0.011	**0.006**	0.002	**99.791**	0.012
7	**4.20E-05**	4.13E-05	**2.06E-03**	4.74E-04	**6.47E-05**	5.59E-05	**0.004**	0.004	**0.203**	0.047	**0.006**	0.006	**99.787**	0.048
8	**1.57E-05**	1.05E-05	**2.05E-03**	1.26E-04	**4.56E-05**	1.82E-05	**0.002**	0.001	**0.202**	0.012	**0.005**	0.002	**99.792**	0.013
9	**5.57E-05**	3.77E-05	**2.16E-03**	2.51E-04	**1.04E-04**	5.60E-05	**0.005**	0.004	**0.213**	0.025	**0.010**	0.006	**99.771**	0.026
10	**1.37E-05**	1.46E-05	**2.10E-03**	1.84E-04	**3.40E-05**	1.97E-05	**0.001**	0.001	**0.207**	0.018	**0.003**	0.002	**99.788**	0.018
11	**1.80E-05**	8.53E-06	**2.03E-03**	1.49E-04	**5.27E-05**	2.27E-05	**0.002**	0.001	**0.200**	0.015	**0.005**	0.002	**99.793**	0.015
12	**2.03E-05**	1.46E-05	**2.08E-03**	2.23E-04	**6.45E-05**	3.73E-05	**0.002**	0.001	**0.205**	0.022	**0.006**	0.004	**99.787**	0.023
Average	**2.27E-05**		**2.05E-03**		**5.14E-05**		**0.002**		**0.202**		**0.005**		**99.791**	

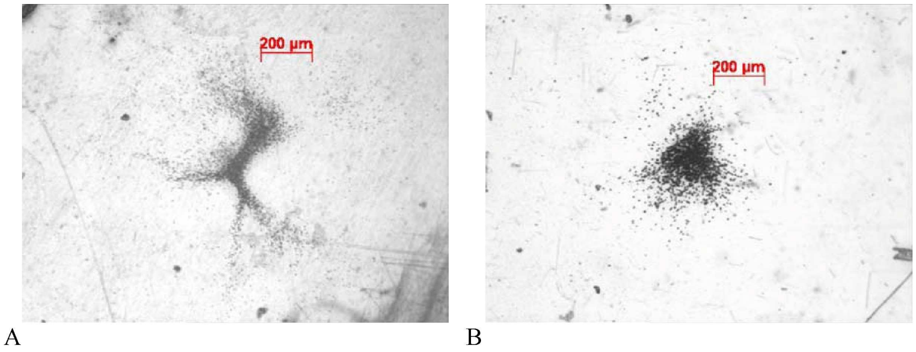

Fig. 4.9. Alpha track images of two radioactive particles separated from the sediment. Exposure time for particle A was 43 days, for particle B 8 days. (Reproduced with permission of the Royal Society of Chemistry from Jernström et 2004).

The highest level of activity was associated with hot particles, typically less than 20×50 μm in size, originating from spent nuclear fuel debris from the BNFL plant. These most radioactive particles usually contained uranium together with plutonium, americium and curium as major alpha emitters. Jernström *et al.* (2004) separated radioactive particles from an Irish Sea sediment core after having been localized using solid state nuclear track detection (SSNTD).

Figure 4.9 shows the alpha tracks images of two radioactive particles separated from the sediments. Then the particles were characterized with electron microscope and different X-ray microanalysis methods including micro X-ray fluorescence spectroscopy (μ-XRF) and micro X-ray absorption near edge structure spectroscopy (μ-XANES). After these investigations the particles resulted to be intact and available for further studies.

Due to the fact that the bulk analysis revealed the presence of Pu and Am, the isolated particles were investigated also as for these radioisotopes. Only in one particle it was possible to detect a weak signal of Pu by μ-XRF. Using the same technique, elemental maps were constructed in order to find out the position of the highest U intensity, and any existence of elemental correlation. In particular, only for two particles trace amounts of thorium in the same region as the high U intensity were detected. A comparison was made with the results obtained from a particle originating from the same sediment core but one layer below. The measuring of this particle revealed high intensity of zirconium located with thorium, uranium, yttrium (Y) and hafnium (Hf). During the scanning of the U-rich particles additional uranium signals with lower intensity were detected. A common factor for these other few particles is a slightly higher Th intensity compared to U intensity, the Th/U ratio being approximately from 1 to 4. This strongly differs from the Th/U intensity ratio as measured for other particles.

Oxidation states were also investigated by μ-Xanes. Comparing to the μ-XANES spectra of the U(IV), U_3O_8 and U(VI) standards, the shift in the inflection point energy in the spectra of all three analysed particles indicates an increase in the uranium oxidation state. Uranium is present in the particles mostly in the U(IV) form, the ratio of U(VI) to the total U content was between 34 ± 6 % and 40 ± 6 %. The uranium in the particles was found to be in two oxidation states at different percentages: 60-66 % as U(IV) and 34-40 % as U(VI).

4.3.5 U/Pu Particles from an Inadvertent Destruction of Nuclear Weapons

A lot of attention has been focused on the identification of Pu and U particles released as a consequence of an accident with nuclear weapons which occurred in the Thule area (NW-Greenland) in January 1968. Details of this accident and obtained results have been published elsewhere (USAF, 1970; Aarkrog, 1971, Aarkrog *et al.*, 1984; MacMahon *et al.*, 2000; Moring *et al.*, 2001.). Moring *et al.* (2001) identified particles containing U and Pu originating form this accident in sea sediment samples. The environmental radioactive particles, as those analysed in our laboratory, are generally embedded in a bulk matrix, therefore, it is necessary to isolate them and perform specific single grain analysis to provide unbiased results. The analytical approach has been to perform non-destructive measurements in order to reveal their chemical composition (Eriksson *et al.*, 2005). One of the advantages of using non-destructive methods is the direct analysis of the samples. Thus avoiding problems of cross-contamination, particularly important for U at ng levels, as contained in the particles here studied.

Characteristic L X-rays and gamma rays from the radioactive disintegrations were measured. This provides information on the specific radionuclide composition of the radioactive particles. Before analysing the particles by microscopic X-ray fluorescence (μ-XRF), they have been examined by scanning electron microscopy (SEM) combined with energy-dispersive X-ray (EDX) or wavelength-dispersive X-ray (WDX) spectrometry. This is of particular interest when the particles are supposed to contain a mixture of U and Pu, revealing the surface and to some extent subsurface composition. Utilising μ-XRF at a synchrotron radiation (SR) facility, information on the elemental composition of the particles has been obtained. In particular, by using a beam size of 2.5 μm the fine structure of the material was observed. The elemental distributions of U and Pu in a particle were also studied with the μ-XRF tomography technique. Microscopic X-ray absorption near-edge structure (μ-XANES) has been exploited to study the oxidation states of uranium and plutonium in U/Pu mixed particles.

In order to obtain single grain hot particles from bulk sediment samples, a sample splitting technique was used. The technique is based on the decay of the plutonium isotope ^{241}Pu ($T_{1/2} = 14.35$ y), which is present in the weapons material, to the gamma emitting daughter ^{241}Am ($T_{1/2} = 432.2$ y, gamma line: 59.54 keV, intensity: 35.9 %), measurable by gamma spectrometry. When ^{241}Am activity is identified, the sample is split into two equal halves and measured again. The part with the activity is again divided and measured. After about 20 sample splitting, starting with about 150 g of bulk material, only a few grains ($\sim$ μ g) remain. This technique is explained in detail elsewhere (Eriksson *et al.*, 2002). Only one single radioactive particle remains after a complete sample splitting of the bulk material. The longest working time spent on the sample splitting (the particle with the lowest activity, ~ 2.5 Bq) was around 4 h. The single radioactive particle was attached to an adhesive carbon tape. To identify and locate the particle position on the tape, the Beta Camera was used. Since the Beta Camera is also a light-sensitive device, and there is need for a position reference system on the tape, five holes were punched out in a special pattern. The holes were superimposed by light on the image obtained from the acquisition of the hot particle. For all the particles in the present study, the acquisition time on the Beta Camera was less than 30 minutes. This is a very short time compared to the more common autoradiographic film technique, which usually takes weeks before an image is produced.

All the particles were analysed by SEM with an EDX detector attached. The morphology, size and the surface elemental composition of the particles were studied. The secondary (SE) and back-scattered electron (BE) images also served as guiding maps when relocation of the particles was done at the SR-facilities ANKA and HASYLAB. The SEM used has a maximum acceleration voltage of 20 kV, which did not allow the efficient excitation of U and Pu L shells. In the EDX spectra the M X-ray peaks of U and Pu were not resolved due to the strong overlap between the M_α peaks of Pu and the M_β peaks of U. Absolute determination of the Pu/U element ratio could not be done, as standard mixed Pu/U particles would be required to calibrate the pulse height spectra in combination with deconvolution of the spectra or a Monte Carlo simulation of the source-sample-detector system (Ro *et al.*, 2003).

From the BE images with the EDX spectra it resulted that both U and Pu are present on the surface of all the particles. The particle sizes ranged from 15 to 42 μm and some of the particles are embedded or to some extent coated. These coatings were analysed with EDX and contained elements typical in sediment material, i.e. Si, Al, Mg and Fe. Several spots on the high atomic number areas of the particles where analysed with EDX. All the analyses showed that U and Pu co-exist on the whole high atomic number surface. From the U and Pu M X-ray peak intensities variations between different particles were observed, however the magnitude of the variations could not be determined with this system (Figure 4.10).

In addition, one particle (Thu 79-3) was measured with a SEM equipped with a WDX analyser. The difference between the two systems is that EDX uses a Si(Li) detector with a multichannel analyser (MCA), while WDX is based on the diffraction of the produced characteristic X-rays in a crystal lattice and the X-ray quanta are detected by a proportional counter. WDX measures only one energy (wavelength) at a time, leading to a better resolution but a lower efficiency. However, the low efficiency leading to low count-rate can be compensated to some extent by the use of a higher beam current from the filament. With the WDX system used it was possible to determine the Pu/U elemental ratios from the M X-ray lines without deconvolution of the spectra. This was done by correcting the area for the U M_α and Pu M_β peaks (non overlapping peaks) with the emission probabilities. This particle is constituted of many small fragments/inclusions. Carbon is the main constituent of the particle, indicating that it was formed during the accident, probably from burning of rubber or similar materials. When the weapons were disintegrated by conventional explosion, fragments from them were trapped in this piece of burning material. Five spots/inclusions of this particle were analysed with the respect on the Pu/U elemental ratio. The determined Pu/U elemental ratios by SEM-EDX were 0.09 to 0.43 in these five spots. The large variations in the ratio are probably due to the fact that the inclusions originated from different parts of the weapons rather than to an effect of their preferential leaching.

By performing μ-XRF, it was obtained that U and Pu are homogeneously distributed in the particles. The Pu/U intensity ratios vary between 0.22 and 0.36. This variation may reflect several phenomena. Among these we can consider a preferential leaching of one element respect to the other one; the origin of the particles from different parts of one of the involved nuclear weapons; or that the particles stem from a different source term. Detailed investigation on the Pu isotopic ratios by mass-spectrometry, that are on going at the present in our laboratory, complementary to those below described as micro-spatial elemental distribution and micro tomography, can help in concluding which of the above mentioned causes is the most probable.

The same particle analysed with the SEM-WDX system was analysed using a 2.5 μm μ-XRF beam at ANKA (Forschungszentrum, Karlsruhe). The particle, with the size of 350×250 μm^2, was scanned over an area of 130×100 μm^2 with step sizes of 1.25 μm in both z and y directions

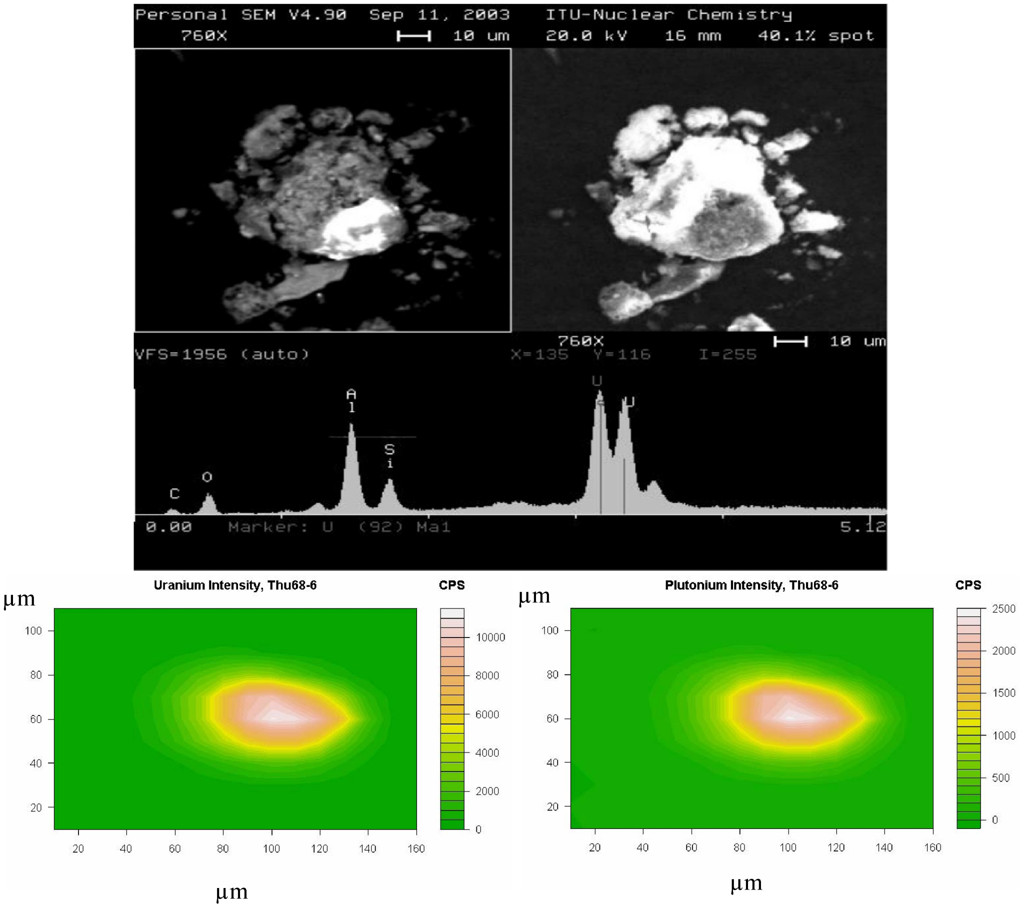

Fig. 4.10. SEM back scattered image (top) of one Thule hot particle with corresponding EDX-spectrum. Uranium and plutonium intensity maps as obtained by μ-XRF are shown in bottom of the figure. (Reproduced with the permission of Elsevier from Eriksson *et al.* 2005).

and 3 s per point as measuring time. It was observed that the U and Pu L_α intensity maps correspond fairly well, however, in the U/Pu intensity ratio there are variations. Some regions have a U/Pu intensity ratio as high as 20 (Pu/U 0.05). This means that the inclusions in the particle originate from different parts of the weapons or from different weapons, rather than due to an effect of leaching, as the inclusions have been more or less isolated from the aquatic environment in this large particle. μ-XRF measurements with 20 μm beam would have never revealed the fine structure of the particle due to the "low" spatial resolution. When analysing individual Pu/U particles in order to identify the source term and the leachability behaviour, the use of the larger (20 μm) and the smaller (2.5 μm) spot size is complementary. The large beam provides the average elemental ratio in the particles and the small beam the possible heterogeneity in the elemental distribution.

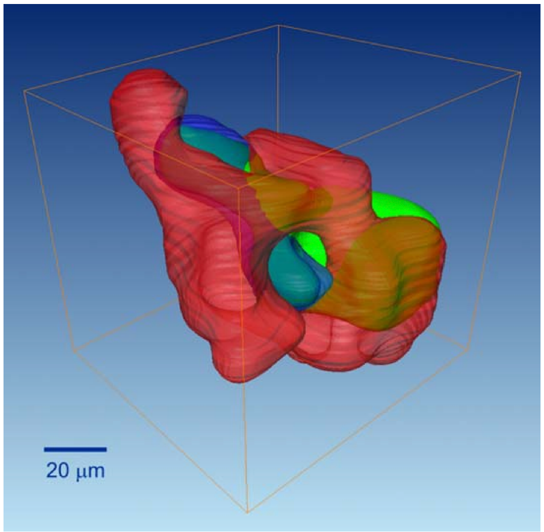

Fig. 4.11. Reconstructed distribution of elements in U/Pu rich particles recovered from see sediment, Thule Greenland. The plutonium (blue) and uranium (green) are coated with iron (red) rich sediment matrix. (Reproduced with the permission of Elsevier from Eriksson *et al.* 2005).

The elemental distribution in two particles was investigated: in a U/Pu-rich particle recovered from the sea sediment near Thule, NW Greenland, and in a Pu-rich particle embedded in a coral matrix, collected from the surface soil in the Mururoa Atoll. The particles were scanned in pencil-beam geometry. For each particle, 64 area projections, separated by 5.625 degrees, consisting of 64 (horizontal) by 10 (vertical) pixels were collected simultaneously in X-ray fluorescence and X-ray absorption modes. The horizontal beam spacing was 19 μm and 11 μm for the Mururoa and the Thule particles, respectively. The corresponding vertical beam spacing were 42 μm and 20 μm. The 3D distributions of Pu, U and the matrix elements (Sr for the Mururoa particle and Fe for the Thule particle) were reconstructed. The individual slices of the tomographic reconstruction were obtained using a filtered backprojection algorithm. A preliminary method of absorption effect correction was applied. In this method the data collected by the X-ray fluorescence detector, the XRF sinograms, were corrected for absorption effects using the X-ray absorption sinograms collected with the Silicon Drift Detector (SDD) placed behind the analysed sample. The reconstructed slices were processed by a 3D rendering software AMIRA to obtain 3D element distribution models. From the reconstructed data it can be noticed that the Thule particle, recovered from the sea sediment, has been partially coated with Fe-rich sediment matrix during its long residence (29 y) in the seabed. Uranium and plutonium elemental distribution is not even in the particles. The Mururoa particle, recovered from the surface of the coral atoll, was found to be attached to the coral matrix only from one side. It suggests that the merging of plutonium with the matrix material occurred during the nuclear test explosion, the source term of this particle. In Figure 4.11 the reconstruction of the U and Pu distribution in the particle stemming from Thule sea sediments, as obtained by tomography measurements at the synchrotron, is reproduced.

In order to study the reactivity of the particles in terms of mobility, leachability, weathering and transport/transfer of radionuclides into the environment and from the environment to the humans, the determination of their oxidation states is essential to predict fate and transport. XANES is an established technique for the determination of oxidation states and local chemical environment, even at relatively low concentrations. As already asserted, studies have systematically been performed for actinides as aqueous ions (Conradson *et al.*, 1998, Conradson et., 2004) and it has been recently exploited also for U particles (Salbu *et al.* 2001; Salbu *et al.*, 2003; Török *et al.* 2004; Jernström *et al.*, 2004). The particles separated from the Thule sediments were investigated by μ-XANES as for U and Pu oxidation states. This was for the first time that studies on Pu oxidation states in environmental particles has been carried out systematically.

In order to study uranium oxidation states in individual particles U-L_3 μ-XANES spectra were collected from the centre as well as from the edge region of each particle. The U XANES spectra collected at the centre of four U/Pu particles sampled at Thule (Thu68-3, Thu68-5, Thu68-6, 975374-5) was compared with the spectra of the standards. The zero of the energy scale was set to the inflection point of the U(IV) standard. All spectra were processed using the least-squares fitting method described above. No significant difference was encountered between the results obtained for spectra collected from the centre and from the edge of the same particles. The error of the fitting method is within 5 % (absolute). Uranium is present in the particles mostly in the U(IV) form, the maximum ratio of U(VI) to the total U content was obtained as 25 % indicating that the particles contained mainly the less mobile form U(IV).

Plutonium oxidation states were studied in the same way than those of uranium, i.e. through recording and fitting Pu-L_3 μ-XANES spectra from different regions of each individual particle. The Pu-L_3 XANES spectra collected at the centre of four U/Pu particles (Thu68-3, Thu68-5, Thu68-6, 975374-5) were compared to the standard spectra. The zero of the energy scale was set to the inflection point of the Pu(IV) standard. The plutonium oxidation state was also not significantly different in different regions of the same particle. Two kinds of particles could be distinguished. The particles Thu68-3 and Thu68-5 contain Pu mostly (more than 90 %) in the Pu(IV) form. In the particles Thu68-6 and 975374-5, however, the Pu(VI) form is dominant (67-75 %).

Lind *et al.* (2005) have recently examined particles stemming from Thule environment by μ-XANES. Their measurements showed that U and Pu are present in the particles as mixed oxides. U was found in the oxidation state IV whereas Pu apparently is a mixture of Pu(III) and Pu(IV).

From the results obtained it is clear that the reactivity of the particles in the environment as well as in human fluids will be different and therefore it would be worthwhile to study to which extent the preponderance of one or another oxidation state will influence Pu fate and transport. In order to obtain this information, leaching of the particles in environmental media and human body fluids needs to be carried out.

4.4 Thermal Ionisation Mass Spectrometry

TIMS belongs to the most sensitive methods for absolute isotope abundance measurements, and until the introduction of ICPMS, it was the most widely used technique for ultra-low analysis of long-lived radionuclides (especially actinides) in the environment. TIMS has proved to be a highly sophisticated analytical method providing the most precise isotope ratio determinations with precision down to a few ppm (White and Wood, 1988).

With TIMS positive ions are produced in the spectrometer's ion source by evaporation of a sample from a heated metal surface. Source filaments are usually chosen from metals with relatively high work functions, high melting points and the necessary purity and mechanical properties (e.g. platinum, rhenium, tantalum or tungsten). After heavy separation chemistry, samples are loaded as highly purified solutions onto the filament or by electrodeposition. By adding a known quantity of yield tracer to the sample, isotope dilution analysis is used to measure concentrations below the fg scale (Dixon *et al.*, 1997; Inkret *et al.*, 1998).

Interferences from isobars and mass discrimination between isotopes of a given element need to be carefully evaluated and excluded by chemical purification and control of ionization conditions. Nevertheless the problem of interferences with TIMS is not as great as in ICPMS. Isotope fractionation is more difficult to control, but usually produces smaller systematic errors. However, using total sample evaporation method this problem has been solved as the sample is completely evaporated from the filament. The final results are given in averaged isotopic mean values when measurement has been completed and no measurable amount of sample is left on the filament. Thus, the limiting factor of TIMS in environmental analysis is very often the purity of the sample, as improvements and innovations in mass spectrometer hardware have augmented analytical precision. The new state of the art TIMS machines with multi-collector arrays have considerably improved operation in multi-dynamic mode (e.g. the TRITON from Finnigan Co.), producing a sensitivity of around 10^5 atoms for ^{239}Pu, which is comparable to AMS.

When using measurement techniques with the extreme sensitivity of TIMS at levels below 10^{-15} g per sample, it is very important to minimize the effects of airborne dust particles, reagents, glassware, etc. which can all contribute significantly to the sample blank, and as a result, to analytical detection limits which are actually defined by the contamination of the blank sample. For this reason, successful TIMS requires more careful sampling, very clean chemical processing and a higher level of instrumental expertise than any other method.

TIMS has not been widely used in environmental studies because of the high cost of the machine and the expertise required for its operation (Buesseler, 1993). The main advantage is its high sensitivity for actinides (more than an order of magnitude higher than for SAS), as well as the possibility of measuring ^{240}Pu/^{239}Pu ratios in low-level samples and identifying the origin of plutonium in environmental samples (Bertine *et al.*, 1986; Buesseler and Halverson, 1987; Buesseler and Scholkovitz, 1987). A wide range of ^{240}Pu/^{239}Pu atom ratios have been found in the marine environment: from 0.05 in Mururoa lagoon sediment, through global fallout ratio (0.186) to discharges of plutonium from reprocessing plants (e.g. 0.24 for Irish Sea water or 0.20 for Irish Sea sediment, (Kershaw *et al.*, 1999) to 0.30 for Bikini lagoon sediment (Muramatsu *et al.*, 2001). It has been found (Buesseler, 1997) that plutonium delivered as stratospheric fallout appears to be relatively soluble and has a longer residence time in seawater than plutonium from close-in fallout which is more rapidly removed from the water column to deep ocean sediments. High sensitive TIMS has recently been used for size-fractionated plutonium isotope studies in the coastal environment (Dai *et al.*, 2001).

Several studies on natural U and Th in the environment have also used TIMS. It has proved to be especially efficient for the precise determination of e.g. ^{234}U/^{238}U and ^{236}U/^{238}U ratios on small samples giving highly sensitive and very accurate measurements (Chen *et al.*, 1986). This has lately become of great interest in connection with the use of depleted uranium in military weapons. For Th isotopes (^{228}Th, ^{230}Th, ^{232}Th), TIMS has been even more effective because of their lower concentrations in seawater (in comparison with U isotopes (with the exception of

^{236}U)) when performing analysis with RMT, requiring large volume samples (1000 L). TIMS permits reduction by a factor of 1000 of the size of the sample (Chen *et al.*, 1986; Dixon *et al.*, 1997). Other long-lived actinides such as ^{231}Pa, ^{237}Np, ^{243}Am, ^{244}Cm and ^{246}Cm as well as some long-lived fission products (e.g. ^{99}Tc, ^{135}Cs) have been analysed by TIMS, as well (Dixon *et al.*, 1997; Cooper *et al.*, 2000;), yet more work is needed for the full exploitation of these tracers in marine studies. Moreover, TIMS can be effectively used in speciation and size-fractionation studies (Dai *et al.*, 2001) and also for certification of marine reference materials (Inn *et al.*, 2001; Lewis *et al.*, 2001).

4.5 Resonance Ionisation Mass Spectrometry

Resonance Ionisation Mass Spectrometry (RIMS), which is based on highly efficient and selective ionization of elements by tuneable lasers (and subsequent analysis of ions by a mass spectrometer) has been found to be a powerful technique whose main advantages are almost complete isotopic suppression, high ionization efficiency, low background ion detection and high isotopic selectivity, resulting in an overall sensitivity of detection limits down to the fg scale (Wendt *et al.*, 2000). As only atoms of the desired element (or isotope) are excited and ionized by laser (Wendt *et al.*, 2000), undesired ions in the mass spectrometer can be suppressed to a significant extent. Therefore, of the various applications of RIMS, ultra low-level determination of long-lived radionuclides in the environment has been the most widely acknowledged. As ICPMS is very often limited by molecular effects which very often create isobaric interferences (as occasionally occurs with TIMS as well), RIMS together with AMS is currently the most selective technique with minimum interferences for the analysis of long-lived radionuclides in the environment at very low levels. For a recent review on RIMS see the paper of Erdemann *et al.* (2008).

However, compared to the more widely used ICPMS or TIMS, RIMS is still a too complicated technique requiring a lot of skill and a strong technical support. It would seem that RIMS will remain an alternative technique to AMS where AMS cannot be used effectively because of insufficient or no production of negative ions (e.g. in the case of ^{81}Kr), strong isobaric interferences or other sources of background.

RIMS has been successfully applied in the analysis of several long-lived radionuclides in the environment such as, ^{81}Kr, ^{90}Sr, ^{99}Tc (Wendt *et al.*, 2000) with a detection limit for ^{239}Pu down to 10^6 atoms. Especially, ultratrace isotope detection of noble gases (^{39}Ar, ^{81}Kr) are still a challenging task which has recently been addressed also by AMS, as well as by optical spectroscopy using a magneto-optical trap and collinear laser photon burst spectroscopy (Kutschera *et al.*, 2000; Bailey *et al.* 2000).

Although the application of RIMS in environmental radionuclide studies has been very limited, its great potential could be in speciation studies, especially when it is coupled to chromatographic systems. As an alternate mass spectrometry technique it may also play an important role in certification of reference materials.

5 Accelerator Mass Spectrometry

The development of accelerator mass spectrometry (AMS) and recent new AMS designs have transformed the methods to the stage when it has become valuable technique for climate change studies. In addition to the large emphasis on ^{14}C (radiocarbon), other radionuclides such as ^{10}Be, ^{26}Al, ^{36}Cl, ^{129}I and uranium and plutonium isotopes can be measured using AMS.

AMS revolutionized the way that radionuclides could be analysed at very low levels. It is easy to understand the usefulness of AMS by looking at the radioactive decay equation

$$dN/dt = -\lambda N, \tag{5.1}$$

where the number of ^{14}C atoms N, is related directly to the rate of radioactive decay (dN/dt) through the decay constant λ. The decay rate is very slow, for 1 g of carbon the decay rate is 13.59 decays per minute. In AMS, we typically measure a sample of 0.5 mg C, and we can count over 120,000 atoms from a modern sample. If we take a counting rate of 120,000 atoms in 1080 seconds, or 111 s^{-1} — from 0.5 mg of carbon, then this translates to $\sim 2.22 \times 10^5\ \mathrm{s}^{-1}\mathrm{g}^{-1}$, a difference compared to decay counting of over a million.

In this chapter, we first discuss the capabilities of AMS and we will then highlight some climatic signals, which can be dated using the small-sample capabilities of AMS. We will also discuss the use of AMS for ^{10}Be and ^{129}I and how they can be applied to climatic studies.

5.1 AMS Methodology

Since the beginning of radiocarbon dating (Arnold and Libby, 1949; Libby, 1955), the field of radionuclide studies has expanded widely both as a dating tool and as a tracer. Some early studies also highlighted the use of radiometrics techniques for analysis of cosmogenic radionuclides, e.g. ^{10}Be and ^{36}Cl (Lal, 1957), but with extremely large sample requirements. A fundamental change occurred when much smaller samples became feasible with the development of AMS in the late 1970s (Tuniz *et al.*, 1998). Since then, AMS machines have evolved from the large accelerators ($\sim$ 10 MV) and cyclotrons in early 1980 to much smaller accelerators (as low as 250 kV) recently designed specifically for AMS. Commonly measured radionuclides by AMS in the above research fields are ^{3}H, ^{14}C, ^{10}Be, ^{26}Al, ^{36}Cl, ^{41}Ca, ^{129}I and uranium and plutonium isotopes.

It is important to understand that radionuclide measurement using AMS differs from earlier decay-counting methods in that the amount of the radionuclide in the sample is measured directly, rather than determining individual radioactive decay events (e.g. Jull and Burr, 2006). For nuclides like ^{14}C, this greatly enhances sensitivity by 3 to 4 orders of magnitude. For longer-lived radionuclides, such as ^{26}Al, ^{10}Be, ^{36}Cl and ^{129}I, the analytical advantages of AMS are even greater. The sensitivity is achieved by ionizing sample atoms efficiently, accelerating them to high energies and counting individual isotopes using particle detection techniques developed for nuclear physics. Longer-lived radionuclides, which were very difficult to measure using decay counting techniques, such as ^{10}Be, are now routinely measured with AMS (Tuniz *et al.*, 1998; Fifield, 1999; Kutschera 2005; Jull and Burr, 2006).

In the case of ^{14}C, the AMS technique is 1,000 to 10,000 times more sensitive than decay counting techniques. We can achieve an external precision of about ± 0.35 % in ^{14}C content, or ±30 years in uncalibrated radiocarbon age is possible on a single 0.5-milligram-sized sample

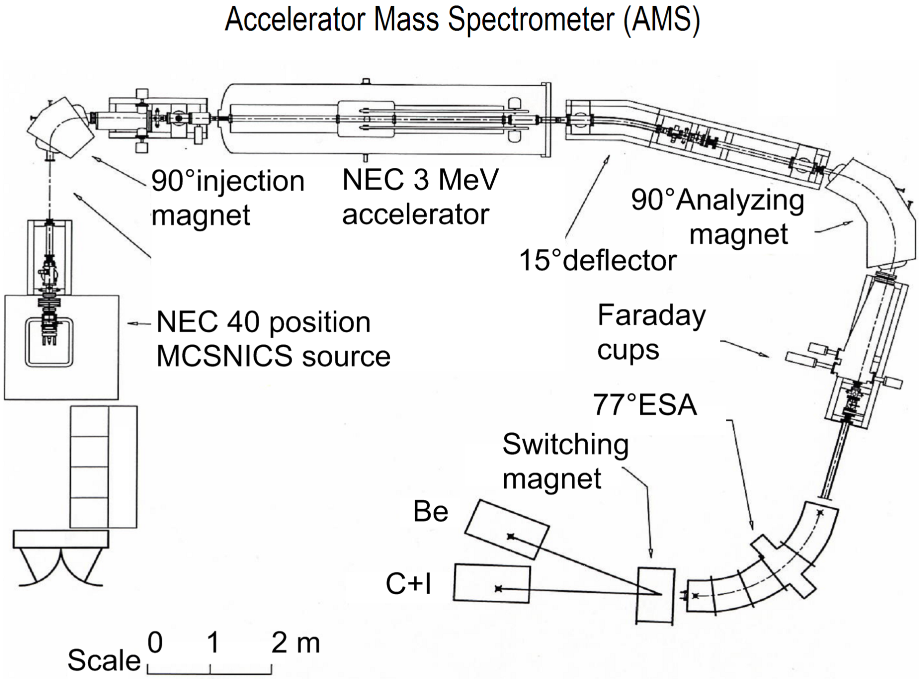

Fig. 5.1. A diagram of 3 MV Pelletron accelerator mass spectrometer

target in 20 minutes of measurement time. Samples as small as 100 micrograms or less have been successfully dated to about ±80 years BP and even smaller samples ($\sim$ 10-20 μg) have been measured for special experiments (e.g. Jull *et al.*, 1998). With longer counting times or when multiple targets are measured, we can reduce the single target error to about 0.2 %, or better than ±20 years in radiocarbon age (McNichol *et al.*, 2001; Donahue *et al.*, 1990a; 1990b). This increased sensitivity on very small samples allows us to date samples which would not previously have been possible.

In the case of longer-lived radionuclides such as ^{26}Al, ^{10}Be, ^{36}Cl, ^{41}Ca, ^{129}I and uranium and plutonium isotopes, which were very difficult or impossible to measure using counting techniques, AMS has made measurements of small amount of these radionuclides routine (Tuniz *et al.*, 1998; Fifield, 1999; Jull and Burr, 2006; Fifield, 2008).

A diagram of a typical AMS instrument, the 3 MV AMS machine operating at the University of Arizona, is shown in Figure 5.1. For example in AMS radiocarbon measurements, the sample of interest is usually after cleaning and its combustion to carbon dioxide converted into graphite, although the successful use of gas ion sources is now increasing. The graphite powder is pressed into a sample target holder, which is then loaded into the AMS machine ion source, shown on the left-hand side of Figure 5.1. The graphite is bombarded with Cs^{+} ions under vacuum, and the sputtered ions include many C^{-} ions. The C^{-} ions from the ion source are extracted by placing the ion source at a negative potential of about -50 kV. The accelerated C^{-} ions are then deflected in a 90° magnet, which allows us the first separation of ions of different mass. Because ^{14}C has a modern natural abundance of 10^{-12}, a further separation is still needed. Hence, C^- ions are accelerated to 2.5 MV in the accelerator (at the center of Figure 5.1) and these ions then pass through a gas canal (often called the “stripper canal”), where they lose electrons and become positively charged. The C^{3+} ions are then accelerated out of the machine and pass through electrostatic filters (to select ions of one energy (E) /charge (q) ratio) and magnetic elements (to select ions of the same ME/q^2). The separated ions of $^{14}C^{3+}$ can be completely distinguished from any other ions in the detector, in part because $^{14}N^-$ ions are unstable.

We shall focus in this paper on AMS measurements of radiocarbon, ^{10}Be and ^{129}I, together with their applications in environmental and climate change studies. AMS analysis of heavier isotopes, including transuranics can be found in the recent review of Fifield (2008).

5.2 New Machines and Ideas

A recent trend in the AMS field has been the development of increasingly smaller AMS instruments (Hughey *et al.*, 1997; Suter *et al.*, 1997, 2000). Currently, a “small” AMS is one which has a maximum terminal voltage of less than 1MV. Recent developments have even pushed the lower limit to about 250kV. These desk-top machines require less space and resources than larger AMS instruments, and are adequate for standard radiocarbon measurements. Starting in the mid-1990’s, there was a developing trend to make small AMS machines. The first design for a $<$ 1MV AMS was that of Hughey *et al.* (1997), who developed the instrument for biomedical work. About the same time, scientists at the ETH in Zurich, (Suter *et al.*, 1997) discussed the possibilities of a 0.5 to 1MV AMS machine which would operate in the 1+ or 2+ ion charge state (as opposed to 3+, which the reader will recall, is used in the larger machine example given above). Suter *et al.* (2000) later reported on the design of a prototype 0.5MV machine which would use the 1+ ion charge state. In this case, the design resulted in a compact machine of about 4-5 meters on each side. Although the machine could operate in other than the 1+ charge state, due to transmission considerations most of the discussion on these small machines has involved the 1+ charge state.

The principal disadvantage of small AMS machines is that their relatively low terminal voltages prohibit the use of stripping to high charge states ($\gtrsim$ 2+), where filtering techniques used in nuclear physics are most efficient. A number of 0.5MV machines (Figure 5.2) built by National Electrostatics Corporation (NEC) are now in use.

5.2.1 Small AMS Machines - the Single Stage AMS

A more recent NEC design, called the Single-Stage AMS (SSAMS) (Skog, 2007) eliminated the need for a costly pressure tank, so that the SSAMS is now a reality (Figure 5.3) and this design is now in use at several laboratories and is proposed for many more.

The convenience of this design for radiocarbon laboratories is the absence of the pressure tank, a ubiquitous feature of accelerators. This device generates the 300 kV by floating the high-energy part of the machine at 250 kV with a commercial power supply, and having the ion source at -50 kV. A section of accelerator tube in air provides the acceleration. The stripper is then at ground potential and the high-energy mass spectrometry is performed following the stripper without any further acceleration.

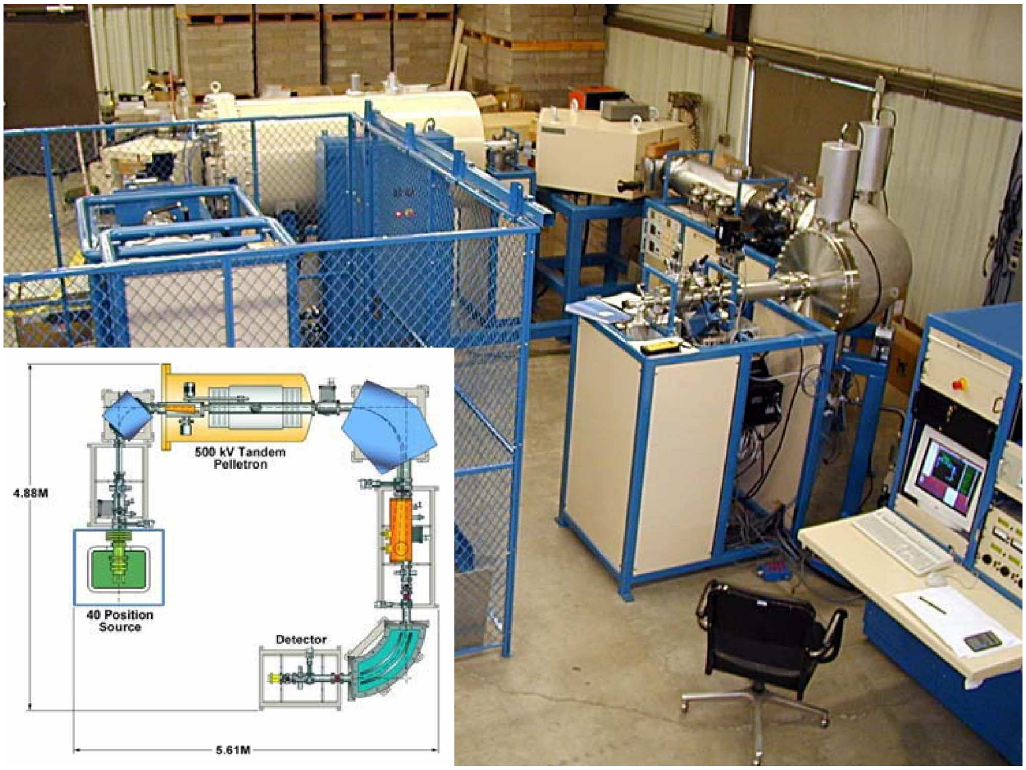

Fig. 5.2. The 500 kV AMS machine developed by National Electrostatics Corporation. (used with permission from NEC).

This interesting design apparently has similar backgrounds to the 0.5MV machines and is a new competitor to larger AMS machines for ^{14}C dating. There are some potential drawbacks to the in-air design, since some labs have reported corona discharges occurring under certain conditions (e.g. Skog, 2007).

5.2.2 Even Smaller AMS Machines

An alternative small machine, which also eliminates the pressure vessel and uses a 200 kV power supply was constructed in ETH Zürich (Synal et al, 2006). In general, as the operating terminal voltage used for AMS decreases, the technical engineering difficulties increase. Below 200 kV, stripping efficiencies become lower and it is not expected that AMS machines will drop in voltage below this limit. Synal *et al.* (2006) also discussed the development of a 200 kV machine which eliminated both the accelerator tank and also the accelerator tubes.

The device designed by Synal and co-workers consists of two gap lenses and a stripper tube. The potential is generated by a commercial power supply. The device, of course, must be placed in the mass spectrometer (which makes it much larger). They reported that a background of

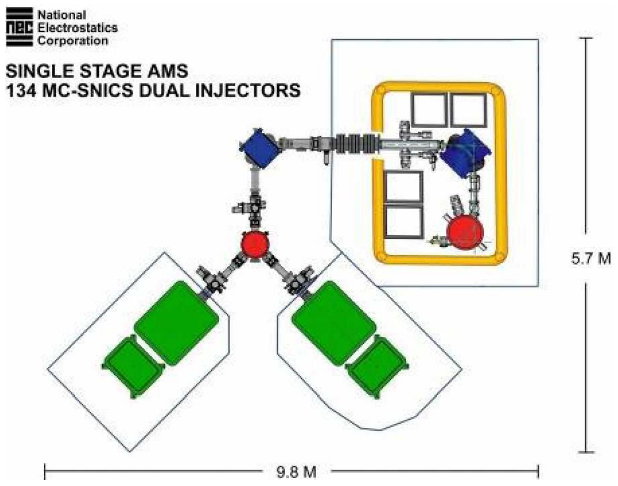

Fig. 5.3. Diagram of the 250 kV Single-Stage Accelerator Mass Spectrometer.

$< 10^{-14}$ could be obtained, and this machine is now being produced for other laboratories.

These small AMS machines have considerable potential for applications to ^{10}Be as well (Grajcar *et al.*, 2004), ^{129}I (Synal *et al.*, 2006) and Pu (Fifield *et al.*, 2004).

However, there are a number of practical limitations to these very small machines. The control of the stripper-gas pressure is delicate and essential. In the 1+ charge state, molecular ions can exist. The assumption used for higher energy AMS operating conditions that the molecular ions are destroyed, cannot be taken for granted at very low energies. Therefore high stripper gas pressure is needed to remove molecular interferences. Southon *et al.* (2004) have also reported on the technical difficulties of these operating conditions.

5.3 Radiocarbon Studies Using AMS

5.3.1 Preparation of Samples and Stable-Isotope Analysis

A very important factor in AMS measurements is proper sample preparation. It is important that the sample is clean and all contaminants have been removed. In all cases, after cleaning and combustion, samples are converted to graphite using an Fe catalyst and Zn as the reducing agent for the reaction $2CO \rightarrow CO_2 + C$. Finally, the graphite powder is pressed into a target holder of Arizona design, which is now widely used in all NEC ion sources. The measurement of ^{14}C follows the procedures and calculations described in detail by Donahue *et al.* (1990a, 1990b).

Some basic procedures for AMS radiocarbon samples carried out at Arizona laboratory were summarized by Jull *et al.* (2004) and Hatté and Jull (2007):

(i) Acid-base-Acid method for charcoal, wood, cellulose, plant material, animal tissue: After physical inspection, samples are cleaned with 1N HCl acid, 0.1% NaOH and 1N HCl (acid-base-acid (ABA) pretreatment), washed with distilled water, dried, and combusted at

900°C with CuO. Hatté *et al.* (2001) discussed some modifications and potential problems with the acid-base-acid method.

(ii) Carbonates: In general, samples are etched with 100% H_3PO_4 to remove 50-85 % of the carbonate, dried and hydrolysed with H_3PO_4.

(iii) Selective combustion for sediments. After cleaning in 1N HCl and drying, the sample is combusted at 400 ^{o}C in $\sim$0.3 atm. oxygen gas (McGeehin *et al.* 2001; 2004).

(iv) Oxidative acid cleaning for old charcoal. Pigati *et al.* (2006) have constructed a new line to clean charcoal samples using the oxidative acid method of Bird *et al.* (1999). This is of particular interest for charcoal samples $>$ 20 ky. We have also applied this method to sediments from archaeological settings with the possibility of extending the limit of dating to 60 ky.

(v) Textiles, parchment, canvas, art works and artifacts: The samples are given the ABA pretreatment and after washing and drying, they are Soxhlet extracted with hexane, then ethanol and finally methanol. After washing in distilled water, and drying, they are combusted at 900°C with CuO. Bruhn *et al.* (2001) proposed a more complex, 6-stage cleaning procedure for art works.

Of course, for some specialized samples, other methods need to be developed for these applications. For example, recently, Hatte *et al.* (2008) discussed a complex procedure for extraction of organic material in diatoms from sediments.

Specialized Sediment Sample Pre-Treatment. For sediment dating, methods which combine physical and chemical pretreatments, followed by stepped-combustion at different temperatures (McGeehin *et al.*, 2001, 2004) are useful. Inherited clay- or silt-bound carbon can be an important contaminant for conventional bulk sediment analysis. In some sediments, the humin fraction (material resistant to the acid and base pretreatment) combusting at 400°C ("low temperature fraction") appears to be to most promising for dating sediment. In some sediments, the humin fraction could contain pollen, macrofossils, wood or charcoal.

We can apply this method to a wide range of sedimentary environments. For low organic concentration sediments from the last glacial maximum age, the low temperature fraction can be 2-4 ky younger than the bulk fraction. We can refine the stepped combustion method by improving our understanding of temperature oxidation thresholds and by characterizing the organic materials in each temperature fraction.

Another sediment dating technique of interest was designed to remove contaminants left after a conventional acid-base-acid pretreatment. Preliminary results using a dichromate-wet oxidation (1M dichromate plus 1M sulfuric acid) method (ABOX), initially developed as a way to purify old charcoals (Bird *et al.* 1999) show significant reductions in the amount of total organic carbon in sediments. The remaining "oxidation-resistant" components are likely to be composed of charcoal or soot, as opposed to other forms of organic material in soils (Bird *et al.*, 1999). However, a recent paper by Rebollo *et al.* (2008) raises some questions about the removal of too much of the charcoal, since very severe pretreatments probably also remove much of the sample material of interest. It might be that in some cases, removal of the more soluble material is not the best method of achieving the best possible age measurement.

Compound-Specific Studies and Bone Chemistry. There are also other new techniques and strategies for extracting carbon from highly contaminated materials that are difficult or impossible to obtain accurate radiocarbon dates using standard methods, e.g. a separation of specific compounds from food remains on pottery, dating of separated fatty acids from marine sediments. Other alternatives include releasing carbon from bone-specific proteins using Ninhydrin (Nelson, 1991; Tisnérat-Laborde *et al.*, 2003; Hodgins and Jull, 2004). This approach of selective collagen dissolution using ninhydrin is being applied to bones found in tar pits (see Jull *et al.*, 2002, Hodgins and Jull, 2004). These environments are highly preservative, and thus rich repositories of animal and plant remains. However the tar hydrocarbons that thoroughly contaminate the samples present large challenges for dating. In another new approach, Hatte and Jull (2004) have also developed a method for cleaning diatom samples from sediments. This method uses a series of oxidative-acid cleanings and may also pave the way for the use of diatom dating in future studies. It is to be expected that such compound or compound-class specific methods will become more important in future research.

5.3.2 Measurement of Radiocarbon

Calculation and Normalization to Standards. The measurement of ^{14}C follows the procedures and calculations described in detail by Donahue *et al.* (1990a, 1990b). Further discussion on the question of interlaboratory differences in calculations was highlighted by McNichol *et al.* (2001). The results from radiocarbon measurements are expressed in the form of faction of modern carbon

$$F = A_{\mathrm{SN}}/A_{\mathrm{1950AD}} \tag{5.2}$$

where A_{SN} is the activity of ^{14}C in the sample compared to the value for “modern carbon”, arbitrarily defined as the value of 1950AD wood. All radiocarbon measurements are normalized to a common ^{13}C/^{12}C ratio quoted as δ^{13}C of -25 ‰, to eliminate any effects of isotopic fractionation which could originate either in the sample and/or during measurement.

Because of depression of the ^{14}C signal due to fossil-fuel burning, the value of 1950AD material is taken to be

$$A_{\mathrm{1950AD}} = 0.95 A_{HOxI}, \tag{5.3}$$

where $HOxI$ is the original Oxalic acid-I standard. Since that time, a second primary Oxalic acid standard known as $HOxII$ was developed by the US National Institute of Standards and Technology (NIST) as is designated as standard reference material SRM-4990C by NIST. This material can be related to $HOxI$ as

$$A_{\mathrm{1950AD}} = 0.95 A_{HOxI} = 0.7459 A_{HOxII} \tag{5.4}$$

It is important to note that the value of A_{HOxI} was normalized to a δ13C value of -19 ‰ instead of the $0.7459A_{HOxII}$which was normalized to -25 ‰.

Donahue *et al.* (1990a, 1990b) discussed the derivation of the calculation of F from the raw AMS results, depending on the isotopic ratio actually measured (^{14}C/^{13}C or ^{14}C/^{12}C). The calculation procedures were also discussed by McNichol *et al.* (2001). The reader is referred to these papers for details of the calculation and in particular, the importance of the isotopic corrections.

Uncertainties. Uncertainties are calculated from the larger of the Poisson uncertainty (determined from $\sqrt{N}/N$) and the standard uncertainty of the individual measurements. Various laboratories use different methods to estimate the total uncertainty, but the best practice is to take the larger of these two uncertainties as the minimum uncertainty. Donahue *et al.* (1990a) discussed the practices used at the Arizona laboratory, where an additional uncertainty known as the "machine random error" is added to the Poisson uncertainty before comparing this uncertainty to the estimate derived from the standard deviation of the individual measurements.

Blank Corrections. During the processing of samples in the chemistry laboratory, it is impossible to avoid some small amount of contamination introduced either during the chemistry or the sample conversion into graphite target. The "blank" in the machine itself is negligible. We can define a blank component, f, as

$$f = F_B / F_{\mathrm{std}} \tag{5.5}$$

where F_B is the fraction of modern carbon in the blank material itself, this is often assumed to be recent or modern carbon. However, other studies suggest one component of the blank may be an "average" contamination from the last samples run on the line. Donahue *et al.* (1990a, 1990b) showed that the fraction of modern F for the sample can be expressed as

$$F = F_m \left[1 - f \left\{1/F_m - 1\right\}\right], \tag{5.6}$$

where F_m is the value of the fraction modern measured for the sample and F is the final corrected value.

5.3.3 Improvements in the Radiocarbon Calibration

A basic understanding of past climatic changes must include a good chronology in order to determine the time relationship between events. To correlate distinct climatic features, we must be able to correlate independently-dated events. Hence, the improvement in the radiocarbon calibration curve has allowed to cross-correlate fluctuations in the ^{14}C curve with climatic fluctuations observed in such isotopic archives as ice-core records (Reimer *et al.* 2004). This capability has improved attempts to cross-correlate different climatic events observed in one record with other proxy records. This extension of the calibration curve used tree rings to about 11,500 calibrated years. Beyond this time record, dated corals and varved marine sediments have been used to extend the calibration curve (Reimer *et al.* 2004). Other newer records can take us back to the limits of radiocarbon dating, using corals (e.g. Fairbanks *et al.*, 2005), lake sediments and speleothem records (Hughen *et al.*, 2004).

Libby (1955) was the first to note that radiocarbon ages sometimes diverged from the "true" calendar age with his famous "Curve of Knowns". Since about 1980, a vast amount of time and energy has been devoted by scientists in the radiocarbon field to calibration of the radiocarbon time-scale. This eliminated a growing discord of different methodologies for calibration of radiocarbon dates (Stuiver and Kra, 1993; Stuiver and van der Plicht, 1998; Reimer, 2004).

The radiocarbon "calibration curve" was originally established by studying the changes in ^{14}C content of known-age tree rings. The first trees studied were Bristlecone Pines from the White Mountains of California, but this was later expanded to European oaks. Tree ring ^{14}C measurements from living and dead wood from these long-lived trees were cross-correlated to establish a ^{14}C chronology longer than the life of a single tree. Dendrochronology is the science of correlating and cross-referencing variations in the widths of tree-rings has been used to produce even longer chronologies using German and Irish Oak tree records, incorporating sub-fossil wood recovered from buried logs in river sediments and peat bogs. Currently, the continuous tree ring sequence extends back 11,500 years.

We know that the production rate of radiocarbon in the atmosphere changes with time and there are also changes in the amount of CO_2 exchange with the oceans. Both these effects lead to changes in the "apparent" age, which we term the radiocarbon age of the sample. The radiocarbon age is defined simply from the amount of ^{14}C relative to "modern carbon", defined as 1950AD wood, where the industrial effect of reduced ^{14}C has been removed, effectively this is 1850AD wood age-corrected back to 1950AD.

Using these assumptions, the radiocarbon age is easily computed as a modification of the radioactive decay equation

$$Age = -8033 \ln(^{14}\mathrm{C}_{\mathrm{sample}}/^{14}\mathrm{C}_{\mathrm{modern}}). \tag{5.7}$$

There have been continuing improvements in the length of the calibrated radiocarbon timescale. The improvement in the radiocarbon calibration curve over the last 26,000 y (Reimer *et al.*, 2005) and perhaps beyond to 50,000 y (Fairbanks, *et al.* 2005), has allowed us to cross-correlate fluctuations in the ^{14}C curve directly with those in the ice-core record (Reimer et al, 2005). This capability has improved attempts to cross-correlate different climatic events observed in one record with other proxy records. This extension of the calibration curve used tree rings to about 11,500 calibrated years and beyond that corals and varved marine sediments were used. There are also newer but as yet less well-established records which should take us back to the limits of radiocarbon dating ($\sim 50,000$ years), using lake sediments and speleothem records (Hughen *et al.*, 2004).

An example of a section of the calibration curve is given in Figure 5.4. The fluctuations in this curve demonstrate changes in the ^{14}C production rate and/or changes in the terrestrial carbon cycle have occurred. Intriguingly, excursions of the ^{14}C signal to apparent younger ages (i.e. higher ^{14}C production) are often associated with cold climatic events, this could be due to reduced solar activity or lowered carbon content of the atmosphere. This suggests a possibility of linkages to climate driven by carbon-cycle changes, such as might be produced by ocean circulation changes. Excursions to higher ^{14}C age are likely due to reductions in production rate or increases in the ventilation of ^{14}C-depleted carbon from the deep ocean. Conversely, excursions to lower ^{14}C age are likely due to reductions in production rate or attenuated ocean ventilation rates. Periods of constant ^{14}C over an extended period of time can also be explained by reductions in production rate.

These differences can be understood as the number of ^{14}C atoms in a given column of atmosphere, which can be approximated for times short compared to the half-life as

$$N_{14} = P_{14}t, \tag{5.8}$$

where P_{14} is a complex function of production rate over the period the ^{14}C remains in the atmosphere (1-2 y) and t is the (short) residence time of ^{14}C in the atmosphere. This approximation is valid since the residence time is very short compared to the mean life of radiocarbon of 8,267 y.

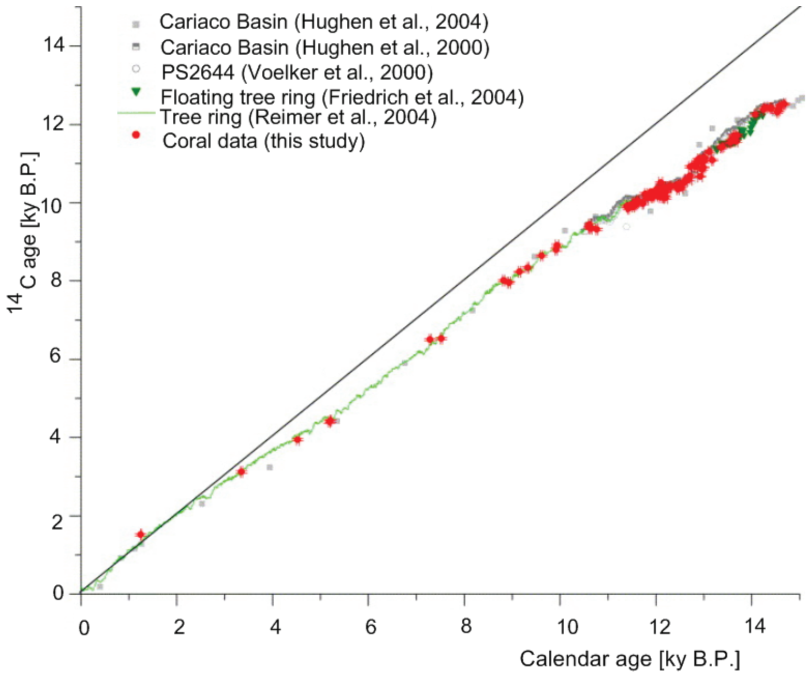

Fig. 5.4. New comparison curve of radiocarbon vs. U-Th ages from Bahamas and other corals, from Fairbanks *et al.* (2005), showing the good agreement between corals and tree-ring dates in the period up to 15,000 y.

Beck *et al.* (2001) suggest that the major features of the ^{14}C record cannot be produced with solar variability or terrestrial magnetic field modulation alone, but also require significant changes in the carbon cycle. Superimposed on these large scale trends are millennial and sub-millennial variations that apparently coincide with abrupt shifts in climate as recorded in the Greenland ice cores. We expect that these shorter-term shifts are driven by solar effects (Dergachev *et al.*, 2005).

Coral records offer the highest possible resolution for radiocarbon calibration beyond the limit of the tree-ring chronologies, because of their relatively fast growth rate. However, the existing radiocarbon calibration contains few continuously banded examples from corals. Two exceptions are a *Diploastrea* coral head from Vanuatu which lived during the Younger Dryas (Burr *et al.*, 1998) and a *Goniastrea* coral from Papua New Guinea which lived approximately 13,000 years ago, according to U-Th dating. This subannual record (Figure 5.4) is the highest resolution radiocarbon calibration record from that time period.

Speleothems offer similar advantages to coral, with a time resolution of decades or better. One such record-obtained from a stalagmite recovered from a cave in the Bahamas- provides a nearly continuous record of atmospheric Δ^{14}C from 45 to 11 ka (Beck *et al.*, 2001; Richards & Beck, 2001). However, this record differs substantially from recent coral and varved-sediment data, which raises the question about reliability and consistency between datasets or whether

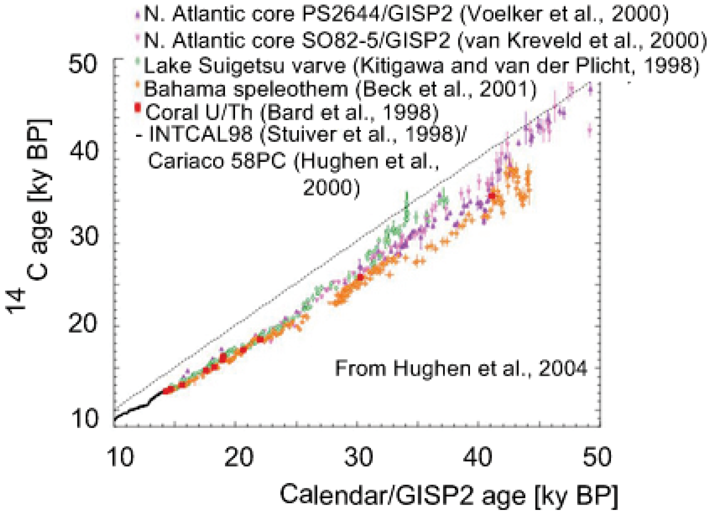

Fig. 5.5. Data for the last 50,000 y, excluding the new results of Fairbanks *et al.* (2005). The radiocarbon calibration up to 26,000 y was agreed at the 18th International Radiocarbon Conference in Wellington, in 2003. Hughen *et al.* (2005) and Fairbanks *et al.* (2005) discuss various possible extensions to this curve.

different proxy records are indeed equivalent.

Extension of the Tree Ring Record. An extended tree ring curve was first published in 1998, after the success of the initial curves published in 1986 and 1993. This curve included U-Th dated coral records from the Atlantic and Pacific, and varved marine sediment records from the Cariaco Basin (Stuiver and van der Plicht, 1998). The International Calibration team (known as IntCal) established rigid protocols for data integrity for inclusion in the calibration database. In 2004 the IntCal04 calibration dataset was introduced, and is currently incorporated into a number of computer programs, such as Calib 5.1 (`www.calib.org`), for dates up 26,000 calendar years BP (cal. BP).

Because of discrepancies between various records beyond that time, it was decided at the 2003 Radiocarbon Conference business meeting in Wellington, New Zealand, to officially recognize a record up to 26,000 cal. y BP until these questions were resolved. The records eventually included in the most recent INTCAL04 volume (Radiocarbon, vol. **46**, no. 3) include tree ring data, coral data (e.g. Burr *et al.* 1998, 2004) and varved sediments from the Cariaco Basin (Hughen *et al.*, 2004). The decision to include the Cariaco sediment record in the INTCAL98 calibration was explained by Stuiver and van der Plicht (1998) as follows – "In addition, as an exception to the rule, it was decided to include Late Glacial marine varves because this newly developed data set strengthened the coral/tree ring link considerably".

An extended curve of Fairbanks *et al.* (2005) is given in Figure 5.5. This, combined with new information on the Cariaco marine sediments, show that an extension of the calibration curve to the last 50,000 y will be completed by the time of the 20th International Radiocarbon Conference (2009).

Coral records appear to have wide acceptance as proxy records of atmospheric ^{14}C at a given time, but even this might be a problem. Since corals sample bicarbonate in the surface ocean, not the atmosphere directly, one needs to make a reservoir correction, often assumed to be around 400 y (e.g. Fairbanks *et al.* 2005), and the compilation of Hughen *et al.* (2004) make site-specific reservoir corrections. However, an unsolved problem is whether even site-specific corrections can be assumed to be constant in the Pleistocene, and, if not, how much error this might create. Recent discussions at the 10th International Conference on Accelerator Mass Spectrometry (Berkeley, 2005) and the 19th International Radiocarbon Conference (Oxford, 2006) demonstrated that reservoir variations are significant for intermediate and deep waters, especially at high latitudes.

Other Calibration Records. Many other proxy records have been studied, with the intent of extending the radiocarbon calibration curves. These included studies of marine sediment records (e.g. Voelker *et al.*, 2001), lake sediment records (Kitagawa and van der Plicht, 1998), speleothems (Beck *et al.*, 2001) and Lake Lisan sediments (Schramm *et al.* 2000). However, these records are generally considered to be not precise enough for calibration and are referred to as "comparison/calibration records" by INTCAL (van der Plicht *et al.*, 2004).

5.3.4 Paleoclimate Studies

In order to correlate distinct climatic features, it is important to be able to correlate independently-dated events. The improvement in the radiocarbon calibration curve over the last 26,400 y (and possibly to 50,000 y) permits the cross-correlation of fluctuations in the ^{14}C curve with climatic fluctuations in such isotope archives as ice-core records (Reimer *et al.* 2005; Fairbanks *et al.* 2005), as we have already mentioned.

We should also note that the same event might not be expressed in the same way everywhere and might also have a phase shift (later or earlier) in different regions. Hence, it is also important that the underlying geochronology is sound for different records to be compared. This is particularly true during the Glacial/Interglacial transition, which is of great interest due to the scale of climatic change at that time (e.g. Markgraf, 2001). During the Holocene, we also observe appreciable climatic fluctuations. These are less well understood, but may also be associated with solar forcing (Damon and Sonnett, 1991). Other periodicities in the Holocene climatic record can often be related to solar fluctuations, the most obvious being in the medieval warm period and the Maunder minimum, periods associated with colder weather in Europe (Damon and Sonnett, 1991; Dergachev *et al.* 2005).

We must also recognize that millennial-scale periodicities (e.g. Bond *et al.*, 1997; Alley *et al.* 1999; 2001) are observed in a wide variety of records, including varved lake sediments, loess deposits, marine records and forest-fire records.

AMS Studies of Natural Climatic Change. We have both direct and indirect evidence of climatic changes in the past. We know, for example, that the movement of some peoples, such as the paleoindians in North America was affected by climate and we also know, for example, that the climate of Europe was much cooler in the 14-19th centuries than it is today (Jull *et al.*, 2003). Climate has also been proposed as a driver of human movement in Siberia (e.g. Goebel, 2002; Graf, 2005), although Fiedel and Kuzmin (2007) present a case against this. An important unresolved question is whether the displacement of Neanderthals by modern humans in Eurasia was climatically-driven. It is also important to try to understand the past climatic record, since this gives us important keys to the future. We know that rapid changes are occurring in CO_2 concentration in the atmosphere, as well as other greenhouse gases (Keeling *et al.*, 2005).

Ice cores give us a long record of temperature changes during the past 450,000 y. Long-term records of climatic change over this time interval have been recovered by oxygen-isotope studies of ice cores. These records show that the climate oscillates in response to orbital forcing which causes the amount of solar radiation arriving at the surface of the earth to vary with time. This cyclic behaviour can be tied to the oscillations of the Earth's orbital motion, particularly the eccentricity of the Earth's orbit around the sun (100,000 y) and the tilt angle or obliquity (41,000 y). Finally, the precession (21,000-23,000 y) of the Earth's axis around its own center of mass, causes changes in the timing of seasons as well as the intensity of solar radiation reaching the northern hemisphere during the summer months (De Pater and Lissauer, 2005).

It has long been recognized that the fluctuations in the ^{14}C record were often coincident with major climatic events, particularly cold ones. A period of "apparent" radiocarbon age which is flat is observed at various major cold phenomena such as the Oldest Dryas (15.1-14.5 cal BP), Younger Dryas (12.9-11.6 cal BP), the 8,200 y "cold event", 2,500 y and the Maunder Minimum (17-19$^{\mathrm{th}}$ century). Dergachev *et al.* (2005) noted a striking similarity between the Δ^{14}C and δ^{18}O records in speleothems analysed by Neff *et al.* (2001) between 10,000-6,000 y.

It is important to understand these phenomena, since in recent time, we also have evidence of changes in atmospheric composition. The record of CO_2 from Mauna Loa (Keeling *et al.* 2005), see Figure 5.6, demonstrates that we have seen a continuous increase of CO_2 in the atmosphere since the mid-19$^{\mathrm{th}}$ century, consistent with production from industrial sources. In addition, we know that perhaps a ~ 0.5-1°C change in average temperature has already occurred and this may be correlated with the increase in CO_2 in the atmosphere.

Use of ^{14}C in Modern Corals and as a Tracer in the Ocean. The in-growth of bomb ^{14}C into the oceans has been studied since the early GEOSEC cruises of the 1970s. Δ^{14}C variations in dissolved inorganic carbon in seawater were used to follow the different rates of carbon uptake from different parts of the world. These experiments were repeated in much detail in the 1980s and 1990s as part of the WOCE programme (Key. 1996). Both of these studies represent the distribution of radiocarbon at the time the samples were collected.

Corals, which grow in the surface waters of the ocean, have since been the object of extensive study, because they preserve a record of the radiocarbon content of the surface ocean which allows temporal variations at a particular site to be studied (Schmidt *et al.*, 2004). In addition to Δ^{14}C variations, modern corals also preserve a record of other geochemical proxies such as Sr-Ca and δ^{18}O (Gagan *et al.* 2002; Druffel *et al.* 2004). This signal can also be correlated with the intensity of the El-Niño Southern Oscillation. There have also been extensive studies of the ^{14}C record in the oceans, as part of the WOCE, Joint Global Ocean Flux Study (JGOFS) and other large international programs (Key, 1996). This has resulted in very detailed maps of ^{14}C in the ocean as a function of location and depth.

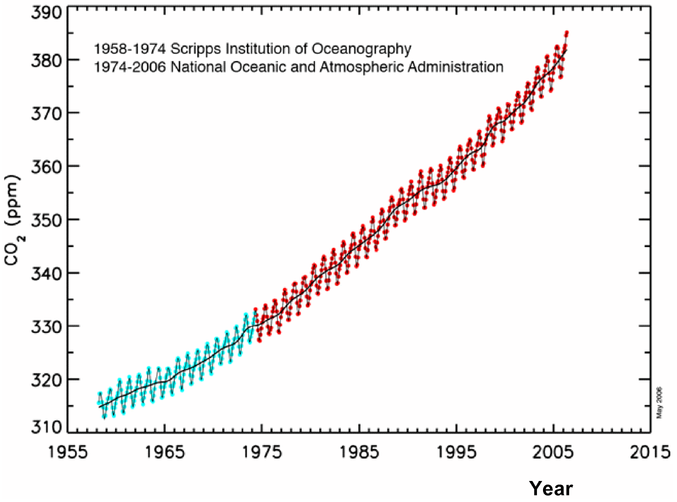

Fig. 5.6. Monthly mean CO_2 levels from Mauna Loa observatory, Hawaii.

Record of Forest Fires. There is a sizeable literature on forest-fire history from different regions of the world (see, for example, Meyer *et al.*, 1995, 2001; Hallett *et al.* 2004; Turcq *et al.* 1998; Lertzman *et al.* 2003; Hallett and Walker 2000; Pierce *et al.* 2004). A characteristic of many of these studies is evidence for marked periodicities, especially on century and millennial time scales of fire frequency. Typically, these studies involve either direct dating of charcoal found in alluvial and colluvial deposits (e.g. Meyer et al;, 1995, 2001; Lertzman *et al.*, 2003; Pierce *et al.*, 2004) or studies of the charcoal record found in lake sediments (e.g. Long *et al.* 1998; Cumming *et al.* 2002).

Meyer et al (1995) demonstrated a spectacular record of forest fires from the Yellowstone National Park, which is now cited in all subsequent papers. They noted a millennial-scale forcing and proposed that "Bond" cycles might be a forcing mechanism. Later studies showed similar periodicities, but a different phase relation at a location in southern Idaho (Pierce *et al.*, 2004).

Jull and Geertsema (2006) reported on radiocarbon dating of charcoal from paleosols and buried charcoal horizons in a unique sequence which potentially records the last 36,000 ^{14}C years from a fan at Bear Flat, British Columbia. This site included evidence for forest fire charcoal found over the last ca. 13,500 ^{14}C years before present (y BP) or 16,250±700 calibrated y BP. The latest evidence of fire is during the Medieval Warm Period. The charcoal ages show a periodicity in large fires on a millennial scale through the Holocene - an average of 4 fires per thousand years, with increases at intervals of 1-2 thousand years. These authors concluded that fire frequency was driven by regional or global climate, as well as local phenomena. Over 50 discrete fire-related horizons have been observed. For comparison, Alley (2001) noted that forest fire frequency increases during North Atlantic cold events. In particular, times of higher fire frequency may follow North Atlantic ice-rafting events (Bond *et al.*, 1997). A parallel study has been conducted in collaboration with colleagues at the University of New Mexico on the forest-fire history in Idaho, this record shows similar periodicities, but with a different phase relationship to the fires in British Columbia and Yellowstone Park (Pierce *et al.*, 2004).

Megafaunal Extinctions and Connection to Climatic Change. Apart from some isolated evidence for earlier settlement with good associations, the predominant view is that early man arrived in the western hemisphere close to the end of the last Glacial (see Nuñez *et al.* 1994; Haynes *et al.* 1992; Martin and Klein, 1984; Meltzer *et al.* 1997). The conventional model assumes that early humans arrived in the new world via a Bering land bridge. We note that since the Bering Strait is only 30 m deep at its shallowest point, and we can assume that the last sea-level rise would have closed off this route between Asia and the Americas, which occurred in two stages of $\sim$ 60 m and $\sim$ 50 m. The Bering land bridge should have remained intact until $\sim 10,000$ radiocarbon years BP (11,000 calendar years) based on our knowledge of sea-level rise.

Hence, we can see there must be a direct connection between global warming at that time, causing the separation of the Laurentide and Cordilleran ice sheets (c.f. Dyke *et al.* 2001) and other factors which drove the expansion of early man further into the New World. The rapid expansion of early man into central North America does not appear to have occurred until about 12,000 radiocarbon years BP, although the dating of the Monte Verde site in Chile ($\sim 12,500$ ^{14}C y BP; Meltzer *et al.*, 1997) suggests a slightly older time.

This period appears to be during the "Older Dryas", which is observed in many records $\sim 12,200^{14}$C y BP (e.g. Goslar *et al.*, 2000). Dyke *et al.* (2001) have summarized the available radiocarbon records for the margins of the Laurentide ice sheet, which indicate that regions east of the Rocky Mountains were largely free of ice at that time. In addition, the results of Jull and Geertsema (2006) and others suggest that much of this region may have been ice-free even earlier. The extinction of many mega fauna at the end of the late Pleistocene is well known (Martin and Klein, 1984). Hence, the exact time of these extinctions, and whether they are caused by climate alone, or by a combination of factors, such as the expansion of humans into previously unoccupied areas is a matter of great interest. Indeed, neither of these factors alone seems to explain all the observations.

Taylor (2000) has summarized the earliest radiocarbon dates on human bones from the new world. In all cases, these dates are close to the dates for the last evidence for mammoths and other large megafauna (e.g. Martin and Klein, 1984) About one half of all species of large land mammals of North America disappeared at the close of the Pleistocene (Martin and Klein, 1984).

At some locations, we can observe the interplay of climate, early man and megafauna. The Murray Springs site in Arizona (Jull *et al.*, 1998) is only one of many which show the interplay of climate, the expansion of humans and the disappearance of large mammals such as mammoths. In this location, radiocarbon ages on algal mats, which overly the mammoth remains, also fall into the period of the Younger Dryas cold event at 10,300 to 10,600 y BP (Jull *et al.*, 1998). This evidence suggests that the Clovis expansion occurred during the European Allerød warm period, and that we can perhaps associate the period of arid conditions during Clovis time discussed by Haynes (1991) with the Intra-Allerød cold period (IACP) which occurred about 11,400 to 11,100 ^{14}C y BP and was followed by a short warmer epoch before the rapid onset of the Younger Dryas at 10,900 ^{14}C y BP. In addition, we can also compare these radiocarbon ages to the estimates of sea level rise. In either case, the algal mat deposits date to 10,200 to 10,600 y, within the Younger Dryas epoch (Jull *et al.*, 1999). This cold event post-dates Clovis, and all Clovis radiocarbon

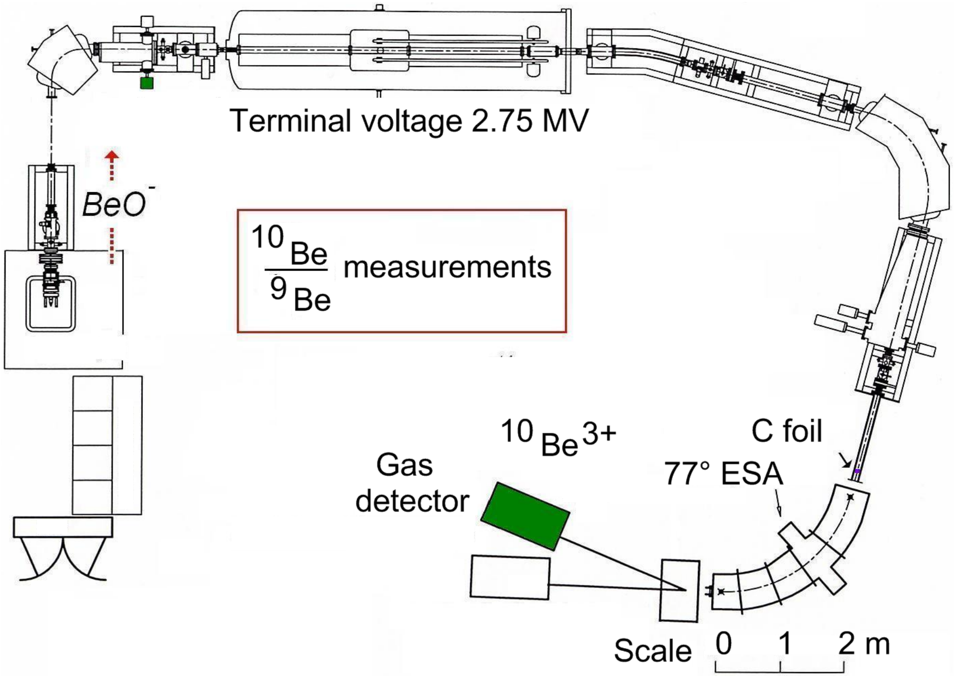

Fig. 5.7. The setup for ^{10}Be at the University of Arizona AMS system.

measurements fall between these two sea-level rise events (see Haynes, 1984, 1991, 1992).

5.4 ^{10}Be Studies

The cosmogenic-radionuclide ^{10}Be is produced in the atmosphere by spallation of oxygen and nitrogen by cosmic rays. The intensity of the cosmic-ray flux depends on galactic and solar sources, and modulation by the heliomagnetic and geomagnetic fields. After formation, ^{10}Be is quickly removed from the atmosphere by precipitation and deposited onto the surface of the Earth, where it is transported throughout the ocean and is eventually sequestered within marine sediments. A record of the cosmic-ray flux, modified by marine processes, may be interpreted from marine sediment cores and provides a valuable record of past geomagnetic and cosmic-ray phenomena.

In contrast to ^{14}C, the ^{10}Be sample is processed into the form of BeO, so that the material pressed into the ion source is BeO. The injected ion is the molecular ion, BeO$^-$ and we then select ^{10}Be^{2+} after the accelerator. A post-accelerator stripper foil is used to strip the ions to 3+ which are then analysed in a gas detector. The somewhat different setup is shown in Figure 5.7.

Previous work documented the ^{10}Be record in the authigenic fraction of marine sediments from the Gulf of California, Leg 64, site 480 (McHargue *et al.*, 1995), and the Blake Ridge, CH88-10P, (McHargue *et al.*, 2000). The ^{10}Be data, normalized to the mass of the authigenic sediment fraction, is shown in Figure 5.8. Normalization of ^{10}Be to the mass of the authigenic

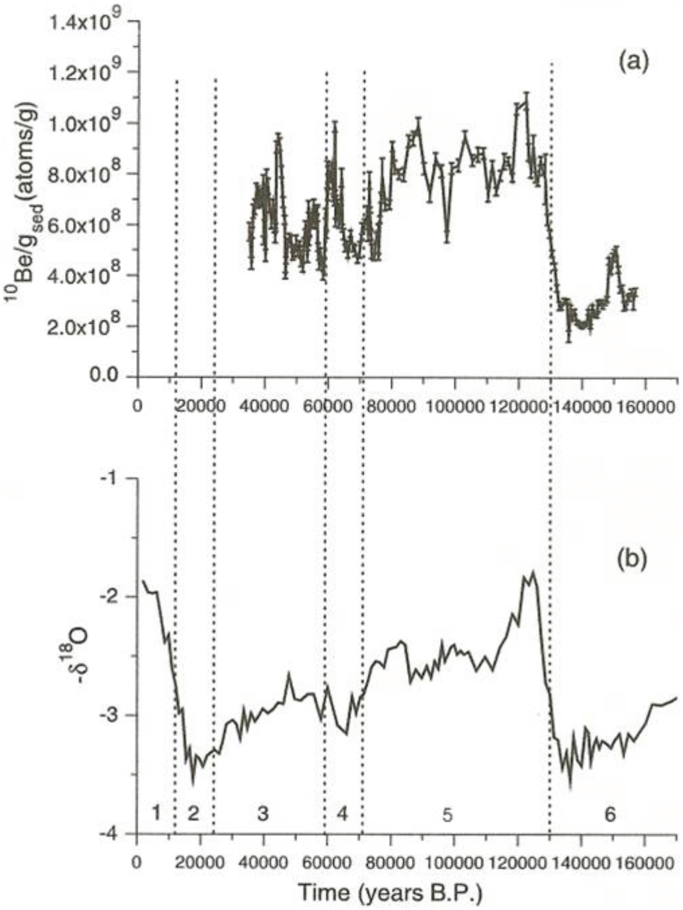

Fig. 5.8. Correlation of ^{10}Be and δ^{18}O observed in marine sediment from the Blake Outer Ridge (DSDP site 72) showing a climatic effect on the ^{10}Be record in addition to cosmogenic effects (McHargue and Donahue, 2005).

fraction provides a better proxy of paleomagnetic intensity in this core than normalization to the bulk sample mass or to ^{9}Be. In addition, normalizing ^{10}Be to the authigenic fraction provides good correlation with ^{10}Be from cores CH88-10P and DSDP 480 normalized in the same manner. This normalization makes the ^{10}Be increase at approximately 60,000 years (observed in polar ice), and at the Laschamp geomagnetic excursion and possible Mono Lake excursion more apparent.

Recent lake-sediment studies have highlighted progress done in measuring ^{10}Be in lake sediments. These are from Lake Malawi and Lake Bosumtwi, in Africa and Lake Qinghai in China. The possibility that ^{10}Be can be used to date lake sediments arose from the observation that in marine sediments the minimum concentrations of ^{10}Be in the overall data set are similar due to comparable attenuation of its production in the atmosphere when the intensity of the geomagnetic field is near maximum. In addition, we also know that the variations that are expected in the production of ^{10}Be through time are large (up to two times or more) and that determining a chronology based solely on the radioactive decay of ^{10}Be alone will not be sufficient. ^{10}Be is always being produced in the atmosphere and removed within a year by dry and wet precipitation in the lake. The supply of ^{10}Be is continuous to a lake from precipitation and from runoff into the lake. The ^{10}Be should be rapidly precipitated and ^{10}Be can be measured from all the sediments throughout cores.

We also know that the production of ^{10}Be with time varies significantly. This variance in production is random in time due to the randomness in the intensity of the dipole field that modulates it. Thus, a ^{10}Be record can be correlated to the paleomagnetic record and should be unique. The record of the intensity of the dipole field has been progressively pushed back over the last decade. The long two million record of paleointensity derived from stacked marine sediment cores is available for comparison. The concentrations of the cosmogenic radionuclide ^{10}Be in marine and lake sediments can serve as a proxy for the cosmic-ray flux. In turn, the intensity of the cosmic-ray flux is inversely related to the intensity of the geomagnetic field, the history of the latter can be derived. The geochemical cycle of ^{10}Be on the Earth begins as high energy cosmic-rays, primarily in the upper atmosphere, create ^{10}Be from spallation of O and N atoms. Thus, the production of ^{10}Be at any one time is proportional to the cosmic-ray flux incident upon the Earth which, in turn, is a function of the intensity of the primary galactic and solar cosmic rays, and their modulation by the solar and geomagnetic fields. Once ^{10}Be is produced in the atmosphere, it is quickly scavenged by particulate matter, and is precipitated within a year onto the surface of the earth. Most ^{10}Be (that which has not decayed) is eventually sequestered in ice, soils, and lake and marine sediments (e.g. McHargue *et al.*, 2000).

We expect that the ^{10}Be in sediments should reflect the variations in the ^{10}Be concentrations which are consistent with its production as might be expected from the long-term secular variations in the geomagnetic field. However, because ^{10}Be is transported through the environment after production it is subject to environmental influences, such as climate. Hence, there is also the potential for ^{10}Be to be used as a proxy indicator for climatic effects. We expect that the ^{10}Be data will give us additional insight into the processes affecting the ^{14}C sources.

5.5 ^{129}I Studies

Iodine-129 is easily measured using even a small AMS, since it has no interfering isobar which makes a negative ion. Sufficient data is now available to show a machine random uncertainty of 0.4 % for iodine samples. Repeated analysis of the low-level Woodward iodine standard has yielded results in the low 10^{-14} range for ^{129}I/^{127}I ratios. Chemical extraction techniques for a variety of environmental samples including seawater, corals, stalagmites and seaweed have been developed. With these techniques we can measure ^{129}I/^{127}I ratios in samples with as little as 5 μg total iodine content.

Corals are also known to concentrate iodine. The Arizona AMS Facility has successfully produced ^{129}I time series from Pacific corals from the Solomon Islands and Easter Island (Biddulph, 2004; Biddulph *et al.*, 2006). Banded corals are well known for their facility in reconstructing surface temperature, salinity and radiocarbon time series (Burr *et al.*, 1998; Burr *et al.*, 2004). A summary of this work is shown in Figure 5.9. This plot shows anthropogenic iodine invasion into corals in the South Pacific. Biddulph (2004) has also reported on a 20,000 y record of cosmo-

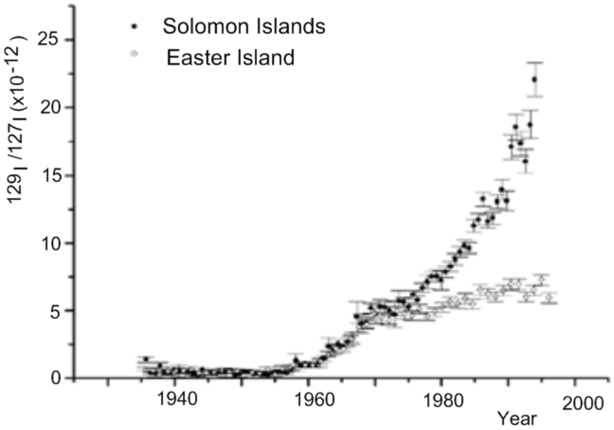

Fig. 5.9. In-growth of ^{129}I into corals from Solomon Islands (western Pacific) and Easter Island (South-eastern Pacific), adapted from Biddulph *et al.* (2006).

genically produced iodine in a stalagmite from the Bahamas islands. These results indicate that transport of ^{129}I is much more rapid than previously thought. There is some preliminary data suggesting that ^{129}I may track changes in the geomagnetic field and the cosmic ray flux. Data from a stalagmite (Biddulph, 2004) seems to reproduce magnetic excursions that have been seen in other radioisotope records such as ^{10}Be and ^{36}Cl. The relatively long half-life of ^{129}I (15.7 million years) would enable us to analyze records that go back nearly 100 million years.

6 Comparison of Detection Limits for Radiometrics and Mass Spectrometry Techniques

Results of analysis of long-lived radionuclides in reference materials using various techniques (Table 6.1) indicate that a reasonable agreement has been obtained. The most sensitive technique for all presented analyses has been AMS.

Tab. 6.1. A comparison of results of analysis of Pu and U isotopes in IAEA Reference Materials (compiled from Povinec, 2004; Lee *et al.*, 2008).

Method	^{238}Pu Bq kg^{-1}	^{239}Pu Bq kg^{-1}	^{240}Pu Bq kg^{-1}	^{239,240}Pu Bq kg^{-1}	^{241}Pu Bq kg^{-1}	^{242}Pu Bq kg^{-1}	^{238}U Bq kg^{-}	^{236}U Bq kg^{-1}
IAEA-134 Irish Sea cockle flesh								
SAS	3.0 ± 0.2			16.3 ± 0.8				
AMS								
ICPMS		9.8 ± 0.8	7.7 ± 0.6	17.5 ± 1.0				
LSS								
IAEA-135 Irish Sea sediment								
SAS	42 ± 1			222 ± 8				
AMS		129 ± 13	92 ± 9	221 ± 16				(11.2±2.2) 10^{-3}
ICPMS		127 ± 10	98 ± 8	221 ± 13	3970 ± 200	0.051 ± 0.001		(10.3±3.0) 10^{-3}
LSS					3000 ± 650	0.056 ± 0.006		
IAEA381 Irish Sea water								
SAS	3.3 ± 2			14.0 ± 1.0			0.042±0.004	
AMS		8.2 ± 0.3	7.0 ± 0.2	15.7 ± 0.4		0.0046 ± 0.0005		(0.019±0.003) 10^{-3}
ICPMS		8.1 ± 0.8	7.0 ± 0.7	15.1 ± 1.1		0.0047 ± 0.0002		(0.023±0.006) 10^{-3}
LSS					200 ± 60			
IAEA-384 Fangataufa lagoon sediment								
SAS	40 ± 2			111 ± 3			35.3±1.7	
AMS		109 ± 11	14 ± 1	123 ± 11		2.5 ± 0.4		(8.4±1.7) 10^{-6}
ICPMS		102 ± 8	18 ± 2	120 ± 8	240 ± 20	1.9 ± 0.5		
LSS					100 ± 70			
IAEA-385 Irish Sea Sediment								
SAS	0.45±0.03			2.94±0.09			29±1	
AMS		1.79±0.28	1.15±0.14					< 0.0001
ICPMS								
LSS					30±2			
IAEA-414 Irish and North Sea fish								
SAS	0.025 ± 0.002			0.120 ± 0.005		0.044 ± 0.004	1.112±0.070	
AMS		0.087 ± 0.003	0.053 ± 0.005	0.14 ± 0.01		0.068 ± 0.010		(0.024±0.007) 10^{-3}
ICPMS		0.063 ± 0.007	0.046 ± 0.005	0.11 ± 0.02	2.7 ± 0.6			
LSS								

A comparison of detection limits for a number of long-lived radionuclides measured by radiometrics techniques (RMT), ICPMS, TIMS, RIMS and AMS is given in Table 6.2. It can be seen again that the most sensitive technique is AMS which gives the lowest detection limits with the exception of ^{3}H where the ^{3}H-^{3}He method dominates. The detection limits obtained by RMT are from three to eight orders of magnitude lower than for the AMS technique.

Tab. 6.2. A comparison of detection limits (compiled from Povinec, 2004; Erdman *et al.*, 2008; Roos, 2008; Lee *et al.*, 2008) for frequently analysed long-lived radionuclides in the environment (in Bq).

Method	^{3}H	^{14}C	^{99}Tc	^{129}I	^{236}U	^{237}Np	^{240}Pu
RMT NAA	10^{-3}	10^{-4}	10^{-2} 1	10^{-2} 10^{-7}	10^{-3}	10^{-4} 5×10^{-4}	$10^{-5\#}$
ICPMS	10^{-3*}		10^{-5}	10^{-3}	5×10^{-9}	5×10^{-6}	5×10^{-6}
TIMS			8x10^{-6}	10^{-8}	10^{-10}	10^{-9}	0.5×10^{-6}
RIMS			10^{-5}				$\sim 10^{-6}$
AMS	10	10^{-7}	6×10^{-6}	10^{-10}	10^{-10}	10^{-10}	0.4×10^{-6}

* ^{3}He in-growth MS

\# ^{239,240}Pu

7 Data Management

7.1 Management of Data Quality

Data credibility is becoming essential in regional and world-wide programmes to which laboratories with different practices contribute, especially if the resulting data are input into regional and global radionuclide databases. Therefore accurate and precise determinations of radionuclide concentrations in environmental samples are important aspects of the assessment of the environment and the use of radionuclides in studies of oceanographic processes. Quality assurance (QA) as a system of activities and actions has two main components:

i) Quality assessment – a mechanism to verify that the system is operating within acceptable limits;

ii) Quality control (QC) – a mechanism to control data quality (errors).

The objectives of the QA programme include maintaining a continuous assessment and control of data quality, identifying proper analytical methods, providing permanent records of the performance of instruments, standardising analytical procedures, ensuring sample integrity, improving record-keeping and identifying training needs. The common aim of all these objectives is to provide high quality data. The QA functions include the development (or selection) of proper methods of sampling, sample preservation, sample pre-treatment, sample analysis and methods for evaluation and reporting of results. Further, they include intralaboratory and interlaboratory methods of validation and evaluation, establishing quality control guidelines and maintaining quality control sample programmes. A laboratory without a proper QA programme cannot operate successfully. This is especially important when the laboratory produces series of data that are of interest in regional or world-wide programmes (Povinec, 2004).

A QA programme (including good laboratory practices) should be described in one of the most important laboratory documents – the QA manual. It should contain QA policy and objectives, staff responsibilities, analytical methods (including sampling, field measurements, sample handling, protocols, data reduction and evaluation (including uncertainty budget (e.g. Dovlete and Povinec, 1999), materials and standards used, QA procedures, results of interlaboratory comparisons, the recording system and database. The QA manual should be regularly up-dated with any new developments in the laboratory.

7.1.1 Intercomparison Exercises

Both world-wide and regional intercomparison exercises are the most important part of a laboratory's QA programme. They have considerably helped laboratories to assess their performance, supplied them with reference materials and enabled them to gather information on their performance. Although there has been remarkable growth both in the number of participating laboratories (from 40 to more than 150) and in the quality of data, the performance of all participating laboratories is not yet satisfactory.

We shall illustrate recent developments in the performance of laboratories in the intercomparison exercise organised recently by IAEA-MEL on Fangataufa Lagoon sediment (IAEA-384) influenced by atom weapons testing on this atoll. Figure 7.1 compares the results obtained by different laboratories for ^{137}Cs, ^{40}K, ^{235}U and ^{238}Pu. It can be seen that about 20-25 laboratories

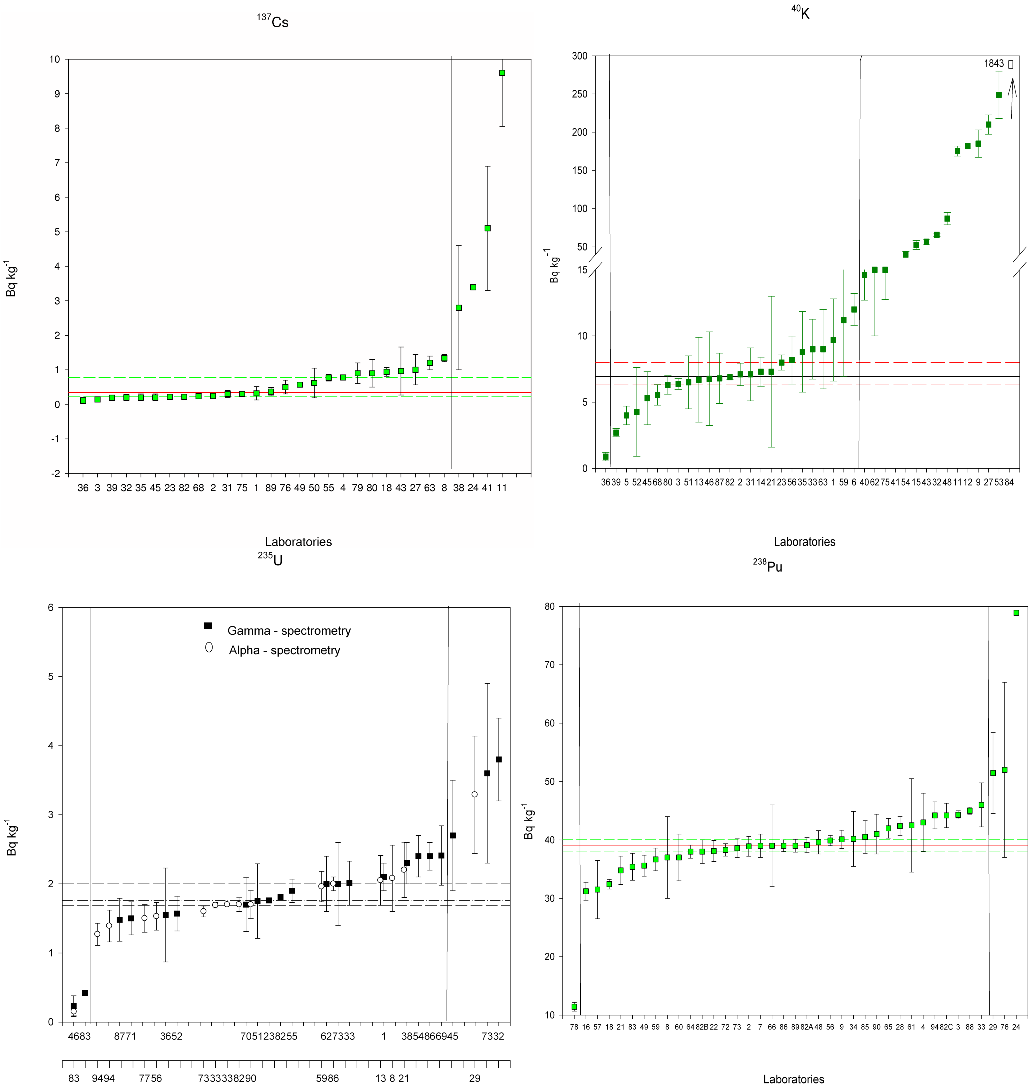

Fig. 7.1. Results of the intercomparison exercise organised by IAEA-MEL on natural and anthropogenic radionuclides in Fangataufa lagoon sediment (IAEA-384). Values behind the vertical lines are outliers. The median (solid line) and corresponding 95 % confidence intervals (dashed lines) are also shown.

out of the 30-40 which submitted their results (the total number of participating laboratories was much higher – about 140 laboratories), performed well in this intercomparison exercise (Povinec and Pham, 2000). Although ^{137}Cs is the most frequently analysed anthropogenic radionuclide in the environment, surprisingly some of the laboratories had problems when analysis this radionuclide in the sediment, mainly because its concentration was relatively low (0.3 Bq kg^{-1}

dry weight). However, the laboratories' performance was not great even when analysing natural ^{40}K in the sediment, as some of them encountered problems with calibration and the correct estimation of the background under the ^{40}K photopeak. For ^{238}Pu alpha-ray spectrometry and for ^{235}U both alpha- and gamma-ray spectrometry was used, which showed reasonable agreement between laboratories.

Z-score methodology has been recommended by the IUPAC (International Union of Pure and Applied Chemistry) for assessment of laboratory performance in the evaluation of intercomparison results (ISO, 1997)

$$Z = (x_i - x_a)/s_b, \tag{7.1}$$

where x_i is the robust mean of the reported values of massic activity in the sample, x_a is the assigned value (a mean value of accepted results), s_b is the target standard deviation. The selection of the right target value depends on the objectives of the exercise, usually it is required to have a relative bias below 20 % ($s_b < 10$). The uncertainty of the assigned value s_{tu} is included in the target value for bias as

$$Z = (x_i - x_a)/\sqrt{(s_b^2 + s_{tu}^2)}. \tag{7.2}$$

The performance of a laboratory is considered acceptable if the difference between the robust mean of the laboratory and the assigned value (in s_b units) is less than or equal to two. The analysis is regarded as being out of control when $|Z| > 3$. The Z-score evaluation represents a simple method which gives participating laboratories a normalised performance score for bias. As an example, Figure 7.2 shows a symmetric Z-score distribution for ^{137}Cs and ^{235}U (after excluding outliers) with Z-scores below 2, indicating that the performance of the laboratories was satisfactory.

7.1.2 Reference Materials

Reference Materials (RMs) represent samples of well established properties used for the assessment of analytical methods. More rigorous materials – Certified Reference Materials (CRMs) or Standard Reference Materials (SRM, issued by the National Institute of Standards and Technology – NIST, USA) have property values certified by technically valid procedures (at least with two independent methods) traceable to SI units (ISO, 1996).

RMs and CRMs have great impact on the development of methods of known accuracy. They represent important benchmarks in QA, identifying weak methodologies, detecting training needs, up-grading the quality of laboratories' performances and assessing the validity of analytical methods. The reference methods can only be accepted on the basis of interlaboratory tests performed on selected CRMs.

In order to improve data quality, to provide the required traceability to SI standards and to improve the accuracy and precision of laboratories' measurements, priority should be given to the production of CRMs. The CRMs should be available for the different environmental matrices e.g. sediment, water and biota (Povinec *et al.*, 2002). The required long-term availability of CRMs (over 10 years) necessitates their long-term stability and the collection and preparation of large volume samples (over 100 kg). The relative precision of all reported data should be better than 5 %. This would require highly homogenised samples thoroughly tested for any inhomogeneities

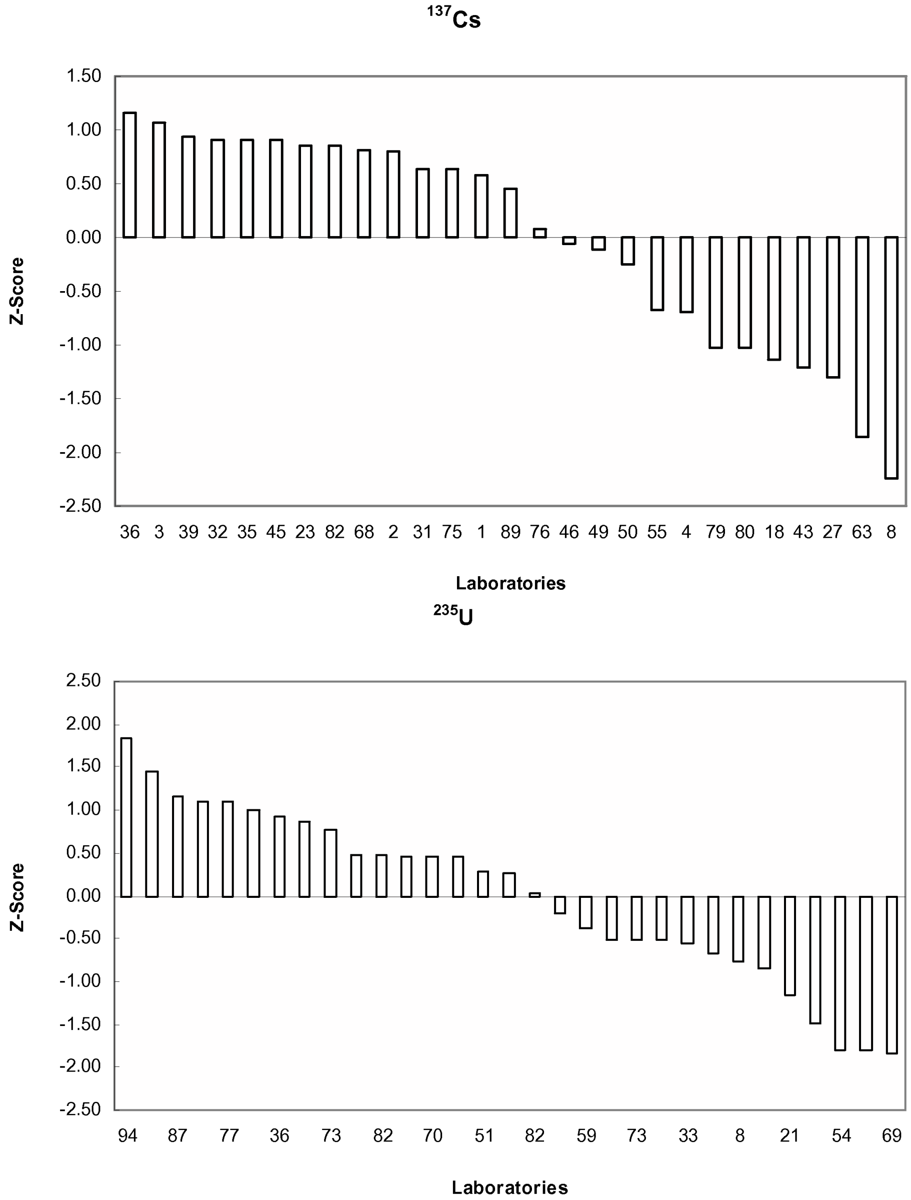

Fig. 7.2. Z-score values (after excluding outliers) of ^{137}Cs and ^{235}U for participating laboratories in the intercomparison exercise IAEA-384. For $|Z| \leq 2$ the performance of a laboratory was considered acceptable.

of major elements (inhomogeneities should be below 1 %). The principal analyses should be accompanied by supporting characterisation e.g. for multielemental composition, mineralogy, particle size distribution, radionuclide speciation studies etc. At least two independent analytical methods should be used for reporting certified values (Povinec *et al.*, 2001). This may not be a major problem in the case of radionuclides, where different methods are available (e.g. RMT, ICPMS, TIMS, AMS, NAA, etc.).

The specific needs for the production of CRMs for mass spectrometric methods (e.g. AMS, ICPMS, TIMS), where usually small samples with very low radionuclide concentrations are necessary and which require special treatment, should be addressed. Table 7.1 lists RMs produced by IAEA for the analysis of anthropogenic and natural radionuclides in environmental samples.

7.2 Database Management

In order to study the spatial and temporal distribution of radioactive and stable isotopes in the environment it is necessary to organize and storage the data in a database. For example if we need to estimate radionuclide inputs from local sources, radionuclide distributions in the local/regional environment must be well known so that results from recent sampling missions can be reviewed objectively, comparatively and comprehensively. This requires a detailed study of the present distributions of the main radionuclides of interest in the environment, as well as possible predictions of their concentrations in the near future. As an example we shall introduce the IAEA-MEL GLOMARD (Global Marine Radioactivity Database) database which was developed in collaboration with several institutes in the framework of the WOMARS (Worldwide Marine Radioactivity Studies) project (Povinec *et al.*, 2004). The GLOMARD has been created to serve the following important functions: (i) provide a snap-shot of activities at any time, which may be used as a baseline for any impact assessment studies; (ii) provide immediate and up-to-date information on the levels of radionuclides in the world's seas in different environmental matrices; (iii) permit investigation of temporal trends in environmental levels of radionuclides

Tab. 7.1. IAEA Reference Materials for anthropogenic and natural radionuclides in the marine environment.

Code	Matrix	Place of origin	Reference
IAEA-MA-B3/RN	Fish flesh	Baltic Sea	`www.iaea.org`
IAEA-135	Sediment	Irish Sea	`www.iaea.org`
IAEA-300	Sediment	Baltic Sea	`www.iaea.org`
IAEA-315	Sediment	Arabian Sea	Pettersson *et al.*, (1997)
IAEA-352	Tuna fish flesh	Mediterranean Sea	`www.iaea.org`
IAEA-381	Seawater	Irish Sea	Povinec *et al.* (2002)
IAEA-384	Sediment	Fangataufa Lagoon	Povinec *et al.* (2007)
IAEA-385	Sediment	Irish Sea	Pham *et al.* (2008)
IAEA-414	Fish	Irish and North Seas	Pham *et al.* (2006)
IAEA-418	Water	Mediterranean Sea	In preparation
IAEA-415	Fish flesh	Atlantic Ocean	In preparation
IAEA-412	Sediment	Pacific Ocean	In preparation
IAEA-410	Sediment	Bikini Atoll	In preparation

and identify gaps in available information. To satisfy these aims, the final system should be flexible and extendible and should be able to be interrogated by region/sea, by time period, by nuclide and by environmental matrix. The GLOMARD database is available on IAEA web site as a part of Marine Information System (`www.IAEA.org/MARIS`).

7.2.1 Design of a Database

The data requirements for recording marine radioactivity measurements are relatively complex and extensive but can be functionally divided into two categories: (i) definition of the environmental sample and its processing; (ii) radioanalytical procedures undertaken and their results. A complete data profile provides sufficiently detailed information to ensure that data verification and evaluation can be carried out. Such detail strengthens the data interpretation and analysis and forms the basis of data validation. The division into these two distinct data categories is reflected in the database structure which has two primary data files. A further reason for this structure is that frequently a single sample will give results on several radionuclides. Four broad classes of sample type were defined, namely water, suspended matter, sediment and biota. These are the main marine environmental media considered. Associated with each are a number of further data fields which together provide a complete sample profile. A complete profile incorporates the sample description (including volume, salinity, temperature, oxygen content, pH, as appropriate), sampling location and pre-treatment (ashing, drying etc.).

The second category defines the data profile for the radionuclide information and includes method of analysis as well as results. The main considerations in the design of the data requirements were the different ways of reporting results, the difficulties in dealing with the limits of detection, the possibility of decay corrected results and the various uncertainties which could be quoted.

The information incorporated in the database is both current as well as retrospective. It reflects current research and environmental priorities as well as those of the past. Retrospective data acquisition is a demanding task and/as there are a variety of sources of the necessary data, providing varying degrees of detail concerning the samples and results. In the initial development of the database, it was decided to undertake a retrospective search for data making use of published literature and research reports. Particular areas of the world's oceans and seas were targeted and an intensive data search begun. Currently, the database holds a great deal of historical data from a number of technical reports and papers. Laboratories have been asked to provide data directly to the database. Therefore, consideration has been given to prospective data entry, through electronic transfer of data from the source laboratory to the central database. Various data transfer protocols and programmes have been developed to facilitate the exchange of data. The general organisation of the database is shown in Figures 7.3 and 7.4. There are several suitable software packages available which can be used for the database construction (e.g. Oracle, SQL, Access, etc.). The sample description has been classified into seven key areas.

Sample Type. Four sample types were identified; water, suspended matter, sediment and biota corresponding to the environmental media most commonly used. The biota data entries are accompanied by further information which details the species and general classification of organisms. An internal coding scheme has been developed by IAEA-MEL staff and forms the basis of the organism classification. Such a design allows broad interrogation of the database,

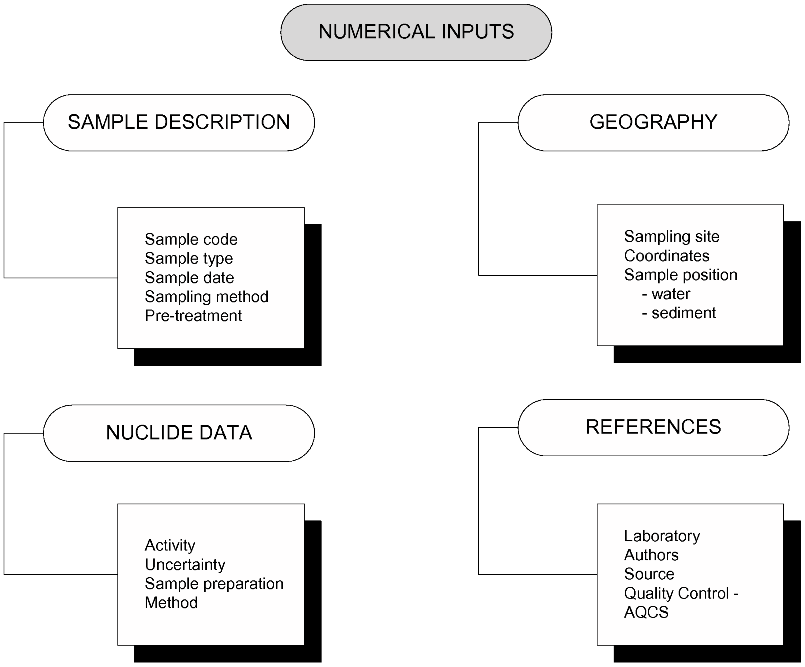

Fig. 7.3. General organisation of the database (inputs).

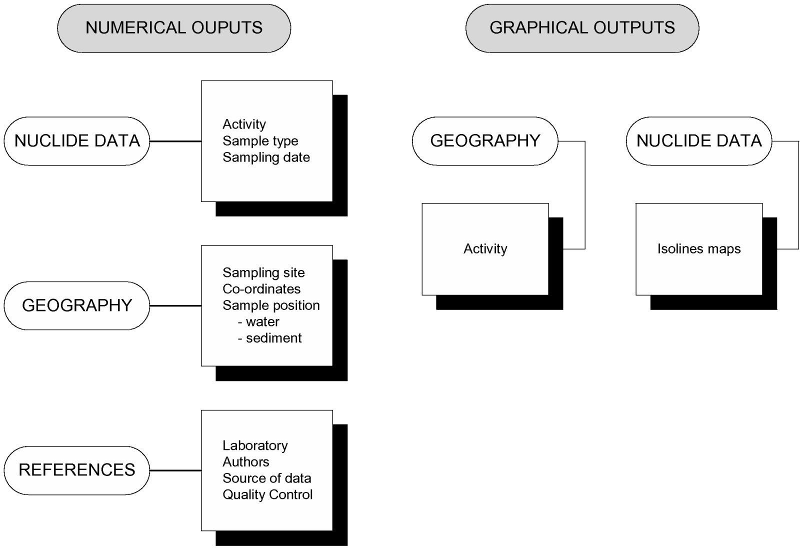

Fig. 7.4. General organisation of the database (outputs).

but also will permit very specific queries since sample type is one of the key fields. For biological samples, the hierarchical description of the sample allows user choice in the specificity of the query.

Laboratory Information. As the primary data source, laboratory information provides the necessary background information. Participation in proficiency tests and intercomparison exercises provides a broad indicator of good laboratory practice and may be used in individual cases to assess the validity of observations.

Sampling Period. The date of sample collection or period of sampling (for suspended matter), defined by two limiting dates is required. Since temporal features will be an important analysis product from the database, these fields are essential and form the basis for temporal interrogation.

Sample Location. All the data entered in the database are geographically registered. The degree of spatial registration recorded will, of course, be varied, ranging from precise (i.e. latitude and longitude) to less specific information (e.g. a specific sea). Provision has been made for this information to be entered in a variety of forms following a hierarchical structure. Level 1: information on the region in which the sample was collected is sought. The regions are defined according to the nine principal regions of the International Hydrographic Bureau (IHB: `www.iho.shom.fr`). In addition, direction may also be specified, encouraging more detailed descriptions. Level 2: at this level, the area within the region is defined again using IHB criteria. Level 3: the primary data is the exact location given by the latitude and longitude of the sampling location. The name of the sampling station may also be entered and used in data searching.

Sampling Method. Information on the specific sampling method used to collect the sample is requested. Although not considered as a central data requirement, availability of such information may be used in the data evaluation and description stages.

Laboratory Treatment. A number of physical and chemical treatments may be applied to the sample prior to radionuclide analysis. General information on the processes to which the sample has been subjected is required as part of the profile. As for the sampling method, the primary function of this data is for data verification and in certain circumstances, e.g. in the identification of outliers it may be used in the validation process. Again, when results from different laboratories are being combined, such information may be used to ensure the comparability of results and to explain any observed discrepancies.

Data Source and Reference. Given a primary database function as a data archive and repository, it is important that the source of any data be fully referenced, thus part of the database system includes a full reference to the primary source, be it a published paper or internal laboratory report. Although within the main database only a limited entry is made, a further third database file contains the full bibliographic reference with key words.

7.2.2 Presentation of Results

Analytical information in the database is less complex than for the environmental description of the sample. It does, however, have a number of features which must be accommodated within the primary data file. Key issues which had to be resolved included the different uncertainty structures, data recorded at the limit of detection, below detection or not detected and the information concerning the different counting methods. The nuclide is identified by standard convention using scientific notation.

Results - Units of Measurement. Although an international convention on units does exist, it is noticeable and to be expected that results are presented in a variety of units. The primary database file holds the information on radionuclide activities in the original units. Later, the data management system converts the data to a standard form for further manipulation and analysis.

Uncertainty and Limit of Detection. Uncertainties in both absolute and percentage form are accommodated (at 1σ level). Measurements made at the limit of detection or recorded as below detection or not detected are flagged in an additional character field.

Method of Measurement. The particular analytical method of sample analysis is incorporated. The analytical data file also includes the sampling date (a secondary link to the environmental data file), date of measurement, whether a decay correction has been made and to which date. A further series of data fields is used to accommodate a further data format, namely summary data.

Bibliographic References. The third basic information type gives details of the bibliographic information on the data source. It includes the authors/source of the data, if from a report, the full title and date of publication and a number of keywords.

7.3 Examples of Data Evaluation

Well organized data then can be used for data evaluation, e.g. spatial and temporal variations, estimation of residence time of isotopes in different environmental compartments (atmosphere, soil, groundwater, etc.). Of course, suitable software is required for data evaluation and viewing (e.g. Surfer, VoxPro, ArcView/ArcInfo, etc.). As an example we present in Figures 7.5 a spatial distribution of ^{137}Cs in surface water of the Northern European Seas in different time intervals, documenting an impact of the nuclear reprocessing facility located in Sellafield (UK) on the Irish Sea and the North European Seas. Possible results after evaluation then could be a mean concentration in a given sea, a mean residence time, a mean transit time, etc. (Povinec *et al.*, 2003b). For example the mean transit time of surface waters from the central Irish Sea has been estimated to be 0.5 ± 0.1 y to the North Channel, 2 ± 0.2 y to the north of Scotland, 2.5 ± 0.2 y to the east coast of England, 3 ± 0.5 y to the southern North Sea, 4 ± 0.5 y to the central and eastern North Sea, 1.5 ± 0.2 y to the Celtic Sea, 2 ± 0.2 y the English Channel, 5 ± 1 y to the Baltic Sea, 4.5 ± 0.5 y to the Norwegian Sea, 5 ± 1 y to the Barents Sea and 6 ± 1 y to the Kara Sea (Novaya Zemlya).

As another example we present in Figure 7.6 an impact of the Chernobyl accident (26th April 1986) on the ^{137}Cs concentration in surface waters of the Baltic Sea. We see clearly

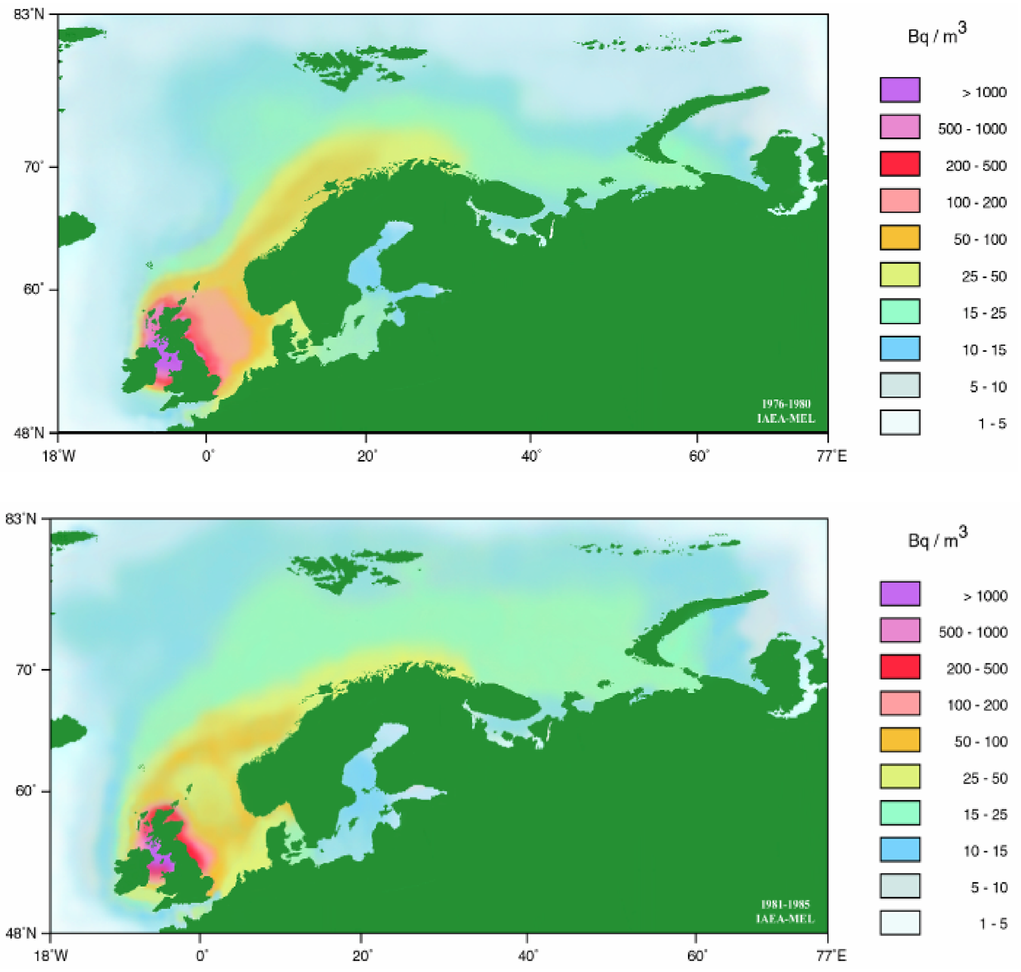

Fig. 7.5. Spatial distribution of ^{137}Cs in surface waters of the North European Seas compiled from the GLOMARD/MARIS database, documenting an impact of the nuclear reprocessing facility located in Sellafield (UK) on the Irish Sea coast. (1976-1980 (top); 1981-1985 (bottom)). The authorised ^{137}Cs discharges from the Sellafield plant peaked in 1975 at 5.2×10^{15} Bq, the recent discharges have been below 1 TBq.

elevated ^{137}Cs concentrations exceeding 1 kBq m^{-3} in the central Baltic Sea, which then have been decreasing with time. Due to the Chernobyl accident the Baltic Sea has been the most contaminated sea with ^{137}Cs in the world.

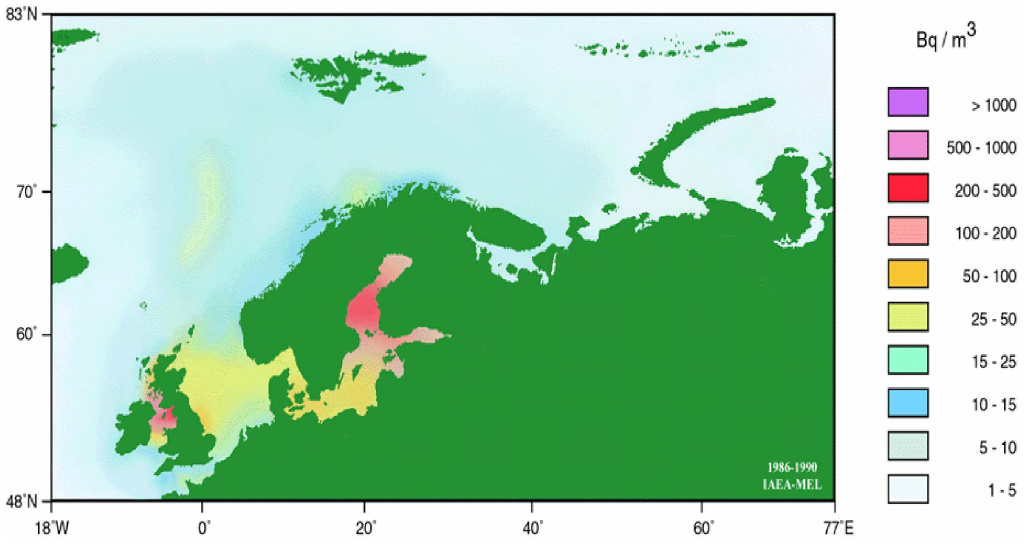

Fig. 7.6. ^{137}Cs in surface water of the North European Seas compiled from the GLOMARD/MARIS database after the Chernobyl accident (1986-1990).

8 Conclusions and Outlook

The main conclusions may be summarised as follows:

(i) A real breakthrough in radiometrics techniques for analysis of environmental radionuclides at very low-levels (down to μBq kg^{-1} scale) has been the development of underground laboratories and their applications in environmental studies. HPGe detectors of 200 % relative efficiency (in comparison to 76 × 76 mm NaI(Tl) crystals) have become available, and they can be produced with minimum radioactive contamination. Semiconductor alpha-ray spectrometry and liquid scintillation spectrometry remain powerful technique for the analysis of alpha- and beta-emitters because of the simplicity of measurement, reasonable resolution and sensitivity. Generally, the radiometrics sector will dominate also in future in the analysis of short- and medium-lived radionuclides. Monte Carlo simulation codes have become an important pre-requisite for the design and formulation of detection system characteristics before the detectors are constructed and installed.

(ii) *In situ* underwater gamma-ray spectrometers based on NaI(Tl), BGO and HPGe detectors, sometimes working with satellite data transmission from the field to the laboratory, considerably improved analytical capabilities in cases when large surfaces should be scanned, or continuous monitoring should be carried out. It would be of great public interest if such monitoring devices would accompany in real-time all releases of radionuclides from nuclear installations to the aquatic environment, so information on radionuclide levels would be accessible to the public, e.g. by Internet. Such monitoring systems can also be adapted for environmental monitoring for safeguards purposes with the aim to search for undeclared nuclear activities in regions of interests.

(iii) In the mass spectrometry sector the most exciting breakthrough in the analysis of long-lived radionuclides in the environment has been made by AMS which offers the best sensitivity, requires minimum sample size and minimizes matrix and interference effects. However, its operation is complex and experienced staff is needed, which means that analysis is more expensive. On the other hand, desk-top AMS machines have become available, which will further increase their applications in environmental studies. A direct coupling of AMS with new generation of chromatographs has enabled to proceed from a bulk sample analysis to a compound specific analysis.

(iv) SIMS matured into powerful technique for isotopic analysis of surfaces. It represents a real breakthrough in the philosophy of analysis, jumping from a bulk sample analysis into isotopic analysis of micro-particles, which open new possibilities in many investigations, including speciation studies of isotopes associated with colloids and particles, important for better understanding of processes in the aquatic environment, and biological uptake of isotopes.

(v) ICPMS has proved to be powerful tool for the analysis of long-lived radionuclides because of its high sensitivity, rapid analysis, multi-isotopic composition and the low cost per analysis. Nevertheless, there could be problems with molecular, isobaric and isotopic interferences even if careful purification procedures are used. A new state of the art TIMS operating in multi-dynamic mode with a multi-collector detection system has produced even better precision and accuracy in isotopic ratio and concentration measurements. RIMS, although still very sophisticated technique, represent important innovation especially as an alternative method in areas where other techniques have difficulties, e.g. with production of positive ions (analysis of ^{39}Ar, ^{81}Kr).

(vi) A few applications of radiometrics and mass spectrometry techniques in environmental research and climate change studies presented in this paper were not possible to carry out before either because of lack of sensitivity or absence of suitable samples.

It is expected that due to decreasing concentrations of anthropogenic radionuclides in the environment, and applications of lower radiation dose limits for public, more sensitive methods will be needed, which may include quicker and simpler methods of chemical multi-radionuclide separations from one sample and a decrease in manpower by the use of new generation of chromatographs and robotic systems, directly coupled with spectrometers. These new techniques will not only greatly improve detection limits, but they will also decrease required sample volumes. Bulk sample analysis will be replaced by isotope analysis of different minerals and organic compounds present in samples, thus contributing to better understanding of biogeochemistry of different elements in the environment. Quality assurance and quality control including the certification of laboratories, will further improve the data quality to the extent that national, regional and global isotope information systems will be built. More attention will be devoted to the protection of the total environment (a transfer from the egocentric to the ecocentric approach).

New isotope techniques will be mastered, e.g. Laser Microprobe Mass Analysis (LAMMA), Fourier Transform-Ion Cyclotron Resonance (FT-ICR) and others, which may further improve detection limits. More isotope tracers (e.g. ^{39}Ar, ^{81}Kr, ^{135}Cs, and others) will be frequently applied in environmental and climate research. Thanks to new isotopic tracer techniques new exciting investigations are expected to be carried out, which will further improve our knowledge of environmental processes, and they will also contribute to better understanding and protecting the total environment.

The authors hope that this review will help readers in better orientation on recent developments in the field of ultra low-level spectrometry, and it will advice potential investigators on construction principles of underground laboratories, as well as on criteria when and how to apply low or high energy mass spectrometers in environmental investigations.

References

Aarkrog, A., 1971. Radioecological investigations of plutonium in an arctic marine environment. *Health Phys.* 20, 31–47.

Aarkrog, A., Dahlgaard, H., Nilsson, K., 1984. Further studies of Plutonium and Americium at Thule, Greenland, *Health Phys.* 46, 29–44.

Aarnio, P.A. *et al.*, **1990**. *Fluka user's guide.* Technical Report TIS-RP-190, *CERN,* Geneva.

Alessandrello, A., Belloti, E., Cattadori, C., Camin, D., Cremonesi O., Fiorini, E., Liguori, C., Pulla, A., Rossi, L., Ragazzi, S., Sverzellati, P.P., Zanotti, L., 1986. Underground laboratory and Milano double beta decay experiment. *Nucl. Instr. Methods in Phys. Res.* B17, 411-417.

Alley, R. A., Clark, P. U., Keigwin, L. D. and Webb, R. S., 1999. Making sense of millennial-scale climate change. In Mechanisms of global climate change at millennial time scales, 385-394, Clark, P. U. ed., *Geophysics Monograph, American Geophysical Union*, 112, Washington, DC.

Alley, R. B., Anandakrishnan, S., Jung, P. and Clough, A., 2001. Stochastic resonance in the North Atlantic: Further insights. In *The Oceans and Rapid Climate Change: Past, Present and Future*, 57-68, Seidov, D., Haupt, B. J. and Maslin, M., eds., American Geophysical Union, Washington, DC.

Allkofer, O.C., Karstensen, K., and Dau. W.D., 1971. The absolute cosmic ray muon spectrum at sea level. *Phys. Lett.* B36, 425-427.

Allkofer, O.C., 1975. *Introduction to Cosmic Radiatio*n, *Thieming,* München.

Allkofer, O.C. and Grieder, P.K.F., 1984. *Cosmic Rays on Earth, Physics Data 25. Kiel University*.

Aoyama, M. and K. Hirose, 2008. Radiometric determination of anthropogenic radionuclides in seawater. In *Analysis of Environmental Radionuclides*, 137-162, P.P. Povinec, ed., *Elsevier*, Amsterdam.

Aoyama, M., M. Fukasawa, K. Hirose, P. P. Povinec, J. A. Sanchez-Cabeza, and D. Tsumune, 2008. Evidence for unexpected transport of pollutants from the North Pacific to the South Pacific subtropical gyre. *Nature,* submitted.

Arnold, J. R., W. F. Libby, 1949. Age determination by radiocarbon content: checks with samples of known age, Science 110, 678-680.

Arnold, J., *et al.*, **2005.** Technical description and performance of the NEMO3 detector. *Nucl. Instrum. Methods in Phys. Res.* A536, 79-122.

Bailey, K., Chen, C.Y., Du, X., Li, Y.M., Lu, Z-T., O'Connor, T.P. & Young, L., 2000. ATTA – A new method of ultrasensitive isotope trace analysis. *Nuclear Instruments and Methods in Physics Research, B 172,* 224-227.

Barton, J.C., 1991. A comparison of sodium iodide and germanium low background counting systems. *J. of Phys. G*, 17, S415-S418.

Beck, J.W., Richards, D. A. Edwards, R. L. Silverman B. W., Smart P. L., Donahue D. J., Herrera Osterheld S., Burr G. S., Calsoyas LJull ., A. J. T. and Biddulph D., 2001. Extremely large variations of atmospheric ^{14}C concentration during the last Glacial period, *Science 292*, 2453-2458.

Becker, J., 2008. *Inorganic Mass Spectrometry*, New York, *Wiley*.

Beláň T., Chudý, M., Ďurana, L., Grgula, M., Holý, K., Levaiová, D., Povinec, P., Richtáriková, M., and Šivo, A., 1992. Investigation of radionuclide variations in the Bratislava air. In P. Povinec (Ed.). *Rare Nuclear Processes.* Singapore: World Scientific, pp. 345-366.

Benninghoven, A.F. G. Rüdenauer, H. W. Werner, 1987. Secondary Ion Mass Spectrometry: Basic Concepts, Instrumental Aspects, applications and Trends, Wiley, New York, 1987.

Bertine, K.K., Chow, T.J., Koide, M., Goldberg, E.D., 1986. Plutonium isotopes in the environment: Some existing problems and some new ocean results. *Journal of Environmental Radioactivity, 3,* 189.

Betti, M., Tamborini, G., Koch, L., 1999. Use of secondary ion mass spectrometry in nuclear forensic analyis for the characterization of plutonium and highly enriched uranium particles. *Anal. Chem*., 71, 2616-2622.

Betti, M., 2003. Civil use of depleted uranium. *J. Environ. Radioactivity,* 64(2), 113 – 119

Betti, M, Aldave de las Heras, .L., Janssens, A., Henrich, E., Hunter, G., Gerchikov, M., Dutton, M., van Weers, A. W., Nielsen, S., Simmonds, J., Bexon, A., Sazykina, T., 2004. *J. Environ. Radioactivity*, 74, 243-254.

Betti, M., 2005. Isotope ratio measurements by secondary ion mass spectrometry (SIMS) and flow discharge mass spectrometry (GDMS). *Int. J. Mass Spectrom.,* 242, 169-182.

Betti, M. , Aldave de las Heras, L., Tamborini, G., 2006. *Applied Spectroscopy Reviews,* 41, 491-514

Betti, M., M. Erikson, J. Jernström, and G. Tamborini, 2008. Environmental radioactive particles: A new challenge for modern analytical instrumental techniques in support of radioecology. In *Analysis of Environmental Radionuclides*, 355-370, P.P. Povinec, ed., *Elsevier*, Amsterdam.

Biddulph, D. L., 2004. Development and applications of the NSF Arizona AMS ^{129}I program. Ph. D. thesis, University of Arizona.

Biddulph, D. L., J. W. Beck, G. S. Burr and D. J. Donahue, 2006. Two 60-year records of 129I from coral skeletons in the South Pacific Ocean. In: *Radionuclides in the Environment* (P.P. Povinec and J.A. Sanchez-Cabeza, eds.) Elsevier, Amsterdam, p. 592-598.

Bird, M. I. Ayliffe L. K., Fifield L. K., Turney C. S. M., Cresswell R. G., Barrows T. T., David B., 1999., Radiocarbon dating of "old" charcoal using a wet oxidation, stepped-combustion procedure, *Radiocarbon 41*, 127-140.

Bird M. I., Fifield L. K., Santos G. M., Beaumont P. B., Zhou Y., di Tada M. I. and Hausladen P. A., 2003. Radiocarbon dating from 40 to 60ka BP at Border Cave, South Africa, *Quarternary Scence. Reviews, 22* 943-947.

Bond, G., Showers, W., Cheseby, M., Lotti, R., Almasi, P., deMenocal, P., Priore, P., Cullen, H., Hajdas, I. and Bonani, G., 1997. A pervasive millennial-scale cycle in North Atlantic Holocene and glacial climates. *Science, 278,* 1257-1266.

Brodzinski, R.L., Miley, M.S., Reeves, J.H., Avignone F. T. 1990. Further reduction of radioactive backgrounds in ultra sensitive germanium spectrometers. *Nucl. Instr. Methods* A292, 337-342.

Brodzinski, R.L., 1991. Low-level gamma-ray spectrometry. *J. Phys. G.: Nucl. Part. Phys.* 17, S403-414.

Brodzinski, R.L., 2005. Next generation germanium spectrometer background reduction techniques at 2 MeV. *J. Radioanal. Nucl. Chem.*, 264, 139-143.

Bruhn F., Duhr A., Grooter P. M., Minitrop A. and Nadeau M., 2001. Chemical removal of conservation ubstances by Soxhlet-type extraction. Radiocarbon 43, 229-237.

Buesseler, K.O. and Halverson, J.E., 1987. The mass spectrometric determination of fallout ^{239}Pu and ^{240}Pu in marine samples. *Journal of Environmental Radioactivity, 5.* 425.

Buesseler, K.O. and Scholkovitz, E.R., 1987. The geochemistry of fallout plutonium in the North Atlantic: I. A pore water study in shelf, slope and deep-sea sediments. *Geochimica Cosmochimica Acta, 51,* 2605.

Buesseler, K.O., 1993. Thermal Ionization Mass Spectrometry. In: *Development and evaluation of alternative radioanalytical methods, including mass spectrometry for marine materials.* IAEA-TECDOC-683, *IAEA,* Vienna, 45-52.

Buesseler, K.O., 1997. The isotopic signature of fallout plutonium in the North Pacific. *Journal of Environmental Radioactivity, 36*, 69-83.

Burnett, W.C., P.K. Aggarwal, A. Aureli, H. Bokuniewicz, J.E. Cable, M.A. Charette, E. Kontar, S. Krupa, K.M. Kulkarni, A. Loveless, W.S. Moore, J.A. Oberdorfer, J. Oliveira. N. Ozyurt, P. P. Povinec, A.M.G. Privitera, R. Rajar, R.T. Ramessur, J. Scholten, T. Stieglitz, M. Taniguchi, and J.V. Turner, 2006. Quantifying submarine groundwater discharge in the coastal zone via multiple methods. *Science of the Total Environment, 367*, 498-543.

Burr, G. S., Beck J. W., Taylor, F. W., Récy J., Edwards R. L., Cabioch G., Corrège T., Donahue D. J. and O'Malley J. M., 1998. High resolution radiocarbon calibration between 11.7 and 12.4 kyr BP derived from ^{230}Th ages of corals from Espiritu Santo Island, Vanuatu. *Radiocarbon, 40*, 1085-1092.

Burr, G. S., C. Galang, F. W. Taylor, C. Gallup, R. L. Edwards, Kirsten Cutler and Bill Quirk, 2004. Radiocarbon results from a 13ka BP coral from the Huon Peninsula, Papua New Guinea, *Radiocarbon 46*, 1211-1224.

Caldwell, D.O., 1991. Double beta decay experiments – present and future. *J. Phys. G.,* 17, S137-S144.

Castagnoli G.C., Lal, D., 1980. *Radiocarbon*, 22, 133.

CERN, 1985. Yellow Report 85-03, *CERN,* Geneva.

CERN, 1990. *GEANT Detector Description and Simulation Tool.* CERN Program Library Office. *CERN*, Geneva.

CERN, 1992. *Particle Data Group*. *CERN*, Geneva.

CERN, 1993. *GEANT Detector Description and Simulation Tool.* CERN Program Library Office. *CERN*, Geneva.

Chen, J.H., Edwards, R.L. & Wasserburg, G.J., 1986. ^{238}U, ^{234}U and ^{232}Th in seawater. *Earth Planetary and Science Letters, 80*, 241.

Cockburn, H. A. P. and Summerfield, M. A., 2004. Geomorphological applications of cosmogneic isotope analysis. *Progress in Physical Geography, 28,* 1-42.

Conradson, S. D., Ilham Al Mahamid, Clark, D. L., Hess, N. J., Hudson, E. A., Neu, M. P., Palmer, Ph. D., Runde, W. H., Tait, C. D., 1998. Oxidation state determination of plutonium aquo ions using x-ray absorption spectroscopy. *Polyhedron.* 17, 599–602.

Conradson, S. D., Abney, K. D., Begg, B. D., Drady, E. D., Clark, D. L., den Auwer, Ch., Ding, M., Dorhout, P. K., Espinosa-Faller, F. J., Gordon, P. L., Haire R. G., Hess, N. J., Hess, R. F., Keogh, D. W., Lander, G. H., Lupinetti, A. J., Morales, L. A., Neu, M. P., Palmer, Ph. D., Paviet-Hartmann, P., Reilly, S. D., Runde, W. H., Tait, C. D., Veirs, D. K., Wastin F., 2004. Higher order speciation effects on Plutonium L3 X-ray absorption near edge spectra. *Inorg. Chem.* 43, 116–131.

Cooper, J.A., and Perkins, R.W., 1971. An anticoincidence shielded dual Ge(Li) gamma-ray spectrometer for environmental and biological samples. *Nucl. Instr. Methods* 99, 125-146.

Cooper, L.W., Kelley, J.M., Bond, L.A., Orlandini, K.A. & Grebmeier, J.M., 2000. Sources of the transuranic elements plutonium and neptunium in Arctic marine sediments. *Marine Chemistry, 69,* 253-276.

Cumming, B. F., Laird, K. R., Bennett, J. R., Smol, J. P. and Salomon, A. K., 2002, Persistent millennial-scale shifts in moisture regimes in western Canada during the last six millennia, *Proceedings of the National Academy of Sciences, USA, 99*, 16117-16121.

Currie, L.A., 2008. Detection and quantification capabilities in nuclear analytical measurements. In *Analysis of Environmental Radionuclides*, 49-136, P.P. Povinec, ed., *Elsevier*, Amsterdam.

Dai, M.H., Buesseler, K.O., Kelley, J.M., Andrews, J.E., Pike, S. & Wacker, J.F., 2001. Size-fractionated plutonium isotopes in a coastal environment. *Journal of Environmental Radioactivity, 53*, 9-25.

Damon, P. E. and C. P. Sonnett, 1991. Solar and terrestrial components of the atmospheric ^{14}C variation spectrum. In *The Sun In Time*, (Sonnett, C.P., Giampapa, M.S., Matthews, M.S., eds) Tucson, Arizona: The University of Arizona Press, p. 361-388.

Danesi, P. R., Markowicz, A., Chine-Cano, E., Burkarrt, W., Salbu, B., Donohue, D., Ruedenauer, F., Hedberg, M., Vogt, S., Zahradnik, P., Ciurapinski, A., 2003. Depleted uranium particles in selected Kosovo samples. *J. Environ. Radioactivity, 64*(2), 143-154.

Davis, R., Harmer, D.S., Hoffman, K.C., 1966. *Phys. Rev. Letters,* 20, 1205

Debertin, K., and Helmer, R.G., 1998. *Gamma and X-Ray Spectrometry with Semiconductor Detectors. Elsevier,* Amsterdam.

De Chambost, E., F. Fercocq, F. Fernandes, E. Deloule, M. Chaussidon, 1997. In: Proceedings of the International Conference on SIMS, vol. XI, New York, *Wiley.*

De Pater I., Lissauer, J.J., 2005. Planetary sciences, *Cambridge University Press*, Cambridge.

Deloule, E., F. Allegre and S.M.F. Sheppard, 1991. *Earth Planet. Sci. Lett.* 105, 543-553.

Dergachev, V. A., Raspopov, O. M., Damblin, F., Jungner, H. and Zaitseva, G. I., 2005. Natural climate variability in the Holocene. Radiocarbon 47, 837-854.

Dixon, P., Curtis, D.B., Musgrave, J., Roesnch, F., Roach, J. & Rokop, D., 1997. Analysis of naturally produced technetium and plutonium in geologic materials. *Analytical Chemistry, 69,* 1692-1699.

Donahue D. J., Jull A. J. T., Linick T. W. and Toolin L. J., 1990a. Radiocarbon measurements at the University of Arizona AMS Facility. *Nuclear Instruments and Methods in Physics Research, B 52*, 224-228.

Donahue D. J., Linick T. W., Jull A. J. T., 1990b. Isotope-ratio and background corrections for accelerator mass spectrometry radiocarbon measurements, *Radiocarbon 32* 135-142.

Dovlete, C. & Povinec, P.P., 1999. Quantification of Uncertainty in Gamma-spectrometry – a Monte Carlo Approach. *Acta Physica Universitatis Comenianae, XL*, 43-55.

Druffel E. R. M., Griffin, S., Hwang J., Komada T., Beupre S. R., Druffel-Rodriguez K. C., Santos G. M. and Southon J., 2004. Variability of monthly radiocarbon during the 1760s in corals from the Galapagos Islands. *Radiocarbon, 46*, 627-631.

Dyke, A. S., Andrews J. T., Clark P. U., England J., Miller G. H., Shaw J. and Veillette J. J., 2001. Radiocarbon dates pertinent to defining the last glacial maximum for the Laurentide and Innuitian ice sheets. *Geological Survey of Canada, Open File 4120*, 54 pp.

Erdmann, N., Betti, M., Stetzer, O., Tamborini, G., Kratz, J.V., Trautmann, N., van Geel, J., 2000. Production of monodisperse uranium oxide particles and their characterization by scanning electron microscopy and secondary ion mass spectrometry. *Spectrochim. Acta B* 55, 1565-1575.

Erdmann, N., G. Passler, N. Trautmann, and K. Wendt, 2008. Resonance ionization mass spectrometry for trace analysis of long-lived radionuclides. In *Analysis of Environmental Radionuclides*, 331-354, P.P. Povinec, ed., *Elsevier*, Amsterdam.

Eriksson, M., Ljunggren, K., Hindorf, C., 2002. Plutonium hot particle separation techniques using real-time digital image systems. *Nucl. Instrum. Methods Phys. Res. Sect. A. 488*, 375–380.

Eriksson, M., Osán, J., Jernström, J., Wegrzynek, D., Simon, R., Chinea-Cano, E., Markowicz, S., Bamford, A., Tamborini, G., Török, S., Falkenberg, G., Alsecz, A., Dahlgaard, H., Wobrauschek, P., Streli, C., Zoeger, N., M. Betti., 2005. Source term identification of environmental radioactive Pu/U particles by their characterisation with non-destructive spectrochemical analytical techniques. *Spectrochim. Acta,* B60, 455–469.

Fairbanks, R.G. *et al.*, **2005.** Radiocarbon calibration curve spanning 0 to 50,000 years BP based on paired ^{230}Th/^{234}U/^{238}U and ^{14}C dates on pristine corals. *Quatern. Sci. Rev.* 24, 1781-1796.

Fesefeldt, H.C., 1985. *Simulations of Hadronic Showers, Physics and Applications*. Technical Report PITHA 85-02. RWTH, Aachen.

Fiedel, S. J. And Kuzmin, Y. V., 2007. Radiocarbon date frequency as an indx of intensity of Paleolithic occupation of Siberia: Did humans react predictably to climate oscillations? RADIOCARBON, Vol. 49, Nr. 2, 2007, p 741–756

Fifield L. K., 1999. Accelerator mass spectrometry and its applications, *Reports of Progress in Physics. 62.* 1223-1274.

Fifield, L.K., 2008. Accelerator mass spectrometry of long-lived heavy radionuclides. In *Analysis of Environmental Radionuclides*, 263-295, P.P. Povinec, ed., *Elsevier*, Amsterdam.

Fifield, L.K., 2004. Accelerator mass spectrometry of plutonium at 300 kV. Nucl. Instr. Methods B 223, 802-806.

Fitzsimons, I.C.W., B. Harte and R. M. Clark, 2000. *Mineral. Mag.* 64(1), 59-65.

Gagan M. K., Ayliffe L. K., Beck J. W., Cole J. L., Druffel E. R. M., Dunbar R. and Schrag D. P., 2000. New views of tropical paleoenvironments from corals. *Quaternary Science Reviews 19,* 45-64.

Gaiser, T., 1990. *Cosmic Rays and Particle Physics. Cambridge University Press.*

Garcia-León, M., Garcia-Tenorio, eds., 1994. *Low-level Measurements of Radioactivity in the Environment. World Scientific,* Singapore, 563p.

Goebel T., 2002. The "microblade adaptation" and recolonization of Siberia during the late Upper Pleistocene. In: Elston RG, Kuhn SL, editors. *Thinking Small: Global Perspectives on Microlithization*. Arlington, Virginia: American Anthropological Association., p 117, 31.

Goslar T., Arnold M., Tisnérnat-Laborde N., Hatté C., Paterne M. and Ralska-Jasiewiczowa M., 2000. Radiocarbon calibration by means of varves versus 14 C ages of terrestrial macrofossils from Lake Gociaz and Lake Perespilno, Poland. *Radiocarbon, 42,* 403-414.

Graf, K.E., 2005. Abandonment of the Siberian mammothsteppe during the LGM: evidence from the calibration of 14C-dated archaeological occupations. *Current Research in the Pleistocene* 22:25.

Grajcar, M., M. Döbeli, P. W. Kubik, C. Maden, M. Suter, H. A. Synal, 2004. ^{10}Be measurements with terminal voltages below 1MV, Nucl. Instrum. and Methods in Phys. Res. B. 223-224, 190-194.

Hallett, D. J. and Walker, R. C., 2000. Paleoecology and its application to fire and vegetation management in Kootenay National Park, British Columbia, *Journal of Paleolimnology*, 24, 401-414.

Hallett, D. J., Lepofksy, D. S., Mathewes R. W. and Lertzman, K. P., 2003. 11,000 years of fire history and climate in the mountain hemlock rain forests of southwestern British Columbia based on sedimentary charcoal, *Canadian Journal of Forest Research*, 33, 292-312.

Hatté C., Morvan J., Noury C. and Paterne M., 2001. Is classical acid-alkali-acid treatment responsible for contamination? An alternative proposition. *Radiocarbon* 43, 177-182

Hatté C. and Jull A. J. T., 2007. Radiocarbon dating: Plant macrofossils. In "Encyclopedia of Quaternary Science" (ed. S. Elias), Elsevier: Amsterdam. Pp. 2958-2965

Hatté C., Hodgins, G., Jull, A. J. T., Bishop, B. And Tesson, B., 2008. Marine chronology based on 14C dating of diatom proteins. *Marine Chemistry* 109: 143-151.

Haynes C. V., 1984. Stratigraphy and Late Pleistocene extinctions in the United States. In Martin P. S. and Klein R. G. (eds), *Quaternary Extinctions*, Tucson: University of Arizona Press.

Haynes C. V., 1991. Geoarchaeological and paleohydrological evidence for a Clovis-age drought in North America and its bearing on extinction. *Quaternary Research,* 35, 438-450.

Haynes C. V., 1992. Contributions of radiocarbon dating to the geochronology of the peopling of the New World. In: Taylor R. E., Long A. and Kra R. S. (eds) *Radiocarbon after four decades.* New York: Springer-Verlag.

Heusser, G., Hampel, W., Hübner, M., 1982. Low-level instrumentation of the Max-Planck-Institut für Kernphysik. In: *Low-level Counting*, 127-134, P. Povinec, Usav, S. eds., *VEDA*, Bratislava.

Heusser, G., 1992. Progress in Ge-spectrometry at the Max-Planck-Institut für Kernphysik Heidelber. In P. Povinec (Ed.). *Rare Nuclear Processes*. Singapore: World Scientific, pp. 247-255.

Heusser, G., 1993. Cosmic ray-induced background in Ge-spectrometry. *Nucl. Instrum. Methods* B83, 223-228.

Heusser, G., 1994. Background in ionising radiation detection. In: M. Garcia-Leon, R. Garcia-Tenorio (Eds.), *Low-Level Measurements of Radioactivity in the Environment*. Singapore, World Scientific, 69-112.

Heusser, G., 1995. Low-radioactivity background techniques. *Ann. Rev. Nuclear Part. Sci.* 45, 543-590.

Heusser, G., Laubenstein, M. and Neder, H., 2006. Low-level germanium gamma-ray spectrometry at the μBq/kg level and future developments towards higher sensitivity. In P.P. Povinec and J.A. Sanchez-Cabeza (Eds.), *Radionuclides in the Environment*, Amsterdam, Elsevier, pp. 495-510.

Hodgins, G.W.L. and Jull, A.J.T., 2004. Radiocarbon dating of petroleum-impregnated bone from Tar Pits using the ninhydrin reaction. Abstract, 34th *International Symposium on Archaeometry,* 3-7 May 2004 Zaragoza, Spain.

Holm, E., Jerome, S., Hurtgen, C., eds., 2000. *Proceedings of the ICRM Low-level Radioactivity Measurement Techniques Conference. Applied Rad. Isotopes,* 410p.

Hou, X., 2008. Activation analysis for the determination of long-lived radionuclides. In *Analysis of Environmental Radionuclides*, 370-406, P.P. Povinec, ed., *Elsevier*, Amsterdam.

Hughen K. A., Baillie M. G. L., Bard E., Beck J. W., Bertrand C. J., Blackwell P. G., Buck C. E.. Burr G. S., Cutler K., Damon P. E., Edwards R. L., Fairbanks R., Friedrich M., Guilderson T. P., Kromer B., McCormac G., Manning S., Bronk Ramsey C., Reimer P. J., Reimer R. W., Remmele S., Southon J. R., Stuiver M., Tamalo S., Taylor F. W., van der Plicht J. and Wehenmeyer C. E., 2004. MARINE04 Radiocarbon age calibration 0-26 ka cal BP. *Radiocarbon, 46,*1059-1086.

Hughey, B., R. E. Klinkowstein, R. E. Shefer, P. L. Skipper, S. R. Tannenbaum, J. S. Wishnok, 1997. Design of a compact 1 MV AMS system for biomedical research, Nuclear Instrum. Methods Phys. Res. B 123, 153-158.

Hult, M., Martinez Canet, M.J., Koehler, M., Das Neves, J., and Johnston, P.N., 2000. Recent developments in ultra low-level γ-ray spectrometry at IRMM. *Appl. Radiation Isotopes,* 53, 225-230.

Hult, M., Gasparro, J., Marissens, G., Lindahl P., Waetjen, U., Johnston, P., Wagemans, C., Koehler, M., 2006. Underground search for the decay of ^{180}Ta. *Phys. Rev. C* 74, 054311.

Inkret, W.C., Efurd, D.W., Miller, G., Rokop, D.J. & Benjamin, T.M., 1998. Applications of thermal ionization mass spectrometry to the detection of ^{239}Pu and ^{240}Pu intakes. *International Journal of Mass Spectrometry 178,* 113-120.

Inn, K.G.W., McCurdy, D., Bell III, T., Loesch, R., Morton J.S., Povinec, P., Burns, K., Henry, R. and Barss, N.M., 2001. Standard, intercomparisons and performance evaluations for low-level and environmental radionuclide mass spectrometry and atom counting. *Journal of Radioanalytical and Nuclear Chemistry, 249, 1,* 109-113.

ISO, International Standardisation Organisation, 1996. Quality system guidelines for the production of reference materials. Guide 34. ISO/IEC, Geneva.

ISO International Standardisation Organisation, 1997. Proficiency Testing and Interlaboratory Comparisons, Guide 43 1. ISO/IEC, Geneva.

Ito, M., H. Nagasawa and H. Yurimoto, 2004. *Geochim. Cosmochim. Acta* 68, 2905-2923.

JERN, 2003. *Journal of Environmental Radioactivity*, 64, 87-259 (special issue on depleted uranium).

Jernström, J.; Eriksson, M., Osán, J., Tamborini, G.; Török, S.; Simon, R.; Falkenberg, G.; Alsecz, A.; Betti, M., 2004. Non-destructive characterisation of low radioactive particles from Irish Sea sediment by micro X-ray synchrotron radiation techniques: micro X-ray fluorescence (μ-XRF) and micro X-ray absorption near edge structure (μ-XANES) spectroscopy, *J. Anal. At. Spectrom.,* 19, 1428-1433.

Jones D.G., 2001. Development and application of offshore gamma-ray spectrometry measurements: a review. *Journal of Environmental Radioactivity*, 53, 313-333.

Jones, R.H., L. A. Leeshin, Y.Guan, Z. D. Sharp, T. Durakiewicz, A. J. Schilk, 2004. *Geochim. Cosmochim. Acta* 68, 3423-3438.)

Jull, A.J.T., C.V. Haynes, Jr., D. J. Donahue, G. S. Burr and J. W. Beck, 1999. Radiocarbon ages of early man in the New World and the influence of climate change. Proc. 3^{rd} International Conference "Archaeologie et ^{14}C" (eds. J. Evin *et al.*), Lyon, France, 6-10 April, 1998, *Revu d'Archaeometrie*, *Suppl. 1999 et Soc. Préhist. Fr. Mémoire no. 26*, p. 339-343.

Jull, A.J.T., D.J. Donahue, G.S. Burr, J.W. Beck, L.R., McHargue, A.L. Hatheway, T.E. Lange, J.M. O'Malley and D. Biddulph, 2002. Radiocarbon and other radionuclide studies using accelerator mass spectormetry. In: Tenth ISMAS Workshop on Mass Spectometry. S.K. Aggarwal and D. Alamelu, eds. Indian Society of Mass Spectrometry, Mumbai, India. p. 25-34.

Jull, A.J T., G S. Burr, J. W. Beck, D. J. Donahue, D. Biddulph, A. L. Hatheway, T. E. Lange and L. R. McHargue, 2003. Accelerator mass spectrometry at Arizona: Geochronology of the climate record and connections with the ocean. *Journal of Environmental Radioactivity, 69,* 3-19.

Jull, A.J.T., G. S. Burr, L. R. McHargue, T. E. Lange, N. A. Lifton, J. W. Beck and D. J. Donahue, 2004. New Frontiers in Dating of Geological, Paleoclimatic and Anthropological applications using accelerator mass spectrometric measurements of ^{14}C and ^{10}Be in diverse samples. *Global and Planetary Change, 41,* 309-323.

Jull, A.J.T. and Burr, G. S., 2006. Accelerator Mass Spectrometry: Is the future bigger or smaller? *Earth and Planetary Science Letters*, 243, 305-325.

Jull, A.J.T, Geertsema, M., 2006. Forest fire frequency over the last 16,500 years in northern British Columbia determined from AMS radiocarbon dating of charcoal and sediments. *Radiocarbon* 48, 435-456.

Jull, A.J.T., G.S. Burr, J.W. Beck, G.W.L. Hodgins, D.L. Biddulph, L.R. McHargue, and T.E. Lange, 2008. Accelerator mass spectrometry of long-lived light radionuclides. In *Analysis of Environmental Radionuclides*, 240-262, P.P. Povinec, ed., *Elsevier*, Amsterdam.

Kalin, R.M., Long, A., 1989. Radiocarbon dating with the Quantulus in an underground counting laboratory: Performance and background sources. *Radiocarbon* 31, 359-367.

Kaye, J.H., Brauer, F.P., Conally, R.E., Rieck, H.G., 1972. Background reductions obtained with gamma-detectors by use of massive cosmic-ray shielding. *Nucl. Instr. Methods* 100, 333-348.

Keeling, C. D., S. C. Piper, R. B. Bacastow, M. Wahlen, T. P. Whorf, M. Heimann, and H. A. Meijer, 2005. Atmospheric CO_2 and $^{13}CO_2$ exchange with the terrestrial biosphere and oceans from 1978 to 2000: observations and carbon cycle implications. In *A History of Atmospheric* CO_2 *and Its Effects on Plants, Animals, and Ecosystems*, 83-113, J. R. Ehleringer, T. E. Cerling, M. D. Dearing, eds., *Springer Verlag*, New York.

Kershaw, P.J., McCubbin, D. & Leonard, K.S., 1999. Continuing contamination of north Atlantic and Arctic waters by Sellafield radionuclides. *The Science of the Total Environment, 237/238,* 119-132.

Key, R.M., 1996. WOCE Pacific Ocean Radiocarbon Program. *Radiocarbon* 38, 3, 415-423.

Kim, L., Pratt, R.H., Seltzer, S.M., and Berger, M.J., 1986. *Phys. Rev* A 33, 3002.

Klapdor-Kleingrothaus, H.V. *et al.*, 2004. Data acquisition and analysis of the ^{76}Ge double beta experiment in Gran Sasso 1990-2003. *Nucl. Instrum. Methods in Phys. Res.* A522, 371-407.

Klimenko, A.A., Pomansky, A.A., Smolnikov, A.A., 1986. Low background scintillation installation for double beta decay experiments. *Nucl. Instrum. Methods in Phys. Res.* B17, 445-449.

Kobayashi Y., Takahashi R., Shima S., Katagiri M., and Takahashi K., 1998. Development of a submersible Ge gamma-ray detector system. In *Int. Symp. on Marine Pollution,* 530-531, *IAEA,* Vienna.

Kolb, W.A., 1988. Background reduction of a semi-planar Ge(HP) detector. *Environment International,* 14, 367-370.

Komura, K. and Hamajima, Y., 2004. Y. Ogoya underground laboratory for the measurement of extremely low levels of environmental radioactivity: review of recent projects carried out at OUL. *Appl. Rad. Isotopes* 61, 185-190.

Kozlowski, T., W. Bertl,m H.P. Powell, U. Sennhauser, H.K. Walter, A. Zglinski, A. Engler, C.H. Grab, E.A. Hermes, H.P. Isaak, A. Van Der Schaaf, J. Van Der Pluym, and W.H.A. Hesselink, 1985. Energy spectra and asymmetries of neutrons emitted after muon capture. *Nucl. Phys.* A436, 717-732.

Kutschera, W., Golser, R., Priller, A and Strohmeier, B., eds., 2000. Accelerator Mass Spectrometry. Proceedings of the 8th International Conference on Accelerator Mass Spectrometry. *Nuclear Instruments and Methods in Physics Research, B, 172,* 997 pp.

Kutschera, W., 2005. Progress in isotope analysis at ultra-trace level by AMS. *International Journal of Mass Spectrometry, 242*, 145-160.

Lal, D., 1957. Ph. D. Thesis, *Banaras Hindu University*, Varanasi.

LANL, 1986. *MCNP Code. Los Alamos National Laboratory*, Los Alamos.

Laubenstein, M., Hult, M., Gasparro, J., Arnold, D., Neumaier, S., Heusser, G., Kohler, M., Povinec, P.P., Reyss, J-L., Schwaiger, M. and Theodorsson, P., 2004. Underground measurements of radioactivity. *Appl. Rad. Isotopes* 61, 167-172.

Lee, S-H., Gastaud, J., La Rosa, J.J., Liong Wee Kwong, L., Povinec, P.P., Wyse, E., Fifield, L.K., Hausladen, P.A., De Tada, L.M. and Santos, G.M., 2001. Analysis of plutonium isotopes in marine samples by radiometric, ICP-MS and AMS techniques. *Journal of Radioanalytical and Nuclear Chemistry, 248, 3,* 757-764.

Lee, S.H., P.P. Povinec, E. Wyse and M.A.C. Hotchkis, 2008. Ultra-low-level determination of ^{236}U in IAEA marine reference materials by ICPMS and AMS. *Applied Radiation and Isotopes*, submitted.

Lefèvre, O.; Betti, M.; Koch, L.; Walker, C.T., 1996. EMPA and mass spectrometry of soil and grass containing radioactivity from the nuclear accident at Chernobyl, Mikrochimica Acta, 13, 399-408.

León Vintro, L. *et al.*, **1996.** Determination of the ^{240}Pu/^{239}Pu atom ratio in low activity environmental samples by alpha- spectrometry and spectral deconvolution. *Nucl. Instr. Meth.* A369, 597-602.

Lertzman, K., Gavin, D., Hallett, D., Brubaker, L., Lepofsky, D. and Mathewes, R., 2002. Long-term fire regime estimated from soil charcoal in coastal temperate rain forests, *Conservation Ecology, 6* (2), paper 5 [on-line journal].

Leshin, L.A., A.E. Rubin and K.D. McKeegan, 1997. Geochim. Cosmochim. Acta, 61, 835-845.

Lewis, D., Miller, G., Duffy, C.J., Efurd, D.W., Inkret, W.C. & Wagner, S.E., 2001. Los Alamos National Laboratory thermal ionisation mass spectrometry results from intercomparison study of inductively coupled plasma mass spectrometry, thermal ionization mass spectrometry, and fission track analysis of μBq quantities of ^{239}Pu in synthetic urine (LA-UR-001698). *J. Radioanal. Nuclear Chemistry, 249,* 115-120.

Libby W. F., 1955. *Radiocarbon Dating. University of Chicago Press*, Chicago.

Lind, O.C., Salbu, B., Janssens, K., Proost, K., Dahlgaard, H., 2005. *J. Envioronmental Rad.* 81, 21-32.

Lindström, R.M, Lindström, D.J., Slaback, L.A., Langland, J.K., 1990. A low background gamma-ray assay laboratory for activation analysis. *Nucl. Instrum. Methods* A299, 425-429.

Liong Wee Kwong, L., La Rosa, J., Lee, S-H. and Povinec, P.P., 2001. Liquid scintillation spectrometry of beta-emitters in marine samples. *Journal of Radioanalytical and Nuclear Chemistry, 248, 3,* 751-755.

Litchfield et al., 1991. First results from the Soudan proton decay experiment. *J. Phys. G*, 17, S393-S402.

Long, C. J., Whitlock, C., Bartlein, P. J. and Millspaugh, S. H., 1998. A 9000-year fire history from the Oregon Coast Range, based on a high-resolution charcoal study, *Canadian Journal of Forest Research, 28,* 774-787.

Loosli, H.H., Moll, M., Oeschger, H and Schotterer, U., 1986. Ten years low-level counting in the underground laboratory in Bern, Switzerland. *Nucl. Instrum. Meth. Phys. Res. B 17*, 402-405.

Lyon, I.C., J.M. Saxton, P.J. McKeever, E. Chatzitheodoridis, P. Van Lierde, 1995 *Int. J. Mass Spectrom.* Ion Processes, 9, 1-16.

Macášek, F., 2008. Sampling techniques. In *Analysis of Environmental Radionuclides*, 17-48, P.P. Povinec, ed., *Elsevier*, Amsterdam.

Markgraf, V., 2001. *Interhemispheric climate linkages.* New York: Academic Press.

Martin, P. S. and Klein, R. G., 1984. *Quaternary Extinctions: A Prehistoric Revolution.* Tucson: University of Arizona Press.

Martineau, O., *et al.*, 2004. Calibration of the EDELWEISS cryogenic heat-andionisation germanium detector for dark matter search. *Nucl. Instrum. Methods in Phys. Res.* A530, 426-439.

McGeehin, J., G. S. Burr, A. J. T. Jull, D. Reines, J. Gosse, P. T. Davis, D. Muhs and J. Southon, 2001. Stepped-combustion ^{14}C dating of sediment. Radiocarbon 43(2A), 255-262.

McGeehin, J., G. S. Burr, G. Hodgins, S. J. Bennett, J. A. Robbins, N. Morehead and H. Markewich, 2004. Stepped-combustion ^{14}C dating of bomb carbon in lake sediment. *Radiocarbon, 46,* 893-900.

McHargue L. R., Damon P. E. and Donahue D. J., 1995. Enhanced cosmic-ray production of ^{10}Be coincident with the Mono Lake and Laschamp geomagneitc excursions. *Geophysical Research Letters, 22*, 659-662.

McHargue L. R., Donahue D. J., Damon P. E., Sonett C. P., Biddulph D. and Burr G. S., 2000. Geomagnetic modulation of the late Pleistocene cosmic-ray flux as determined by ^{10}Be from Blake Outer Ridge sediments, *Nuclear Instruments and. Methods in Physic Research, B 172*, 555-561.

McHargue L. R., Donahue D. J., 2005. *Earth and PlanetaryScience Lett., 232*, 193-207.

McMahon, C. A., Vintró, L. L., Mitchell, P. I., Dahlgaard, H., 2000. Oxidation state distribution of plutonium in surface and subsurface waters at Thule, northwest Greenland, *Appl. Radiat. Isot.* 52, 697–703.

McNichol, A. P., A. J. T. Jull and G. S. Burr, 2001. Converting AMS data to radiocarbon values: considerations and conventions. *Radiocarbon, 43,* 313-320.

Meltzer, D. J., Grayson, D. K., Ardila, G., Barker, A. W., Dincauze, D. F., Haynes, D. V., Mena, F., Nuñez, L. A. and Stanford, D. J., 1997. On the Pleistocene antiquity of Monte Verde, southern Chile. *American Antiquity,* 62, 659-663.

Meyer, G. A., Wells, S. G. and Jull, A. J. T., 1995. Fire and alluvial chronology in Yellowstone National Park: Climatic and intrinsic controls on Holocene geomorphic processes, *Geological Society of America Bulletin, 107,* 1211-1230.

Meyer, G. A., Pierce, J. L., Wood, S. H. and Jull, A. J. T., 2001. Fire, storms and erosional events in the Idaho batholith, *Hydrological Processes, 15,* 3025-3038.

Michel, R., 2001. Environmental radioactivity measuring methods. In: Radioactive Pollutants. (Brechignac, F. & Hoeard B.J, Eds.). EDP Sciences, Les Ulis. 27-62.

Morales, A., 1991. Searching for rigth-handed current couplings in ^{76}Ge double beta decays. *J. Phys G,* 17, S203-S210.

Moring, M., Ikäheimonen, T. K., Pöllänen, R., Ilus, E., Klemola, S., Juhanoja, J., Eriksson, M., 2001. Uranium and Plutonium containing particles in a sea sediment sample from Thule, Greenland., J. *Radioanal. Nucl. Chem.* 248, 623–627.

Morita, M., 1973. *Beta Decay and Muon Capture*. Reading: Benjamin.

Muramatsu, Y., Hamilton, T., Uchida, S., Tagami, K., Yoshida, S. & Robison, W., 2001. Measurement of ^{240}Pu/^{239}Pu isotopic ratios in soils from the Marshall Islands using ICP-MS. *The Science of the Total Environment, 278*, 151-159.

Neder, H., Heusser, G.. & Laubenstein, M., 2000. Low-level gamma-ray germanium spectrometer to measure very low primordial radionuclide concentrations. *Appl. Radiat. Isotopes* 53, 191-195.

Neff, U., Burns, S.J., Mangini, A., Mudelsee, M., Fleitmann, D., Matter A., 2001. Strong coherence between solar variability and the monsoon in Oman between 9 and 6 kyr ago. *Nature* 411(6835):290–3.

Nelson D. E., 1991 A new method for carbon isotopic analysis of protein. *Science, 251*, 552-554.

Neumaier, S., Arnold, D., Böhm, J. and Funck, E., 2000. The PTB underground laboratory for dosimetry and spectrometry. *Appl. Radiat. Isotopes* 53, 173-178.

Niese, S., Köhler, M. and Gleisberg, B., 1998. Low-level counting techniques in the underground laboratory Felsenkeller, Dresden. *J. Radioanal. Nucl. Chem.* 233, 167–172.

Niese, S., 2008. Underground laboratories for low-level radioactivity measurements. In *Analysis of Environmental Radionuclides, 209-240*, P.P. Povinec, ed., *Elsevier*, Amsterdam.

Nuñez, L. A., Varela, J., Casamiquela, R. and Villagrán, C., 1994. Reconstrucción multidisciplinaria de la occupación prehistórica de Quereo, Centro de Chile. *Latin American Antiquity, 5,* 99-118.

Osvath, I., Povinec P.P., and M. S. Baxter, M.S., 1999a. Kara Sea radioactivity assessment. *Sci. Total Environ.* 237/238, 167-179.

Osvath, I., Povinec, P.P., Huynh-Ngoc, L., and Comanducci, J-F., 1999b. Underwater gamma surveys of Mururoa and Fangataufa lagoons. *Sci. Total Environ.* 237/238, 277-286.

Osvath, I., and Povinec, P.P., 2001. Seabed γ-ray spectrometry: applications at IAEA-MEL. *J. Environ. Radioact.,* 53, 335-349.

Osvath, I., P.P. Povinec, H.D. Livingston, T.P. Ryan. S. Mulsow, and J.F. Comanducci, 2005. Monitoring of radioactivity in NW Irish Sea water using a stationary underwater gamma-ray spectrometer with satellite data transmission. *Journal of Radioanalytical and Nuclear Chemistry* 263, 437-440.

Pagava, S. Burchuladze, A., Robakidze, T., Rusetski, L., Tsintsadze, D., Povinec, P., Chudý, M., and Staníček, J., 1992. Tbilisi underground laboratory. In *Rare Nuclear Processes*, 300-304, P. Povinec, ed., *World Scientific*, Singapore.

Perna, L., Jernström, J., Aldave de las Heras, L, Hrnecek, E., de Pablo, J., Betti, M., 2005. Characterization of Irish Sea radioactively contaminated marine sediment core by radiometric and mass spectrometric techniques. *J. Radioanal. Nucl. Chem.,* 263, 367-373.

Pham, M.K., Sanchez-Cabeza, J.A., Povinec, P.P., *et al.*, **2006.** Certified reference material for radionuclides in fish flesh sample IAEA-414 (mixed fish from the Irish Sea and North Sea). Appl. Rad. Isotopes 64, 1253-1259.

Pham. M.K., Sanchez-Cabeza, J.A., Povinec, P.P. *et al.*, **2008.** Certified Reference Material IAEA-385 (Irish Sea sediment). *Applied Radiation and Isotopes*, in print.

Pettersson, H., Ballestra, S., Gastaud, J., Povinec, P.P., 2000. Report on the Worldwide Intercomparison IAEA-315. Radionuclides in the Arabian Sea sediment. Run and Reference Material IAEA-384, Radionuclides in Fangataufa Lagoon Sediment. IAEA/MEL/68, Vienna, 2000, 43p.

Pierce J. L., Meyer G. A., Jull A. J. T., 2004. Fire-induced erosion and millennialscale climate change in northern ponderosa pine forests. *Nature, 432,* 87-90.

Pigati J., Quade J., Wilson J., Jull A. J. T. and Lifton N. A., 2006. Development of low-background vacuum extraction and graphitization systems for ^{14}C dating of old (40–60 ka) samples. Quaternary International 166, 4-14.

Plastino, W., Kaihola, L., 2006. Radiocarbon measurement by liquid scintillation spectrometry at the Gran sasso National laboratory. In: In P.P. Povinec and J.A. Sanchez-Cabeza (Eds.), *Radionuclides in the Environment*, Amsterdam, Elsevier, pp. 520-528.

Pomansky, A.A., 1986. Underground low background laboratories of the Baksan Neutrino Observatory. *Nucl. Instr. Methods in Phys. Res.* B17, 406-410.

Povinec P., 1978. Multiwire proportional counters for low-level ^{14}C and ^{3}H counting, *Nucl. Instr. Methods* 156, 441-445.

Povinec, P., ed., 1982a. Low-Level Counting. *Proc. of the Second International Conference, Low Radioactivities '80.* VEDA, Bratislava, 434 pp.

Povinec, P.P., 1982b. Dual parameter gamma-ray spectrometer for low-level counting. *Isotopenpraxis* 18, 423-428.

Povinec, P., ed., 1986. Low-level Counting. *Proc. Third International Conference, Low Radioactivities '85. Nucl. Instr. Meth. Phys. Res., B17, 377-588.*

Povinec, P., ed., 1987. Low-Level Counting and Spectrometry. *Proceedings of the Third International Conference, Low Radioactivities '85.* VEDA, Bratislava, 308 pp.

Povinec, P.., ed., 1991a. Rare Nuclear Decays and Fundamental Physics. *Proc. 14th Europhysics Conference on Nuclear Physics. Journal of Physics G., 17,* 543 pp.

Povinec, P., 1991b. Low-level Gas Counting. In: *Proceedings of the Second International Summer School.* (Garcia-Leon, M. & Madurga, G., Eds). World Scientific, Singapore. 38-72.

Povinec, P., 1992. Rare Nuclear Processes. *Proc. 14th Europhysics Conference on Nuclear Physics*. World Scientific, Singapore. 441 pp.

Povinec, P., 1994. Underground low-level counting. In: *Low-level Measurements of Radioactivity in the Environment*, 113-140 . M. Garcia-Leon, M. Garcia-Tenorio, eds., *World Scientific*, Singapore.

Povinec, P.P., ed., 1999. Marine Environment – Understanding and Protecting for the Future. Sci. Total. Environm. 237/238, 1-526.

Povinec, P.P., 2004. Developments in analytical technologies for marine radionuclide studies. In: *Marine Radioactivity*, 237-294, H.D. Livingston, ed., *Elsevier*, Amsterdam.

Povinec, P.P., 2005. Ultra sensitive radionuclide spectrometry: Radiometrics and mass spectrometry synergy. *J. Radioanal. Nuclear Chemistry*, 261, 413-417.

Povinec, P.P., ed., 2008. *Analysis of Environmental Radionuclides*, *Elsevier*, Amsterdam, in print.

Povinec, P., S. Usačev, eds., 1977. Low-radioactivity Measurements and Applications. *Proceedings of the International Conference. SPN, Bratislava.* 542 pp.

Povinec, P.P., Osvath, I., and Baxter, M.S., 1996. Underwater gamma-spectrometry with HPGe and NaI (Tl) detectors, *Appl. Radiat. Isot.* 47, 1127-1133.

Povinec, P.P., Osvath, I., Baxter, M.S. Harms, I., Huynh-Ngoc, L., Liong Wee Kwong, L., and Pettersson, H.B.L., 1997. IAEA-MEL's contribution to the investigation of Kara Sea radioactivity and radiological assessment, *Marine. Poll. Bull.* 35, 235-241.

Povinec, P.P., Woodhead, D., Blowers, P., Bonfield, Cooper, M., Chen, Q.J., Dahlgaard, H., Dovlete, C., Fox, V., Froehlich, K., Gastaud, J., Gröning, M., Hamilton, T., Ikeuchi, Y., Kanisch, G., Krüger, A., Liong Wee Kwong, L., Matthews, M., Morgenstern, U., Mulsow, S., Pettersson, H.B.L., Smedley, P., Taylor, B., Taylor C., and Tinker, R., 1999. Marine Radioactivity Assessment of Mururoa and Fangataufa Atolls. *Sci. Total Environ.* 237/238, 249-267.

Povinec, P.P. and Pham, M.K., 2000. Report on the Intercomparison Run IAEA-384. Radionuclides in Fangataufa Lagoon sediment. IAEA/AL/126. *IAEA*, Vienna.

Povinec, P.P., La Rosa, J.J., Lee, S.H., Mulsow, S., Osvath, I., and Wyse, E., 2001. Recent developments in radiometric and mass spectrometry methods for marine radioactivity measurements. *J. Radioan. & Nuc. Chem.,* 248, 713-718.

Povinec, P.P., Badie, C., Baeza, A., Barci-Funel, G., Bergan, T.D., Bojanowski, R., Burnett, W., Eikenberg, J., Fifield, L. K., Serradell, V., Gastaud, J., Goroncy, I., Herrmann, J., Hotchkis, M.A.C., Ikaheimonen, T. K., Jakobson, E., Kalimbadjan, J., La Rosa, J.J., Lee, S-H., Liong Wee Kwong, L., Lueng, W.M., Nielsen, S.P., Noureddine, A., Pham, M.K., Rohou, J-N., Sanchez-Cabeza, J.A., Suomela, J., Suplinska, M. and Wyse, E., 2002. Certified Reference Material for radionuclides in seawater IAEA-381 (Irish Sea water). *Journal of Radioanalytical and Nuclear Chemistry 251, 369-374.*

Povinec, P.P. *et al.*, **2003a.** IAEA'97 expedition to the NW Pacific Ocean – results of oceanographic and radionuclide investigations of the water column. *Deep-Sea Research* II, 50, 2607-2638.

Povinec, P.P., Bailly du Bois, P., Kershaw, P.J., Nies, H., Scotto, P., 2003b. Temporal and spatial trends in the distribution of ^{137}Cs in surface waters of Northern European Seas – a record of 40 years of investigations. Deep Sea Res. II50, 2785-2802.

Povinec, P.P., Comanducci, J.F., and Levy-Palomo, I., 2004. IAEA-MEL's underground counting laboratory in Monaco – background characteristics of HPGe detectors with anti-cosmic shielding. *Appl. Rad. Isotopes* 61, 85-93.

Povinec, P.P. and Sanchez-Cabeza, eds., 2006. Radionuclides in the Environment, *Elsevier*, 646 p.

Povinec, P.P., Comanducci, J.F., and Levy-Palomo, I., 2006a. IAEA-MEL's underground counting laboratory – The design and main characteristics. In *Radionuclides in the Environment*, 538-553, P.P. Povinec and J.A. Sanchez-Cabeza, eds., *Elsevier,* Amsterdam.

Povinec, P.P., P.K. Aggarwal, A. Aureli, W.C. Burnett, E.A. Kontar, K.M. Kulkarni, W.S. Moore, R. Rajar, M. Taniguchi, J.-F. Comanducci, G. Cusimano, H. Dulaiova, L. Gatto, M. Groening, S. Hauser, I. Levy-Palomo, B. Oregioni, Y. R. Ozorovich, A. M. G. Privitera, and M. A. Schiavo, 2006b. Characterisation of submarine groundwater discharge offshore south-eastern Sicily. *Journal of Environmental Radioactivity,* 89, 81-101.

Povinec, P.P. *et al.*, 2007. Reference material for radionuclides in sediment IAEA-384 (Fangataufa Lagoon sediment). *Journal of Radioanalytical and Nuclear Chemistry,* 273, 383-393.

Povinec, P.P., M. Aoyama, M. Fukusawa, K. Hirose, K. Komura, J.-A. Sanchez-Cabeza, J. Gastaud, M. Ješkovský, I. Levy-Palomo, and I. Sýkora, 2008a. Profiles of ^{137}Cs in South Indian Ocean water along the 20°S latitude – an evidence for accumulation of pollutants in the subtropical gyre. *Progress in Oceanography*, submitted.

Povinec, P.P., H. Bokuniewicz, W.C. Burnett, J. Cable, M. Charette, W.S. Moore, J.A. Oberdorfer, J. de Oliveira, T. Stieglitz, M. Taniguchi, 2008b. Isotope tracing of submarine groundwater discharge offshore Ubatuba, Brazil: Results of the IAEA-UNESCO SGD project, *Journal of Environmnetal Radioactivity*, submitted.

Povinec, P.P., Betti, M., Lee, S.H., *et al.*, 2008c. Evidence for the presence of enriched uranium particles in Mediterranean sediment, in preparation.

Rebollo N. R., Cohen-Ofri I., Popovitz-Biro R., Bar-Yosef O., Meignen L., Goldberg P., Weiner S. and Boaretto E., 2008. Stuctural characterization of charcoal exposed to high and low pH: Implications for ^{14}C sample preparation and charcoal preservation. *Radiocarbon*, in press.

Reimer, P.J., 2004. IntCal04 Calibration issue. *Radiocarbon* 46, 1029-1304.

Reimer, P. J., M. G. Baillie, E. Bard, A. Bayless, J. W. Beck, P. G. Blackwell, C. E. Buck. G. S. Burr, K. Cutler, P. E. Damon, R. L. Edwards,R. Fairbanks, M. Friedrich, T. P. Guilderson, C. Herring, K. A. Hughen, B. Kromer, G. McCormac, S. Manning, C. Bronk Ramsey, R. W. Reimer, S. Remmele, J. R. Southon, M. Stuiver, S. Tamalo, F. W. Taylor, J. van der Plicht C. E. Wehenmeyer, 2005. IntCal04 Terrestrial radiocarbon calibration 0-26 ka cal BP. *Radiocarbon,* 46, 1029-1058.

RPP, 1994. *Review of Particle Properties. Physical Review* D50, 1173.

Reyss, J.-L., Schmidt, S., Legeleux, F. & Bonté, P., 1995. Large, low background well-type detectors for measurements of environmental radioactivity. *Nucl. Instrum. Methods* A357, 391-397.

Richards, D. A. and J. W. Beck, 2001. Dramatic shifts in radiocarbon dating the last glacial period. *Antiquity,* 75, 482-485.

Riciputi, L.R., Cole, D.R., Machel, H.G., 1996. Sulfide formation in reservoir carbonates of the Devonian Nisku Formation, Alberta, Canada: An ion microprobe study. *Geochimica et Cosmochimica Acta* 60 (2), pp. 325-336.

Riciputi, L.R., Paterson, B.A., Ripperdan, R.L., 1998. Measurement of light stable isotope ratios by SIMS: Matrix effects for oxygen, carbon, and sulfur isotopes in minerals, *International Journal of Mass Spectrometry* 178 (1-2), pp. 81-112.

Ro, C.-U., Osán, J., Szalóki, I., de Hoog, J., Worobiec, A., Van Grieken, R., 2003. A Monte Carlo program for quantitative electron-induced X-ray analysis of individual particles, *Anal. Chem.* 75, 851–859.

Roos, P., 2008. Analysis of radionuclides using ICPMS. In *Analysis of Environmental Radionuclides, 295-330*, P.P. Povinec, ed., *Elsevier*, Amsterdam.

Saito, M., Iwamoto, S, Sumino, T., 2000. Tritium concentration in Aquatic environment determined by SPE tritium enrichment apparatus. In *Distribution and Speciation of Radionuclides in the Environment*, 130-132. J. Inaba, S. Hisamatsu, Y. Ohtouka, eds., *IES,* Rokkasho.

Salbu, B., 2001. Actinides associated with particles. In: *Plutonium in the Environment* A. Kudo, ed., Oxford, *Elsevier,* p. 121-138.

Salbu, B., Janssens, K., Lind, O.C., Proost, K., Danesi, P.R., 2003. Oxidation states of uranium in DU particles from Kosovo. *J. Environ. Radioact.,* 64(2), 167–173.

Salbu, B., Janssens, K., Lind, O.C., Proost, K., Gijsels, L. Danesi, P.R., 2005. Oxidation states of uranium in DU particles from Kuwait. *J.Environ.Radioact.,* 78, 125-135.

Schlosser, P. *et al.*, **1999.** Pathways and residence times of dissolved pollutants in the ocean derived from transient tracers and stable isotopes. *Science of the Total Environment* 237/238, 15-30.

Schmidt, A., G. S. Burr, F. W. Taylor, J. O'Malley and J. W. Beck, 2004. A semiannual radiocarbon record of a modern coral from the Solomon Islands, *Nuclear Instruments and Methods in Physics Research, B*223, 420-427.

Schumacher, M., F. Fernandes, E. de Chambost, 2004. *Appl. Surf. Science* 231-232, 878-882.

Schramm, A., Stein, M., Golstein, S.I., 2000. Calibration of the ^{14}C time scale to over 40 ka by ^{234}U/^{230}Th dating of Lake Lisan sediments. *Earth Planet. Sci. Lett.* 175, 27-40.

Schroettner, T., Schwaigerm M. and Kindl, P., 2004. Optimization of an active cosmic veto shielding. *Applied Radiation and Isotopes* 61, 133-138.

Schröder, W.U., Jahnke, U., Lindenberger, K.H., Röschert, G., Engfer, R. & Walter, H.K., 1974. *Z. Physik* 268, 57.

Schwaiger, M., Edelmaier, R., Holm, E., Jerome, S., eds., 2004. *Low-Level Radionuclide Measurement Techniques – ICRM. Applied Rad. Isotopes,* 419p..

Scott, E.M., and Ph.M. Dixon, 2008. Statistical sampling design for radionuclides. In *Analysis of Environmental Radionuclides*, P.P. Povinec, ed., *Elsevier*, Amsterdam, in print.

Seltzer, S.M. and Berger, M.J., 1985. *Nucl. Instr. Methods*, B12, 95.

Semkow, T.M., Parekh, P.P., Schwenker, C.D., Khan, A.J., Bari, A., Colaresi, J.F., Tench, O.K., David, G. and Guryn, W., 2002. Low-background gamma spectrometry for environmental radioactivity. *Appl. Rad. Isotopes* 57, 213-223.

Simons, D. S., 1986. Single particle standards for Isotopic measurements of Uranium by Secondary Ion Mass Spectrometry, *J. Trace Microprobe Tech.,* 4, 185-195.

Skog, G., 2007. The single stage AMS machine at Lund University: Status report. *Nuclear Instruments and Methods in Physics Research, B*259, 1-6.

Slodzian, G. *et al.*, **2001.** *EPJ Appl. Phys.* 14 (3), 199–231.

Smith, P.F. and Levin, D.J., 1990. Dark matter detection. *Physics Reports* 187, 203-280.

SNO Collaboration, 2005. A search for periodicities in the ^{8}B solar neutrino flux measured by the Sudbury Neutrino Observatory, *Phys. Rev. D* 72, 052010.

Southon, J., G. Santos, K. Druffel-Rodriguez, E. Druffel, S. Trumbore, X. Xu, S. Griffin, S. Ali, M. Mazon, 2004. The Keck Carbon Cycle AMS Laboratory, University of California, Irvine: initial operation and a background surprise, *Radiocarbon* 46, 41-49.

Staníček, J. and Povinec, P.P., 1986. Internal pair production in alpha-decaying nuclei and gamma-ray intensities of ^{241}Am. *Nucl. Instr. Methods* B17, 462-466.

Sternheimer, R.M., 1971. *Phys. Rev.* B3, 3681.

Stoffels, J. J.; Briant, J. K.; Simons, D. S., 1994. A Particulate Isotopic Standard of Uranium and Plutonium in an Aluminosilicate Matrix, *J. Am. Soc. Mass Spectrom.* 5, 852-858.

Stuiver, M. and Kra, R., eds., 1993. Calibration issue. *Radiocarbon* 35, 1-244.

Stuiver, M., and van der Plicht, J., eds., 1998. INTCAL98: Calibration issue. *Radiocarbon* 40, 1041-1159.

Suter, M., Jacob St. and Synal, H.-A, 1997. AMS of ^{14}C at low energies, Nuclear Instrum. Methods Phys. Res. B 123, 148-152.

Suter, M., Jacob, S. W. A. and Synal, H. A., 2000. Tandem AMS at sub-MeV energies. Nuclear Instrum. Methods Phys. Res. B 172, 144-151.

Suzuki, T., Maesday, D.F. and Roalsvik, J.P., 1987. *Phys. Rev* C35, 2212.

Sýkora, I. and Povinec, P.P., 1986. Measurement of electron capture to positron emission ratios in light and medium nuclides. *Nucl. Instr. Methods,* B17, 467-471.

Sýkora, I., Ďurčík, M., Staníček, J. and Povinec, P.P., 1992. Radon problem in low-level gamma-ray spectrometry. In: P.P Povinec (Ed.). *Rare Nuclear Processes*. World Scientific, Singapore, pp. 321-326.

Synal, H.A., Stocker, M., Sutter, M., 2006. MICADAS: a new compact radiocarbon AMS system. 60-61. In *Proc. 10^{th} Intern. AMS Conference, UCLA,* Berkeley.

Tamborini, G.; Betti, M.; Forcina, V.; Hiernaut, T.; Koch, L., 1998. Application of Secondary Ion Mass Spectrometry to the identification of single particles of Uranium and their isotopic composition, *Spectrochimica Acta,* B53, 1289-1302.

Tamborini. G., Donohue, D.L., Rudenauer, F.G., Betti, M., 2004. Evaluation of practical sensitivity and useful ion yield for uranium detection by secondary ion mass spectrometry. *J. Anal. At. Spectrom.* 19, 203-208.

Tamborini, G., Betti, M., 2000. Characterisation of radioactive particles by SIMS. *Mikrochim. Acta*, 132, 411-417.

Tamborini, G., Phinney, D., Bildstein, O., Betti, M., 2002. Oxygen Isotopic Measurements by Secondary Ion Mass Spectrometry in Uranium Oxide Microparticles: A Nuclear Forensic Diagnostic. *Anal.Chem.,* 74, 6098-6101.

Taylor, R.E., 2000. The contribution of radiocarbon dating to New World archaeology. *Radiocarbon* 42, 1-21.

Taylor, R.N., Croudace, I.W., Warwick, P.E. & Dee, S.J., 1998. Precise and rapid determination of ^{238}U/^{235}U and uranium concentration in soil samples using thermal ionisation mass spectrometry. *Chem. Geology, 144,* 73.

Theodorsson, P., 1996. *Measurement of Weak Radioactivity*. World Scientific, Singapore, 333 p.

Tisnérat-Laborde, N., Valadas, H., Kaltnecker, E. and Arnold M., 2003. AMS radiocarbon dating of bones at LSCE. *Radiocarbon, 45,*, 409-419.

Török, S., J. Osán, L. Vincze, S. Kurunczi, G. Tamborini, M. Betti, 2004. *Spectrochim. Acta* B 59, 689-699.

Treichel, M., Boehm, F., Broggini, C., Reusser, D., Fisher, P., Fluri, L., Gabathuler, K., Henrikson, H., Joergens, V., Mitchell L.W., Nussbaum, C., Vuilleumier, J.-L., 1991. Double beta decay and dark matter in the Gotthard germanium experiment. *J. Phys. G,* 17, S193-S201.

Tuniz C, Bird J. R., Fink D.and Herzog G. F., 1998. *Accelerator Mass Spectrometry: Ultrasensitive analysis for global science*, CRC Press, Boca Raton, 371pp.

Turcq, B., Siffedine, A., Martin, L., Absy, M. L., Soubies, F., Suguio, K. and Volkmer-Ribeiro, C., 1998. Amazonia rainforest fires: A lacustrine record of 7000 years, *Ambio 27,* 139-142.

Tyler, A.N., 2008. In situ and airborne gamma-ray spectrometry. In *Analysis of Environmental radionuclides, 407-448*, ed. P.P. Povinec. *Elsevier,* Amsterdam.

UNSCEAR, 1993. *Sources and Effects of Ionizing radiation. United Nations,* New York, 922p.

Van der Plicht, J. *et al.*, **2004.** NOTCALO4-comparison calibration ^{14}C records 26-50 cal kyr BP. *Radiocarbon 46*, 1225-1238.

Van Put, P., Debauche, A., De Lellis, C. and Adam, V., 2004. Performance level of an autonomous system of continuous monitoring of radioactivity in seawater. *Journal of Environmental Radioactivity,* 72, 177-186.

Vojtyla, P. Beer, J. and Stavina, P., 1994. Experimental and simulated cosmic muon induced background of a Ge spectrometer equipped with a top side anticoincidence proportional chamber. *Nucl. Instrum. Methods* B86, 380-386.

Vojtyla, P., 1995. A computer simulation of the cosmic-muon background induction in a Ge γ-spectrometer using GEANT. *Nucl. Instr. Methods,* B100, 87-96.

Vojtyla, P., 1996. Influence of shield parameters on cosmic-muon induced backgrounds of Ge γ-spectrometers. *Nucl. Instr. Methods,* B111, 163-170.

Vojtyla, P. and Povinec, P.P., 2000. A Monte Carlo simulation of background characteristics of low-level HPGe detectors. *Appl. Rad. Isotopes* 53, 185-190.

Vojtyla, P. and Povinec, P.P., 2006. Monte Carlo simulation of the muon-induced background of an anti-Compton gamma-ray spectrometer placed in a surface and underground laboratory. In: *Radionuclides in the Environment*, 529-537, P.P. Povinec and J.A. Sanchez-Cabeza, eds., *Elsevier*, Amsterdam.

Watt, D.E. and Ramsden, D., 1964. *High Sensitivity Counting Techniques. Pergamon,* Oxford.

Wedekind, Ch., Schilling, G., Grüttmüller, M. and Becker, K., 2000. Marine environmental radioactivity monitoring by "in-situ" radiation detection. *Kerntechnik*, 65, 190-194.

Wendt, K., Trautmann, N. & Bushaw, B.A., 2000. Resonant laser ionization mass spectrometry: An alternative to AMS? *Nucl. Instr. Meth. Phys. Res., B 172,* 162-169.

White, F. A. & Wood, G.M., 1988. Mass spectrometry – Applications in Science and Engineering. Wiley-Interscience, New York.

Wyse, E., Lee, S.H., La Rosa, J., Povinec, P.P., de Mora, S.J., 2001. ICP sector field mass spectrometry analysis of plutonium isotopes: recognizing and resolving potential interferences. *J. Anal. At. Spectrom.* 16, 1107-1111.

Zdesenko, Y., 1991. Double beta decay experiment at Kiev. *Journal of Physics* G, 17, S243-S250.

Zvara, I., Povinec, P.P. and Sýkora, I., 1994. Determination of very low-levels of radioactivity. *Pure and Appl. Chem.* 66, 12, 2537-2586.